

JAERI-M

5984

702  
NEANDC(J)38L  
INDC(JAP)25L

PROCEEDINGS OF THE EANDC TOPICAL DISCUSSION ON  
"CRITIQUE OF NUCLEAR MODELS AND  
THEIR VALIDITY IN THE EVALUATION OF NUCLEAR DATA"

February 1975

Edited by Toyojiro FUKETA

日本原子力研究所  
Japan Atomic Energy Research Institute

この報告書は、日本原子力研究所が JAERI-M レポートとして、不定期に刊行している研究報告書です。入手、複製などのお問い合わせは、日本原子力研究所技術情報部（茨城県那珂郡東海村）あて、お申しこしてください。

JAERI-M reports, issued irregularly, describe the results of research works carried out in JAERI. Inquiries about the availability of reports and their reproduction should be addressed to Division of Technical Information, Japan Atomic Energy Research Institute, Tokai-mura, Naka-gun, Ibaraki-ken, Japan.

Proceedings of the EANDC Topical Discussion on  
"Critique of Nuclear Models and Their Validity  
in the Evaluation of Nuclear Data"

Editor: Toyojiro FUKETA  
Division of Physics, Tokai, JAERI  
(Received January 21, 1975)

The topical discussion meeting was held on March 27, 1974 in the middle of the 17th meeting of the European-American Nuclear Data Committee (EANDC)\* from March 25 through 29, 1974 at Akasaka Prince Hotel, Tokyo. The topical discussion meeting was organized jointly by JAERI and Japanese Nuclear Data Committee. About 70 researchers including the attendants of the EANDC meeting participated in the discussion.

The proceedings consist of 18 papers and the records of discussion prepared later by each speaker. Most of the papers are kept intact by photo-offsetting the manuscripts; the editorial arrangement was intended to be minimal.

Organizing Committee

Kineo Tsukada (Member of the EANDC; JAERI)  
Toyojiro Fuketa (Local Secretary of the EANDC meeting; JAERI)  
Kichinosuke Harada (JAERI)  
Sin-iti Igarasi (JAERI)  
Mitsuji Kawai (Tokyo Institute of Technology)  
Yasuyuki Kikuchi (JAERI)  
Ryuzo Nakasima (Hosei University)  
Kazuaki Nishimura (JAERI)  
Shigeya Tanaka (JAERI)  
Tokuo Terasawa (University of Tokyo)  
Nobuhiro Yamamuro (Tokyo Institute of Technology)

---

\* now Nuclear Energy Agency Nuclear Data Committee (NEANDC).

“核データの評価における原子核模型と  
その妥当性の評論”に関するEANDC  
トピカル・ディスカッション報告

日本原子力研究所東海研究所物理部

(編集者) 更田豊治郎

(1975年1月21日受理)

1974年3月25日から29日に東京の赤坂プリンスホテルで行われた欧米核データ委員会(EANDC)\*の第17回会合の中間の一日、3月27日に表記の研究会が開催された。研究会は原研とシグマ委員会との共同で準備された。研究会にはEANDC会合の出席者を含めて約70名の研究者が参加した。

この報告書は18編の論文と、後で発言者によって書きとめられた討論記録から成っている。この報告書では、提出された原稿のオフセット写真印刷によって、大部分の論文がもとのままに保たれており、編集上の整理は最小限にとどめるようにした。

研究会世話人

塚田 甲子男	(EANDC委員, 原研)
更田 豊治郎	(EANDC会合ロ-カル・セクレタリー, 原研)
原田 吉之助	(原研)
五十嵐 信一	(原研)
河合 光路	(東京工業大学)
菊池 康之	(原研)
中嶋 龍三	(法政大学)
西村 和明	(原研)
田中 茂也	(原研)
寺沢 徳雄	(東京大学)
山室 信弘	(東京工業大学)

---

\* 現在NEA核データ委員会 (NEANDC) と改称。

## CONTENTS

### SESSION I (Chairman: H. Condé)

I-1	Models Based on Multichannel R-Matrix Theory for Evaluating Light Element Reactions .....	1
	D. C. Dodder, G.M. Hale, R.A. Nisley, K. Witte and P.G. Young (presented by H.T. Motz) Discussion .....	31
I-2	A Study on the Hierarchy Model of Nuclear Reactions .....	34
	Y. Kitazoe and T. Sekiya Discussion .....	49
I-3	Effects of Nuclear Deformations on Neutron Total Cross Sections ....	51
	Ch. Lagrange	
I-4	Evaluation of Neutron-Nucleus Cross Sections in Heavy Nuclei with a Coupled Channel Model in the Range of Energy from 10 keV to 20 MeV .....	58
	Ch. Lagrange	
I-5	Calculation of $(n, n'\gamma)$ Cross Sections from 2 to 7 MeV Neutron Energy for Light Nuclei .....	68
	B. Duchemin	
I-6	Statistical Model Evaluation of Neutron-Induced Fission and Capture Cross Sections of Heavy Nuclei for Energies in the Range 3 keV to 1 MeV .....	71
	P. Thomet	
I-7	Evaluation of the $(n, xn)$ and $(n, xnf)$ Cross Sections for Heavy Nuclei with the Statistical Model .....	76
	J. Jary (The above five papers were presented all together by A. Michaudon.) Discussion .....	82
I-8	Some Remarks on the Use of Nuclear Models in the Evaluation Work ...	83
	V. Benzi, F. Fabbri and G. Reffo (This paper was not orally presented.)	

### SESSION II (Chairman: K. Harada)

II-1	On the Calculation Methods of the Neutron Capture Cross Sections ...	103
	S. Igarasi, A. Mori and K. Harada Discussion .....	118
II-2	Status of Predictions of Photon Strength Functions by Giant Dipole Resonance and Valence Models .....	119
	H. E. Jackson Discussion .....	136
II-3	Calculation of the Collective Radiative Capture Cross Sections for 5-20 MeV Neutrons .....	137
	H. Kitazawa and N. Yamamuro Discussion .....	158

SESSION III (Chairman: P. Ribon)

III-1	Optical Model Analysis for $^{56}\text{Fe}$ .....	159
	H. Yamakoshi	
	Discussion .....	191
III-2	Optical Model Calculations at Rensselaer Polytechnic Institute, ...	193
	J. M. Sierra and P.J. Turinsky	
	(presented by R.C. Block)	
	Discussion .....	211
III-3	Analysis of Neutron Cross Sections Using the Coupled-Channel Theory .....	212
	S. Tanaka	
	Discussion .....	229
III-4	Optical Model Analysis of Neutron Cross Sections and Strength Functions .....	230
	C. M. Newstead and S. Cierjacks	
	Discussion .....	244

SESSION IV (Chairman: W. G. Cross)

IV-1	Evaluation of Neutron Elastic and Inelastic Scattering of Cr and Ni Isotopes Using Coupled-Channel Calculations .....	245
	A. Prince and M.R. Bhat	
	(presented by R.E. Chrien)	
	Discussion .....	256
IV-2	The Effect of Gamma Ray Strength Function on the Neutron Capture and Gamma Ray Production Cross Section of Manganese and Europium .....	257
	H. Takahashi	
	(presented by R.E. Chrien)	
	Discussion .....	268
IV-3	Models, Measurements and Evaluation .....	269
	P. Guenther, P. Moldauer and A. Smith	
	(presented by H.E. Jackson)	
	Discussion .....	298

SESSION V (Chairman: G. L. Rogosa)

V-1	Free Discussion .....	299
	List of Participants of the 17th EANDC Meeting .....	301
	Author Index .....	304

I-1. Models Based on Multichannel R-Matrix Theory  
for Evaluating Light Element Reactions<sup>\*</sup>

D. C. Dodder, G. M. Hale, R. A. Nisley, K. Witte, and P. G. Young

Los Alamos Scientific Laboratory, University of California

Los Alamos, New Mexico 87544

Abstract

Multichannel R-matrix theory has been used as a basis for models for analysis and evaluation of light nuclear systems. These models have the characteristic that data predictions can be made utilizing information derived from other reactions related to the one of primary interest. Several examples are given where such an approach is valid and appropriate.

---

\* Work performed under the auspices of the United States Atomic Energy Commission.

Models Based on Multichannel R-Matrix Theory  
for Evaluating Light Element Reactions

D. C. Dodder, G. M. Hale, R. A. Nisley, K. Witte, and P. G. Young

As has no doubt been emphasized in the other papers in this symposium, the reason for using models in data evaluations is to try to make use of more information than is just contained in the measurements under consideration. This additional information ranges all the way from knowledge of the general laws of nature to results of explicit measurements closely related to those being evaluated. In the same way models range, in their philosophy, from little more than mathematical parameterizations of data to detailed and realistic constructs clearly based on our knowledge of physics. We would like to show that the R-matrix formalism of Wigner and Eisenbud<sup>1)</sup> offers a framework for embodying a number of different model concepts in nuclear data evaluation.

The R-matrix theory is a general formalism that is really a method of description that insures compatibility with fundamental physical laws. Invariance principles such as unitarity and conservation of total angular momentum are maintained, and in addition it can be shown that its content is closely related to requirements of causality. Within this framework it is an economical and appropriate description for many observed phenomena. In its most general form it is already a model in the sense that it does insist on compliance with the general laws involved in its derivation; on the other hand much more model-like behavior can be imposed by constraining the values of its parameters in appropriate ways. We shall give a number of examples of this.

Even an outline of the derivation of R-matrix theory<sup>2)</sup> is beyond the scope of this report. Some idea of its structure however is essential to understanding our point of view. The entire observational content of collision processes is contained in the so-called collision matrix (S-matrix). This matrix, relying on the superposition principle of quantum mechanics, essentially gives the outgoing amplitudes of a collision in terms of the incoming ones. At this descriptive level of procedure certain general symmetry principles are directly reflected in the structure of the collision matrix. The conservation of particles is imposed by having the matrix unitary. Time reversal invariance is equivalent to having the matrix symmetric in a suitable representation. And finally conservation of total angular momentum and parity means that the matrix can be so chosen as to reduce to a series of disconnected submatrices along the diagonal, each submatrix referring to a state of given J and parity and each submatrix being individually unitary and symmetric. It is evident that already a description of scattering and reaction processes at this level demands relationships between the different processes and that the requirement of consistency is a valuable aid to data evaluation.

The energy dependence of the collision matrix elements is, however, quite complicated, and depends on the external Coulomb and centrifugal barriers as well as the nuclear forces. This is seen even in the simple case of a single isolated energy level, where the cross section for a transition from state i to state f is given by:

$$\sigma_{fi} \approx \frac{\Gamma_i \Gamma_f}{(E - E_r)^2 + \frac{1}{4}(\Gamma_i + \Gamma_f)^2}$$

Here the widths  $\Gamma_i$  and  $\Gamma_f$  have factors (the so-called penetration factors) which are often strongly energy dependent, and the resonant energy  $E_r$  is also in general energy dependent. The R-matrix formalism deals with this situation by dividing the configuration space in each channel into an inner and an outer region, the inner region being that where the strong interaction predominates, and the outer that where only the Coulomb force exists, and where the main effect of the centrifugal barrier is felt. The R-matrix itself is a relationship between the values and derivatives of the wave functions at the boundary between the two regions. The theory shows that the R-matrix must, under very general assumptions about the nature of the interaction in the inner region, have the form

$$R_{\alpha's'l',\alpha s l}^J = \sum_{\lambda} \frac{\gamma_{\lambda\alpha s l}^J \gamma_{\lambda\alpha's'l'}^J}{E_{\lambda}^J - E}$$

where  $J, s, l$  have their usual meanings,  $\alpha$  is the channel label,  $E$  is the C.M. energy,  $E_{\lambda}^J$  are the eigenvalues of the Hamiltonian operator in the interior region with a certain set of boundary conditions on the logarithmic derivatives of the wave functions, and the  $\gamma_{\lambda\alpha s l}$ , the reduced width amplitudes, are essentially the values of the wave functions on the boundaries. The collision matrix can be expressed in terms of the R-matrix but we shall not give the expression here. We usually let the computing machine do this rather tedious work. The point is that the rather simple form of the R-matrix allows model-like behavior to be used in parameterization of the nuclear data. And the main reason this is appropriate is that the values of radii in the different channels which are the boundaries between the inner

and outer regions, correspond in a real way to the actual nuclear radii in the different configurations. This means that the physically occurring cutoff in  $l$  values is naturally accounted for in R-matrix calculations through the dependence of the phase shifts on the penetration factors.

In the employment of the R-matrix approach as a model it is clear that it will be macroscopic like the optical model, rather than microscopic like the shell model. Its usefulness is indicated by a few general observations. The levels and widths occurring in the general R-matrix expression can be made to correspond to real energy levels of physical systems and frequently relatively few suffice to entirely describe a given ( $J$ , parity) state. Furthermore, symmetries of the internal Hamiltonian can be applied directly to the R-matrix. In cases where the internal interaction is dominated by nuclear forces, for instance, it is appropriate to impose constraints reflecting parity conservation and charge symmetry or charge independence (isospin conservation) on the R-matrix parameters.

The application of such an R-matrix model to the elastic scattering of nucleons from  ${}^4\text{He}$  has been highly successful. Almost all available measurements for p- $\alpha$  and n- $\alpha$  scattering at lab energies in the 0-20 MeV range were analyzed simultaneously, with R-matrix parameters in the two systems related by a simple model of the charge symmetry. Specifically, for common boundary conditions imposed at the same channel radius, the reduced width amplitudes for a given level were constrained to be equal ( $\gamma_{\lambda p} = \gamma_{\lambda n}$ ), and the level energies were constrained to differ by a Coulomb

"shift"  $\Delta E$  ( $E_{\lambda p} = E_{\lambda n} + \Delta E$ ) that was taken to be the same for all levels. In addition to the known p-wave levels, distant-level contributions were represented in each state by single pole terms. Partial waves having  $l > 3$  were neglected. Thus constrained and truncated, the combined R-matrix analysis required 15 free parameters, just one parameter ( $\Delta E$ ) more than the number needed to analyze either p- $\alpha$  or n- $\alpha$  scattering separately.

Figure 1<sup>3)</sup> shows the resulting least squares fit (solid line)\* to a segment of the n- $\alpha$  total cross section over the 1.25 MeV resonance (the dotted curve is ENDF/B III). Figures 2-4 show representative fits to the n- $\alpha$  differential cross sections, while Figs. 5 and 6 show representative fits to the n- $\alpha$  analyzing powers (or polarizations) over the energy range considered. On Fig. 7 is given a sampling of the fits to the p- $\alpha$  differential cross sections, and Fig. 8 shows fits to various p- $\alpha$  polarization measurements. Note that the top two curves in the right column of Fig. 8 represent measurements ( $K_x^{x'}$ ,  $K_z^{x'}$ ) of outgoing proton polarization with a polarized proton beam incident. In general, the p- $\alpha$  experiments were more numerous and more precise than the n- $\alpha$  experiments, and we feel that even this simple charge-symmetric model has imposed better accuracy on the predicted n- $\alpha$  observables than can be attained in most present n- $\alpha$  measurements.

Interestingly, the parameters which fit the data indicated that an even more stringent model might have been imposed. The channel radius preferred a value (2.9 f.) close to that expected from the nuclear sizes. The reduced widths of the two p-wave levels became, for the first time

- - - - -

\* The solid line represents the R-matrix fit on this and all succeeding figures.

in such an analysis, approximately equal to each other and to the single-particle width. The phenomenologically determined Coulomb energy shift ( $\Delta E = 1.58$  MeV) agreed well with calculations using realistic  ${}^4\text{He}$  charge densities. It is pleasing that the parameters moved naturally toward values characteristic of a very simple mechanism for the elastic scattering of nucleons from  ${}^4\text{He}$ , namely, single-particle scattering from a simple potential.

The invariance under charge symmetry shown by the nucleon- ${}^4\text{He}$  systems is a manifestation of the more general principle of isospin conservation, and that invariance in the internal region can be applied to the R-matrix parameters. An example is found in the 4-nucleon systems. The p- ${}^3\text{He}$  and n-T elastic scatterings occur only in the  $T = 1$  state, while among the pairs of the system of p-T, n- ${}^3\text{He}$ , and d-D, the d-D channel is only in the  $T = 0$  state while the other two are in both the  $T = 0$  and  $T = 1$  states. By using R-matrix levels of pure isospin states, and constraining the reduced widths in the various channels to being appropriate Clebsch-Gordan fractions of the isospin widths, it is possible to guarantee exact charge independence in the internal region, while still predicting the isospin mixing in the external region which is caused by the different Coulomb potentials in the different channels. The differences in Coulomb energy among the  $Z = 1$ ,  $Z = 2$ , and  $Z = 3$  systems are still expected to be accounted for mainly by a shift in the  $E_\lambda$ 's. Our current analysis is using the  $T = 1$  parameters from the p- ${}^3\text{He}$  system in the  ${}^4\text{He}$  compound system, but eventually all three systems will be analyzed simultaneously.

Although the major concern of evaluation work has been with cross sections for neutron-induced reactions, we feel it is essential in these analyses to include data of various types and from all important reactions that bear on the compound system in which the neutron-induced reactions occur. Primarily through unitarity, data from other reactions determine the model parameters more accurately, which in turn generate more reliable predictions of the neutron cross sections of interest. The analysis we are doing of reactions in the  $^{11}\text{B}$  system among the channels  $n\text{-}^{10}\text{B}$ ,  $\alpha\text{-}^7\text{Li}(\text{g.s.})$ , and  $\alpha\text{-}^7\text{Li}^*(.478)$ , is a case in point. The large spin of  $^{10}\text{B}$  (spin 3) introduces many scattering amplitudes into the problem even for low partial waves, so that including data from a variety of sources is important.

Examples of the types of data we are fitting in our analysis at low energies ( $E_n \leq 1$  MeV) are given in the next few figures. Figure 9 shows the fit to the total neutron cross section for  $^{10}\text{B}$  (again, the dotted curve is ENDF III), while Fig. 10 displays the fits to integrated  $^{10}\text{B}(n, \alpha_0)^7\text{Li}$  and  $^{10}\text{B}(n, \alpha_1)^7\text{Li}^*$  cross sections. As you can see in the bottom part of this figure, there are severe disagreements among the experiments, particularly above 100 keV. Fits to the  $^{10}\text{B}(n, n)^{10}\text{B}$  differential cross section and polarization measurements of Lane are shown at two energies on Fig. 11. The experimental values ( $\bar{X}$ ) shown for the polarizations (on the right) may not be accurate, since they were generated from Legendre coefficients, but the change of sign in the polarization is significant, indicating the presence of a p-wave

resonance in this energy region (at  $\approx 450$  keV). Figure 12 shows examples of the fits to  $^{10}\text{B}(n,\alpha)$  differential cross sections obtained by detailed balance from the recent  $^7\text{Li}(\alpha,n)^{10}\text{B}$  measurements of Van der Zwaan and Geiger. And the last figure in this sequence (Fig. 13) shows representative fits to the  $^7\text{Li}(\alpha,\alpha)^7\text{Li}$  differential cross section measurements of Cusson. These fits, as well as those to the  $^7\text{Li}(\alpha,\alpha)^7\text{Li}^*$  integrated cross section (not shown) indicate that levels with large widths in the  $\alpha$ -channels are as yet unidentified in the  $^{11}\text{B}$  system. Although these fits for the neutron-induced reactions on  $^{10}\text{B}$  represent the most comprehensive analysis effort made thus far at low energies in this system, we feel that the accuracy of the curves is still limited by insufficient data and incomplete knowledge of the level structure of  $^{11}\text{B}$ .

As in the case of  $^{10}\text{B}$ , the cross sections for neutron-induced reactions on  $^6\text{Li}$  are important in applications, and particularly in neutron measurements. Our analysis of reactions in the  $^7\text{Li}$  system gains additional information from including  $\alpha$ -T scattering measurements along with data from the  $^6\text{Li}(n,n)^6\text{Li}$  and  $^6\text{Li}(n,\alpha)\text{T}$  reactions. Figure 14 gives examples of the types of  $\text{T}(\alpha,\alpha)\text{T}$  data that are being fit. The upper left-hand part of the figure indicates that the only existing low-energy differential cross section data, even when renormalized, may be seriously in error at back angles. The curve below that is representative of the generally excellent fit obtained to the angular distributions of Ivanovich, Young and Ohlsen at medium energies. Data on the upper right-hand curve are taken from

excitation functions measured by Spiger and Tombrello at an energy close to the  $5/2^-$  resonance above the  $n-{}^6\text{Li}$  threshold. Below that is shown an example of the fit to double-scattering experiments that measure the outgoing triton polarization.

Attention is focused in the next two figures on the region of the important  $5/2^-$  resonance near  $E_n = 250$  keV, mentioned earlier. Figure 15 shows for  ${}^6\text{Li}(n,n)$  elastic scattering the integrated cross section across the resonance, and (normalized) angular distribution and polarization approximately at resonance. Notice that the fit lies above the experimental points in the peak of the integrated cross section. On Fig. 16 are shown the total neutron cross section for  ${}^6\text{Li}$  (top), and the  ${}^6\text{Li}(n,\alpha)\text{T}$  integrated cross section across the resonance, along with the  ${}^6\text{Li}(n,\alpha)\text{T}$  differential cross section approximately at resonance. Although it is difficult to tell from the figure, the calculated total cross section peaks at the currently accepted value ( $\sim 11.0$  barns), while the calculated peak  $(n,\alpha)$  cross section lies above that of the recent measurements of Coates, Fort, and Poenitz ( $\sim 3.0$  barns). If one believes the total cross section is best determined, then either or both of the observed integrated cross sections is wrong. There are those who feel strongly that the recent measurements of the  $(n,\alpha)$  cross section are correct, and that only the  $(n,n)$  cross section is too low. Our analysis including the  $\text{T}(\alpha,\alpha)\text{T}$  data in this region indicates that both integrated cross sections are too low. It is an important question, since the  ${}^6\text{Li}(n,\alpha)$  cross section is often used as a "standard". Unfortunately, the Spiger and Tombrello data

are not of sufficient quality firmly to resolve the question, but we feel that accurate charged particle measurements in this region might be more useful in resolving these discrepant observations relative to the  $(n,\alpha)$  cross section than another direct measurement.

The examples we have so far given are all actually demonstrations of the detail obtainable with these models in realistic data evaluations. We should mention also an example where the work is of a more exploratory nature, where we are trying at first to gain an understanding of the physics involved. The 5 nucleon systems  $p-\alpha$  and  $d-{}^3\text{He}$  and  $n-\alpha + d-T$  afford this example. The systems are quantitatively understood at energies up through the famous  $3/2+$  resonance that occurs in each at a few hundred keV deuteron energies. Above this energy the systems become very complicated, with the scatterings and reactions dominated by a whole series of overlapping resonances mainly in the even parity states of various spin arrangements which have their spatial configuration mainly in the  $\ell = 2$  state between the deuteron and the 3-nucleon particle. The R-matrix formalism is an almost ideal mode of description of this situation, and we have succeeded in fitting a rather formidable collection of experimental results in a rather satisfactory fashion.

In the  ${}^5\text{Li}$  system, for instance, there have been 39 different types of observables measured for the reactions among  $d-{}^3\text{He}$  and  $p-{}^4\text{He}$ . These include, in addition to the usual differential cross sections and polarizations, measurements made with both first- and second-rank polarized deuteron beams incident on  ${}^3\text{He}$ , and with polarized proton beams incident on  ${}^4\text{He}$ . In some of the experiments, the polarization of the outgoing

particle has been measured. (Examples of these "polarization transfers" have already been shown for  ${}^4\text{He}(p,p){}^4\text{He}$  on Fig. 8.) In others, both polarized and unpolarized deuteron beams have been scattered from polarized  ${}^3\text{He}$  targets.

All these various types of measurements have been included in our analyses of the  $d-{}^3\text{He}$ ,  $p-{}^4\text{He}$  system. The next two figures show examples of fits to a selection of these, taken from an analysis that extends to  $E_d = 4$  MeV. The first of these displays the four independent analyzing tensors (1 first-rank, 3 second-rank) measured by Koenig, et al. for  ${}^3\text{He}(d,d){}^3\text{He}$  at 4 MeV. The second figure gives examples of the fits to measurements made at various energies for  ${}^3\text{He}(d,p){}^4\text{He}$  with both polarized beams and polarized targets.

The examples we have given demonstrate the versatility of the R-matrix approach to data analysis and evaluation. The chief theoretical limitation, which we have not dwelt upon, is the restriction to two-body final states. This can only be avoided at present in those cases where the multi-body final states can be mocked up by quasi-two-body states. We are indeed using this method in the five nuclear system where we take into account the final state  $p + {}^4\text{He}^*$  as an approximation for the whole spectrum of  $p + n + {}^3\text{He}$  and  $p + p + T$  breakup channels. A practical limitation of the approach, is, of course, that computers are only so large, and there definitely are limits to the number of channels,  $\ell$ -values and levels we can consider. This limits the work in its present form to the light nuclei. And finally, just because the method of description

is so comprehensive, it is necessary to have a comprehensive data base before the analysis can be successful. This means many experiments of various kinds must be done over a significant range of energies. This is the price we pay for the checks on consistency and physical reasonableness, and it is perhaps not a disadvantage in the long run, because it never hurts really to know what's going on.

#### References

1. E. P. Wigner and L. Eisenbud, Phys. Rev. 72, 29 (1947).
2. The most complete description is still A. M. Lane and R. G. Thomas, Rev. Mod. Phys. 30, 257 (1958).
3. References to data shown in the figures are given in the Appendix.
4. An equivalent approach in a different formalism has been used by: Barit and Sergeev, Yadernaya Fiz. 4, 712 (1967); Soviet J. Nucl. Phys. 4, 507 (1967).

Appendix

## Data References for Figures

- Fig. 1. C. A. Goulding, P. Stoler, and J. D. Seagrave, Nucl. Phys. A215, 253 (1973);  
 F. J. Vaughn, W. L. Imhof, R. G. Johnson, and M. Walt, Phys. Rev. 118, 683 (1960);  
 Los Alamos Physics and Cryogenics Groups (Battat et al.), Nucl. Phys. 12, 291 (1959).
- Figs. 2-4. G. L. Morgan and R. L. Walter, Phys. Rev. 168, 1114 (1968);  
 D. S. Cramer and L. Cranberg, Nucl. Phys. A180, 273 (1972);  
 John D. Seagrave, Phys. Rev. 92, 1222 (1953);  
 B. Hoop, Jr. and H. H. Barschall, Nucl. Phys. 83, 65 (1966);  
 A. Nifler, M. Drosig, J. C. Hopkins, J. D. Seagrave, and E. C. Kerr, Phys. Rev. C 4, 36 (1971);  
 R. E. Shamu and J. G. Jenkin, Phys. Rev. 135B, 99 (1964).
- Figs. 5-6. T. H. May, R. L. Walter, and H. H. Barschall, Nucl. Phys. 45, 17 (1963);  
 J. R. Sawers, Jr., G. L. Morgan, L. A. Schaller, and R. L. Walter, Phys. Rev. 168, 1102 (1968);  
 Th. Stambach, J. Taylor, G. Spalek, and R. L. Walter, Phys. Rev. C 2, 434 (1970);  
 W. B. Broste, G. S. Mutchler, J. E. Simmons, R. A. Arndt, and L. D. Roper, Phys. Rev. C 5, 761 (1972);  
 F. W. Büsser, F. Niebergall, G. Söhngen, and J. Christiansen, Nucl. Phys. 88, 593 (1966).
- Figs. 7-8. G. Freier, E. Lampi, W. Sleator, and J. H. Williams, Phys. Rev. 75, 1345 (1949);  
 A. C. L. Barnard, C. M. Jones, and J. L. Weil, Nucl. Phys. 50, 604 (1964);  
 N. Jarmie and J. Jett, private communication;  
 D. Garreta, J. Sura, and A. Tarrats, Nucl. Phys. A132, 204 (1969);  
 L. Brown and W. Trächslin, Nucl. Phys. A90, 334, 339 (1967);  
 R. I. Brown, W. Haeberli, and J. X. Saladin, Nucl. Phys. 47, 212 (1967);

P. Schwandt, T. B. Clegg, and W. Haeberli, Nucl. Phys. A163, 432 (1971);

P. W. Keaton, Jr., D. D. Armstrong, R. A. Hardekopf, P. M. Kurjan, and Y. K. Lee, Phys. Rev. Letters 29, 880 (1972).

Fig. 9. K. M. Diment, AERE-R-5224 (1967);

C. K. Bockelman, D. W. Miller, R. K. Adair, and H. H. Barschall, Phys. Rev. 84, 69 (1951).

Fig. 10. R. L. Macklin and J. H. Gibbons, Phys. Rev. 165, 1147 (1968);

E. A. Davis, F. Gabbard, T. W. Bonner, and R. Bass, Nucl. Phys. 27, 448 (1961);

M. Coates, private communication;

S. J. Friesenhan, et al., Gulf-RT-A12210 (1972);

D. O. Nellis, W. E. Tucker, and I. L. Morgan, Phys. Rev. C 1, 847 (1970).

Fig. 11. R. O. Lane, S. L. Hausladen, J. F. Monahan, A. J. Elwyn, F. P. Mooring, and A. Langsdorf, Jr., Phys. Rev. C 4, 380 (1971).

Fig. 12. L. Van der Zwaan and K. W. Geiger, Nucl. Phys. A180, 615 (1972).

Fig. 13. R. Y. Cusson, Thesis, California Institute of Technology (1965).

Fig. 14. A. Hemmendinger, Bull. APS, Series II, 1, 96 (1956);

M. Ivanovich, P. G. Young, and G. G. Ohlsen, Nucl. Phys. A110, 441 (1968);

R. J. Spiger and T. A. Tombrello, Phys. Rev. 163, 964 (1970);

P. W. Keaton, Jr., D. D. Armstrong, and L. R. Veaser, Phys. Rev. Letters 20, 1392 (1968), and private communication.

Fig. 15. R. O. Lane, A. J. Elwyn and A. Langsdorf, Jr., Phys. Rev. B 136, 1710 (1964);

J. C. Overley, R. M. Sealock, and D. H. Ehlers, Nucl. Phys. A221, 573 (1974);

H. H. Knitter and M. Coppola, EANDC (E)-57 (U) (EUR-3454) (1967).

- Fig. 16. C. T. Hibdon and R. R. Weeks, ANL Physics Div. Quarterly Report (1954);
- C. T. Hibdon and F. P. Mooring, Conf. on Neutron Cross Section Technology, Washington, 1968, p. 159;
- G. V. Gorlov, B. M. Gokhberg, V. M. Morozov, and G. A. Otroshchenko, Doklady Akad. 111, 791 (1956); Doklady Akad. 1, 598 (1956);
- J. A. Farrell, Conference on Neutron Cross Section Technology, Washington, 1968, p. 153;
- C. H. Johnson, B. Willard, and J. K. Bair, Phys. Rev. 96, 985 (1954);
- C. A. Goulding and P. Stoler, EANDC (US) - 176 U, p. 161 (1972);
- J. W. Meadows and J. F. Whalen, Nucl. Sci. Eng. 41, 351 (1970);
- S. J. Bame, Jr. and R. L. Cubitt, Phys. Rev. 114, 1580 (1959);
- W. B. Pardo, J. H. Roberts, Bull. Am. Phys. Soc. 4, 218 (1959);
- J. B. Weddell, J. H. Roberts, Phys. Rev. 95, 117 (1954);
- M. Coates, private communication;
- L. G. Stromberg, S. Schwarz, A. Bergstrom, Nucl. Phys. 63, 593 (1965);
- S. A. Cox and F. R. Pontet, J. Nucl. Energy 21, 271 (1967);
- W. P. Poenitz, private communication (1974);
- F. Ribe, Phys. Rev. 103, 741 (1956);
- R. B. Murray, H. W. Schmitt, Phys. Rev. 115, 1707 (1959).
- Fig. 17. V. König, W. Grüebler, R. E. White, P. A. Schmölz bach and P. Marmier, Nucl. Phys. A185, 263 (1972).
- Fig. 18. Ch. Leeman, H. Burgesser, P. Huber, V. Rohrer, H. Schieck, and F. Seiler, Helv. Phys. Acta 44, 141 (1971).
- Ch. Leeman, H. Meiner, V. Rohrer, J. X. Saladin, F. Seiler, P. Huber, W. Grüebler, V. König, and P. Marmier, Polarization Phenomena in Nuclear Reactions, ed. H. H. Barschall and W. Haeberli, Univ. of Wisconsin Press, Madison (1970), p. 548;
- G. G. Ohlsen and K. Mitchell, private communication;
- W. Grüebler, V. König, A. Ruh, P. A. Schmelzbach, R. E. White and P. Marmier, Nucl. Phys. A165, 505 (1971).

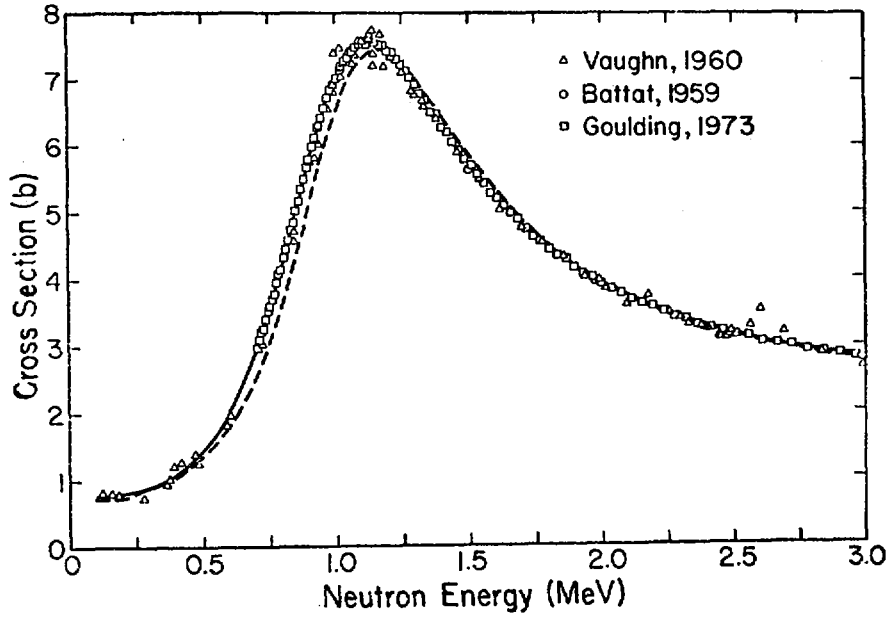


Fig. 1. Total  $n\text{-}^4\text{He}$  cross section,  $E_n = 0\text{-}3$  MeV

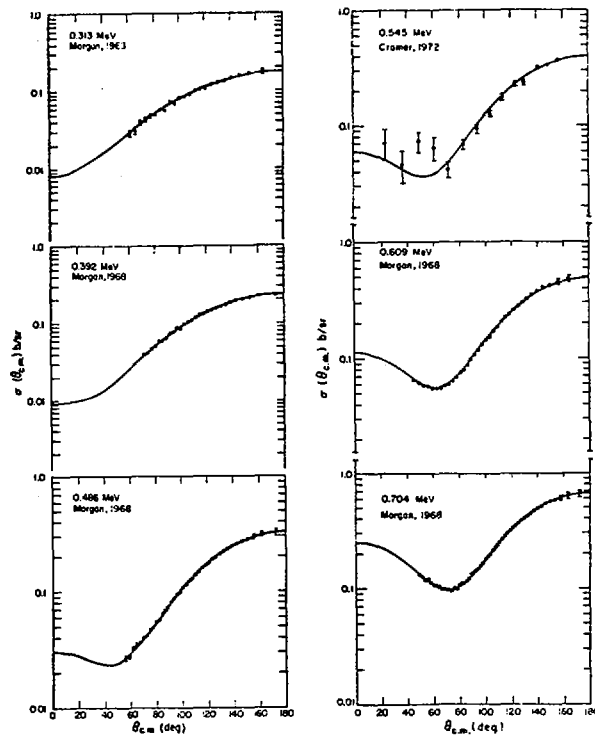


Fig. 2.  $^4\text{He}(n,n)^4\text{He}$  differential cross sections,  $E_n = .3\text{-}.7$  MeV

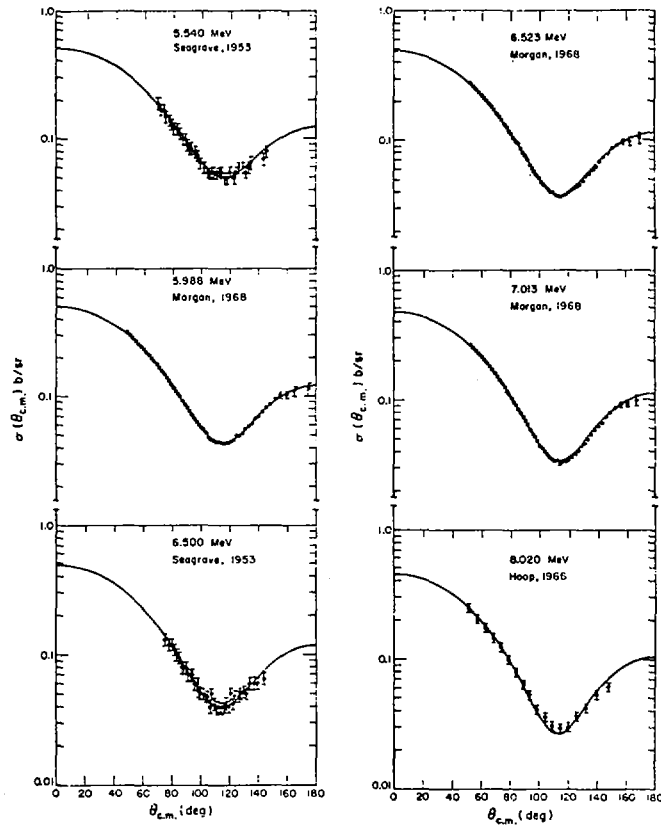


Fig. 3.  ${}^4\text{He}(n,n){}^4\text{He}$  differential cross sections,  $E_n = 5.5\text{--}8$  MeV

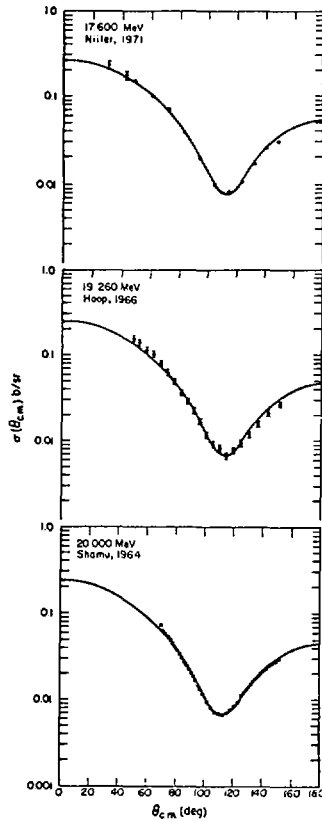


Fig. 4.  ${}^4\text{He}(n,n){}^4\text{He}$  differential cross sections,  $E_n = 17.6\text{--}20$  MeV

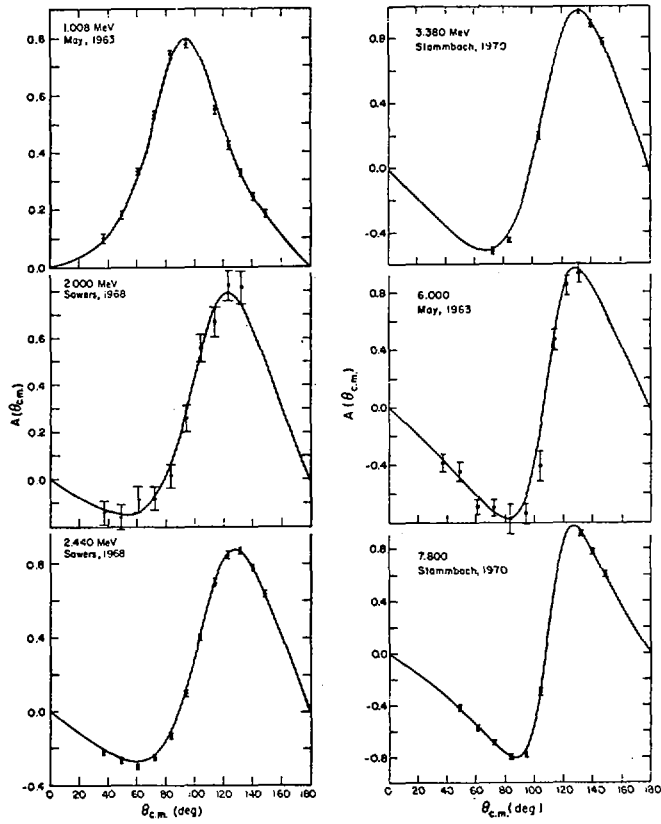


Fig. 5.  ${}^4\text{He}(n,n){}^4\text{He}$  neutron polarizations,  $E_n = 1-7.8$  MeV

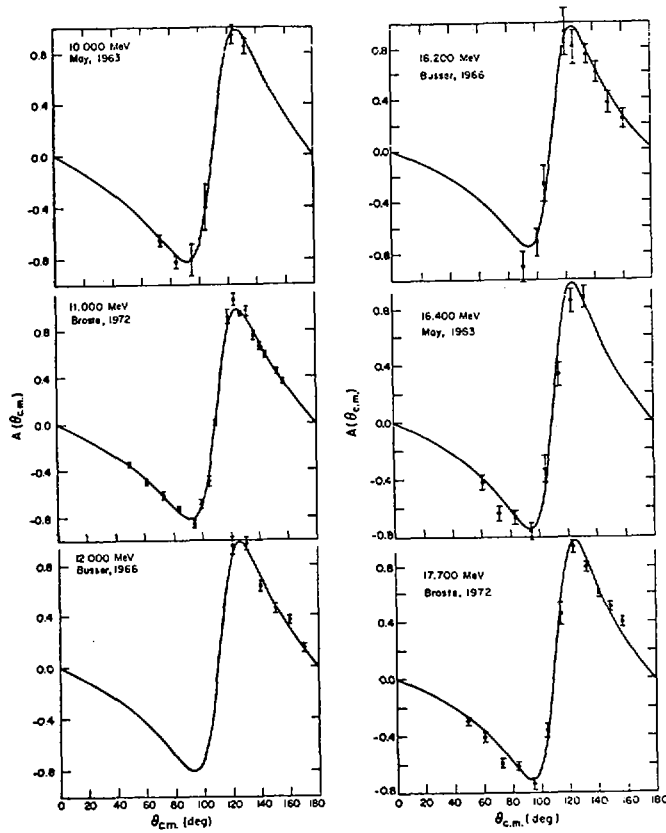


Fig. 6.  ${}^4\text{He}(n,n){}^4\text{He}$  neutron polarizations,  $E_n = 10-17.7$  MeV

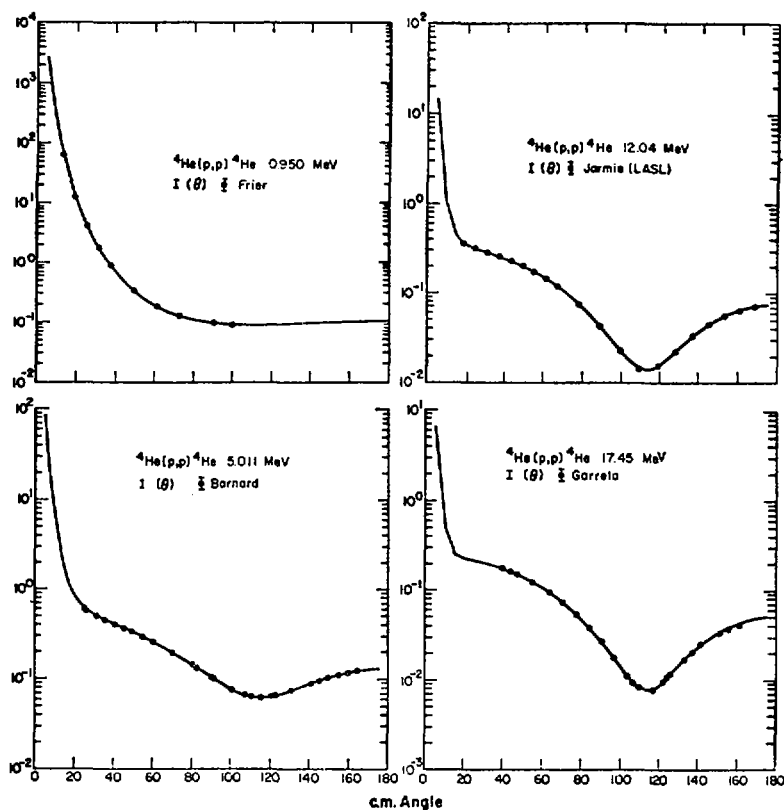


Fig. 7.  ${}^4\text{He}(p,p){}^4\text{He}$  differential cross sections,  $E_p = .95\text{-}17.5$  MeV

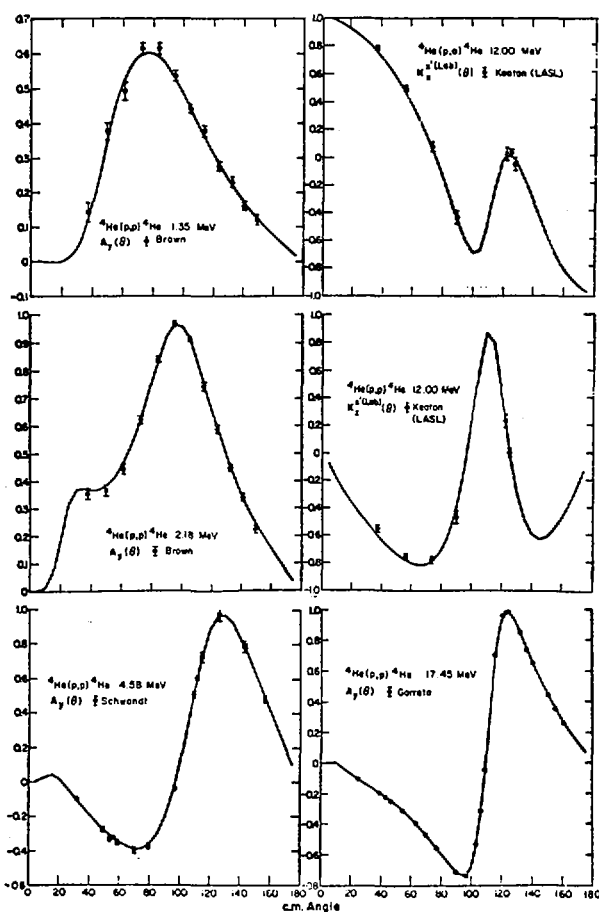


Fig. 8.  ${}^4\text{He}(p,p){}^4\text{He}$  proton polarizations, polarization transfers,  $E_p = 1.4\text{-}17.5$  MeV

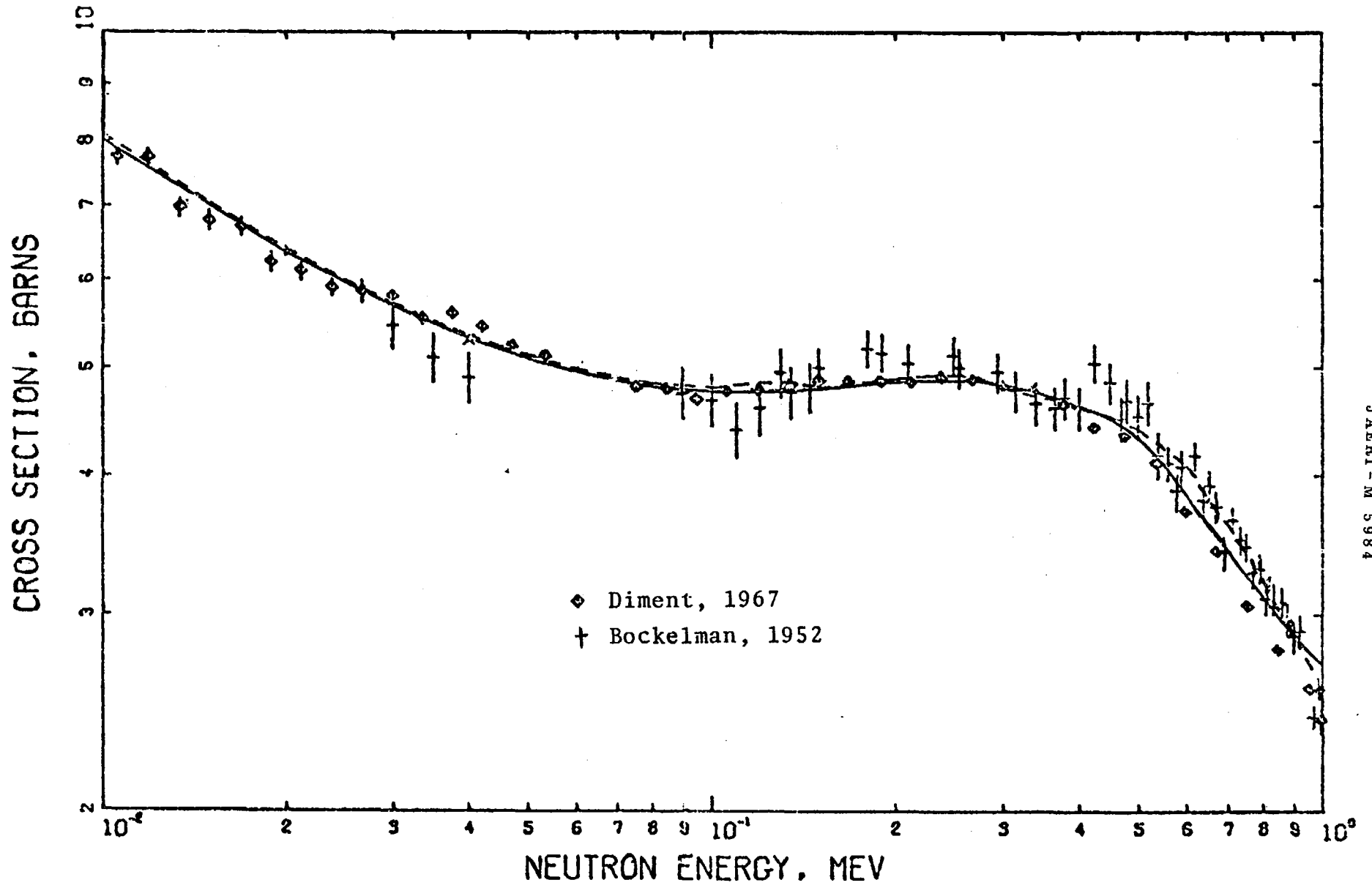


Fig. 9. Total  $n$ - $^{10}\text{B}$  cross section,  $E_n = .01$ - $1.0$  MeV

$^{11}\text{B}$  SYSTEM

<u>Reaction</u>	<u>Observable Types Analyzed:</u>			
	<u>Total Neutron Cross Section</u>	<u>Integrated Cross Section</u>	<u>Differential Cross Section</u>	<u>Polarization</u>
$^{10}\text{B}$	X			
$^{10}\text{B}(n,n)^{10}\text{B}$		X	X	X
$^{10}\text{B}(n,\alpha_0)^7\text{Li}$		X	X	
$^{10}\text{B}(n,\alpha_1)^7\text{Li}^*$		X	X	
$^7\text{Li}(\alpha,\alpha_0)^7\text{Li}$			X	
$^7\text{Li}(\alpha,\alpha_1)^7\text{Li}^*$		X		

Fig. 9a. Types of data included in  $^{11}\text{B}$  analysis.

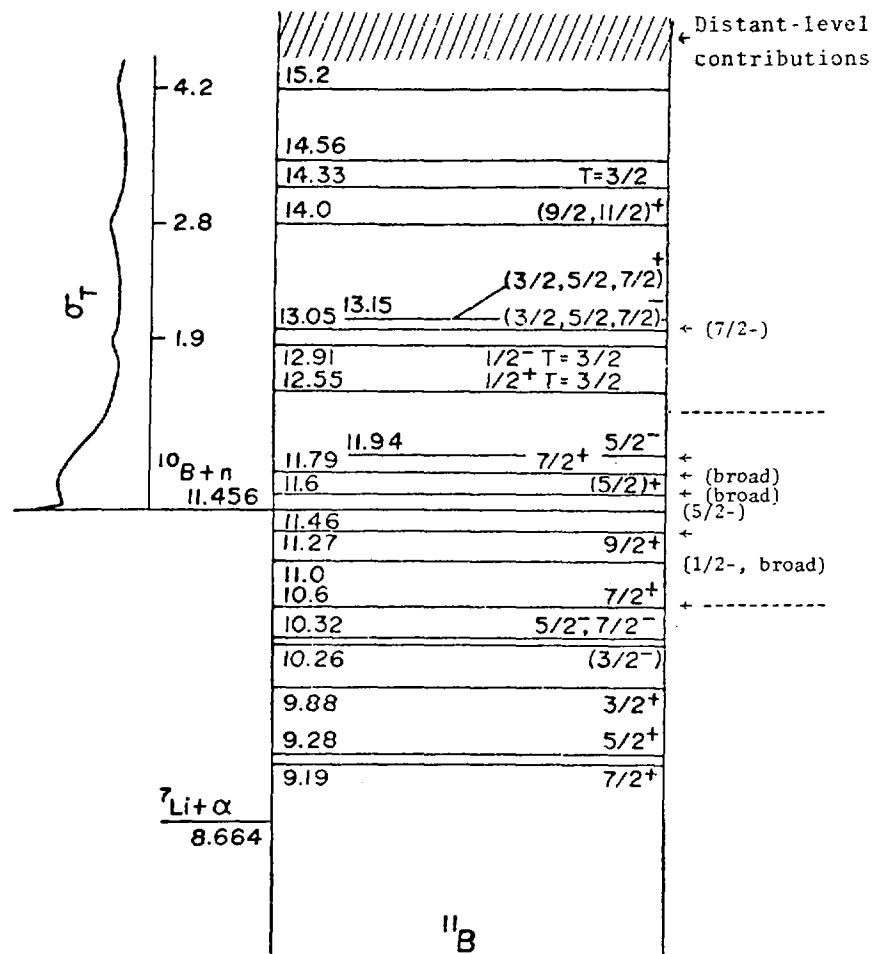


Fig. 9b. Level diagram for  $^{11}\text{B}$ . The dotted lines indicate the range over which data were included. Checked levels correspond approximately to those in our analysis. Additional levels found in the analysis are indicated in parentheses or brackets.

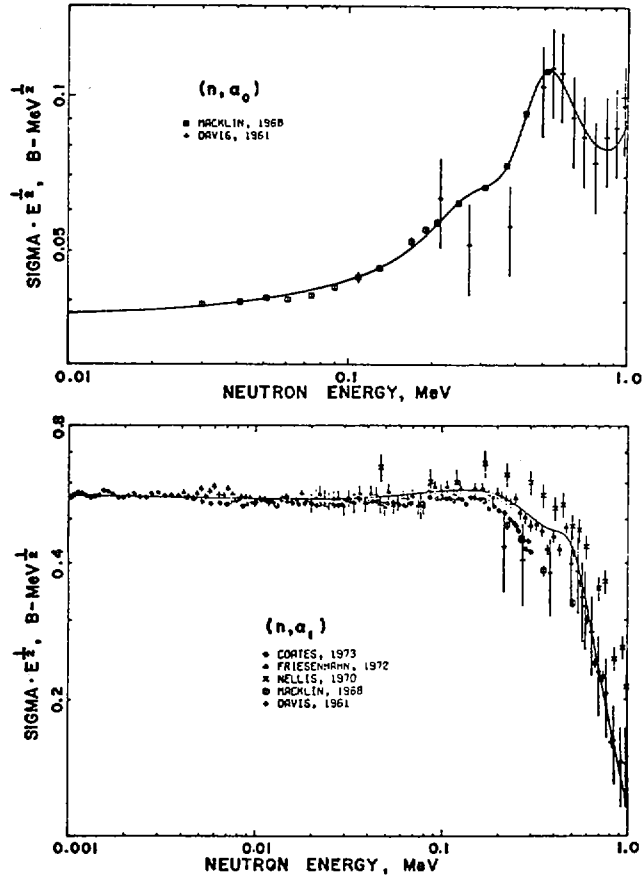


Fig. 10. Integrated  $^{10}\text{B}(n, \alpha_0)^7\text{Li}$  and  $^{10}\text{B}(n, \alpha_1)^7\text{Li}^*$  cross sections below  $E_n = 1$  MeV

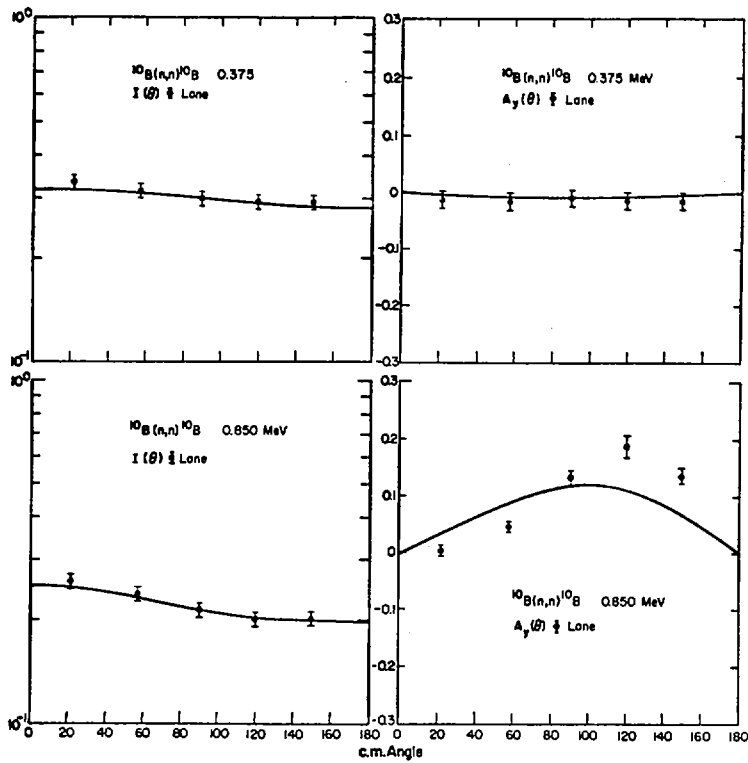


Fig. 11.  $^{10}\text{B}(n, n)^{10}\text{B}$  differential cross sections and neutron polarizations at  $E_n = .375$  and  $.850$  MeV

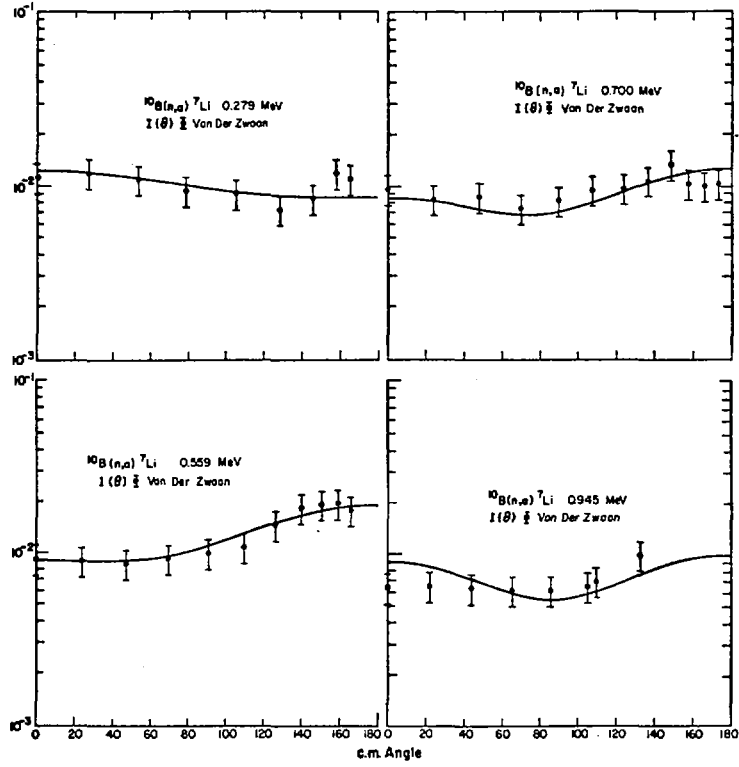


Fig. 12.  $^{10}\text{B}(n, \alpha)^7\text{Li}$  differential cross sections,  $E_n = .28-.95$  MeV

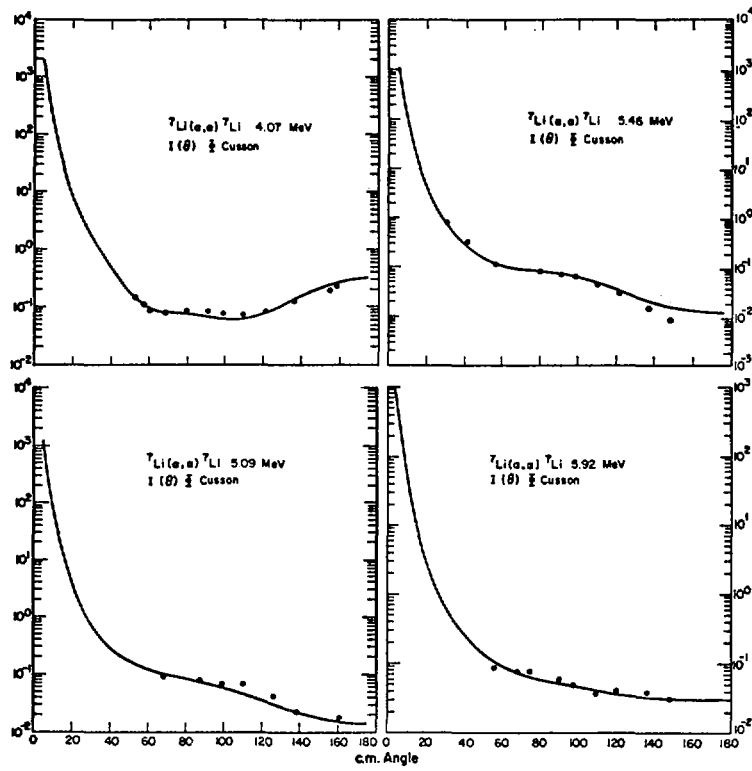


Fig. 13.  $^7\text{Li}(\alpha, \alpha)^7\text{Li}$  differential cross sections,  $E_\alpha = 4.1-6.92$  MeV

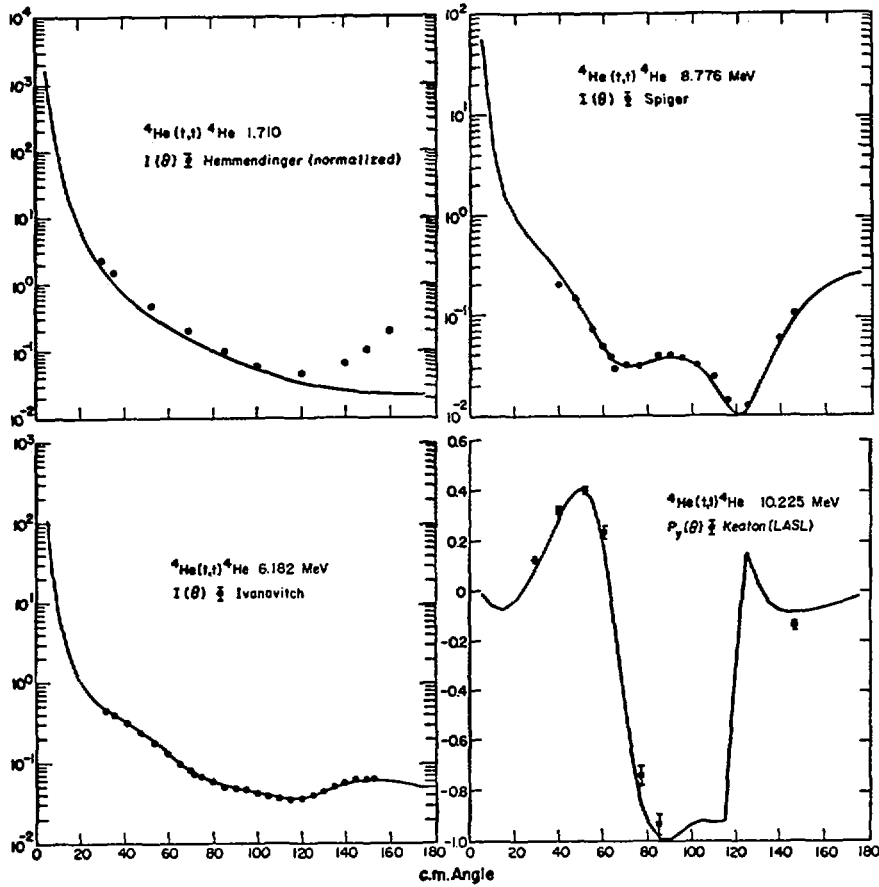


Fig. 14.  ${}^4\text{He}(t,t){}^4\text{He}$  differential cross sections for  $E_t = 1.7$  to  $8.8$  MeV and triton polarization,  $E_t = 10.2$  MeV

${}^7\text{Li}$  SYSTEM

Reaction

Observable Types Analyzed:

	<u>Total Neutron Cross Section</u>	<u>Integrated Cross Section</u>	<u>Differential Cross Section</u>	<u>Polarization</u>
${}^6\text{Li}$	X			
${}^6\text{Li}(n,n){}^6\text{Li}$		X	X	X
${}^6\text{Li}(n,\alpha)\text{T}$		X	X	
${}^4\text{He}(t,t){}^4\text{He}$			X	X

Fig. 14a. Types of data included in  ${}^7\text{Li}$  analysis

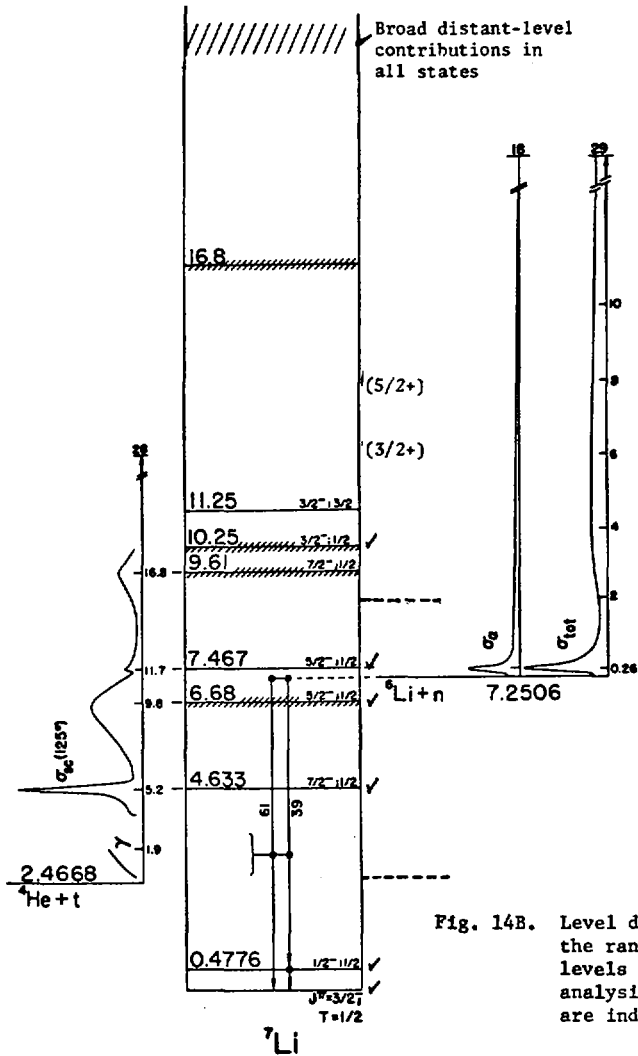


Fig. 14B. Level diagram for  ${}^7\text{Li}$ . The dotted lines indicate the range over which data were included. Checked levels correspond approximately to those in our analysis. Additional levels found in the analysis are indicated in parentheses or brackets.

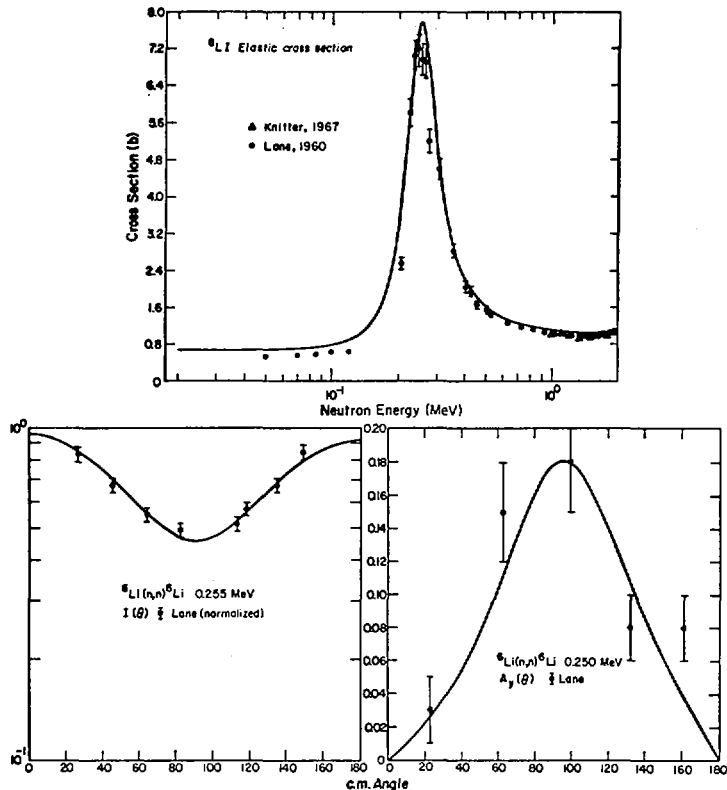


Fig. 15.  ${}^6\text{Li}(n,n){}^6\text{Li}$  observables near the resonance at  $E_n \approx .250$  MeV

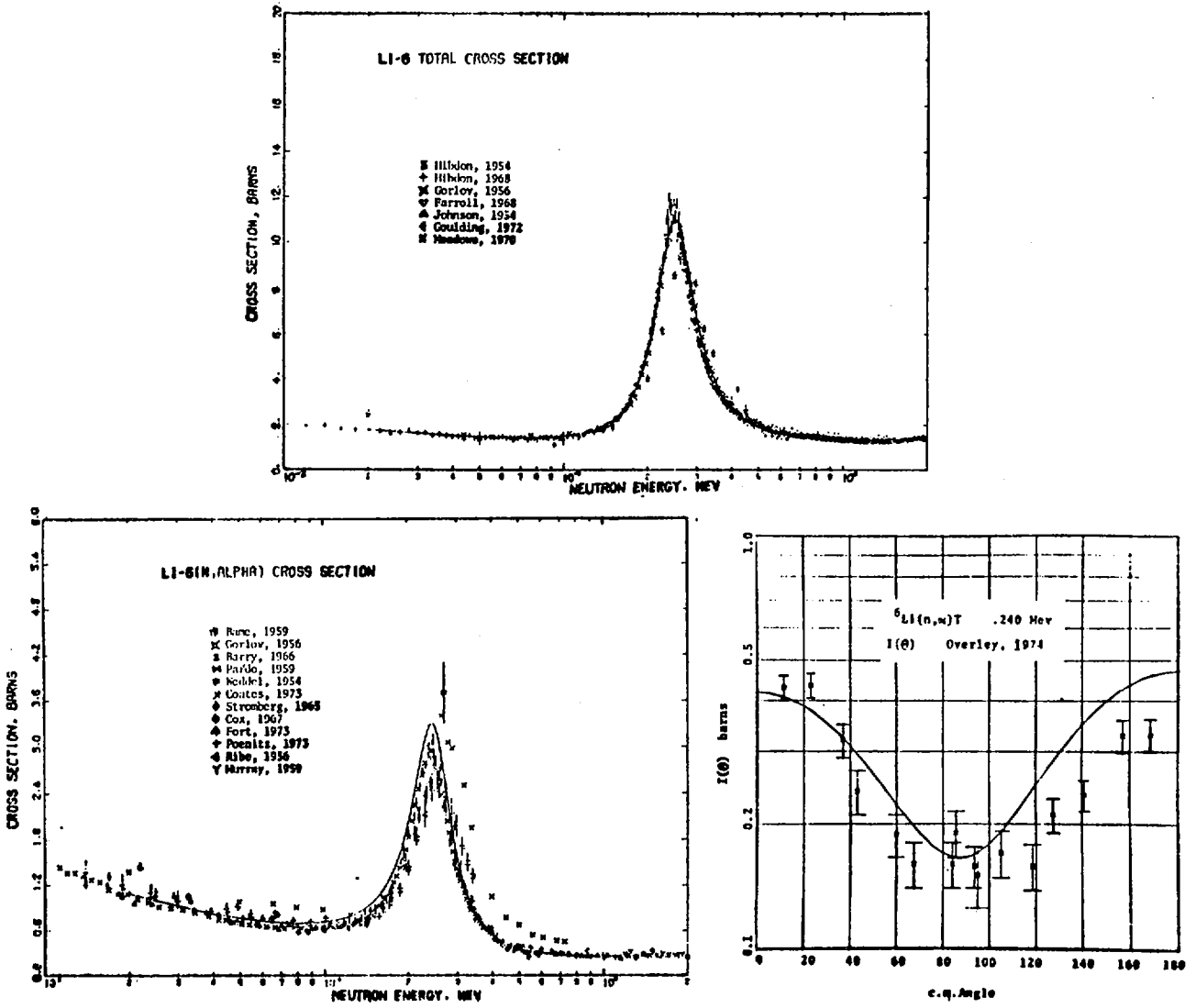


Fig. 16.  $n-{}^6\text{Li}$  total cross section,  ${}^6\text{Li}(n,\alpha)T$  observables near the resonance at  $E_n \approx .250$  MeV

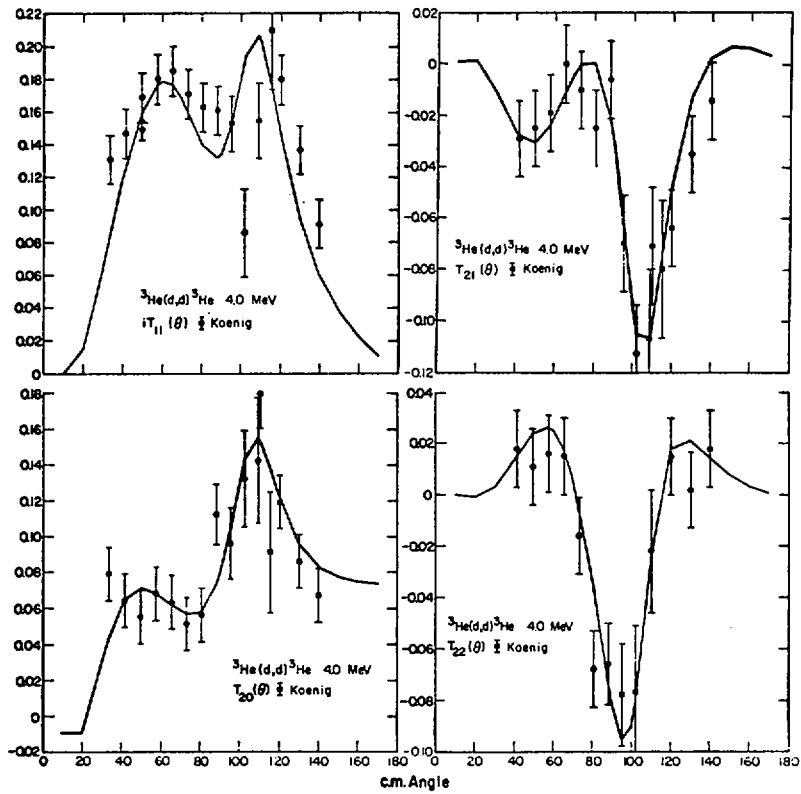


Fig. 17.  ${}^3\text{He}(d,d){}^3\text{He}$  deuteron analyzing tensors  $iT_{11}$ ,  $T_{20}$ ,  $T_{21}$ , and  $T_{22}$  at  $E_d = 4.0$  MeV.

${}^5\text{Li}$  SYSTEM

Reaction

Observable Types Analyzed:

	<u>Integrated Cross Section</u>	<u>Differential Cross Section</u>	<u>Polarization</u> *	<u>Spin Correlation</u>	<u>Polarization Transfer</u>
${}^3\text{He}(d,d){}^3\text{He}$		X	X	X	X
${}^3\text{He}(d,p){}^4\text{He}$	X	X	X	X	X
${}^4\text{He}(p,p){}^4\text{He}$		X	X		X

\*"Polarization" heading is also meant to include analyzing power measurements made with either polarized beam or polarized target.

Fig. 17a. Types of data included in  ${}^5\text{Li}$  analysis.

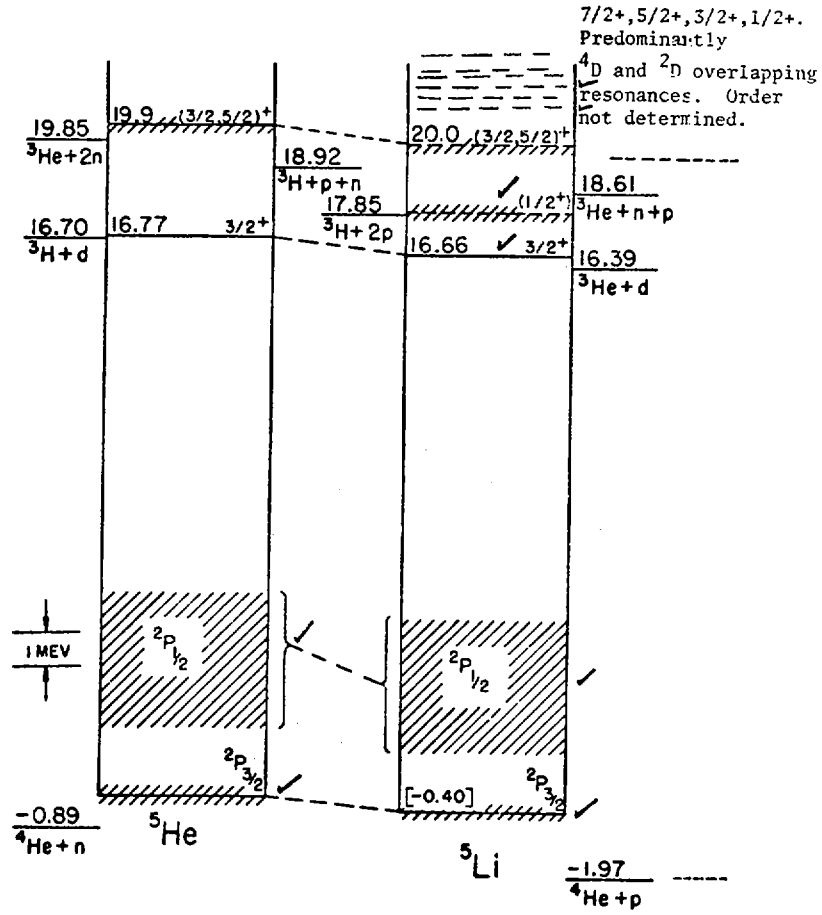


Fig. 17b. Level diagram for <sup>5</sup>He, <sup>5</sup>Li. The dotted lines indicate the range over which data were included. Checked levels correspond approximately to those in our analysis. Additional levels found in the analysis are indicated in parentheses or brackets.

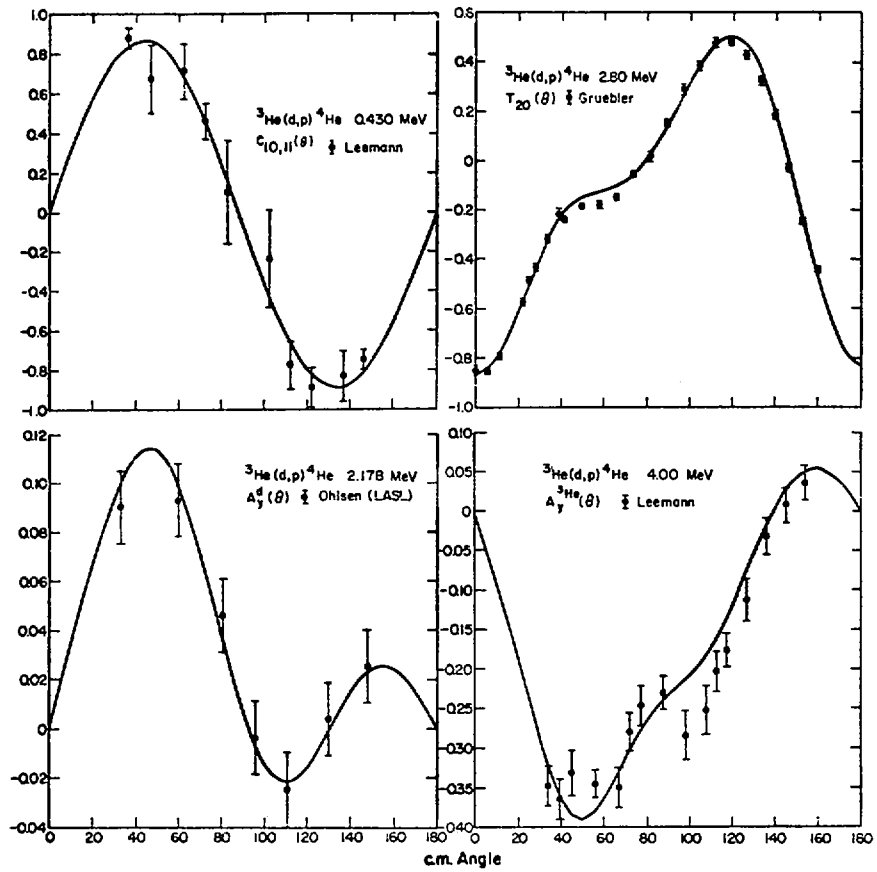


Fig. 18.  ${}^3\text{He}(d,p){}^4\text{He}$  measurements with polarized beams and targets,  $E_d = .43 - 4.0$  MeV.

## DISCUSSION

S. W. CIERJACKS: Do you think that discrepancies in the  ${}^6\text{Li}(n,\alpha)$  peak cross section can be explained in terms of theory? I personally still doubt that the mentioned new U.S. measurements, giving a higher peak cross section, are correct. I rather trust the bulk of earlier measurements with a lower peak cross section.

H.T. MOTZ: More detailed information, such as for  ${}^4\text{He} + t$ , could well permit theoretical insight concerning the  ${}^6\text{Li}(n,\alpha)$  cross section. I would like to see reliable, direct observations as well. But if they are not consistent with other measurements as dependable theoretical analysis might indicate, then lack of confidence would be appropriate. The sensitivity of various quantities on one another is crucial for such conclusions. This sensitivity is not yet determined. I have not yet formed an opinion of the most recent (Friesenhahn) results which indicate very high ( $\sim 3.7b$ ) peak  $\text{Li}(n,\alpha)$  cross sections.

S. W. CIERJACKS: Have the authors included in their R matrix fit of the  ${}^6\text{Li}(n,\alpha)$  peak cross section other resonances, in particular those below neutron binding?

H. T. MOTZ: Levels in Li-7 that were included are:

Energy keV	$J^\pi$
0	$3/2^-$
477	$1/2^-$
4633	$7/2^-$
6680	$5/2^-$
7467	$5/2^-$

(also broad, distant level contributions in all states above 20 MeV).  
The neutron binding in Li-7 is 7251 keV.

R. C. BLOCK: I was delighted to see the RPI He total neutron cross section data of Goulding et al. fit so nicely by the R-matrix theory from 0-3 MeV. Do you have the higher energy fit with you?

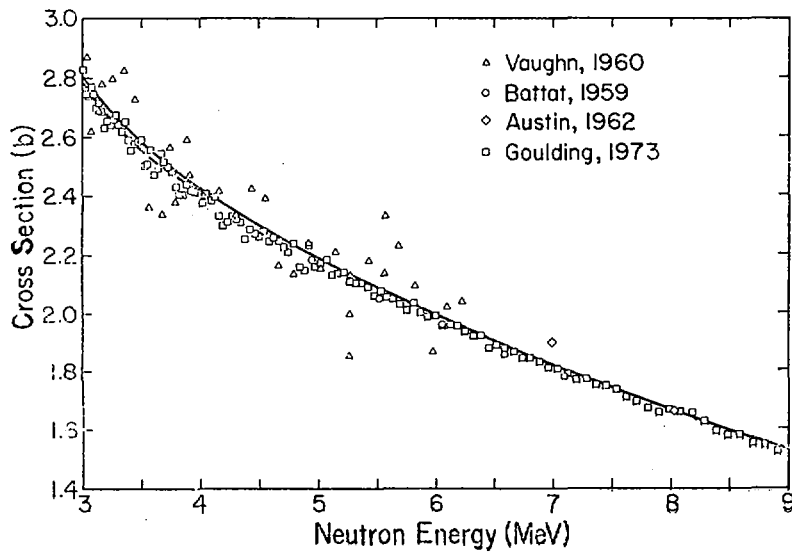
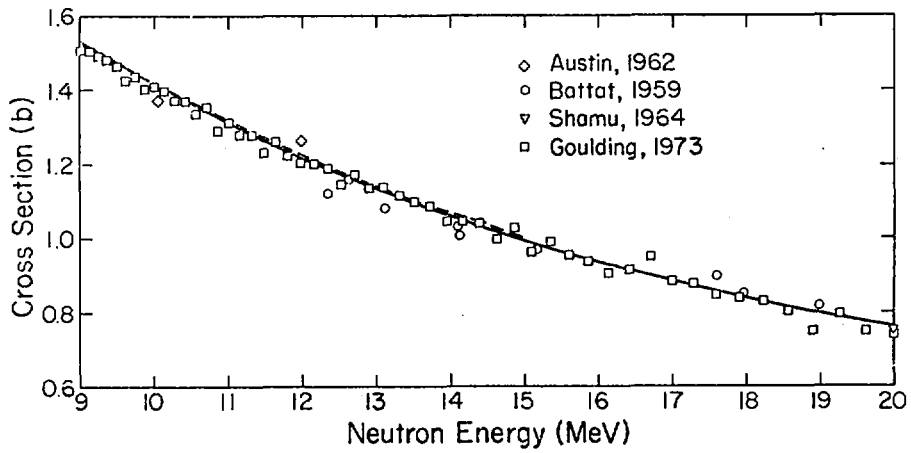
H. T. MOTZ: (No. I am not sure that such a fit has yet been made.)\*  
These fits have been made. (See the following two figures.)

---

\*The comment was changed to the above following one after the meeting.  
The data were not available at the meeting, but are attached.

R. C. BLOCK: Do you feel there is a need for precise (1/2 ~ 1%) total neutron cross section data from 0.5 ~ 20 MeV for the light nuclei to aid in these fits?

H. T. MOTZ: I am sure they would be helpful, but probably not as much as other observations would be, for example, the authors believe that further  $^4\text{He} + t$  data would be crucial to the  $n + ^6\text{Li}$  problem. In the case of  $^{10}\text{B}$ , an accurate total cross section would be very valuable.



Figures: Total neutron cross sections of helium.

I-2. A study on the hierarchy model of nuclear reactions

Yasuhiro Kitazoe and Tamotsu Sekiya

Department of Nuclear Engineering, Osaka University,  
Suita-shi, Osaka, Japan

We would like to discuss the applications of the hierarchy model of nuclear reactions. Here, the hierarchy model means that the compound nucleus states are formed after several steps, at least, one step of the reaction. In this paper, this model is applied to the analysis of the observed cross sections of  $^{235}\text{U}$  and some other elements. Neglecting the exchange scattering effect, we get the following expressions for the total neutron cross section of  $^{235}\text{U}$ ; 1)

$$\sigma'_{cT} = 4\pi a_c^2 + \frac{3.26 \times 10^5}{\sqrt{E}} \sum_m \frac{\Gamma_{mc}^0 (\Gamma_m + \gamma_m)}{(E - E_m - \delta_m)^2 + (\Gamma_m + \gamma_m)^2/4} \quad (1)$$

and

$$\langle \sigma'_{cT} \rangle = 4\pi a_c^2 + \frac{3.26 \times 10^5}{\sqrt{E}} \sum_m \frac{\Gamma_{mc}^0 I_m}{(E - E_m - \langle \delta_m \rangle)^2 + I_m^2/4}, \quad (2)$$

where

$$\delta_m = \sum_s \frac{(E - E_s) |V_{ms}|^2}{(E - E_s)^2 + \Gamma_s^2/4}, \quad (3)$$

$$\gamma_m = \sum_s \frac{\Gamma_s |V_{ms}|^2}{(E - E_s)^2 + \Gamma_s^2/4}, \quad (4)$$

$$I_m = I + \Gamma_m + \langle \gamma_m \rangle, \quad \Gamma_{mc}^0 = 2g \Gamma_{mc} E^{-V_2}, \quad (5)$$

$$\langle \delta_m \rangle = \sum_s \frac{(E - E_s) |V_{ms}|^2}{(E - E_s)^2 + (I + \Gamma_s)^2/4}, \quad (6)$$

$$\langle \gamma_m \rangle = \sum_s \frac{(I + \Gamma_s) |V_{ms}|^2}{(E - E_s)^2 + (I + \Gamma_s)^2/4}. \quad (7)$$

Equation(1) describes explicitly a hierarchy of the transition from the intermediate reaction states  $X_m$  into the compound nucleus states  $X_s$ . As is seen from this equation, the intermediate reaction states have two kinds of widths. One is the escape width  $\Gamma_m$  for direct decay into the open channels. The other is the decay width  $\gamma_m$  into the compound nucleus states. The latter width  $\gamma_m$  is characterized by the strength of the direct coupling  $|V_{ms}|^2$  between the intermediate resonance states and the compound nucleus states. Equation(1) thus is a resonance formula which describes the fine structure of the resonance cross section.

On the other hand, equation(2) is the cross section formula averaged over an energy interval which is larger than the average level spacing of the compound nucleus eigenvalues  $E_s$  but is smaller than that of the simple mechanism eigenvalues  $E_m$ . When the energy interval  $I$  is suitable, the average transition quantities  $\langle \delta_m \rangle$  and  $\langle \gamma_m \rangle$  in eqs.(6) and (7) become almost constant within the level spacing of the eigenvalues  $E_m$ . Thus, we understand that the average cross section formula(2) is substantially reduced to a resonance formula of the well-known dispersion type. This formula is an interesting and useful tool to study the existence of the intermediate resonances, since it is sufficient for us to investigate whether the formula can satisfactorily reproduce an observed cross section averaged over a suitable energy interval.

We have applied the formula(2) to the evaluation of the total neutron cross section of  $^{235}\text{U}$  at low energies. The observed resonances in this cross section are fully resolved

at low energies (  $E < 60$  ev ) and the cross section fluctuates rapidly with energy variance. By a detailed investigation, we find that the cross section consists of different sized resonances and that a few satellite resonances are usually located in the neighborhood of each large sized resonance, as seen from curve A in Fig.1. When this cross section is averaged over the energy interval  $\Delta E = 2.0$  ev, curve B is obtained ( here we have the relation  $I = \Delta E / \sqrt{\pi}$  ). By this average procedure, only the resonance peaks 4, 7, 10 and 14 have clearly been retained but the remainder has almost completely disappeared. We tried to reproduce curve B by using the formula (2) ( see curve C in Fig.1 ). As is evident from Fig.1, curve C is in good agreement with curve B. The obtained resonance parameters are listed in Table 1. Then, the hierarchy model explains the reaction mechanism of the present cross section as follows; at an early stage of the reaction, we first have the simple mechanism states which correspond to the resonance peaks 4, 7, 10, 12 and 14 in Fig.1. Next, in the middle stage of the reaction, further interactions among nucleons of the system produce the more complicated mechanism states which correspond to the resonance peaks 3, 5, 6, 8, 11, and 13 in Fig.1. We examined whether the formula(2) is applicable to the full energy range (  $E = 0 \sim 60$  ev ) of the resolved resonances. From Fig.2, we see that the result of the evaluation is satisfactory from a qualitative view point.

Let us investigate in more detail a hierarchy of the reaction mechanism. Fig.3 shows a typical example of two

resonances at low energies. We suppose that the peaks 1 and 2 correspond to the simple mechanism state  $X_m$  and the complicated mechanism state  $X_s$ , respectively. Then, equation(1) is applicable to the present example. In this simplest case we have

$$\sigma_{cT} = 4\pi a_c^2 + \frac{6.52 \times 10^5}{2\sqrt{E}} \cdot \frac{\Gamma_{mc}^0 (\Gamma_m + \gamma_m)}{(E - E_m - \delta_m)^2 + (\Gamma_m + \gamma_m)^2/4}, \quad (8)$$

$$\langle \sigma_{cT} \rangle = 4\pi a_c^2 + \frac{6.52 \times 10^5}{2\sqrt{E}} \cdot \frac{\Gamma_{mc}^0 I_m}{(E - E_m - \langle \delta_m \rangle)^2 + I_m^2/4}, \quad (9)$$

where

$$\delta_m = \frac{(E - E_s) |V_{ms}|^2}{(E - E_s)^2 + \Gamma_s^2/4}, \quad (10)$$

$$\gamma_m = \frac{\Gamma_s |V_{ms}|^2}{(E - E_s)^2 + \Gamma_s^2/4}. \quad (11)$$

Here the parameters  $\Gamma_{mc}^0$ ,  $E_m$  and  $I_m$  are obtained by applying Eq.(9) to the average cross section( curve D in Fig.3 ) given by averaging the experimental data(  $\langle \delta_m \rangle$  in Eq.(9) can be neglected). Curve B is given using Eq.(8) and curve A by using the R-matrix theory approximated by

$$\sigma_{cT}^R = 4\pi a_c^2 + \frac{6.52 \times 10^5}{2\sqrt{E}} \sum_{\lambda} \frac{\Gamma_{\lambda c}^0 \Gamma_{\lambda}}{(E - E_{\lambda})^2 + \Gamma_{\lambda}^2/4}. \quad (12)$$

There is a remarkable difference of the functional form between Eqs.(8) and (9). In the R-matrix theory we regard the resonance energies  $E_{\lambda}=51.25$  eV and  $E_{\mu}=52.23$  eV as the true eigenvalues of the compound system. On the other hand, in the hierarchy model the above two energies are not the true eigenvalues but they represent only apparent resonant peaks. The

experiment is interpreted as follows; when the compound nucleus state  $X_s$  is formed by the interaction  $V_{12}$ , the original simple mechanism resonance ( curve E in Fig.3) is influenced by the occurrence of the state  $X_s$ , so that the position of this resonance peak is shifted from  $E_m = 51.60$  eV to  $E_m = 51.25$  and then the position of the other peak is also shifted from  $E_s = 51.88$  eV to  $E_s = 52.23$  eV, since the state  $X_s$  is also influenced by the existence of the state  $X_m$ . We here emphasize that the experiment can be explained by a different formalism from that of the R-matrix theory having extensively been used. We also emphasize that the observed cross section in Fig.1 can be reproduced in a similar way to that mentioned above. The point is that the cross section may consist of resonances with the states of different complexities.

We have applied the hierarchy model to the case of the unresolved energy region.<sup>1)</sup> The observed cross section in this energy region is naturally averaged over because of the rough energy resolution and the Doppler effect. In this situation, agreement between curves B and C in Fig.1 predicts that the hierarchy model formula(2) will reproduce the observed cross section at higher energies. We know that the energy resolution  $\Delta E_R$  and the Doppler width  $\Delta E_D$  have the following energy dependences:<sup>2)</sup>

$$\Delta E_R \simeq 2.76 \times 10^{-5} N E^{3/2} \quad (13)$$

and

$$\Delta E_D \simeq 0.023 \sqrt{E} \quad , \quad (14)$$

where  $E$  and  $N$  are in eV and ns/m, respectively. When we put  $E = 200$  eV and  $N = 25$  ns/m, we get  $\Delta E = (\Delta E_R^2 + \Delta E_R^2)^{1/2} = 1.95$  eV. This value of  $\Delta E$  is about equal to the energy interval used to curve B in Fig.1. This fact states that the situation of curve B in Fig.1 will roughly correspond to the observed total cross section in the neighborhood of  $E = 200$  eV, provided that the average level spacing is assumed to be constant. To see this more explicitly, we evaluated the average cross section by using the formula(2). As is clear from the solid line of Fig.4, the evaluation reproduces well the observed cross section. Table 3 explains the relation between the average resonance parameters and the energy intervals in the resolved energy region ( $E < 60$  eV). On the other hand, Table 4 shows the energy dependence of the average resonance parameters in the unresolved energy region ( $E=0 \sim 300$  eV). The average resonance parameters in Tables 3 and 4 ensure the above-mentioned prediction that the observed cross section in the neighborhood of  $E = 200$  eV will correspond to the cross section averaged over the energy interval  $\Delta E=2.0$  eV.

It is found from Tables 3 and 4 that the ratio of the average resonance parameters,  $\langle \Gamma_{mc} \rangle / \langle D_m \rangle$ , remains constant though  $\langle \Gamma_{mc} \rangle$  and  $\langle D_m \rangle$  change fairly with the increasing  $\Delta E$  and  $E$ . This can easily be proved by using (15). Let us consider two different energy intervals  $\Delta E_1$  and  $\Delta E_2$  over which the collision matrix  $U_{cc}$  is averaged. We suppose that each energy interval  $\Delta E_i$  ( $i=1,2$ ) extracts a set of intermediate states,  $\{\chi_{m_i}\}$ . These two sets have different complexities from each other. Then we have

$$\langle U_{cc} \rangle_{\Delta E_1} = \Omega_c^2 \left[ 1 - i \sum_{m_1} \frac{\Gamma_{m_1 c}}{E - E_{m_1} + \langle \delta_{m_1} \rangle + i I_{m_1} / 2} \right] \quad (15)$$

and

$$\langle U_{cc} \rangle_{\Delta E_2} = \Omega_c^2 \left[ 1 - i \sum_{m_2} \frac{\Gamma_{m_2 c}}{E - E_{m_2} + \langle \delta_{m_2} \rangle + i I_{m_2} / 2} \right] . \quad (16)$$

Further averages over the above two kinds of the intermediate resonances should give a same average of  $U_{cc}$  denoted by  $\langle\langle U_{cc} \rangle\rangle$  :

$$\langle\langle U_{cc} \rangle\rangle \cong \Omega_c^2 \left[ 1 - i \pi \frac{\langle \Gamma_{m_1 c} \rangle}{\langle D_{m_1} \rangle} \right] = \langle\langle U_{cc} \rangle\rangle_{\Delta E_2} = \Omega_c^2 \left[ 1 - i \pi \frac{\langle \Gamma_{m_2 c} \rangle}{\langle D_{m_2} \rangle} \right] \quad (17)$$

from which we obtain

$$\frac{\langle \Gamma_{m_1 c} \rangle}{\langle D_{m_1} \rangle} = \frac{\langle \Gamma_{m_2 c} \rangle}{\langle D_{m_2} \rangle} . \quad (18)$$

This fact makes it possible to evaluate the average cross section at the higher energies ( $E > 300$  eV). This result is shown by the solid line of Fig.5.

#### The optical model

This model is the simplest case of the hierarchy model. In this case, the energy interval over which the collision matrix is to be averaged becomes the largest and the states  $X_m$  represent the single particle states of the incident particle. On the other hand, the states  $X_s$  include all the possible reaction states. The optical model regards these reactions as an absorption by the average procedure. There are many experimental facts where the optical potential is considered to have the mass and energy dependences.

A typical example comes from the collective excitation process of the deformed nucleus. This means that the collective excitation states in some mass region are strongly coupled to the initial state. As another example, we have studied the contribution of the exchange scattering. At low energies where the compound nucleus are easily formed, there will be a large possibility with which neutrons different from the incident one are emitted from the compound nucleus. The s-wave strength function is given by

$$S_0 = \text{Re } i \sum_m \frac{\Gamma_m^0}{E - E_m + i U_m + F_m}, \quad (19)$$

where  $F_m$  comes from the channel couplings among different neutrons and can be approximated as follows:

$$F_m = N a_m \sum_{m'} \frac{a_{m'}}{E - E_{m'} + i U_{m'}} \quad (20)$$

Consequently the imaginary part of the optical potential is modified as

$$U_m^{if} = U_m - N a_m \sum_{m'} \frac{a_{m'} U_{m'}}{(E - E_{m'})^2 + U_{m'}^2} \quad (21)$$

Here it is very interesting that the form of this potential is similar to that employed by Dr. Newstead and Dr. Delaroche.<sup>4)</sup> In Eq. (21),  $N$  is the number of the target neutron and  $F_m$  represents the strength of the exchange scattering through the compound nucleus formation. We calculated  $E_m$ ,  $\Gamma_m$  and  $F_m$  by using the square-well potentials

and tried to reproduce the observed strength functions for several elements of recent interest (here the surface thickness of the real potential was taken into account by using the diffuse-edge factor  $f$  of E.Vogt<sup>3)</sup>). Then we get

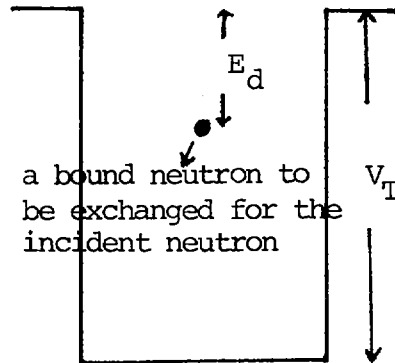
$$a_m = \frac{\mathcal{S} U}{1 - \frac{\sin 2b}{2b}} \cdot \left( \frac{2b \cos b}{b^2 - f_m^2} \right)^2, \quad (22)$$

where

$$b = \frac{\sqrt{2m(V_T - E_d)}}{\hbar} a_c, \quad (23)$$

$$f_m = (m + 0.5) \pi, \quad a_c = 0.7367 + 1.1343 A^{1/3}. \quad (24)$$

The quantity  $\mathcal{S}$  in (22) is a spectroscopic factor and  $E_d$  is the energy of a target neutron bound by the square-well potential  $V_T$ .



Figures 6, 7, 8 and 9 show the results of the evaluation and the parameters used are listed in table 6. The thin line and the dotted line are given by the usual optical model and the isospin model, respectively. The thick full line is given by the exchange scattering model. The rapid variance of the strength function with mass number comes from the change of the depth parameter  $E_d$ . This parameter roughly estimates

the location in the target nucleus of the neutron to be exchanged for the incident neutron. If we have the surface absorption, the value of this parameter is equal to the neutron binding energy of the target. Thus, this value increases with the volume absorption. From table 6, we see that a large part of the isotopes  $\text{Sn}_{50}$ ,  $\text{Xe}_{54}$  and  $\text{Ba}_{56}$  can well explained by using the binding energies. Figure 10 and table 7 give the result of the more kinds of the isotopes. Here we did not try to evaluate the strength functions in the mass region ( $A > 140$ ), since we neglected in this task the effect of the nuclear deformation. This inclusion will be discussed elsewhere.

#### References

- 1) Y.Kitazoe, H.Suzuki and T.Sekiya: Atomkernenergie 20 (1972) 13, 22 (1973) 214.
- 2) J.J.Schmidt: KFK - 120, Part 1, Karlsruhe(1967).
- 3) E.Vogt: Rev. Mod. Phys. 34 (1962) 723.
- 4) C.Newstead and J.Delaroche: "The conference on Nuclear Structure Study with Neutrons" July,1972,Budapest.

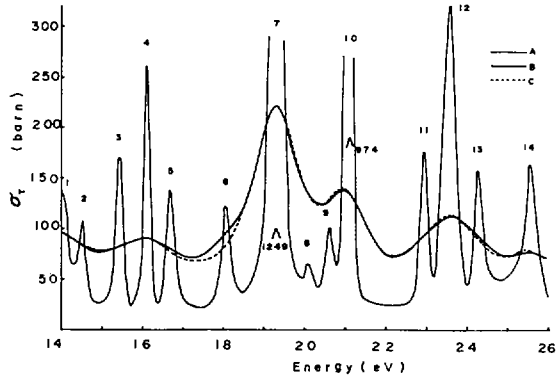


Fig. 1: The observed neutron total cross section (A) and the averaged cross section of  $^{235}\text{U}$  (B).

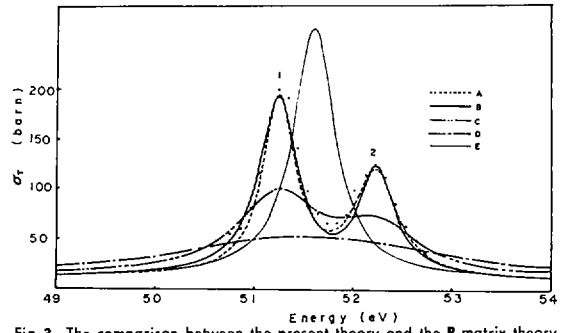


Fig. 3: The comparison between the present theory and the R-matrix theory

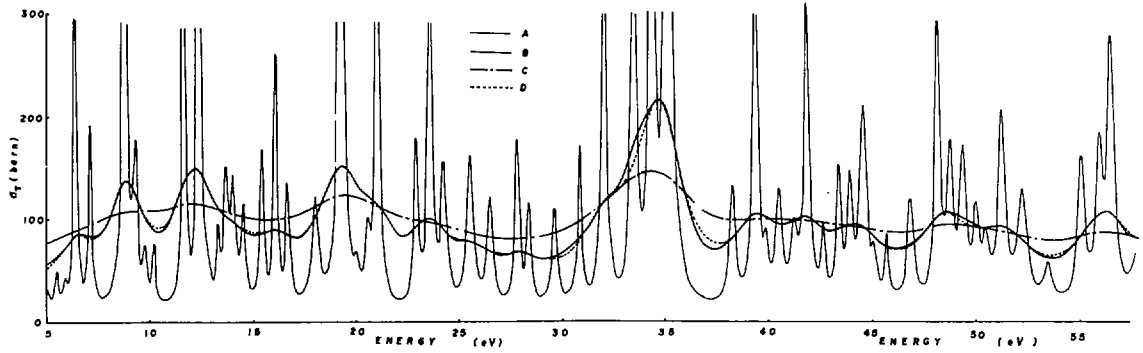


Fig. 2: The total neutron cross section in the energy region ( $E < 60$  eV). Curve A is the observed cross section, and curves B and C are cross sections averaged it over the energy intervals  $\Delta E = 2.0$  eV and  $\Delta E = 8.0$  eV, respectively. Curve D is given by using the present formula (2) with  $\Delta E = 2.0$  eV

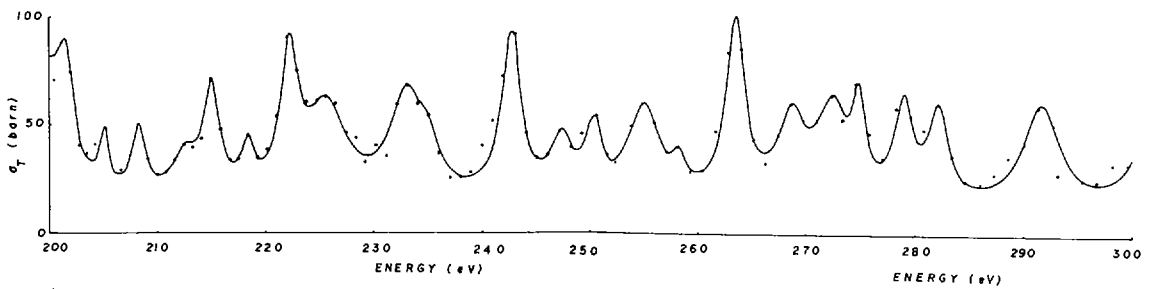


Fig. 4: The total neutron cross section in the energy region ( $E = 200 \sim 300$  eV). The solid points are the experimental data and the solid curve is given by using the formula (2). The parameters used are given in Table 1

Table 1: The resonance parameters of Fig. 1

Res. No.	$E_\lambda$	$\Gamma_\lambda$	$\Gamma_{\lambda c}^0$	$E_m$	$I_m$	$\Gamma_{mc}^0$
1	14.02	0.3099	9.480			
2	14.51	0.2309	5.332			
3	15.42	0.2006	8.938			
4	16.10	0.1863	13.65	16.05	2.148	34.45
5	16.67	0.1877	6.728			
6	18.02	0.3752	12.13			
7	19.28	0.1933	80.13	19.3	1.45	92.21
8	20.05	0.3491	3.437			
9	20.61	0.2413	4.848	20.95	1.4	39.02
10	21.06	0.1772	36.85			
11	22.93	0.2235	12.35			
12	23.61	0.2625	28.89	23.6	2.2	71.98
13	24.26	0.2871	14.0			
14	25.55	0.3731	20.77			

In Table 1, the parameters  $E_\lambda$ ,  $\Gamma_\lambda$  and  $\Gamma_{\lambda c}^0$  were obtained by using the R-matrix formula (12) and the parameters  $E_m$ ,  $I_m$  and  $\Gamma_{mc}^0$  were obtained by using the present formula (2). The  $E_\lambda$ ,  $\Gamma_\lambda$ ,  $E_m$  and  $I_m$  are in eV.  $\Gamma_{\lambda c}^0 = 2g\Gamma_{\lambda c}E^{-1/2}$  and  $\Gamma_{mc}^0 = 2g\Gamma_{mc}E^{-1/2}$  are in  $(\text{eV})^{1/2} \times 10^3$ .

Table 3: The resonance parameters of Fig. 1

No.	$E_m$	$I_m$	$\Gamma_{mc}^0$	No.	$E_m$	$I_m$	$\Gamma_{mc}^0$
1	201.4	2.163	138.1	12	247.4	2.437	75.93
2	205.0	1.092	28.35	13	250.3	1.689	62.52
3	208.3	1.604	54.91	14	254.9	3.420	177.3
4	212.5	2.586	55.85	15	258.9	1.593	24.64
5	215.0	1.839	102.2	16	263.3	2.083	208.7
6	218.4	1.383	30.65	17	268.5	3.087	137.1
7	222.2	1.923	138.9	18	272.3	3.447	182.5
8	225.6	4.523	218.2	19	274.7	1.289	59.95
9	233.1	3.871	213.6	20	278.9	2.089	113.8
10	235.1	2.173	36.94	21	282.1	2.236	113.0
11	242.7	2.110	188.8	22	291.6	4.004	242.0

In Table 1, the parameters  $E_m$ ,  $I_m$  and  $\Gamma_{mc}^0$  were obtained by using the formula (2), where  $E_m$  and  $I_m$  are in eV while  $\Gamma_{mc}^0$  is in  $(\text{eV})^{1/2} \times 10^3$ .

Table 4: The relation between the average resonance parameters and the energy intervals  $\Delta E$  averaged over in the energy region ( $E = 0 \sim 60$  eV)

$\Delta E$	$\langle I_m \rangle$	$\langle \Gamma_{mc}^0 \rangle$	$\langle D_m \rangle$	$\langle \frac{\Gamma_{mc}^0}{D_m} \rangle$
0.0	0.272	20.1	0.882	22.8
2.0	2.09	71.3	2.8	25.5
3.0	2.78	72.1	3.0	24.0

Table 5: The energy dependence of the average resonance parameters

$E$	$\langle I_m \rangle$	$\langle \Gamma_{mc}^0 \rangle$	$\langle D_m \rangle$	$\langle \frac{\Gamma_{mc}^0}{D_m} \rangle$
30	0.272	20.1	0.882	22.8
70	0.516	25.4	1.13	22.4
110	0.91	36.9	1.54	24.0
150	1.19	57.0	2.14	26.6
200	1.78	73.2	3.0	24.4
250	2.43	118.9	4.44	26.8
270	2.69	128.8	5.0	25.8

In Tables 2 and 3, the parameters  $E$ ,  $\Delta E$ ,  $\langle I_m \rangle$  and  $\langle D_m \rangle$  are in eV while  $\langle \Gamma_{mc}^0 \rangle$  is in  $(\text{eV})^{1/2} \times 10^3$ .

Table 2: The resonance parameters in the present formula and those in the R-matrix formula

The present formula	The R-matrix formula
$E_m = 51.6$ $\Gamma_m = 0.52$ $\Gamma_{mc}^0 = 73.05$	$E_\lambda = 51.25$ $\Gamma_\lambda = 0.4019$ $\Gamma_{\lambda c}^0 = 39.34$
$E_s = 51.88$ $\Gamma_s = 0.4$ $ V_{sm}  = 0.22$	$E_\mu = 52.23$ $\Gamma_\mu = 0.5314$ $\Gamma_{\mu c}^0 = 30.57$
$\Delta E = 4.0$ $I_m = 3.2$	

The  $\Gamma_{\lambda c}^0$ , and  $\Gamma_{\mu c}^0$  and  $\Gamma_{mc}^0$  are in  $(\text{eV})^{1/2} \times 10^3$ . The  $|V_{ms}|^2$  is in  $(\text{eV})^2$  and the other parameters are in eV.

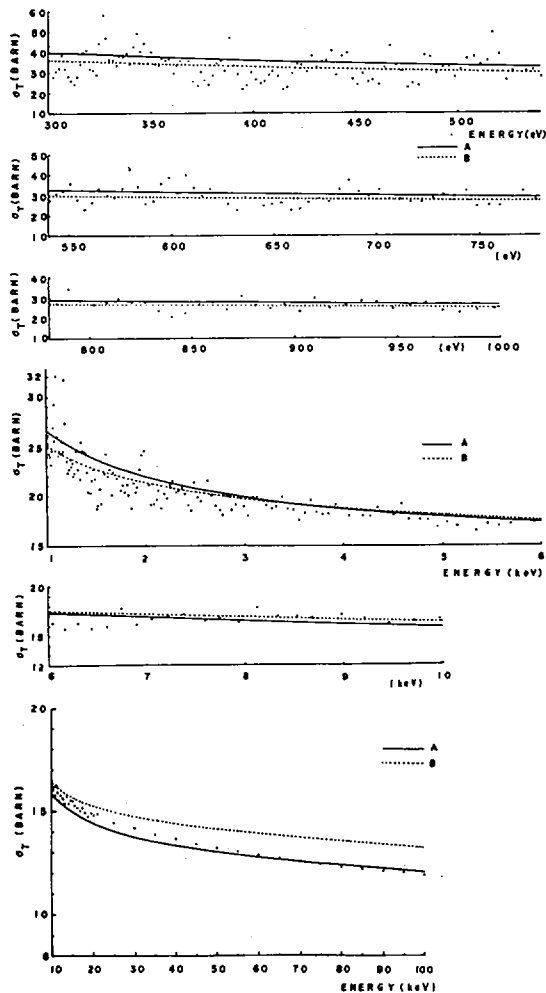


Fig. 5: The total neutron cross section in the energy region ( $E = 300 \sim 10^3$  eV). The solid points are the experimental data. Curve A is given by using Eq. (2.15) and the parameters,  $a_c = 9.097$  fermi,  $\langle \Gamma_{mc}^0 \rangle / \langle D_m \rangle = 2.47 \times 10^{-4} (\text{eV})^{-1/2}$ . On the other hand, curve B is given by using the formula  $\langle \sigma_T \rangle = 4\pi/k^2 \sum (2l+1) \sin^2 \delta_l + \sqrt{E} 2\pi^{3/2} k^2 \sum (2l+1) S_l V_l \cos 2\delta_l$ , and the parameters of reference 2,  $a_c = 9.65$  fermi,  $S_0 = 1.02 \times 10^{-4} (\text{eV})^{-1/2}$ ,  $S_1 = 2.0 \times 10^{-4} (\text{eV})^{-1/2}$ , where  $V_l$  and  $\delta_l$  are the penetration factor and the scattering phase shift, respectively.

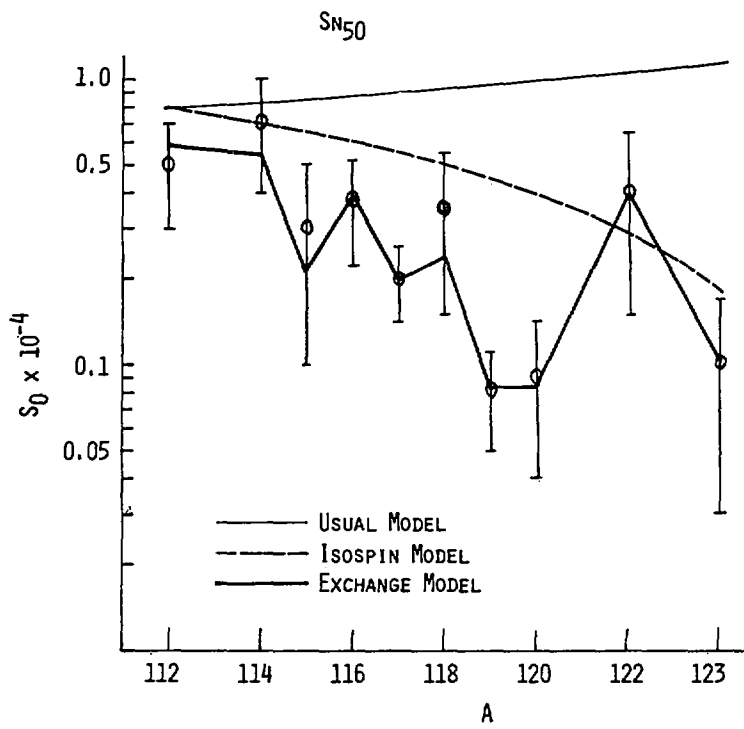


FIG.6

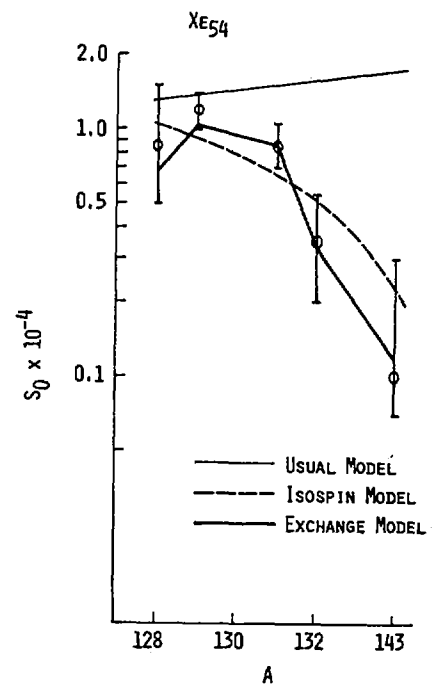


FIG.8

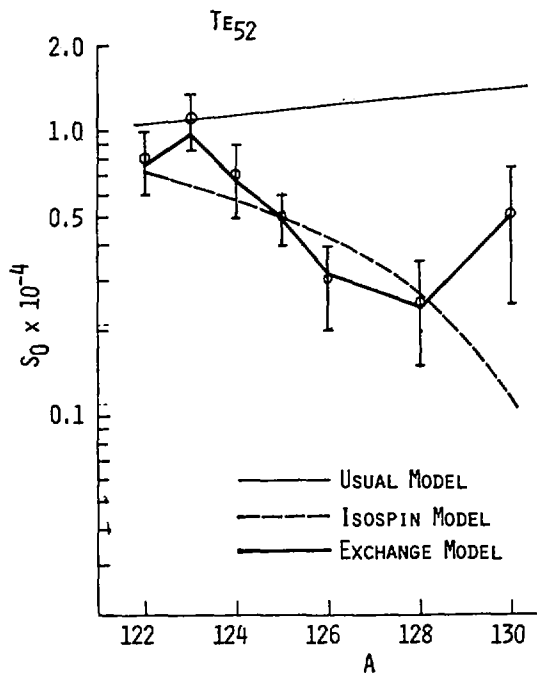


FIG.7

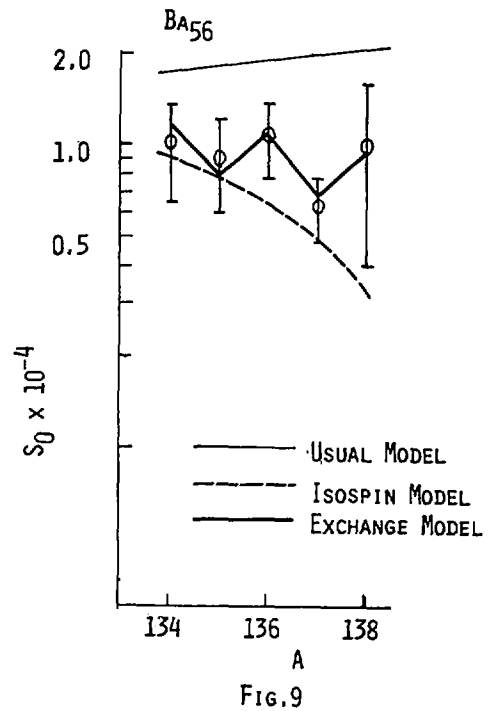


FIG.9

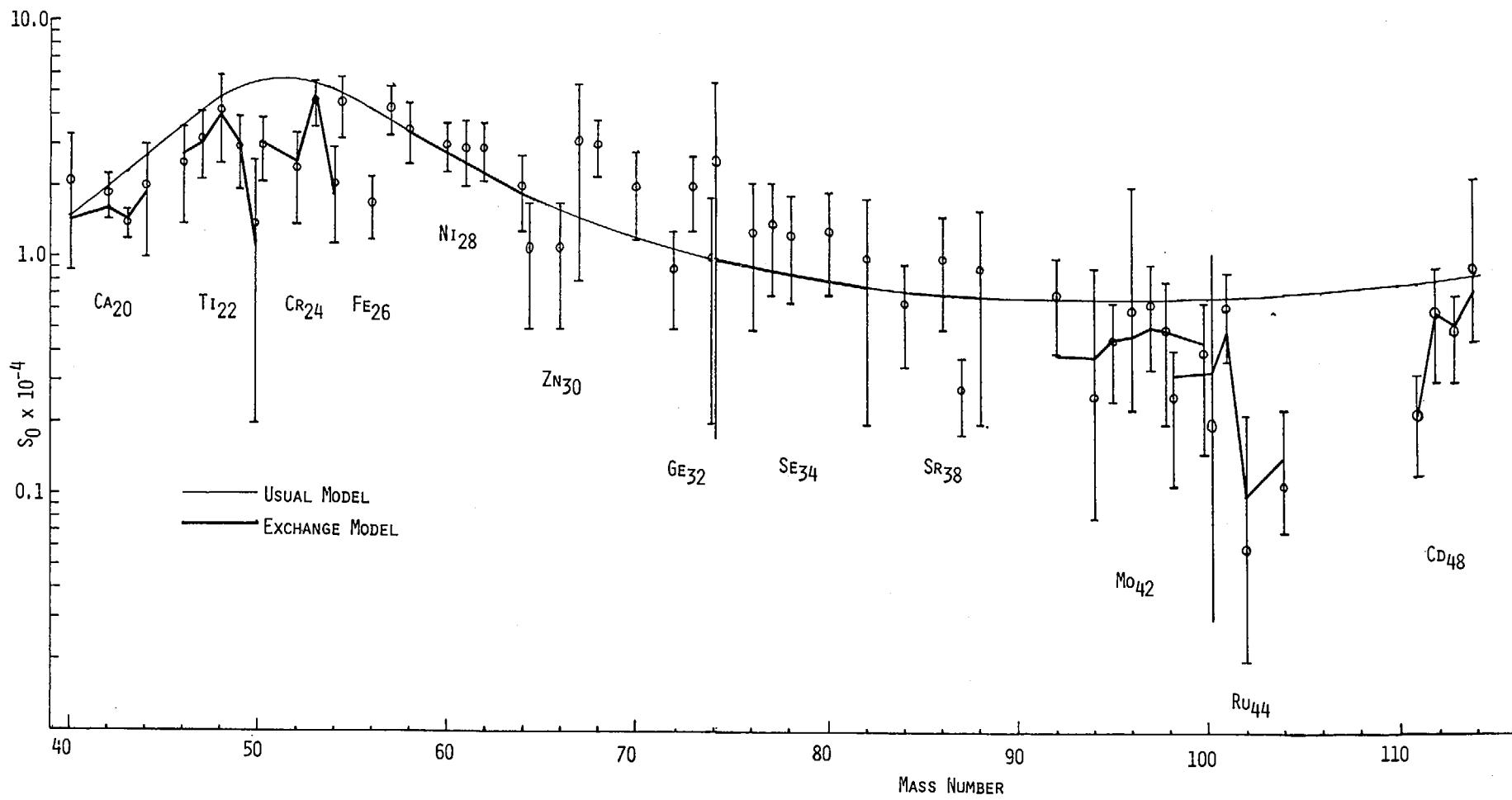


FIG.10

Table 6

JAERI - M 5984

	Fixed Parameters		Variable Parameters	
Usual model	$V_0=53.0$ Mev $f=2.172$	$W_0=4.0$ Mev		
Isospin model	$V_0=53.0$ Mev $f=2.172$	$V_1=30.0$ Mev	$W_0$	$W_1$
Exchange model	$V_0=53.0$ Mev $f=2.172$	$W_0=4.0$ Mev $V_T=56.0$ Mev	$\delta$	$E_d$

A	$W_0$	$W_1$	$\delta$	$E_d$	Binding Energy
Sn 112				10.802	10.802
114				10.320	10.320
115				7.534	7.534
116				9.566	9.566
117	9.3	44.9	0.735	8.500	6.9425
118				9.3273	9.3273
119				8.5	6.485
120				9.1044	9.1044
122				11.5	8.8047
124				11.2	8.493
Te 122				11.0	9.790
123				13.5	6.9299
124				10.8	9.4238
125	12.8	62.8	0.490	9.9	6.5849
126				9.1093	9.1093
128				9.7	8.772
130				11.7	8.413
Xe 128				9.614	9.614
129				12.0	6.905
131	23.1	115.5	0.361	11.4	6.6056
132				8.9361	8.9361
134				8.535	8.535
Ba 134				9.4644	9.4644
135				6.9752	6.9752
136	22.8	115.5	0.200	9.1071	9.1071
137				6.9021	6.9021
138				8.6115	6.6115

Table 7

A	$\delta$	$E_d$	Binding Energy	A	$\delta$	$E_d$	Binding Energy
Ca 40		15.634	15.634	Sr 84			
42	0.249	11.4727	11.4727	86	0.0		
43		7.9326	7.9326	87			
44		11.1361	11.1361	88			
Ti 46		13.1961	13.1961	Mo 92		12.692	12.692
47		13.0	8.8751	94		18.67	9.6722
48	0.249	14.0	11.6281	95		9.375	7.3751
49		11.5	8.1434	96	0.447	9.1542	9.1542
50		10.9480	10.9480	97		6.8161	6.8161
Cr 50		12.940	12.940	98		8.6424	8.6424
52	0.279	14.3	12.0407	100		18.3	8.301
53		16.0	7.9405	Ru 99		9.468	7.468
54		16.0	9.7202	100		9.6335	9.6335
Ni 58				101	1.48	11.80	6.805
60				102		9.2161	9.2161
61	0.0			104		9.912	8.912
62				Cd 111		6.9768	6.9768
64				112	0.806	11.40	9.397
Se 74				113		10.54	6.5398
76				114		14.04	9.0410
77	0.0						
78							
80							
82							

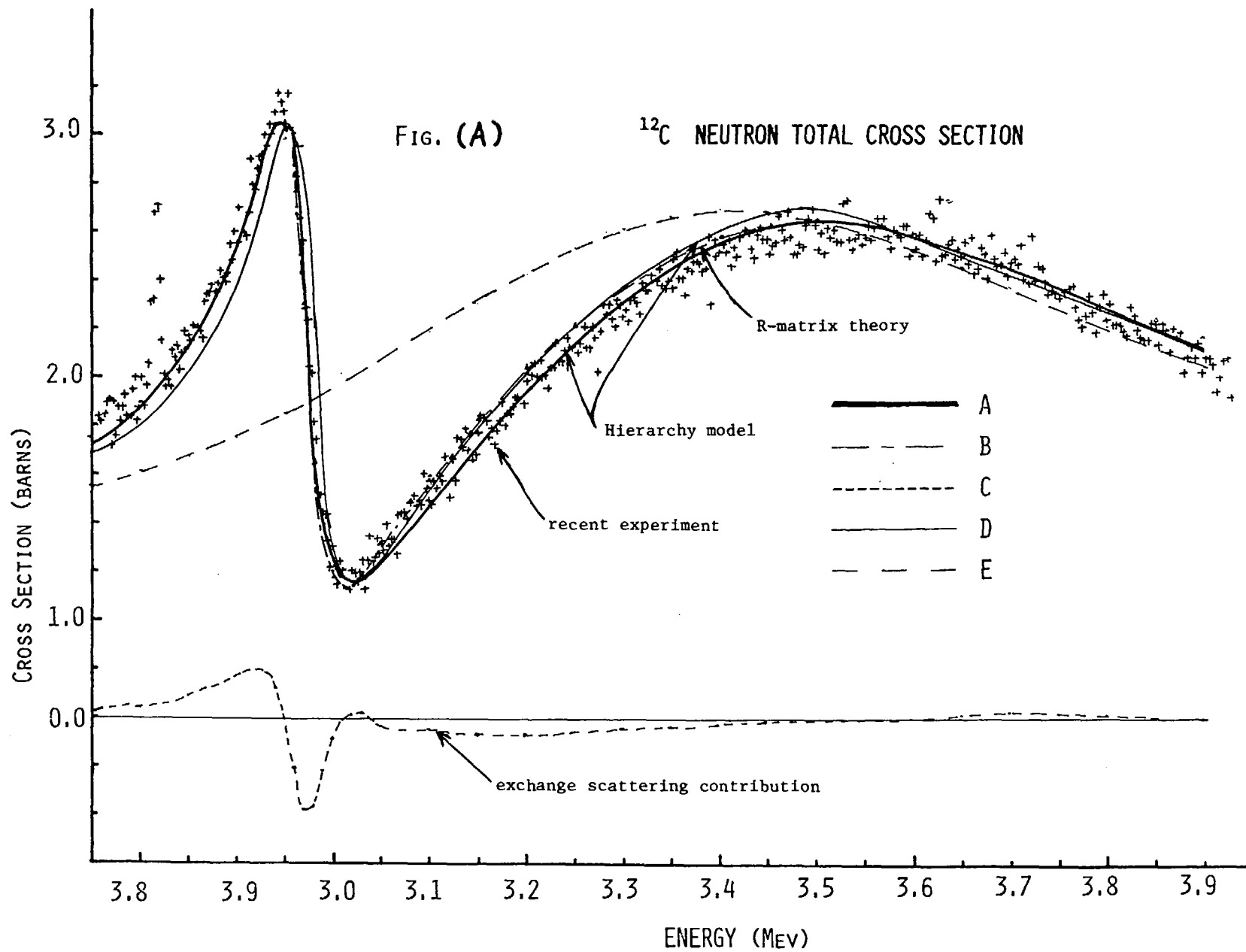
## DISCUSSION

A. MICHAUDON: I would like to mention that the fluctuations of the local average values of the total cross section for heavy nuclei ( $^{235}\text{U}$  for example) can be explained in terms of the fluctuations of the widths and spacings of the resonances. It is not necessary to take into account the effect of intermediate states whose influence has never been proved in such cases. Why do you need to postulate the existence of intermediate states to explain the behavior of the total cross section of  $^{235}\text{U}$ ?

Y. KITAZOE: Our theory does not stand on the nuclear fluctuation concept. We consider that what should be compared with this theory is only the reaction theories of Wigner and Eisenbud, Kapur and Peierls and so on, but not the others. We would like to stress that the hierarchy model describes not only the average cross sections but also the fine structures. We can show practically that the formula(1) reproduces well the observed fine structure of the  $^{235}\text{U}$  total neutron cross section as well as the R-matrix formula. As is seen from equation(1), the number of the parameters used is the same as that in the R-matrix theory. The main feature of equation(1) is that when it is averaged over a suitable energy interval, the obtained formula is substantially reduced to a dispersion type formula with the  $E_m$  which are almost equal to the peak energies of the really obtained quasi-resonances. On the other hand, the R-matrix formula does not give such an explicit description. The formula(2) reproduced well both the averaged cross section in the resolved region and the observed cross section in the unresolved region.

In this work, for simplicity, we decomposed the reaction states of the system into the two kinds of complexities. Therefore, if necessary, more kinds of them must be considered. The present two kinds of the reaction states have only their relative meaning of complexity. Therefore, there may be the cases where the states  $X_m$  are considerably complicated in comparison with the single-particle states of the incident particle. This means that if the states  $X_m$  are the single-particle states, the states  $X_s$  may be the doorway states of the two-particle one-hole type, if the states  $X_m$  consist of the two-particle one-hole states, the states  $X_s$  may be the hallway states, and so on. Any way, the former must be more simpler than the latter.

The hierarchy model formula is considered to be applied to many cases of the other elements. A typical example of them is demonstrated in Fig.(A).



## I-3. Effects of Nuclear Deformations on Neutron Total Cross Sections

Ch. LAGRANGE

Service de Physique Nucléaire  
 Centre d'Etudes de Bruyères-le-Châtel  
 B.P n° 61  
 92120 Montrouge - France

Several different experiments have recently reported total cross sections for deformed nuclei which have not been properly described by calculations using spherical optical models.

Glasgow and Foster [1] used the non-local potential of PEREY and BUCK [2] to represent their extensive measurements of total cross sections, but divergences between calculations and measurements reach 19 % for the deformed nuclei. SHAMU, et al [3] studied deformation effects explicitly in the Sm isotopes, which range from spherical  $^{150}\text{Sm}$  to strongly deformed  $^{154}\text{Sm}$ . They found pronounced differences between the cross sections for  $^{154}\text{Sm}$  and  $^{150}\text{Sm}$ , and also between the cross sections for  $^{152}\text{Sm}$  and  $^{150}\text{Sm}$ . These measured differences are expressed as ratios to the  $^{150}\text{Sm}$  cross section in figs 1a and 1b, respectively. The structure of these differences as a function of incident neutron energy cannot be reproduced with a spherical optical potential, even with a calculation in which the diffusivity of the potential has been strongly increased to approximate the effects of deformation [3]. The study presented here has been undertaken with the goal of seeing to what degree the systematic effects of nuclear deformations could be represented within the framework of coupled channel calculations. The coupled channel code JUPITOR 1 of TAMURA [4] has been modified and used for these tests.

The potential used has the usual form, reported often in reference to nuclear scattering :

$$V(\vec{r}) = V f(r, a, R) + 4iW a' \frac{d}{dr} f(r, a', R') + \left(\frac{\hbar}{m c}\right)^2 \frac{1}{2} V_5 \vec{\ell} \cdot \vec{\sigma} \frac{d}{dr} f(r, a, R) \quad (1)$$

where  $f(r, a, R) = \left\{ 1 + \exp[(r-R)/a] \right\}^{-1}$ ,  $R = r_0 A^{1/3} [1 + \beta_2 Y_2^0(\theta)]$

The parameter  $\beta_2$  fixes the size of the quadrupole deformation, the only deformation envisaged here.

The effects of this deformation have been extensively studied over the range of energies from 2 MeV to 20 MeV, and reported in the form :

$\rho = \sigma_{tot}(\beta_2) / \sigma_{tot}(\beta_2=0)$ . Studies have been completed for the following nuclei :  $^{238}\text{U}$ ,  $^{182}\text{W}$ , and the even isotopes of Sm with  $A = 148$  to  $154$ .

Two sets of potential parameters have been considered in this study :

a) The set 1, in table 1, used by G. PALLA [5] in her demonstration of deformation effects in neutron elastic scattering at small angles. Her calculations were for scattering from  $^{238}\text{U}$  and  $^{232}\text{Th}$  at 14.7 MeV incident energy.

b) The set 2, also in table 1, which we have developed to fit the following experimental data for  $^{238}\text{U}$  : "s" and "p" wave strength functions, potential elastic scattering cross sections, and total cross sections measured by CABE, et al [6] between 200 keV and 6 MeV incident energy. This set of parameters is slightly different from the most recently determined one which is given in ref. [7].

### RESUME OF RESULTS

1) The nuclear deformation induces into the function  $\rho(E_n)$  an oscillatory behaviour, oscillating about the value 1. For a given nucleus, the regions in energy where the effects are either a minimum, that is, the ratio  $\rho = 1$ , or a maximum, are well defined and practically independent of parameters or detailed model assumptions. For  $^{238}\text{U}$  one can see in fig. 2 that minima occur near 4.2 and 8.3 MeV and maxima occur near 6.5 and 13.5 MeV. To be more specific about parameter dependence, the minima and maxima are essentially independent of : the deformation itself, whether one uses potential parameter sets 1 or 2, and the number of collective states coupled to the ground state. In contrast, the positions of minimum effects are rather sensitive to whether one uses real

or complex coupling between the different channels. Depending upon the choice of real or complex coupling, the other parameters of the calculation must be adjusted to produce the same results for both types of coupling. The amplitudes of the oscillations of  $\rho$  are themselves particularly sensitive to the deformation parameter  $\beta_e$ .

2) When the mass of the target nucleus is considerably diminished, the same behaviour of the function  $\rho(E_n)$  is obtained, but with a displacement of the whole pattern to lower energies. Figure 2c compares results for  $^{238}\text{U}$  and  $^{182}\text{W}$ .

3) The oscillatory behaviour of  $\rho(E_n)$  is readily demonstrated also for calculations assuming a vibrational nucleus, just as already discussed for rotational nuclei. Nonetheless the corresponding structures of  $\rho$  are different, as demonstrated in fig. 1d. There the results are shown for the rotational nucleus  $^{154}\text{Sm}$  and for  $^{148}\text{Sm}$ , assumed vibrational.

4) The structure obtained in the recent measurements of SHAMU, et al [3] is well reproduced by the present calculations, as shown in fig. 1. Examination of these results shows the sensitivity of this structure to small differences in deformation or nuclear size; it changes character noticeably between the close neighbours  $^{152}\text{Sm}$  and  $^{154}\text{Sm}$ . In spite of this sensitivity, the calculations do not seem to permit us to decide whether  $^{150}\text{Sm}$  should be treated as a rotational or vibrational nucleus, for the purposes of these calculations.

We thank M. McEllistrem and J. Salvy for their encouragements in this study and for very useful discussions.

#### REFERENCES

- [1] D.W. GLASGOW and D.G. FOSTER, Phys. Rev. C3 (1971) 604
- [2] F. PEREY and B. BUCK, Nucl. Phys. 32 (1962) 353
- [3] R.E. SHAMU, E.M. BERNSTEIN, D. BLONDIN, J.J. RAMIREZ and G. ROCHAU, Phys. Lett. 45B (1973) 241
- [4] T. TAMURA, Computer Program JUPITOR 1 for coupled channel calculations ORNL-4152 (1967)
- [5] G. PALLA, Phys. Lett. 35B (1971) 477
- [6] J. CABE, M. CANCE : Rapport CEA-P-4524 (1973)
- [7] Ch. LAGRANCE : Other communication to this meeting.

	V (MeV)	W (MeV)	V <sub>s</sub> (MeV)	a (fermi)	r <sub>0</sub> (fermi)	a' (fermi)	r' <sub>0</sub> (fermi)
Set 1	47,01 - 0,267E - 0,0018E <sup>2</sup>	8,50 MeV	8,30	0,66	1,25	0,48	1,25
Set 2	47,3 - 0,3 E	3 + 0,3 E si E ≤ 4 MeV 3,72 + 0,12 E si E ≥ 4 MeV	7,50	0,65	1,25	0,70	1,25

TABLE 1

Parameters of the optical model potentials

Figure Captions

Fig. 1

Variations of total cross section differences as a function of incident neutron energy. The relative differences are shown for  $^{154}\text{Sm}$  and  $^{150}\text{Sm}$  in part (a) and for  $^{152}\text{Sm}$  and  $^{150}\text{Sm}$  in part (b). The experimental data have been taken from ref. [3]. The curves are the results of calculations with different hypotheses about the collective character of  $^{150}\text{Sm}$ . The potential parameters are set 1 of table 1; channels coupled are  $0^+$ ,  $2^+$ ; complex coupling has been used between channels.

Fig. 2

Variation in energy of total cross section ratios. The ratio is that of the cross section for the indicated value of  $\beta_2$  divided by that for  $\beta_2 = 0$ . The potential parameters are from table 1: set 1 for a, c, d; set 2 for b.

- (a)  $^{238}\text{U}$  - complex coupling between channels; solid curve - coupled channels, including  $0^+$ ,  $2^+$ ; dashed curve - adiabatic approximation.
- (b)  $^{238}\text{U}$  - channels coupled:  $0^+$ ,  $2^+$ ; solid curve: complex coupling between channels; dashed curve: real coupling.
- (c) Comparison for  $^{238}\text{U}$  and  $^{182}\text{W}$  - channels coupled:  $0^+$ ,  $2^+$  - complex coupling
- (d) Comparison between the rotational nucleus  $^{154}\text{Sm}$  and the vibrational nucleus  $^{148}\text{Sm}$  - channels coupled:  $0^+$ ,  $2^+$  - complex coupling between channels.

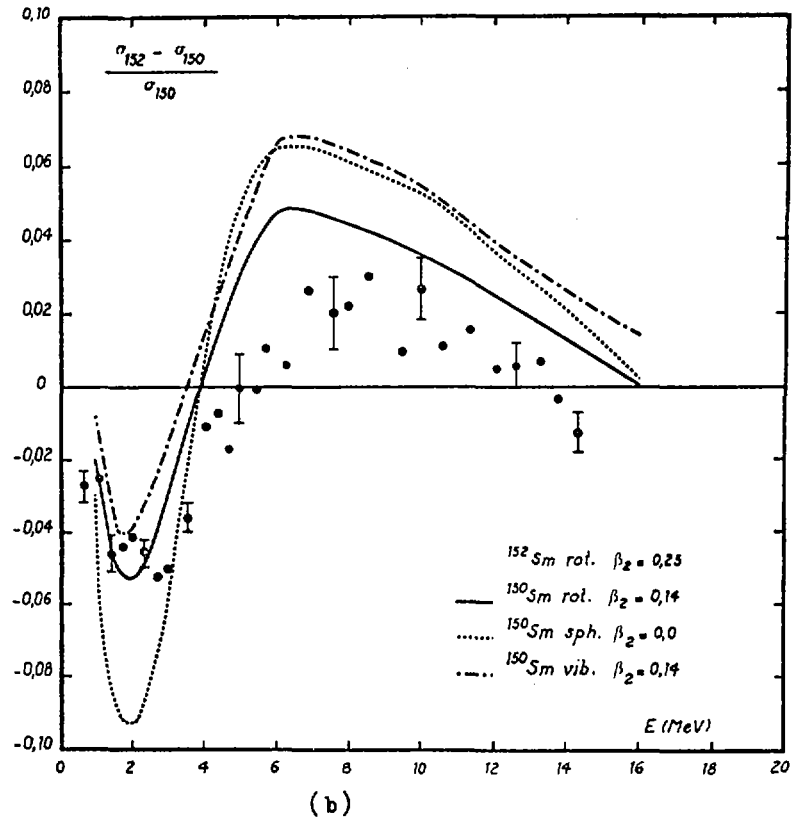
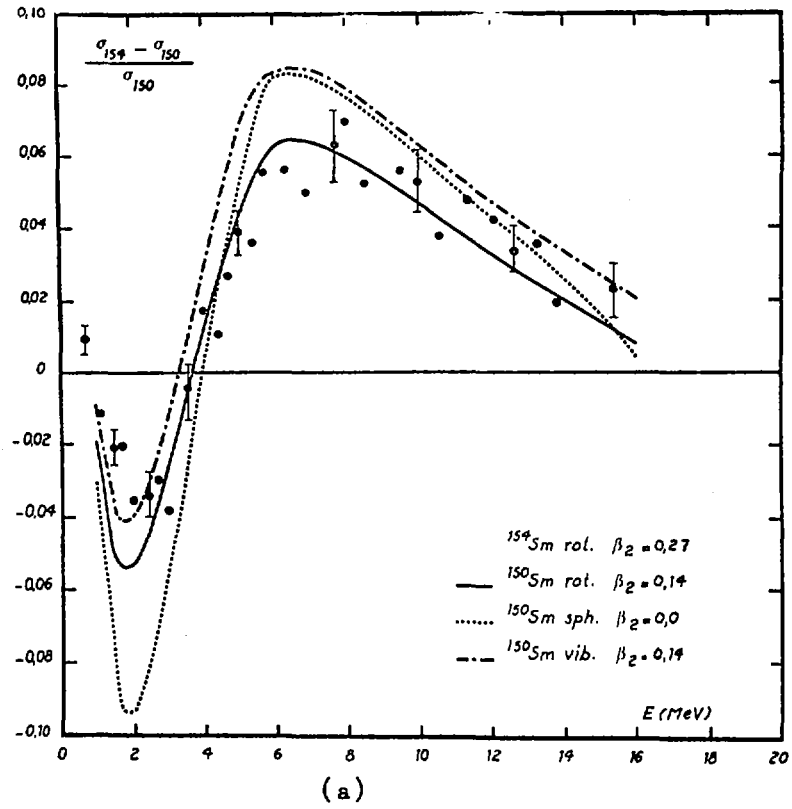
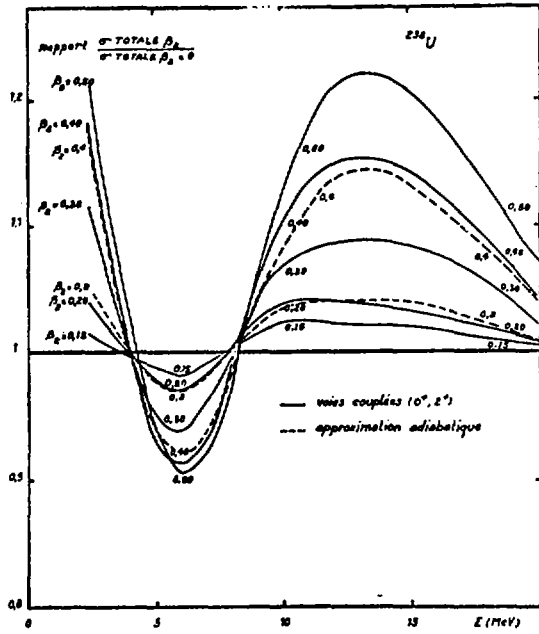
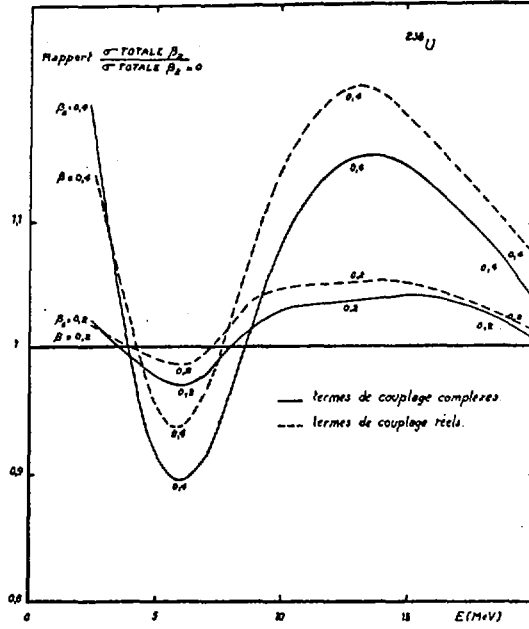


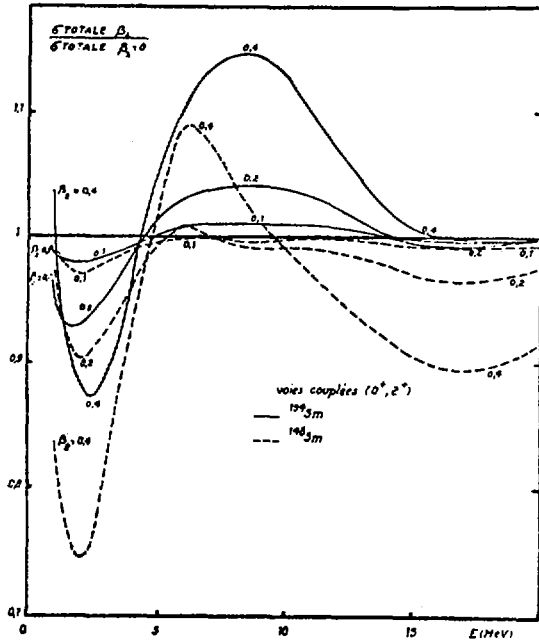
Fig. 1



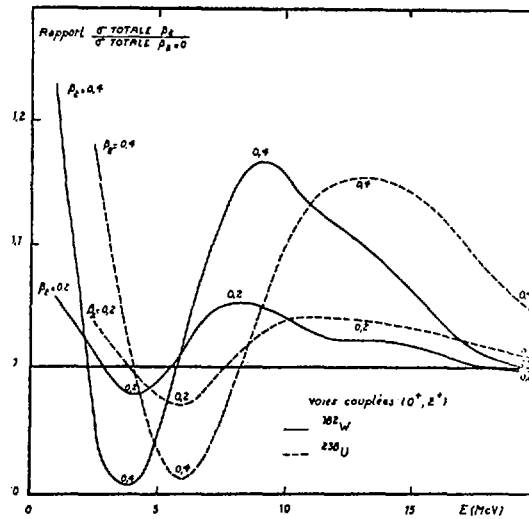
(a)



(b)



(d)



(c)

Fig. 2

I-4. "Evaluation of Neutron-Nucleus Cross Sections  
in Heavy Nuclei with a Coupled Channel Model  
in the Range of Energy from 10 keV to 20 MeV"

Ch. LAGRANGE

Service de Physique Nucléaire  
Centre d'Etudes de Bruyères-le-Châtel  
B.P. n° 61 - 92120 Montrouge - France

The existence of permanent deformations in heavy nuclei makes it necessary to account for the direct excitation of rotational levels explicitly. This can be done using the optical model with coupled channels. In order to exploit this approach in a practical way for the purposes of evaluation, we have developed a code based on JUPITOR 1 of TAMURA [1]. The code developed here is more complete and also more rapid than JUPITOR. The speed has been improved by the utilization of a method of numerical integration called "modified Numerov" as set forth by RAYNAL [2]. This modification of the numerical integration method permits us to adopt a radial mesh much larger than that employed in the Störmer method used initially. The code thus modified has been used to search for a unique and physically coherent parameter set which would cover the range of incident energies from 10 keV to 20 MeV, and notably for nuclei with masses  $232 \leq A \leq 242$ . We calculate not only the total cross sections and the direct scattering cross sections but also the compound nucleus formation cross sections, or the neutron transmission coefficients necessary for evaluations with the statistical model. As test nuclei we have chosen  $^{238}\text{U}$  and, to a lesser degree,  $^{232}\text{Th}$ . We require that we have satisfactory fits, in the order of decreasing importance, to the following experimental results :

1. The strength functions described as  $S_0$  and  $S_1$ , and the potential cross section at low energies as well as the total cross section from 10 keV to 1 MeV.
2. The total cross section from 1 MeV to 20 MeV.
3. The different angular distributions for "elastic" scattering in the range of energy from 2 MeV to 15 MeV. At these energies it is almost impossible to distinguish between the elastic and the inelastic scattering to the first excited states. We will compare the experimental results to calculated values obtained by summing differential scattering to the included nuclear states with energies less than 400 keV.

This order of importance follows from the order of decreasing influence of the parameters of the model on the calculated values. We require a satisfactory overall agreement with all of the data, and refuse to search for alterations of the parameterization which would give better agreement with particular data sets. Thus, for example, we have not implemented an automatic parameter search to fit elastic scattering angular distributions.

Among the parameters of the model only those which describe the quadrupole ( $\beta_2$ ) or hexadecapole ( $\beta_4$ ) deformations and the radius of the nuclear potential vary from one nucleus to another. We have noted that at low energies the total parameterization was very sensitive to the choice of deformation parameters. For this reason, and because of the large experimental errors associated with measurements of deformation parameters issuing from a common model calculation of the nuclei which we have studied. The nuclear model used was based on the Nilsson model modified by the methods of Strutinsky as described by Möller [3]. Some of the deformation parameters obtained in this fashion are the following:

$$\begin{aligned}
 {}^{232}\text{Th} &: \beta_2 = 0.206, \beta_4 = 0.086 \\
 {}^{238}\text{U} &: \beta_2 = 0.216, \beta_4 = 0.067 \\
 {}^{242}\text{Pu} &: \beta_2 = 0.239, \beta_4 = 0.058
 \end{aligned}$$

The parameterization obtained has the following characteristics:

- a) A Coupled Channel model with the base states  $0^+$ ,  $2^+$ ,  $4^+$  up to an energy of 10 MeV. At higher energies, to reduce the extensive calculation time, the adiabatic approximation has been used.

b) Real Potential :  $V_R = 47.5 - 0.3 E_n$  ,  $a_R = 0.62 f$  ,  
 $r_{oR} = 1.24 f$ .

c) Imaginary Potential (surface absorption with a Woods-Saxon derivative form factor) :

$$W_D = \begin{cases} 2.7 + 0.4 E_n & E_n \leq 10 \text{ MeV} \\ 6.7 & E_n > 10 \text{ MeV} \end{cases}$$

$$a_D = 0.58 f , \quad r_{oD} = 1.26 f$$

d) Spin-Orbit Potential :

$$V_{so} = 7.50 \text{ MeV} , \quad a_{so} = 0.62 f , \quad r_{so} = 1.24 f \text{ (Thomas form) .}$$

e) The coupling between channels is taken to be real and the value of the imaginary potential is the same for all channels .

The potential at very low energies was determined by simultaneous adjustment of calculated values of the strength functions  $S_0$  and  $S_1$  and of the potential scattering cross section to the measured values of these quantities . The variation of these parameters with neutron energy has been determined to reproduce the total cross section in the energy range from 10 keV to 10 MeV.

Following this, the theoretical-experimental comparison for the angular distributions of "elastic" scattering has permitted us to judge the well-determined parameterization . In the energy range from 10 to 20 MeV, where the results are much less sensitive to model parameters, we have based our choices on the total cross sections and especially on the angular distributions for elastic scattering . These have been measured by HUDSON [4] at 15 MeV and by GUZHOVSKII [5] at 15.2 MeV .

We present now some results and comments :

1 . Strength functions and potential cross sections .

Our calculated values at 10 keV can be compared to the experimental results obtained by VAN'KOV et al [6] for  $^{238}\text{U}$  and by RIBON [7] for  $^{232}\text{Th}$  :

		$S_0 \times 10^4$	$S_1 \times 10^4$	$\sigma_{pot.}$ (barns)
$^{238}\text{U}$	Theoretical	0.949	2.134	10.73
	Experimental	$0.96 \pm 0.07$	$2.2 \pm 0.3$	$10.7 \pm 0.3$
$^{232}\text{Th}$	Theoretical	1.004	1.719	11.23
	Experimental	$0.87 \pm 0.10$	$S_1 = 1.5 \pm 0.4$	$11.7 \pm 0.24$

## 2. Total cross sections from 10 keV to 1 MeV for $^{238}\text{U}$ .

We have found that a good preliminary fit to the potential cross section at 10 keV was necessary to obtain a good adjustment of the total cross section at low energies with a simple parameterization. In fig. 1a the calculated total cross sections are compared to measurements of CABE et al. [8]. In the range of energies from 30 keV to 1 MeV the calculated values are very near those of the recent evaluation of A. B. SMITH [9], deviating from them by 1 - 2%. On the other hand, in the range of energy 10 - 30 keV the calculated total cross section deviates nearby 5% from the experimental results; we find here again a characteristic fault of the model.

## 3. Total cross sections from 1 to 20 MeV.

We compare the results of our calculations to the measurements of GOULDING et al. [10] and BOWEN et al. [11] in figs. 1b and 2. Our values compare favorably to the experimental evaluation of SMITH [9] the largest deviations being in the region of 18 to 20 MeV, where we have values 3% above those recommended by SMITH.

## 4. Angular Distribution for "Elastic" Scattering by $^{238}\text{U}$ and $^{232}\text{Th}$ .

Figures 3 to 6 show the comparison of calculated and measured angular distributions. The calculations include elastic scattering and inelastic scattering to the first excited levels of the ground state band (The first three nuclear states when the coupling is  $0^+$ ,  $2^+$ ,  $4^+$ , or the first four nuclear states when we apply the adiabatic approximation). The only parameter adjustment for this data has been to adjust  $W_D$  to match the measured distributions near 15 MeV.

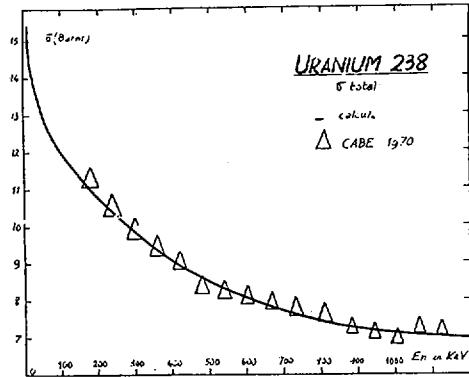
Since there has been no systematic re-determination of parameters, the examination of these results permits one to judge the parameterization adopted. The different measurements reproduced here have been taken from references [12] to [19]. The good overall agreement between theory and experiment developed here is the result of the method of parameterization explained above.

In conclusion, the parameterization obtained proves itself useful for extrapolations over a range quite extended in energy and in target nuclei. This has been exploited in a systematic fashion for a group of even isotopes of Uranium, for  $A = 232$  to  $240$ , and for Plutonium, with  $A = 238$  to  $242$ . In the framework of a first theoretical evaluation we have judged it sufficient

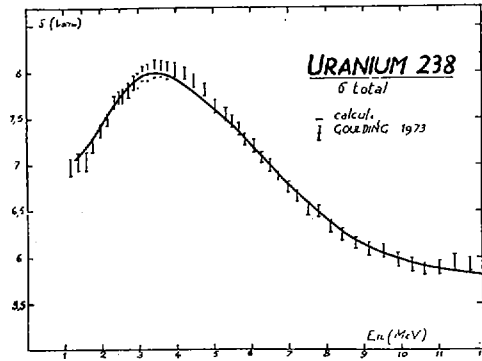
in the case of odd nuclei to interpolate the results furnished by this model from the two neighboring even isotopes .

### REFERENCES

- [ 1 ] T. TAMURA, Computer program JUPITOR 1 for coupled channel calculations ORNL 4152 (1967) and Rev. of Mod. Phys. 37 (1965) 679 .
- [ 2 ] J. RAYNAL, Lectures given at Seminar on computing as a language of Physics ICTP Trieste (2, 20 Août 1971) .
- [ 3 ] P. MOLLER, Nucl. Phys. A 192 (1972) 529 .
- [ 4 ] C. L. HUDSON, W. SCOTT. WALKER, S. BERKO, Phys. Rev. 128 (1962) 1271
- [ 5 ] B. Y. GUZHOVSKII, At. Energ. 11 (1961) 395, trad. Sov. J. At. En. 11 (1962) 1041 .
- [ 6 ] A. A. VAN'KOV, Y. V. GRIGORIEV, V. V. FILIPPOV, M. N. NICOLAEV, B. BIOLER, Z. KOLLATS, L. B. PIKELNER, Nuclear data for Reactors (Proc. Conf. Helsinki) Vol. 1, p. 559 , International Atomic Energy Agency, Vienna, 1970 .
- [ 7 ] J. P. RIBON Note CEA N-1149 (1969)
- [ 8 ] A. ADAM, J. CABE, M. CANCE, M. LABAT, M. LAURAT, M. LONGUEVE C. E. A - Centre d'Etudes de Bruyères-le-Châtel - rapport interne .
- [ 9 ] A. B. SMITH, The inelastic neutron scattering cross section of  $^{238}\text{U}$  . 6 th INDC meeting Vienna (1973) .
- [ 10 ] S. H. HAYES, P. STOLER, J. M. CLEMENT, GOULDING, Nucl. Sci. Eng. 50 (1973) 243 .
- [ 11 ] P. H. BOWEN, J. P. SCANLON, G. H. STAFFORD, J. J. TRESHER, P. E. HODGSON, Nucl. Phys. 22 (1961) 640 .
- [ 12 ] R. BATCHELOR, W. B. GILBOY, J. M. TOWLE, Nucl. Phys. 65 (1965) 236
- [ 13 ] M. WALT, J. R. BEYSTER, Los Alamos LA 2061 (1956)
- [ 14 ] M. M. KNITTER, M. COPPOLA, N. AHMED, B. JAY, Z. Physik 244 (1971) 358 .
- [ 15 ] W. E. KINNEY, F. G. PEREY, ORNL 4804 (1973) .
- [ 16 ] S. G. BUCCINO, C. E. HOLLANSWORTH, P. R. BEVINGTON, Z. Physik 196 (1961) 103 .
- [ 17 ] J. L. KAMMERDIENER, U. C. R. L 51232 (1972) .
- [ 18 ] J. VOIGNIER, CEA-R 3503 (1968)
- [ 19 ] G. MOUILHAYRAT, Centre d'Etudes de Bruyères-le-Châtel - private communication (1969)



(a)



(b)

Fig. 1

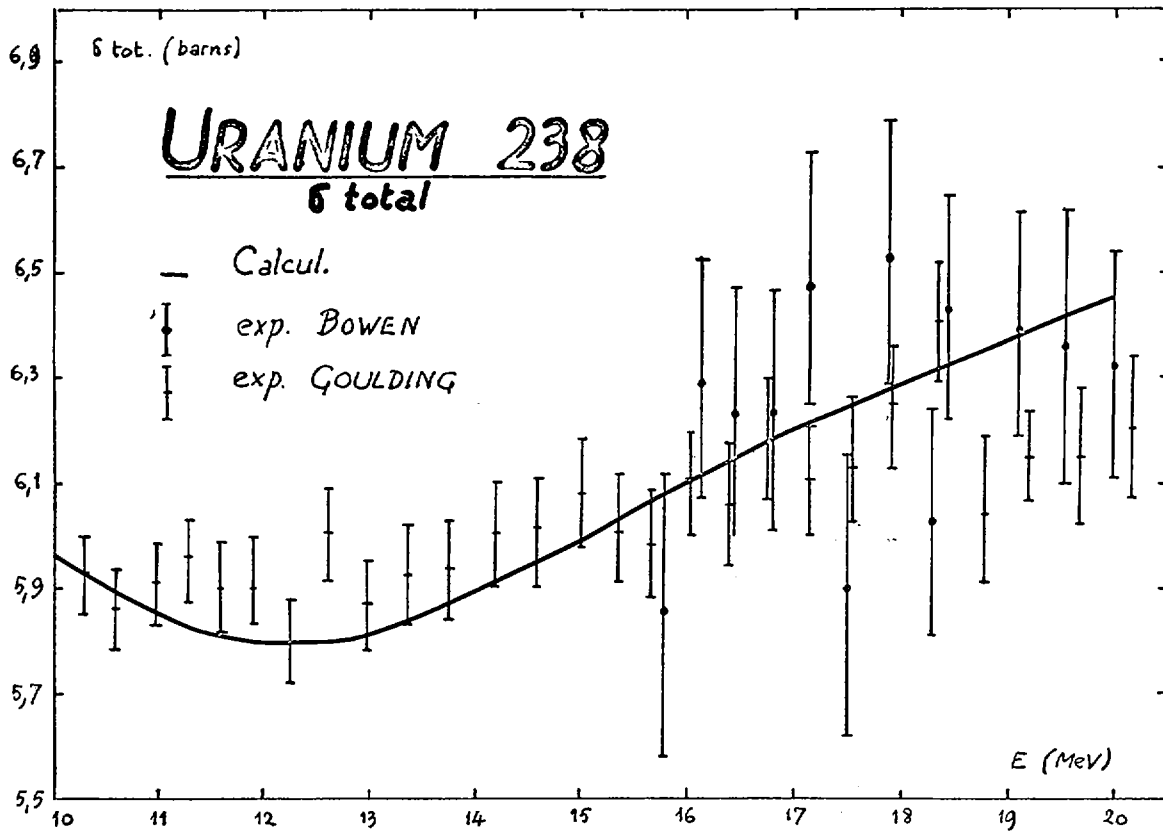


Fig. 2

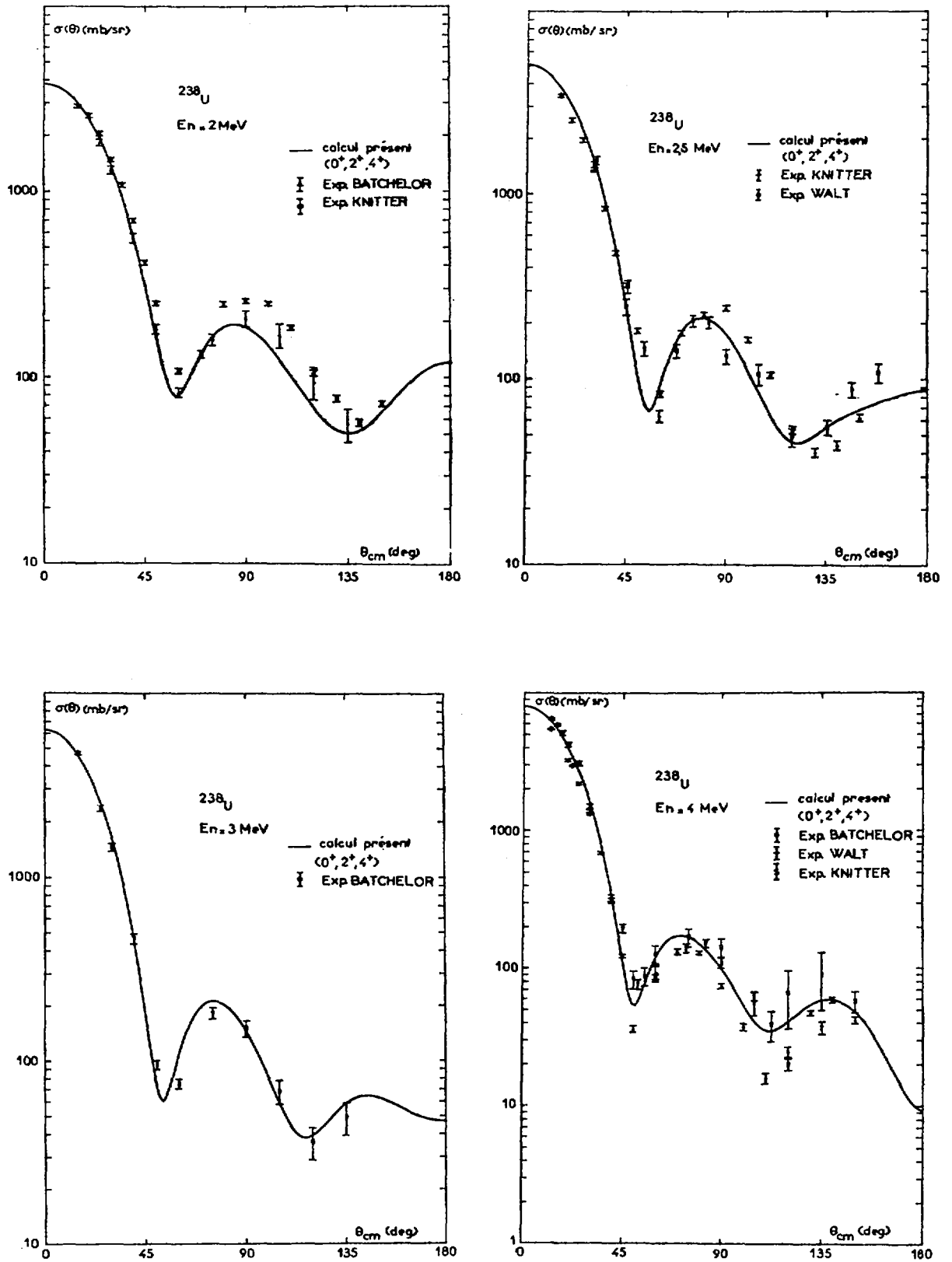


Fig. 3

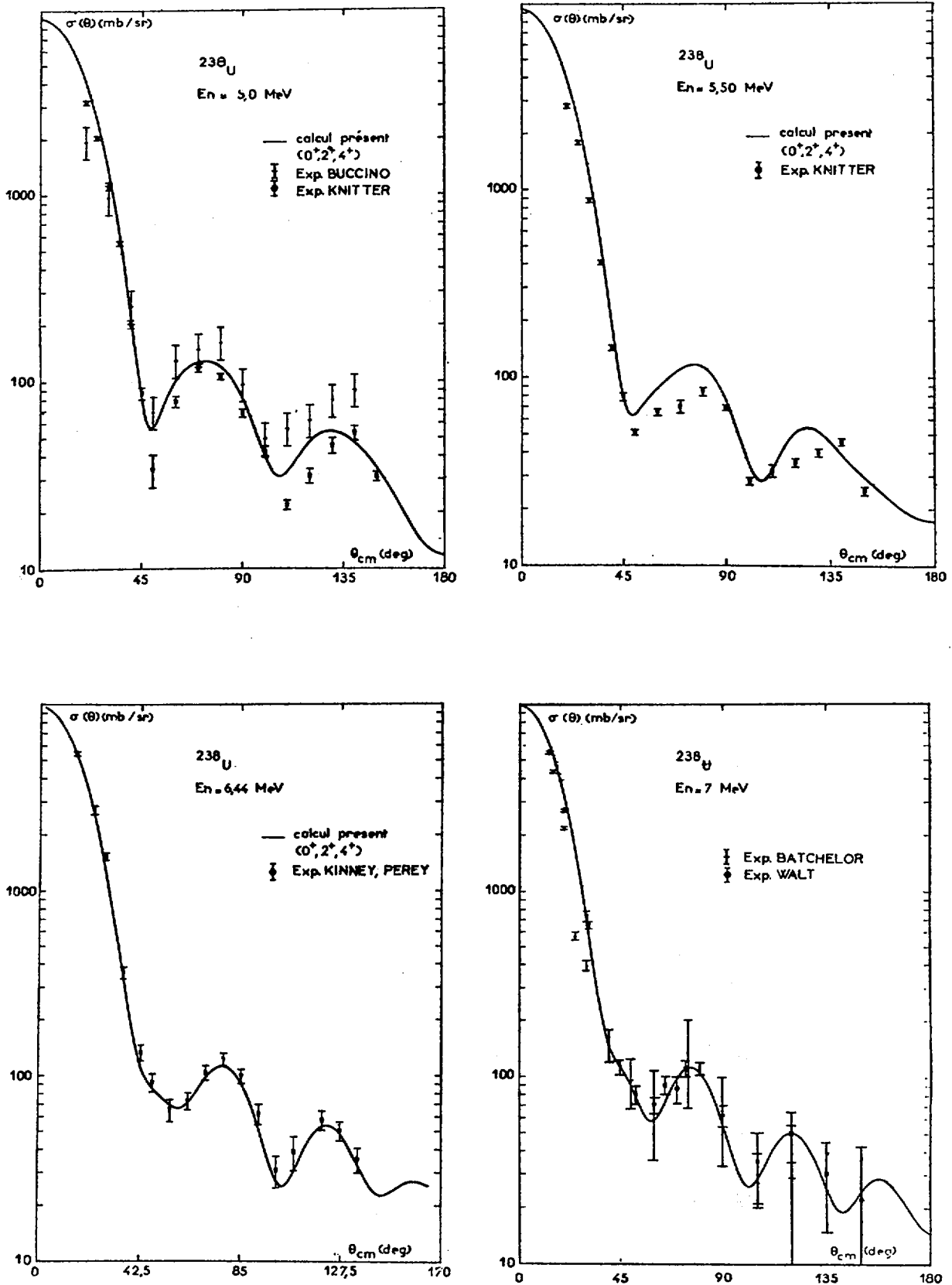


Fig. 4

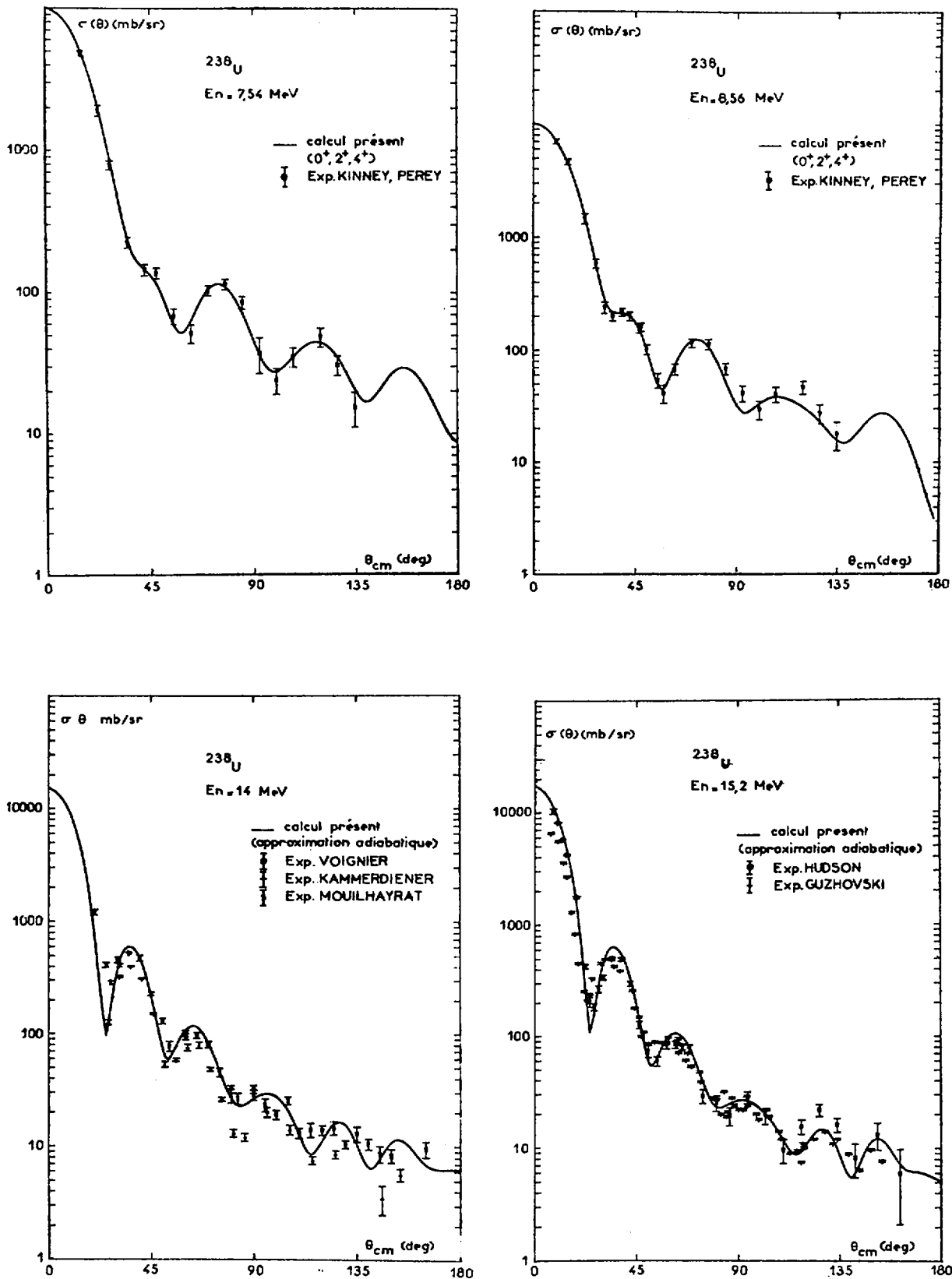


Fig. 5

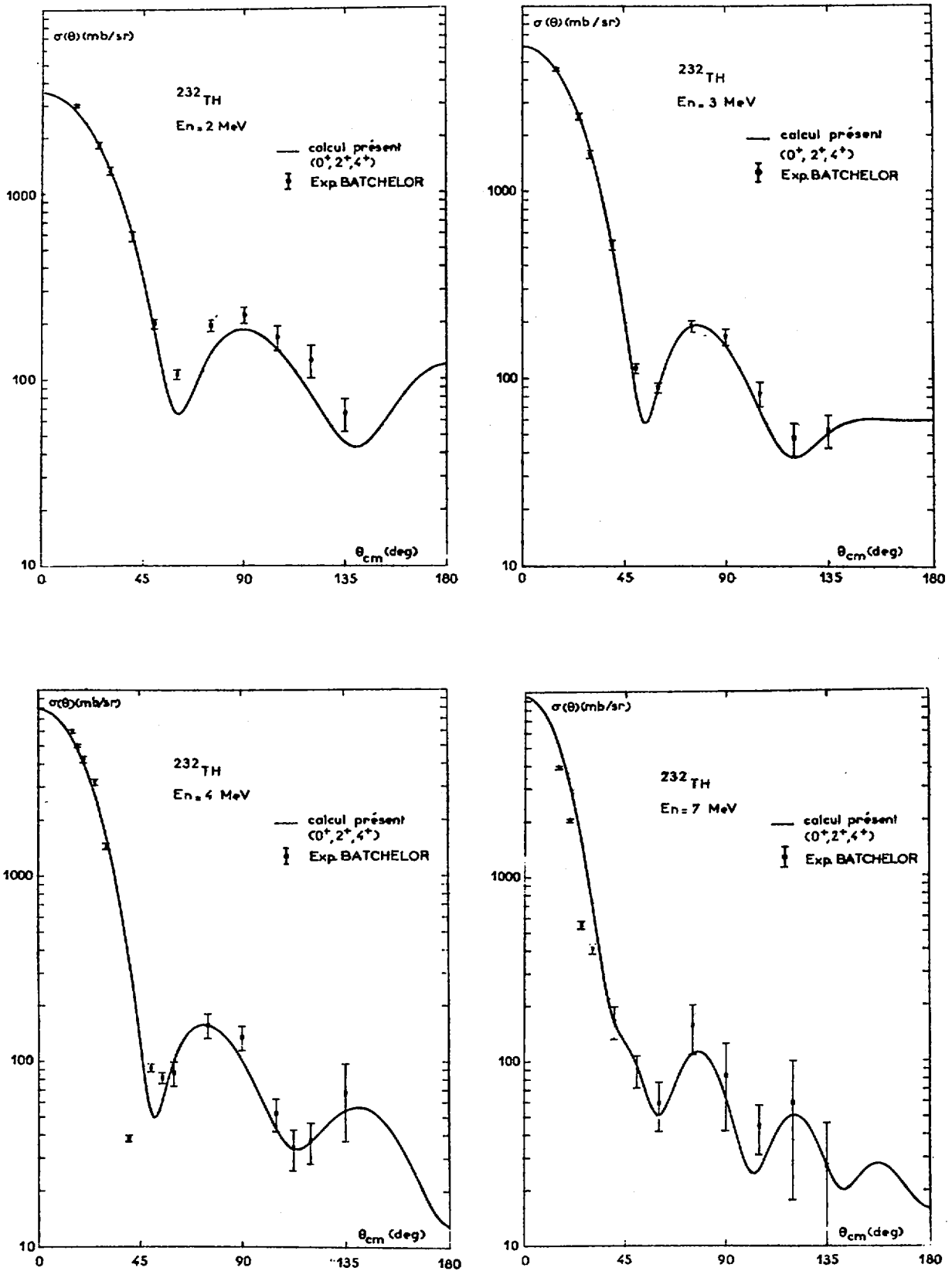


Fig. 6

I-5. Calculation of  $(n, n'\gamma)$  cross sections from 2 to 7 MeV  
neutron energy for light nuclei

B. DUCHEMIN

Service de Physique Nucléaire  
Centre d'Etudes de Bruyères-le-Châtel  
B.P n° 61  
92120 Montrouge - France

Cross sections for the production of deexcitation  $\gamma$  rays following inelastic neutron scattering have been calculated for Si, Cr and Ni isotopes from threshold to 7.0 MeV incident neutron energy. The statistical model [1] with width fluctuation corrections [2] was used, taking into account only the  $Q = 0$  correction. The optical model used is of the form

$$V(r) = -U f(r) + 4iW g(r) + U_{so} \left( \frac{\hbar}{m_{\pi}c} \right)^2 \vec{l} \cdot \vec{\sigma} \frac{1}{r} \frac{d}{dr} f(r)$$

with

$$f(r) = \left\{ 1 + \exp[(r-R_u)/a] \right\}^{-1}, \quad R_u = r_{ou} A^{1/3}$$

and

$$g(r) = \frac{d}{dr} \left\{ \left[ 1 + \exp[(r-R_w)/b] \right]^{-1} \right\}, \quad R_w = r_{ow} A^{1/3}$$

The parameters were chosen from recent work on inelastic neutron scattering. These calculations do not include  $(n,p)$ ,  $(n,\alpha)$  or direct interaction contributions. A calculation done by Kellie and al [3] shows that at 9 MeV excitation energy the influence of  $(n,p)$  and  $(n,\alpha)$  channels is only 2 % of the cross-section in  $^{56}\text{Fe}$ . Perey and Kinney [4] show that at 7 MeV the direct interaction contributes only 5 % to the  $\gamma$  - ray cross-section in  $^{56}\text{Fe}$ .

We compare in figure 1 only the most significant calculational results with recent experimental results from our laboratory [5]

for the transitions  $E_\gamma = 1.779$  MeV in  $^{28}\text{Si}$  and  $E_\gamma = 1.332$  MeV in Ni.

a) Silicon

The optical parameters and the adopted level scheme were taken respectively from Holmqvist and al [6] and Tücker and al [7]. The 1,779 keV  $\gamma$  ray comes from the transition  $1,779 \text{ keV}(2^+) \xrightarrow{E2} 0(0^+)$  in  $^{28}\text{Si}$ .

b) Nickel

The optical model parameters were taken from a study of inelastic neutron scattering on  $^{56}\text{Fe}$  by Rolard and al [8] and they are as follows :

$$r_{ou} = r_{ow} = 1.24 \text{ fm} \quad a = 0.66 \text{ fm} \quad b = 0.48 \text{ fm}$$

$$U = 49.02 - 0.33 E \text{ MeV} \quad W = 10.46 \text{ MeV} \quad U_{so} = 8 \text{ MeV}$$

The adopted level scheme was taken from Tücker and al [9]. The 1.332 MeV  $\gamma$ -ray intensity is composed of two transitions, the  $1,332 \text{ keV}(2^+) \xrightarrow{E2} 0(0^+)$  transition in  $^{60}\text{Ni}$  (26.23%) and the  $2,775 \text{ keV}(2^+) \xrightarrow{M1} 1,454 \text{ keV}(2^+)$  transition in  $^{58}\text{Ni}$  (67.88 %). This last transition contributes 26 % to the total strength. No account has been taken of the levels of excitation energy greater than 4 MeV, but it does not appear that inclusion of these levels would alter the calculated results appreciably.

In the excitation energy range considered here the width fluctuation corrections are necessary to get a satisfactory comparison between experiment and theory for nickel and silicon and also for other cases not reported here. As can be seen from nickel results shown in fig. 1 the two calculations will eventually coincide at sufficiently high energies.

These calculations were done with the code ERMAUD which is a synthesis of HELENE [10], which computes the statistical cross-sections for  $\gamma$  rays following inelastic scattering, and the optical model code MAUD [11], both written for spin 1/2 particles only.

Similar results were obtained for the 1434 keV  $\gamma$ -ray transition to the ground state in  $^{52}\text{Cr}$ .

REFERENCES

- [1] W. HAUSER and H. FESHBACH (1952) Phys. Rev. 87 p.366
- [2] P.A. MOLDAUER (1964) Rev. Mod. Phys. 36 p.1079
- [3] J.D. KELLIE, M.N. ISLAM and C.I. CRAWFORD (1973) Nucl. Phys. A20 p.525
- [4] F.G. PEREY and W.E. KINNEY (1968) ORNL 4249
- [5] G. GRENIER and al (1973)  
(to be published)
- [6] B. HOLMQVIST and T. WIEDLING (1971) AE 430
- [7] W.E. TUCKER, P.S. BUCHANAM and al (1969) DASA 2333
- [8] J.C. ROLARD, B. DUCHEMIN and Ch. LAGRANGE (1971) Internal Report  
(unpublished)
- [9] W.E. TUCKER, J.B. ASHE and al (1969) ORO 2791-30
- [10] J.C. ROLARD, Ch. LAGRANGE and B. DUCHEMIN (1969) Internal Report  
(unpublished)
- [11] Ch. LAGRANGE (1969) (private communication)

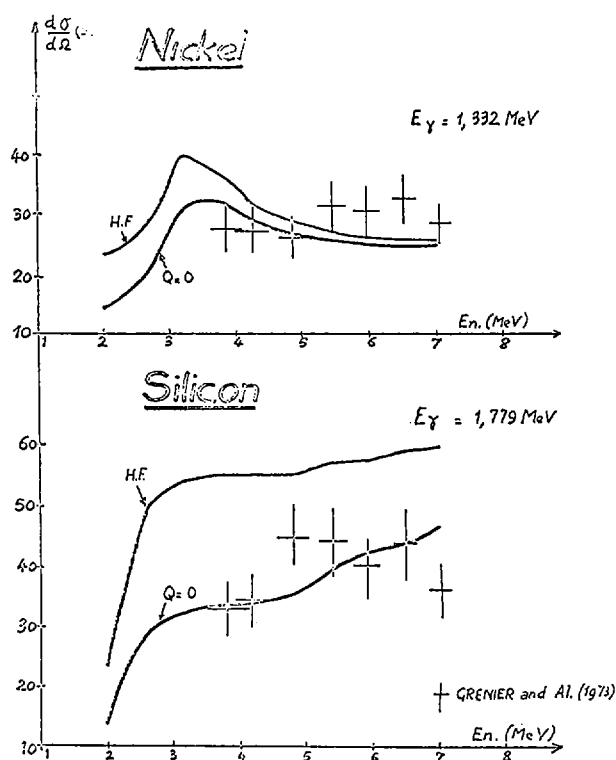


FIG. 1

Experimental and theoretical  $\gamma$ -ray excitation functions at  $55^\circ$  for the  $(n, n'\gamma)$  reactions. The solid curves are the theoretical calculations using the Hauser-Feshbach model with ( $Q = 0$ ) and without (H.F) Moldauer width fluctuation corrections.

I-6. Statistical Model Evaluation of Neutron-Induced Fission  
and Capture Cross Sections of Heavy Nuclei for Energies  
in the Range 3 keV to 1 MeV

P. THOMET

Service de Physique Nucléaire

Centre d'Etudes de Bruyères-le-Châtel

B.P n° 61

92120 Montrouge - France

The purpose of this paper is to present a method which has been used for evaluation of fission and capture cross sections induced by neutrons with energies from 3 keV to 1 MeV on a set of heavy nuclei . The first application of this method has been to the following even-even nuclei :  $U^{236}$ ,  $Pu^{238}$  and  $Pu^{240}$

In the energy range studied , experimental fission cross sections are relatively well known (Fig. 2) . However, there are few experimental values for radiative capture (Fig. 3) .

For the determination of a set of fission, capture, and also inelastic scattering cross sections, we proceeded as follows . Fission channel characteristics (energy, spin and parity) are found by fitting fission cross sections calculated within the framework of the statistical model to the known experimental values . We can then calculate, within the same model, the cross sections for the other decay modes of the compound nucleus : radiative capture, elastic and inelastic scattering . Moreover, this calculation can be extended to low energies where the fission cross section is not always known . It also allows interpolation between various measured values .

The derivation of such a set of cross sections is made through the combined use of several models :

- optical model potentials in coupled-channel equations [1] for the calculation of neutron transmission coefficients and direct inelastic scattering .
- the statistical model to treat the competition between the various modes of decay of the compound nucleus .
- the double-humped fission barrier for the calculation of fission probabilities .

The parameters of these models are obtained by fitting various experimental data . In this paper we concentrate mainly on the general method which is used to determine the properties of the fission channels by fitting appropriately chosen fission data .

The differential and total fission cross sections which are used in the calculations are given by the following expressions :

$$\sigma_f(\theta, E) = \sum_{J\pi} \sum_{KM} \sigma_c(J\pi M, E) B(JK\pi, E) \frac{2J+1}{4} |d_{MK}^J(\theta)|^2 \quad (1)$$

$$\sigma_f(E) = \sum_{J\pi} \sum_K \sigma_c(J\pi, E) B(JK\pi, E) \quad (2)$$

in which :

$\sigma_f(\theta, E)$  is the differential fission cross section at incident neutron energy  $E$  for the emission of fission fragments at angle  $\theta$  ,

$\sigma_f(E)$  is the total fission cross section at incident neutron energy  $E$  ,

$\sigma_c(J\pi M, E)$  is the cross section for the formation of the compound nucleus at energy  $E$  and with quantum numbers  $J$  ,  $\pi$  and  $M$  ,

$B(JK\pi, E)$  is the fission branching ratio including a fluctuation correction [2]

$d_{MK}^J(\theta)$  is the usual reduced rotational function .

The experimental fission data which are used to fix parameters are the following :

- the fission cross section  $\sigma_f(E)$
- the angular distribution  $W(\theta, E)/W(90, E)$  of the fission fragments
- the anisotropy  $a_s = W(0, E)/W(90, E)$

Moreover the anisotropy of the fragments emitted in photofission is also used to determine the imaginary part of the fission potential as will be discussed below .

The fission potential used in the calculation of the fission probabilities is sketched in Fig. 1 .

The real part is a two-humped barrier, as obtained with the Strutinsky's prescription . The various parameters of the barrier can be determined from the analysis of various types of fission phenomena : fission isomerism, vibrational resonances, intermediate structure in subthreshold fission cross sections , near threshold fission cross sections .... [3,4,5]

In the second well, moderate damping is taken into account by introducing a parabolic imaginary part in the fission potential . The maximum value  $W_m$  is adjusted to reproduce the observed anisotropy of the fission fragments emitted in photofission of  $^{232}\text{Th}$ ,  $^{238}\text{U}$ ,  $^{240}\text{Pu}$  and  $^{242}\text{Pu}$  induced by photons having energy  $E_\gamma$  between 5 and 6 MeV . For such even-even nuclei one then obtains :

$$W_m = a (E_\gamma - E_{II} - 2) \quad (3)$$

$$\text{with } a = 0.08 \pm 0.04 \quad \text{for } E_\gamma > E_{II} + 2 \text{ MeV}$$

$$\text{and } a = 0 \quad \text{for } E_\gamma \leq E_{II} + 2 \text{ MeV}$$

Further examination indicates that the above values of  $W_m$  need to be increased by a quantity  $b$  for odd nuclei . In the case of the target nuclei  $^{238}\text{Pu}$  and  $^{240}\text{Pu}$ ,  $b$  has been set equal to 0.1 MeV [4] . In the case of the target  $^{236}\text{U}$ , where the fission occurs much below the threshold, both parameters  $a$  and  $b$  were adjusted directly to the fission cross-sections measured between 24 keV and 500 keV .

In the first well, full damping is assumed .

The main difficulty, when trying to predict such fission cross sections lies in the fact that the fission channels are very poorly known. Therefore, one has to make crude assumptions about them . In fitting the data using the least-squared method, the following parameters are adjusted :

- Height of the fission barrier for the exit channels which are considered in the calculations . For each " $K, J, \pi$ " channel the shape of the barrier remains unchanged but the height is adjusted to a value which is determined by fitting the data .

- The effective number of fission channels . This parameter is adjusted to take into account the effect of other channels, having the same  $K$ ,  $J$ ,  $\pi$  quantum numbers, but situated higher in energy .

We present as an illustration of the use of the method results on the fission and capture cross sections ( $\sigma_f$  and  $\sigma_g$  respectively) for  $^{236}\text{U}$ ,  $^{238}\text{Pu}$  and  $^{240}\text{Pu}$  . The fission data used for the determination of the parameters are  $\sigma_f$  [6] to [9] and  $a_s$  [7, 10, 11] in the energy regions where they are known . The results obtained for the fission and capture cross sections are shown in Fig. 2 and 3 respectively . This method is particularly useful to obtain values of  $\sigma_f$  and  $\sigma_g$  in energy regions where no data are available and also for nuclei for which measurements are very difficult if not impossible .

#### REFERENCES

- [1] Ch. LAGRANGE, communication to this meeting .
- [2] P.A. MOLDAUER, Rev. of Mod. Phys. 36 (1964) 1079 and Phys. Rev. 135 B (1964) 642
- [3] A. MICHAUDON, "Nuclear Fission", Advances in Nuclear Physics, Vol. 6, Plenum-Press New-York-London, 1973 (M. BARANGER and E. VOGT, Eds)
- [4] B.B. BACK et al. , Nucl. Phys. A 165 (1971) 449
- [5] H. WEIGMANN and J.P. THEOBALD , Nucl. Phys. A 187 (1972) 305
- [6] M.G. SILBERT LA-4108-MS (1969)
- [7] K.D. ANDROSENKO and G.N SMIRENKIN  
Sov. Jour. Nucl Phys. 12 n° 2 (1971) 142
- [8] P.H. WHITE et al. , Phys. Chem. Fis. I AEA Vol. 1 Salzburg (1965)
- [9] R.W. LAMPHERE and R.E. GREENE Phys. Rev. 100 (1955) 763
- [10] R. VANDENBOSCH Nuc. Phys. A 101 (1967) 460
- [11] P.E. VOROTNIKOV et al. , Sov. Jour. Nucl Phys. 3 n° 3 (1966) 348
- [12] R.W. HOCKENBURY et al. , Nuc. Sci. Eng. 49 (1972) 153

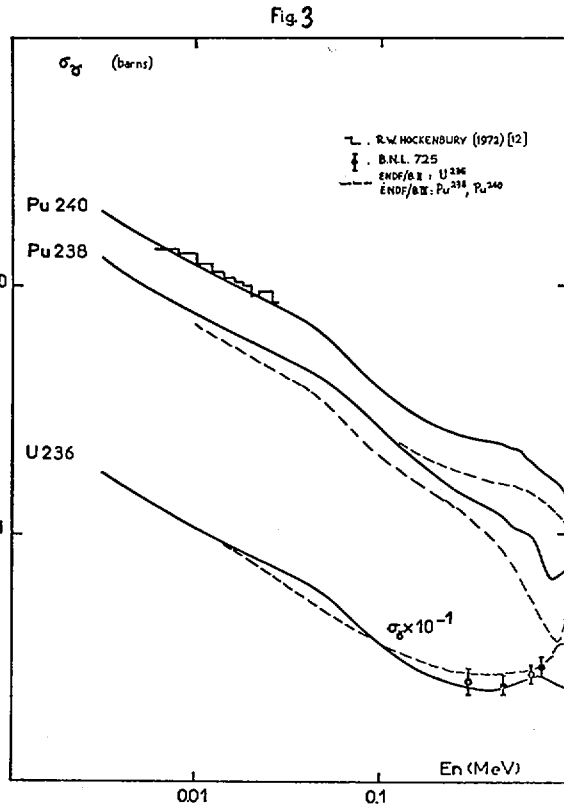
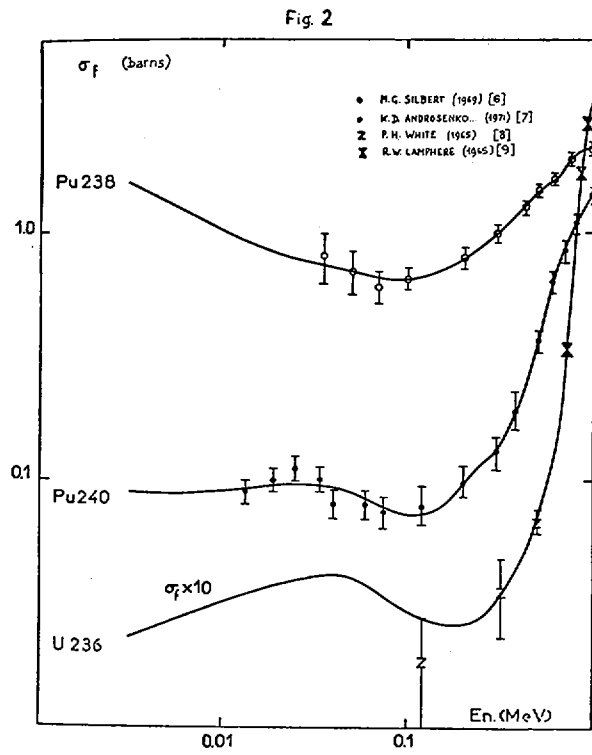
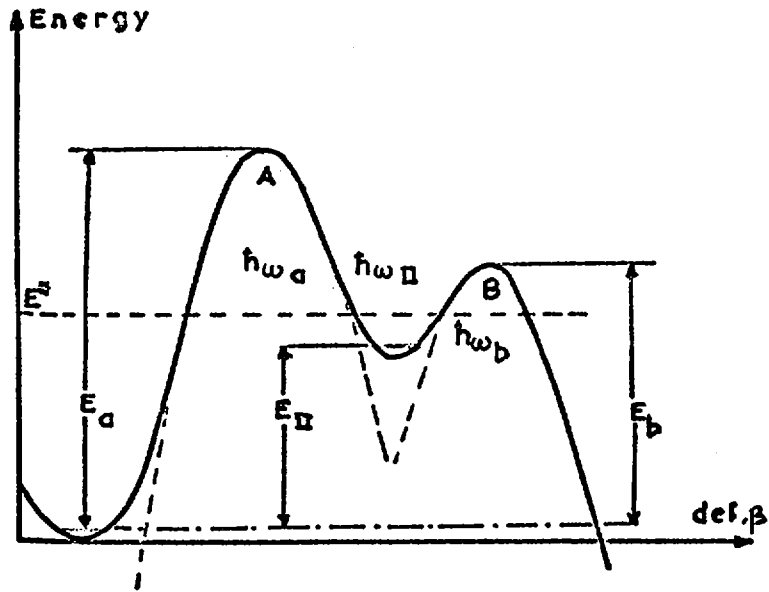


Fig. 1

Definition of the various parameters used to characterize the double-humped fission barrier

I-7. Evaluation of the (n, x n) and (n, x nf) cross sections for  
Heavy Nuclei with the Statistical Model

J. JARY

Service de Physique Nucléaire  
Centre d'Etudes de Bruyères-le-Châtel  
B.P n° 61  
92120 Montrouge - France

This paper presents a method which has been used to calculate the (n,xn) and (n,xnf) cross sections for heavy nuclei having mass numbers  $232 < A < 239$  and for incident neutron energies from 2 MeV to 15 MeV. In the calculations, it is assumed that in the (n,xn) process, the incident neutron is captured by the target nucleus A to form a compound nucleus (A + 1) which then deexcites by the evaporation of x neutrons, (x > 1), without fission, according to the laws of conventional statistical models. For the nuclei and the excitation energies which are considered, fission can also compete with neutron and  $\gamma$ -ray emission. It is therefore necessary to consider also the (n,x'nf) process in which the compound nucleus (A + 1) deexcites by the evaporation of x' neutrons followed by fission.

The cross section for the (n,xn) process, which is illustrated in fig. 1, is given below :

$$\sigma(n, xn) = \sigma_{A+1}(E_n) \cdot \left[ \frac{\Gamma_n(E)}{\Gamma_T} \right]_{A+1} \cdot P_{A+1}(E, x) \quad x > 1 \quad (1)$$

In this expression :

$\sigma_{A+1}(E_n)$  is the cross section for the formation of the compound nucleus (A+1) at incident neutron energy  $E_n$ . The excitation energy of the compound nucleus is then E.

-  $\Gamma_n$  and  $\Gamma_T$  are the neutron width and the total width respectively for the compound nucleus (A+1) at excitation energy E.

-  $P_{A+1}(E, x)$  is the relative probability that the compound nucleus (A+1) at excitation energy E emits x neutrons, without fission.

The expression for  $P_{A+1}(E, x)$  is obtained by conventional theory of neutron evaporation and then reads :

$$P_{A+1}(E, x) = \frac{\int_0^{E-(S_1+S_2+\dots+S_x)} \epsilon_1 \cdot \sigma_{A+1}(\epsilon_1) \cdot \rho_A(E_1) \cdot \left[ \frac{\Gamma_n}{\Gamma_T}(\epsilon_1) \right]_A \cdot P_A(E_1, x-1) \cdot d\epsilon_1}{\int_0^{E-S_1} \epsilon_1 \cdot \rho_A(E_1) \cdot \sigma_{A+1}(\epsilon_1) \cdot d\epsilon_1} \quad (2)$$

$x > 1$

In this expression :

-  $\epsilon_1$  is the center-of-mass kinetic energy of the nuclear system (A+1) after the evaporation of one neutron.

-  $\sigma_{A+1}(\epsilon_1)$  is the cross section for the formation of the compound nucleus (A+1) at the energy  $\epsilon_1$ .

-  $\rho_A(E_1)$  is the level density in the residual nucleus A at excitation energy  $E_1 = E - S_1 - \epsilon_1$ .

-  $S_1, S_2 \dots S_x$  are the neutron separation energies for the nuclei (A+1), A, ... (A-x+1) respectively.

-  $\left[ \frac{\Gamma_n}{\Gamma_T}(\epsilon_1) \right]_A$  is the ratio of the neutron width to the total width, for the residual nucleus A, at excitation energy  $E_1$ .

-  $P_A(E_1, x-1)$  is similar to the expression  $P_{A+1}(E, x)$  but for the residual nucleus A at excitation energy  $E_1$  and for the emission of (x-1) neutrons.

The values of  $P_{A+1}(E, x), P_A(E_1, x-1) \dots$  are then deduced one from the other through a series of equations of the type (2).

The cross section for the (n,x'nf) process, which is also illustrated in fig. 1 is given below :

$$\sigma(n, x'nf) = \sigma_{A+1}(E_n) \cdot \left[ \frac{\Gamma_n}{\Gamma_T}(E) \right]_{A+1} \cdot P_{A+1}(E, x'nf) \quad (3)$$

All the terms used in equation (3) have the same meaning as those used

in equation (2) except for  $P_{A+1}(E, x'nf)$  which represents the relative probability that the compound nucleus (A+1) at excitation energy E emits  $x'$  neutrons and then fissions. The expression for  $P_{A+1}(E, x'nf)$  is very similar to that for  $P_{A+1}(E, x'n)$ .

In order to calculate the various expressions (1), (2) and (3) it is necessary to know the following quantities :

1°) the cross section for the formation of the compound nucleus (A+1) as a function of energy. This cross section is calculated with an optical model code described elsewhere[1].

2°) the partial widths  $\Gamma_n, \Gamma_\gamma, \Gamma_f$  for the nuclei (A+1), A, etc... and excitation energies reached through the various modes of decay.

The neutron width  $\Gamma_n$  is obtained from the neutron penetrability calculated with the optical model code mentioned above[1]. The level density which is needed to extract the neutron width is obtained from the Fermi gas model approximation using tabulated values of the level density parameter  $a$  [2].

The  $\gamma$ -ray width  $\Gamma_\gamma$  is obtained assuming that the radiation is of the electric dipole type, normalised to  $\Gamma_\gamma$  values for slow neutron resonances when they are known.

At excitation energy  $E_A$ , well above the fission barrier height  $B_f$  in the compound nucleus A, the fission width  $\Gamma_f$  is obtained from the following expression :

$$\Gamma_f(E_A) = \left[ 2\pi \rho_A(E_A) \right]^{-1} \int_{B_f}^{E_A} \rho_A^f(\epsilon) d\epsilon \quad (4)$$

where :

-  $\rho_A(E_A)$  is the level density at energy  $E_A$ , as defined above.

-  $\rho_A^f(\epsilon)$  is the level density at energy  $\epsilon$  and at saddle point deformation for which the Fermi level density parameter is  $a_f$  instead of  $a$ . In this work, the parameter  $a_f$  is adjusted to fit the plateaus of the known fission cross sections. A better fit to the data is obtained if  $a_f$ , rather than being constant, is assumed to have an energy dependence of the form

$$a_f = a + \frac{c}{U} \quad (5)$$

At excitation energy close to  $B_f$ , the fission width is determined from the penetrability of the fission barrier, supposed to have a single-humped parabolic shape.

Application of the method to the calculation of (n,xn) and (n,xnf) cross sections for  $^{236}\text{U}$ ,  $^{237}\text{U}$  and  $^{238}\text{U}$ .

The parameterization of the optical model is described elsewhere[1].

The fission cross sections of  $^{235}\text{U}$  and  $^{238}\text{U}$ , recently evaluated by Sowerby[3], and the fission cross section of  $^{236}\text{U}$ [4], have been used to determine the other parameters needed in the calculations.

The fission widths of  $^{239}\text{U}$  and  $^{238}\text{U}$  have been obtained by fitting the first-chance and second-chance fission plateaus of the  $^{238}\text{U}$  cross section.

The fission width of  $^{237}\text{U}$  has been determined in the same manner from the first plateau of the fission cross section of  $^{236}\text{U}$ .

A similar fit to the first-chance and second-chance fission cross sections of  $^{235}\text{U}$  gives the fission widths of  $^{236}\text{U}$  and  $^{235}\text{U}$  respectively.

With the parameters thus obtained, it has been possible to calculate :

1°) fission cross sections in energy ranges where no data are available ; for example, for  $^{236}\text{U}$  between 6 MeV and 14 MeV and for  $^{237}\text{U}$  between 1 MeV and 15 MeV (fig. 2).

2°) (n,2n) and (n,3n) cross sections for  $^{236}\text{U}$ ,  $^{237}\text{U}$ ,  $^{238}\text{U}$  (fig. 3) from threshold up to 15 MeV.

For  $^{238}\text{U}$ , good agreement is observed between the result of our calculations and the experimental data[5]. Note that the calculations are not fitted to such data.

For  $^{237}\text{U}$  and  $^{236}\text{U}$ , theoretical results are obtained where no data are available.

These results show that the statistical and the optical model together with an appropriate fitting procedure to known fission cross sections can be used for the calculation of (n,xn) and (n,xnf) cross sections of heavy nuclei.

## - REFERENCES -

- [1] Ch. LAGRANGE - communication to this Meeting .
- [2] A. GILBERT, A.G.W. CAMERON,- Can. J. of Physics 43 (1965) 1446.  
J.L. COOK, H. FERGUSON, A.R. Del. MUSCPOVE Aust. J. of Physics  
20 (1967) 477.
- [3] M.G. SOWEBY - AERE R 7273 (1973).
- [4] P.H. WHITE and G.P. WARNER - J. Nucl. Energy 21 (1967) p.671.  
W.E. STEIN - Wash 627 (1968).  
H. ROSLER, F. PLASIL, H.W. SCHMITT - Physics letters 38 B (1972) 501.  
LA - ac - unpublished ; quoted in P.H. WHITE and G.P. WARNER (1967).  
R.W. LAMPHERE - Phys. Rev. 104 (1956) 1654.
- [5] J.H. LANDRUM, R.J. NAGLE, M. LINDNER - Phys. Rev. C8 (1973) 1938.  
J.D. KNIGHT, R.K. SMITH, B. WARREN - Phys. Rev. 112 (1958) 259.  
J.L. PEPKIN, R.F. COLEMAN - React. Scien. and Technology 14 (1961) p. 69.  
D.S. MATHER - AWRE 072-72.  
P.H. WHITE - J. of Nucl. Energy 16 (1962) 261.

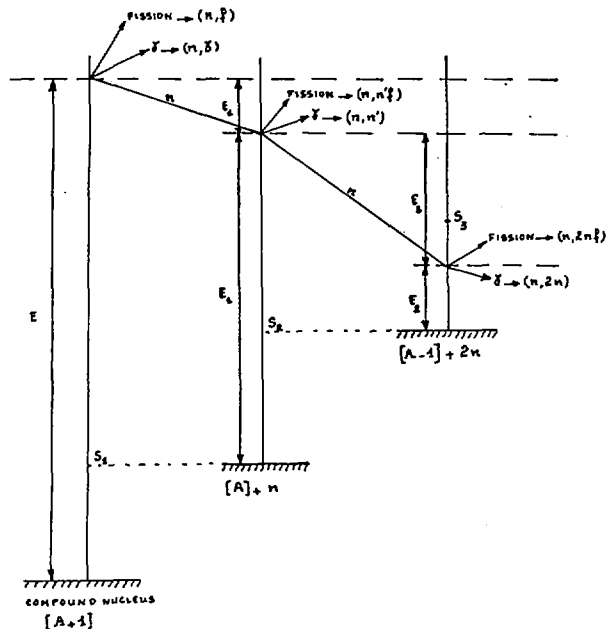


Fig. 1 - Energy diagram for the processes (n,xn) and (n,xnf) with x = 2.

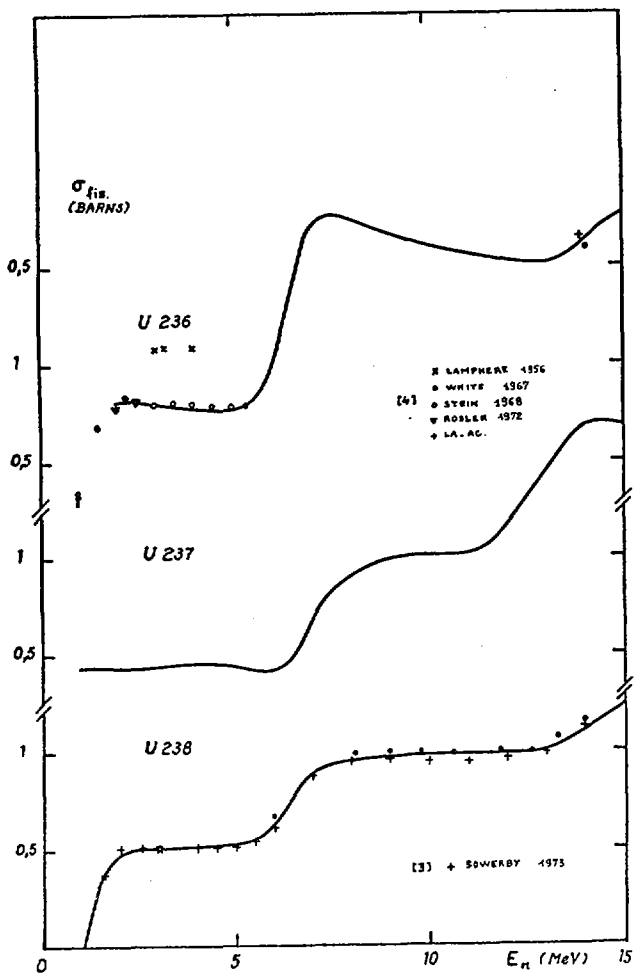


Figure 2.

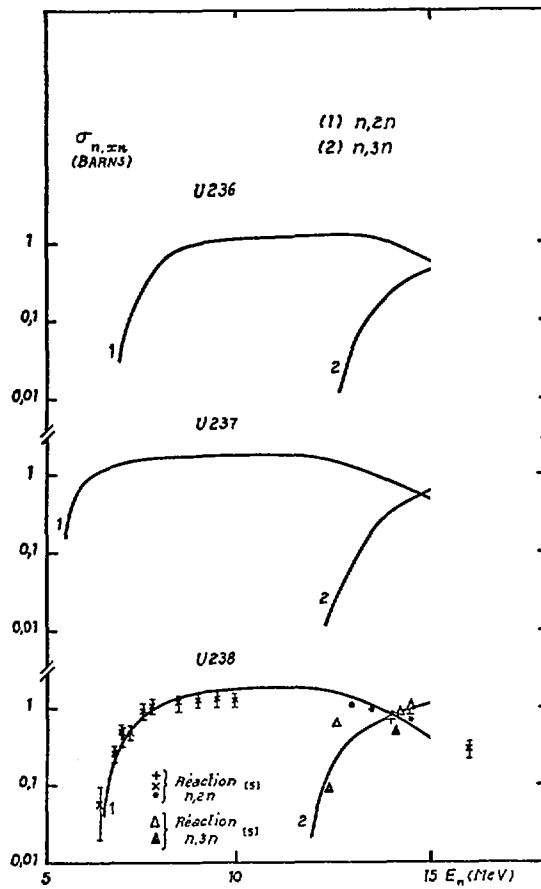


Figure 3

## DISCUSSION

R. C. BLOCK: The RPI  $^{240}\text{Pu}(n,\gamma)$  measurements also produced a fission cross section in the  $10 \sim 30$  keV region (with poorer accuracy than the capture data). The fission cross section appeared high relative to the sparse data (then available) from 100 keV on up. How does your extrapolated  $^{240}\text{Pu}(n,f)$  cross section below  $\sim 100$  keV compare with the RPI data?

A. MICHAUDON: I am afraid that Dr. Thomet who carried out the calculations did not include the RPI data because he was not aware of its existence. Have these data been published?

S. TANAKA: In your talk for  $^{238}\text{U}$ , what value of the coupling parameter did you use? In my analysis, I had to use a little smaller value than the value taken from other bibliography.

A. MICHAUDON: Dr. Lagrange found necessary to use complex values of the coupling parameter, but the actual values are not given in his paper; we would be glad to mail you this information if you are interested in.

I-8. SOME REMARKS ON THE USE OF NUCLEAR MODELS IN THE  
EVALUATION WORK

V. Benzi, F. Fabbri and G. Reffo  
CNEN, Centro di Calcolo, Bologna, Italy

## ABSTRACT

At present, a large number of optical and statistical nuclear model codes having different degree of sophistication is available. The effects of some approximations on the calculated data are briefly discussed from the point of view of the evaluation work.

## INTRODUCTION

Nuclear models are frequently used in the field of neutron data evaluation in order to:

- i) make sophisticated fits of consistent data;
- ii) make a definite choice among inconsistent data;
- iii) fill gaps among loose data;
- iv) predict cross-sections for which no data at all exist.

In the first kind of application, there are no special problems, except the usual ones connected with the selection of a best-fit criterion.

In the remaining applications, however, a number of problems arise, the most important ones being the physical suitability of the model adopted and the determination of the numerical values of the para meters involved.

In solving these two problems, we have to face a dilemma. In fact, in order to achieve better physical adequacy, we are inclined to add more and more details to the models. These details, in turn, involve more and more parameters, whose indetermination introduces a large degree of uncertainty in the result of the calculations.

Thus, a high degree of theoretical reliability in a model might imply a low degree of reliability in the numerical results.

As a provocative example, let us consider the case of the optical model. In its primitive form, the optical potential was

$$-U(r) = \begin{cases} V+iW & \text{if } r < R \\ 0 & \text{otherwise} \end{cases} \quad (1)$$

so that only three parameters, viz.  $V$ ,  $W$  and the nuclear radius constant  $r_0$  ( $R=r_0 A^{1/3}$ ) were required, at the beginning, in order to perform numerical calculations.

At present, one of the suggested forms for the optical potential is the following

$$\begin{aligned} -U(r) = & \left[ V_c + \frac{\alpha(N-Z)}{A} \right] f(r, R_0, a_0) + iW_c \{ \xi g_1(r, R_1, a_1) \\ & + (1-\xi) g_2(r, R_2, a_2) \} + \left( \frac{\hbar}{m_p c} \right)^2 (V_s + iW_s) g_3(r, R_3, a_3) \underline{\underline{xs}} \end{aligned} \quad (2)$$

which contains 18 parameters if one assumes

$$R_i = r_i A^{1/3} + C_i$$

The number of parameters further increases if the energy dependence and the deformation of the potential are taken into account.

Obviously, a potential like (1) cannot very accurately reproduce a given set of experimental data, whereas the use of a potential like (2) enables us to reproduce nearly everything in the smallest details, especially if the various parameters are allowed to vary wildly.

However, good taste (and the worst vulgarities like the cost of the computer time) oblige us to adopt a potential depending on a small number of adjustable parameters, and make a reasonable compromise between physical adequacy and drastic approximations.

The purpose of this paper is to examine, to some extent, the effects of these compromises on the results given by the optical and the statistical models which are by far the most frequently used in evaluation work.

## I. THE OPTICAL MODEL

A very large number of experimental data have been analyzed by various authors in order to produce a "recommended" set of a few (five to six) parameters to be used in connection with some selected form of the optical potential.

From these analyses, it is usually found that the central part of the optical potential ranges between 45÷55 MeV at low ( $\sim 1$  MeV) energy, decreasing smoothly as the energy increases.

The radii are of the order of  $(1.15\div 1.30)A^{1/3}$  fm, whereas the diffusenesses are of the order of 0.4÷0.7 fm, both for the real and the imaginary part of the potential.

The magnitude of the imaginary part is of a few MeV, and is assumed to be constant or smoothly increasing with the energy. The spin-orbit also results as a rather shallow potential, of the order of a few MeV.

The use of the optical model, together with a recommended set of a reasonable number of parameters, enables us to evaluate total and elastic cross-sections which are satisfactory in a large number of cases.

For example, about three years ago Glasgow and Foster [1] compared a large set of experimental neutron total cross-sections with the corresponding optical model cross-sections calculated by using a non-local potential depending on seven parameters. The adopted potential and parameters were those recommended by Perey and Buck [2] fifteen years ago on the basis of an analysis of the elastic scattering angular distributions of Pb at 7 and at 14.5 MeV. It is worth noting that the parameters of a non-local optical potential are usually assumed to be energy-independent, because the non-locality to a large extent replaces the energy dependence required by a local potential.

In the comparison carried out by Glasgow and Foster, 78 elements and 14 separate isotopes were considered, spanning the energy range 2.25÷15 MeV.

For 68 elements or nuclei with  $A \geq 45$  an average deviation smaller than 3% was found in 60% of cases; whereas, such a deviation was between 4% and 17% in the remaining 40% of cases. The biggest discrepancies were always found in the case of hard deformed nuclei.

The foregoing example shows that an optical potential depending on a reasonable number of parameters can be used with confidence in eval-

uating cross-sections in the continuum, provided the nucleus considered is not a very deformed one.

Unfortunately, a number of nuclei of major interest for nuclear reactors are strongly deformed. This is the case, for instance, of U and Pu isotopes, Th-232, Na-23, etc.. For these cases, one has to modify the parameters considerably if the deformation is not explicitly taken into account. On the other hand, if one assumes that the spherical optical potential represents the limit of the deformed one, for  $\beta=0$  (the  $\beta$  being the deformation parameter), the same set of parameters might be used in principle, provided the deformation is taken into account correctly.

However, there are some aspects of non-spherical potential calculations which make the adoption "sic et simpliciter" of the parameters inferred from analyses of spherical nuclei rather questionable. We will examine here some of these aspects.

To solve the appropriate Schrödinger equation with a deformed potential, two different kinds of numerical approximations are frequently used. In the first kind of approximation the potential is expanded into powers of  $\beta$  up to the first order. The second kind of approximation assumes a Legendre polynomial expansion of the potential (in general up to  $\ell=4$ ). Now, there may be rather large differences in the results, depending on the approximation adopted.

As an example, fig. 1 shows the results of calculations of the total cross-section of Gd-156 in the MeV energy range.

Curve (a) was calculated assuming a deformation parameter  $\beta=0.35$  and strong coupling of the first excited  $2^+$  level. The potential was expanded in Legendre polynomials up to  $\ell=4$ . Curve (b) was obtained by using the same parameters of curve (a), but the potential was expanded in power series of  $\beta$  to the first order. It can be seen that there is a systematic difference between the two curves of  $\sim 10\pm 15$  per cent. The total cross-section calculated by assuming  $\beta=0$  (spherical potential) is also shown in order to demonstrate the importance of the deformation effect.

Quite large differences are also found for the shape-elastic angular distribution, as shown in fig. 2.

Another aspect to be considered when the nucleus is a deformed one, concerns the imaginary part of the optical potential. One of the

effects of the nuclear deformation is the damping of the diffraction pattern of the shape-elastic angular distribution. The same effect can be obtained, qualitatively, by using a spherical potential with a large value for the absorption potential  $W$ . Since a rather large number of nuclei are more or less deformed, systematic analyses based on a spherical potential might result in a  $W$ -value which is too high for deformed potential calculations.

In addition, the magnitude of the theoretical cross-sections given by the generalized optical model strongly depends on the coupling scheme used in each particular calculation.

Therefore, the value of  $W$  to be adopted also depends greatly on the coupling scheme assumed. As an example, in fig. 3 the calculated angular distribution for direct inelastic scattering of 1 MeV neutrons by the first  $2^+$  excited state of Gd-156 at 0.09 MeV is shown. All the curves were calculated using the same set of parameters. Curve (a) was obtained by assuming that only the first  $2^+$  excited state channel is strongly coupled with the elastic channel. Curve (b) was calculated under the hypothesis that the second ( $4^+$ ) excited state is also strongly coupled. Curve (c) was calculated in adiabatic approximation, taking into account the coupling of all the excited levels belonging to the fundamental rotational band. It can be seen that there is a rather sensitive dependence of the results on the coupling scheme assumed.

Further difficulties arise as a consequence of the so-called "geometrical  $W.b$  ambiguity",  $b$  being the diffuseness of the imaginary potential. An example of the effects of such an ambiguity is given in fig. 4. The curve labelled (a) shows the theoretical angular distribution of the inelastic cross-section for 1 MeV neutrons scattered by the first  $2^+$  excited level of Gd-156 via compound nucleus. The parameters adopted in the calculations were those of Agee and Rosen [3], with  $W=5.75$  MeV and  $b=0.70$  fm. The dots superimposed on the curve represent the results of a calculation carried out using the same parameters, but with  $W=8.05$  MeV and  $b=0.5$  fm. In both cases one has  $W.b=4.025$  MeV.fm, and the results are identical up to the third significant figure.

The angular distribution for direct inelastic scattering, however, differs markedly in magnitude in the two cases, as can be seen in fig. 4 itself.

Another parameter which may change drastically when deformation effects are taken into account is the depth of the spin-orbit potential

$V_{so}$ . The correlation between  $\beta$  and  $V_{so}$  has been discussed by Thompson et al. [4] who found a lower value of  $V_{so}$  than in a spherical potential calculations when the deformation is taken into account. This correlation mainly depends on the fact that the nuclear deformation effects predominate near the nuclear surface where the phenomenological spin-orbit potential also produces major effects.

From the above considerations, it can be concluded that three parameters at least (i.e.  $W$ ,  $b$  and  $V_{so}$ ) have to be varied when changing from spherical to non-spherical optical model calculations. Thus, the prediction of an unknown cross-section obtained by using "standard" spherical optical model parameters and deformed potentials must be treated with caution, the goodness of the results being strongly influenced by the various approximations adopted in performing the generalised optical model calculations.

## II. THE STATISTICAL MODEL

In the time scale of nuclear theories, the statistical model is an extremely old concept. It was first developed by Bethe [5], who in 1937 derived the following formula for the average reaction cross-section

$$\bar{\sigma}_{cc'} = \frac{2\pi^2 \lambda^2}{(2s+1)(2I+1)} \sum_J (2J+1) \left\langle \frac{\Gamma_c^J \Gamma_{c'}^J}{\Gamma_D^J} \right\rangle \quad (3)$$

where,  $s$  and  $I$  are the spins of the projectile and the target, respectively, and the brackets indicate an average over many resonances. The  $D^J$  is the average spacing of the levels with angular momentum  $J$  in the energy region considered.

By introducing the transmission coefficients  $T_\ell$ , eq. 3 can be expressed in the well-known Hauser-Feshbach form [6]. For elastic and inelastic scattering of neutrons one has

$$\bar{\sigma}_{n,n'}(E,E') = \frac{\pi \lambda^2}{2(2I+1)} \sum_\ell T_\ell(E) \sum_J \frac{\epsilon_{j\ell}^J (2J+1) \sum_{\ell'} \epsilon_{j'\ell'}^J T_{\ell'}(E')}{\sum_{p,\ell''} \epsilon_{j''\ell''}^J T_{\ell''}(E_p)} \quad (4)$$

The  $T_\ell$ 's can be calculated on the basis of a given nuclear model.

If the optical model is adopted, formula (4) can take on a more complicated form, depending on the particular potential adopted (e.g. deformed, with spin-orbit part, etc..).

Some channel transmission coefficients cannot be easily obtained by starting from an optical potential. This is the case of radiative capture and fission channels, for which other semi-empirical tools must be developed to estimate the corresponding transmission coefficients.

The extension of the Hauser-Feshbach formula to the case of capture and fission was made by Margolis [7] ; the formula is

$$\bar{\sigma}_{n,r}(E) = \frac{\pi \lambda^2}{2(2I+1)} \sum_{\ell} T_n(\ell, E) \sum_J \frac{\epsilon_{j\ell}^J (2J+1) T_r(J, E)}{\sum_r T_r(J, E) + \sum_{\ell', E'} \epsilon_{j'\ell'}^J T_n(\ell', E')} \quad (5)$$

In the derivation of eq.(3) , (4) and (5) it has been assumed that the average ratio  $\langle \Gamma_c^J \Gamma_c^J / \Gamma^J \rangle$  could be replaced by the ratio of averages  $(\langle \Gamma_c^J \rangle \langle \Gamma_c^J \rangle / \langle \Gamma^J \rangle)$ . This is not true in general because the various widths are not constant but fluctuate from level to level. Therefore, the above mentioned equations have to be corrected by a factor F given by

$$F = \langle \Gamma_c^J \Gamma_c^J / \Gamma^J \rangle / [\langle \Gamma_c^J \rangle \langle \Gamma_c^J \rangle / \langle \Gamma^J \rangle] \quad (6)$$

The function F depends on the nature of the frequency distribution functions which represent the statistical distribution of various widths.

About ten years ago the Hauser-Feshbach formula was re-examined by Moldauer [8] , [9] , in the more general framework of the statistical theory of R-matrix. One of the results of such a re-examination was that the transmission coefficients  $T_c$  should be replaced by the quantity

$$\theta_c = \frac{2}{Q_c} [1 - (1 - Q_c T_c)^{\frac{1}{2}}] \quad (7)$$

where  $Q_c$  is a parameter with range  $0 \leq Q_c \leq 2$  .

Having briefly recalled the main features of the statistical model, we will examine in the following section the influence on the numerical results of some of the approximations currently adopted for calculating the various quantities which appear in the formulae.

Let us consider the case of radiative capture cross-section calculation first.

A. Radiative capture. To begin with, let us consider the Margolis' formula.

The radiative capture cross-section is obtained from formula (5) by taking

$$T_r(J,E) = T_a(J,E)$$

$$\sum_r T_r(J,E) = T_\gamma(J,E)$$

The absorption term  $T_a(J,E)$  refers to the capture of the neutron with no particle re-emission, whereas  $T_\gamma(J,E)$  refers to all the exit channels in which the compound nucleus initially emits a  $\gamma$ -ray. The usual link between transmission coefficients and strength-functions

$$T_{\gamma,a}(J,E) = 2\pi \frac{\langle \Gamma_{\gamma,a}(J,E) \rangle}{\bar{D}(J,E)} \quad (8)$$

is assumed, so that we must know  $T_\ell(E)$ ,  $\langle \Gamma_\gamma(J,E) \rangle$ ,  $\langle \Gamma_a(J,E) \rangle$  and  $\bar{D}(J,E)$  in order to perform the calculations.

The simplest way to calculate  $T_\ell(E)$  is to assume that the nucleus behaves like a black absorbing sphere of radius  $R$ , so that only incoming waves, like  $\psi \sim \exp(-iKr)$  for s-neutrons, are allowed inside the nucleus.

If this model is adopted, the parameters required by the calculations of the  $T_\ell$ 's are the radius  $R$  and the neutron wave number  $K$  inside the nucleus.

A more sophisticated approach is based on the "cloudy crystal ball" or optical model. In this case what we need to know are the parameters appearing in the optical potential. Fig. (5) shows a comparison of I-127 capture cross-sections calculated according to the two models. All the parameters, except  $T_\ell$ , were kept the same for both calculations; the optical potential adopted was a 5-parameter Saxon-Wood one, whereas a value of  $K=10^{13} \text{ cm}^{-1}$  was assumed for the black nucleus calculations.

The differences in cross-sections are of the order of 10÷15% everywhere, in spite of the fact that the  $T_\ell$  differs by a factor

1.5±2 below 100 KeV.

The explanation of this fact is quite easy. If, for simplicity's sake, we assume no inelastic scattering, then the contribution of the  $\ell$ -th partial cross-section to the total cross-section is given by

$$\bar{\sigma}_a^{(\ell)} \propto [T_\ell(E) \cdot \Gamma_a] / [T_\ell(E) \cdot \bar{D} + 2\pi\Gamma_a] \quad (9)$$

where  $T_\ell \sim 2\pi\Gamma_n / \bar{D}$ . If we express the energies in eV one has, very roughly,  $T_\ell \sim E^{1/2} \cdot 10^{-3}$ ,  $\bar{D} \sim 10^2$  and  $2\pi\Gamma_a \sim 1$ . Thus, for  $E > 10^4$  eV, we can neglect the term  $2\pi\Gamma_a$  in eq. 9, and the  $T_\ell$ 's cancel out.

The above argument shows that capture cross-section greatly depends on the ratio  $\Gamma_a / \bar{D}$  rather than on the particular optical potential adopted in order to calculate the transmission coefficients. For this reason it seems worth considering here some of the various recipes usually adopted in order to estimate such a ratio.

As far as the calculation of  $\Gamma_{\gamma,a}$  is concerned, the simplest approach is represented by the well-known "Weisskopf estimate" which gives

$$\Gamma_{\gamma,a}(B_n + E) = \Gamma_{\gamma,a}(B_n) \left[ \rho_o(B_n) / \rho_o(B_n + E) \right] \int_{\lambda E}^{B_n + E} \epsilon^3 \rho_o(B_n + E - \epsilon) d\epsilon / \int_0^{B_n} \epsilon^3 \rho_o(B_n - \epsilon) d\epsilon \quad (10)$$

$B_n$  and  $E$  being the neutron binding and kinetic energy, respectively, and  $\rho_o$  the nuclear level density of levels with  $J=0$  of the (compound) nucleus considered. The parameter  $\lambda$  takes the values

$$\lambda = \begin{cases} 0 & \text{for } \Gamma_\gamma \\ 1 & \text{for } \Gamma_a \end{cases}$$

In deriving formula (10) a  $(2J+1)$  level density dependence on  $J$  has been assumed, so that  $\Gamma_{\gamma,a}$  is  $J$ -independent.

A more sophisticated formula is given by the so-called "Brink-Axel" estimate [10], [11] which for an arbitrary  $J$ -dependence gives

$$\Gamma_{\gamma,a}(B_n + E; J) = \int_{\lambda E}^{B_n + E} \epsilon^2 \sigma_{\gamma}(\epsilon) \sum_{|J-1|}^{J+1} J' \rho[(B_n + E - \epsilon); J'] d\epsilon / [3(\pi \hbar c)^2 \rho(B_n + E; J)] \quad (11)$$

where,  $\sigma_{\gamma}(\epsilon)$  is the photo-absorption cross-section of the (compound) nucleus considered. Formula (11) gives, in principle, the absolute values of  $\Gamma_{\gamma,a}$ , whereas formula (10) is usually normalised at  $\Gamma_{\gamma,a}(B_n)$ .

Formulae (10) and (11) can be improved, in order to take the transitions to the resolved levels into greater account. For example, for the "Brink-Axel" estimates, one has

$$\begin{aligned} \Gamma_{\gamma}(B_n + E; J, \pi) &= \sum_{i=1}^K \sum_{|J-1|}^{J+1} J' \delta_{J', J_i} (B_n + E - E_i)^2 \sigma_{\gamma}(B_n + E - E_i) / [3(\pi \hbar c)^2 \rho(B_n + E; J, \pi)] \\ &+ \int_0^{B_n + E - E_x} \epsilon^2 \sigma_{\gamma}(\epsilon) \sum_{|J-1|}^{J+1} J' \rho(B_n + E - \epsilon; J') d\epsilon / [3(\pi \hbar c)^2 \rho(B_n + E; J)] \end{aligned} \quad (11')$$

where the  $\delta$ 's take into account the spin and parity selection rules and  $E_x$  is the energy at which the first level of unknown characteristics is assumed to be found.

In order to have an idea of the effects of the various approximations on the numerical results, we have carried out a number of calculations in some significant cases. Let us consider first the Weisskopf estimate. In Table I, columns labelled (1) through (4) show the calculated ratios

$$R_{\gamma,a}(E) = \Gamma_{\gamma,a}(B_n + E) / \Gamma_{\gamma,a}(B_n)$$

for the (compound) nucleus Nb-94. Index (L) means that the Lang-Le Couter level density formula [12] has been adopted in (10), whereas index (C) means that the composite Cameron formula [13] has been used together with the improved formula, like (11'), for the resolved levels. As one can see, there are no significant differences in the results, in spite of the fact that the use of Cameron's formula should imply in principle a J-dependence.

Columns (5) to (8) show some results obtained for Sn-118, using

the Cameron level density formula together with formula (11), (values below  $R_{\gamma,a}$ ) and (11'), (values below  $R_{\gamma,a}^*$ ). Again, there are no significant differences in the results, in spite of the fact that resolved levels are known up to 2.77 MeV.

Similar results were obtained for a large variety of nuclei, leading to the conclusion that the calculated behaviour of the  $\Gamma_{\gamma,a}$ 's is rather insensitive to the assumed level density formula and J-dependence.

Let us now consider the "Brink-Axel" estimate. As far as the dependence on the level density formula is concerned, a large number of numerical calculations lead to the same conclusions as above. In some cases, however, significant differences can be found, as shown in Table II for Se-78, where numerical values in mV of the  $\Gamma_{\gamma,a}$  and  $\Gamma_{\gamma,a}^*$  obtained by means of formulae (11) and (11') respectively are given. In addition, if the results of such an estimate are compared with those given by the Weisskopf formula, as shown in fig. 6 for Nb-94, strong differences are found above a few hundred KeV. These differences are mainly due to the fact that the Weisskopf estimate does not take into account the giant resonance phenomenon. All the conclusions reached so far for the  $\Gamma_{\gamma,a}$ 's, apply to the energy dependence of the ratio  $\Gamma_{\gamma,a}/\bar{D}$ .

As far as the absolute value at neutron binding energy of such a ratio is concerned, the main difficulty is connected with the evaluation of the average level spacing  $\bar{D}$  for those nuclei for which a sufficient number of low energy resonances was not yet measured. Present theoretical models for calculating nuclear level spacings are still unable to give agreements with a large class of observed  $\bar{D}$ -values better than a factor  $\sim 2\div 3$ . A cursory examination of formula (3) shows that an uncertainty of the same order of magnitude has to be expected in the calculated cross-sections whenever empirical  $\bar{D}$ -values do not exist. We should now say a few words concerning the correction factor  $F$  given by formula (6). As an example, in fig. (7), the effects of this correction for I-127 are shown. It can be seen that the corrections may be quite important for neutron energies up to some hundred kiloelectronvolts.

If one assumes a one-degree chi-square distribution for the neutron widths and a  $\delta$ -function for  $\Gamma_{\gamma}$ , one has

$$F_c = (\sum_{c'} T_{c'}^{J\pi}) \int_0^\infty \frac{\exp(-T_\gamma^{J\pi} \cdot x) dx}{(1+2xT_c^{J\pi}) \prod_{c''} (1+2xT_{c''}^{J\pi})} \quad (12)$$

where index  $c''$  refers to all channels except those leading to radiation emission.

The numerical calculation of formula (12) is rather cumbersome. The following approximate formula was suggested by Cameron [14]

$$F_c^* = (\sum_{c'} T_{c'}^{J\pi}) \int_0^\infty \frac{\exp(-T_\gamma^{J\pi} \cdot x) dx}{(1+2xT_c^{J\pi})^{3/2} [1 + \frac{2x}{\eta} \sum_{c''} T_{c''}^{J\pi}]^{\eta/2}} \quad (13)$$

with

$$\eta = (\sum_{c''} T_{c''}^{J\pi}) / M$$

$$M = \max.(T_{c''}^{J\pi})$$

The differences between the numerical results given by formulae (12) and (13) are usually small. Inaccurate results, however, can be obtained with both formulae if the upper limit of the numerical integration is not carefully selected. In order to overcome this difficulty, it is useful to transform formula (12) as follows

$$F_c = [(\sum_{c'} T_{c'}^{J\pi}) / (2T_{\max}^{J\pi})] \int_0^1 \{ \exp[-(1/y-1)T_\gamma^{J\pi} / (2T_{\max}^{J\pi})] \} f(y) dy \quad (12')$$

with

$$[f(y)]^{-1} = y^2 [1 + (T_c^{J\pi} / T_{\max}^{J\pi}) (1/y-1)]^{3/2} \cdot \prod_{c''} [1 + (T_{c''}^{J\pi} / T_{\max}^{J\pi}) (1/y-1)]^{1/2} \quad (14)$$

Formula (12') can be easily integrated by using the Gauss method. A similar transformation can be performed in order to integrate formula (13). The result is formally identical to (12') if one puts

$$[f(y)]^{-1} = y^2 [1 + (T_c^{J\pi} / T_{\max}^{J\pi})(1/y - 1)]^{3/2} \cdot [1 + (\sum_c T_c^{J\pi})(1/y - 1) / \eta T_{\max}^{J\pi}]^{\eta/2} \quad (14')$$

Numerical results obtained by means of the various formulae, are shown in Table III for the case I-127,  $(J^\pi, \ell=2^+, 0)$ .

In order to conclude these remarks on the numerical calculation of the neutron capture cross-sections, it can be pointed out that the use of Moldauer's  $\Theta_\ell$  (see formula (7)) instead of the conventional  $T_\ell$ , does not in practice change the results.

This is due to the rather weak dependence of the results on the  $T_\ell$ , as explained above.

B. Inelastic scattering. The conclusions reached so far about the dependence of the cross-section on  $T_\ell$ 's are no longer valid in the case of inelastic scattering cross-sections. Because of the strong influence of the  $T_\ell$ 's, the calculated cross-sections will be, in general, rather sensitive to the adopted optical potential. In particular, if a local spherical potential is used, the energy dependence of the central and imaginary depths should be accurately known.

In fact, one should remember that the various  $T_\ell$ 's refers to the inverse process so that, near the thresholds, the transmission coefficients have to be calculated for very low neutron energies. Thus, recommended sets of parameters obtained from systematic analyses carried out in the several MeV energy range cannot be used with confidence in this kind of calculations.

To give an example, fig. 8 shows the energy dependence of the central and imaginary part of an optical potential obtained for Cu-63 by means of an analysis of the total, differential-elastic and total non-elastic experimental cross-sections (full line curves).

As one can see, above 3.5 MeV the central part of the potential shows a linear dependence on the neutron energy  $E$ , whereas the

imaginary part is constant. However, below 3.5 MeV a quite different behaviour has to be adopted if one wants to obtain good fits for the inelastic scattering cross-sections of the first and second excited levels (see fig. 8 C) and D), full line curves). In fact, the extrapolation to zero of the results obtained for the potentials above 3.5 MeV (dashed lines in the figure) gives very bad results, as one can see in fig. 8 C) and D) (dashed lines). As in the case of neutron capture, calculated inelastic scattering cross-sections are considerably influenced by the statistical fluctuation correction factor.

Table IV shows some numerical results obtained by means of the "Cerbero" code [15] at 3 MeV for Sn-118. As one can see, the calculated cross-sections are lowered or raised depending on whether the fluctuation factor is used or not. The discrepancies between the two cases are partially reduced if Moldauer's formula is adopted (see Table IV, column C)).

Similar calculations carried out for a large number of nuclei, led to the conclusions that discrepancies of the order of 15-30% among the calculated results are usually found, depending on the particular formalism adopted.

## CONCLUSIONS

From the above cursory examination, it seems that the following conclusions may be drawn:

- i) Optical model calculations for spherical or quasi-spherical nuclei based on recommended parameters are reasonably reliable for total neutron cross-section evaluations above  $\sim 2$  MeV.
- ii) The same conclusion cannot be applied for strongly deformed nuclei, for which consistent sets of recommended parameters have not yet been obtained.
- iii) Coupled-channel calculated cross-sections for direct processes could have at present a very large degree of uncertainty. The same could be true also for compound inelastic cross-sections if the behaviour of the optical potential parameters at low energies is not well known.
- iv) For a given set of basic parameters, calculated compound nucleus capture, elastic and inelastic scattering cross-sections can easily differ by  $\sim 30\%$ , as a consequence of the particular degree of sophistication adopted in the model.

Because of the accuracy usually required by reactor physicists, the above conclusions do not appear to be too optimistic as far as the usefulness of nuclear models as an evaluation tool is concerned. In a number of cases, however, uncertainties of  $\sim 20\div 30\%$  could be accepted, but experimental data are lacking or too scarce. Because of the cost and/or the time required in order to perform the measurements, nuclear model calculations can be useful in these cases, taking into account that, for the wise man, a bird in the hand is worth two in the bush.

TABLE I : EXAMPLES OF NUMERICAL CALCULATIONS OF  $R_{\gamma,a} = \Gamma_{\gamma,a}(Bn+E) / \Gamma_{\gamma,a}(Bn)$  IN THE FRAMEWORK OF THE "WEISSKOPF ESTIMATE".

E (MeV)	< Nb - 94 >				< Sn - 118 >			
	(1) $R_{\gamma}(L)$	(2) $R_{\gamma}(C)$	(3) $R_a(L)$	(4) $R_a(C)$	(5) $R_{\gamma}(C)$	(6) $R_{\gamma}^*(C)$	(7) $R_a(C)$	(8) $R_a^*(C)$
0	1.00	1.00	1.00	1.00	1.00	1.00	1.00	1.00
0.001	1.00	1.00	1.00	1.00	1.00	1.00	1.00	1.00
0.01	1.00	1.00	1.00	1.00	1.00	1.00	1.00	1.00
0.1	1.02	1.03	1.02	1.03	1.02	1.02	1.02	1.02
0.5	1.13	1.13	1.13	1.13	1.13	1.13	1.12	1.12
1	1.28	1.27	1.22	1.23	1.26	1.27	1.20	1.20
2	1.57	1.57	1.24	1.23	1.57	1.57	1.11	1.12
3	1.90	1.90	1.03	1.03	1.90	1.90	0.84	0.84
4	2.27	2.27	0.78	0.77	2.27	2.26	0.55	0.55
5	2.68	2.66	0.54	0.53	2.66	2.66	0.34	0.34
6	3.10	3.08	0.35	0.35	3.08	3.09	0.20	0.20
7	3.55	3.53	0.23	0.22	3.53	3.54	0.11	0.11
8	4.00	4.02	0.14	0.14	4.02	4.04	0.06	0.06
9	4.50	4.54	0.087	0.084	4.54	4.55	0.033	0.033
10	5.10	5.08	0.054	0.051	5.10	5.12	0.018	0.018
11	5.70	5.65	0.033	0.031	5.66	5.68	0.0098	0.0098
12	6.32	6.26	0.020	0.019	6.27	6.30	0.0053	0.0053
13	7.02	6.90	0.012	0.011	6.92	6.95	0.0029	0.0029
14	7.60	7.55	0.007	0.007	7.56	7.61	0.0016	0.0016
15	8.26	8.24	0.004	0.004	8.29	8.33	0.0010	0.0010

TABLE II : EXAMPLES OF NUMERICAL CALCULATIONS OF  $\Gamma_{\gamma,a}(Bn+E;J)$  FOR Se-78 (BRINK-AXEL ESTIMATE).

E (MeV)	$\Gamma_{\gamma}$ ( $J^{\pi}=0^{-}$ )	$\Gamma_{\gamma}$ ( $J^{\pi}=1^{-}$ )	$\Gamma_{\gamma}^*$ ( $J^{\pi}=0^{-}$ )	$\Gamma_{\gamma}^*$ ( $J^{\pi}=1^{-}$ )	$\Gamma_a$ ( $J^{\pi}=0^{-}$ )	$\Gamma_a$ ( $J^{\pi}=1^{-}$ )	$\Gamma_a^*$ ( $J^{\pi}=0^{-}$ )	$\Gamma_a^*$ ( $J^{\pi}=1^{-}$ )
0	182	180	241	285	182	180	241	285
0.001	182	180	241	285	182	180	241	285
0.01	182	181	241	285	182	181	241	285
0.1	187	185	243	285	187	185	243	285
0.5	208	206	255	289	208	206	255	289
1	237	235	276	302	236	234	274	300
2	307	304	333	348	283	280	308	324
3	382	388	409	417	300	297	318	327
4	491	487	503	507	287	284	299	304
5	607	602	616	616	256	252	264	265
6	742	736	747	744	217	215	223	222
7	894	888	898	893	180	179	184	182
8	1069	1061	1071	1064	148	146	149	148
9	1266	1258	1268	1260	121	119	122	120
10	1488	1480	1489	1481	99	98	99	98
11	1737	1728	1738	1729	81	80	81	80
12	2015	2005	2017	2006	66	64	66	64
13	2324	2313	2326	2314	51	50	51	50
14	2666	2654	2668	2655	37	36	37	36
15	3043	3030	3045	3032	23	23	23	23

TABLE III : FLUCTUATION FACTORS F FOR I-127 ( $J^\pi, \ell=2^+, 0$ )  
 ACCORDING TO VARIOUS APPROXIMATIONS.

$E_{\text{Lab}}$	"EXACT"	"EXACT"	"CAMERON"	"CAMERON"
	FORMULA(12) (SIMPSON)	FORMULA(12') (GAUSS)	FORMULA(13) (SIMPSON)	FORMULA(14') (GAUSS)
0.001	0.6787	0.6843	0.6787	0.6843
0.01	0.7296	0.7313	0.7296	0.7313
0.03	0.7483	0.7585	0.7478	0.7581
0.05	0.7609	0.7685	0.7609	0.7685
0.07	0.7728	0.7728	0.7671	0.7671
0.10	0.7690	0.7722	0.7691	0.7724
0.30	0.8098	0.8104	0.8647	0.8676
0.50	0.8449	0.8449	0.9414	0.9416
0.70	0.8807	0.8807	0.9711	0.9711
1.00	0.9175	0.9175	0.9864	0.9864

TABLE IV : INELASTIC SCATTERING CALCULATIONS  
 FOR Sn-118 AT 3 MeV.

LEVEL	$\sigma_{nn}(\text{mb})$		
	(a) H.F.	(b) H.F. (WFC)	(c) MOLD.
FUND.	241	536	434
1°	486	386	420
2°	278	229	246
3°	97	74	82
4°	108	98	101
5°	94	80	85
6°	215	177	190
7°	196	162	174
8°	77	71	73
9°	61	47	52
10°	2	2	2
11°	21	20	21
12°	37	35	36

## REFERENCES

- | 1 | D.W. GLASGOW and D.G. FOSTER Jr.: Phys.Rev.,C,3,604(1971)
- | 2 | F. PEREY and B. BUCK: Nucl.Phys.,32,353,(1962)
- | 3 | F.P. AGEE and L. ROSEN: LA-3538 MS (1966)
- | 4 | W.J. THOMPSON, S. EDWARDS and T. TAMURA: Nucl.Phys.,A105,678(1967)
- | 5 | H.A. BETHE: Rev.Mod.Phys.,9,69,(1937)
- | 6 | W. HAUSER and H. FESHACH: Phys.Rev.,87,366,(1952)
- | 7 | B. MARGOLIS: Phys.Rev.,88,327,(1952)
- | 8 | P.A. MOLDAUER: Phys.Rev.,135B,642,(1962)
- | 9 | P.A. MOLDAUER: Rev.Mod.Phys.,36,1079,(1964)
- | 10 | D.M. BRINK: Thesis,Oxford 1955;see also:Hand.der Physik,vol.XL,  
pg.315,Spring-Verlag(1955)
- | 11 | P. AXEL: Phys.Rev.,126,671,(1962)
- | 12 | J.M.B. LANG and K.J. Le COUTEUR: Proc.Phys.Soc.,A67,586,(1954)
- | 13 | A. GILBERT and A.G.W. CAMERON: Can.Journ.Phys.,43,1446,(1965)
- | 14 | A.G.W. CAMERON, N.H. LAZAR and H.W. SCHMITT: Fast Neutron Physics,  
Part II,Ch.V.M.-J.B.MARION and J.L. FOWLER Ed.-  
- Interscience,New York(1963)
- | 15 | F. FABBRI and G. REFFO: Unpublished

## FIGURE CAPTIONS

- Fig. 1 : Theoretical total cross-sections of Gd-156 calculated with the same set of parameters, but assuming different approximations for the optical potential representation.
- Fig. 2 : Theoretical shape-elastic cross-sections of Gd-156 at 4 MeV corresponding to the various cases of fig. 1.
- Fig. 3 : Theoretical direct inelastic scattering angular distributions for Gd-156 at 1 MeV, according to different channel coupling schemes.
- Fig. 4 : An example of the effects of the "geometrical W.b ambiguity" on the calculation of the inelastic scattering cross-sections.
- Fig. 5 : Theoretical neutron capture cross-section of I-127 according to the "black nucleus" and the "cloudy crystal ball" model.
- Fig. 6 : A comparison of the energy dependence of radiative (curve a) and capture widths (curve b) calculated according to Brink-Axel and Weisskopf.
- Fig. 7 : An example of the effects of the width fluctuation correction factor on the theoretical radiative capture cross-section of I-127.
- Fig. 8 : An example of the effects of the optical potential parameters on calculated inelastic scattering cross-sections of Cu-63.

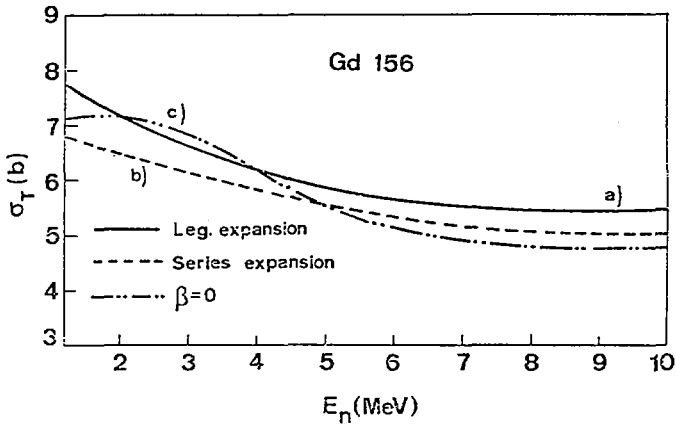


Fig. 1

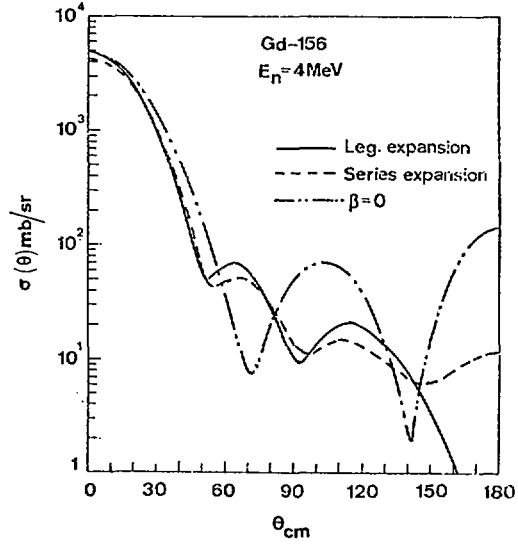


Fig. 2

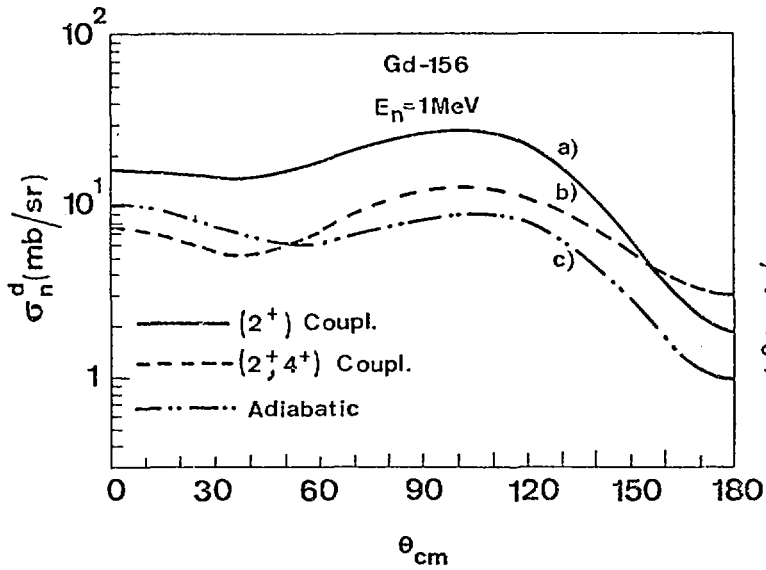


Fig. 3

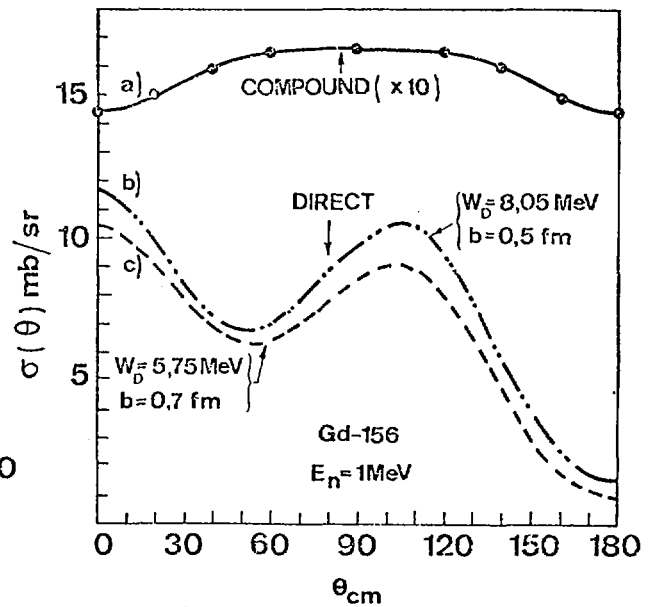


Fig. 4

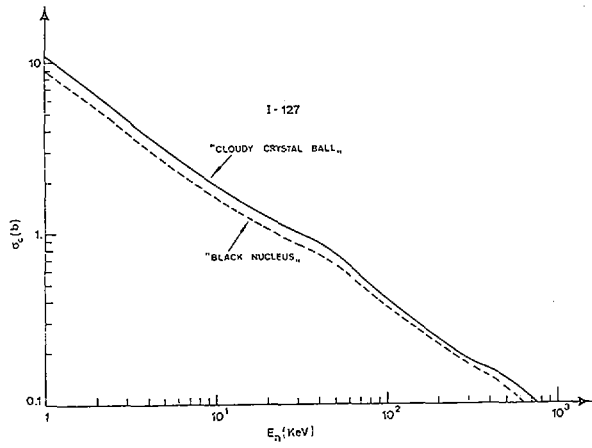


Fig. 5

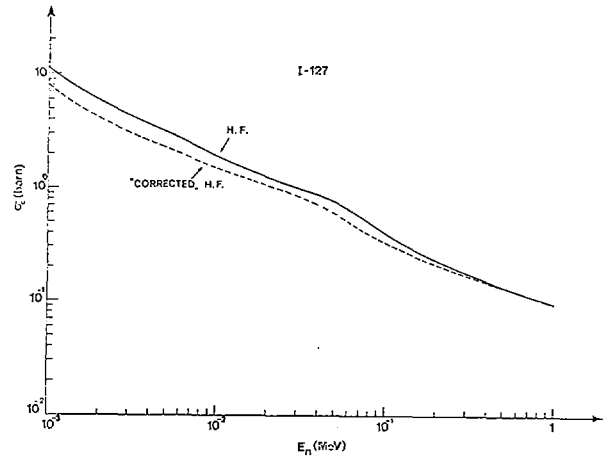


Fig. 7

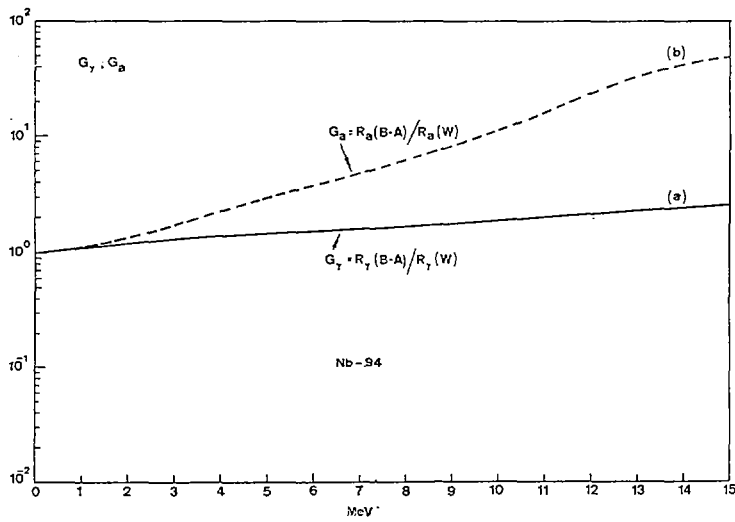


Fig. 6

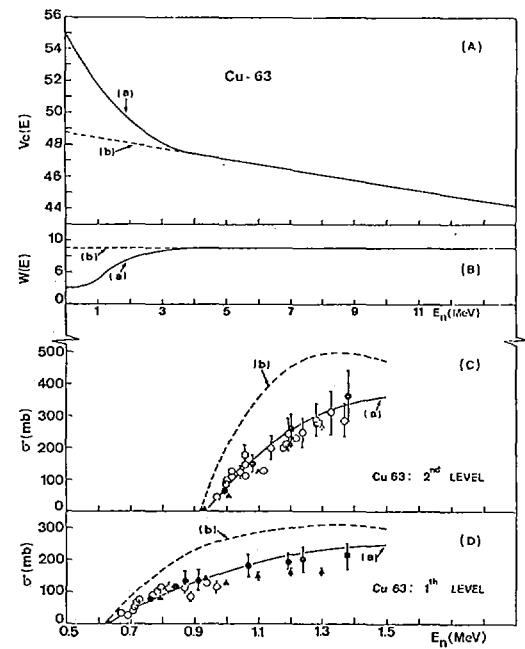


Fig. 8

II-1. On the Calculation Methods  
of the Neutron Capture Cross Sections

by

S. Igarasi, A. Mori\* and K. Harada

Japan Atomic Energy Research Institute

Tokai-mura, Naka-gun, Ibaraki-ken

Some remarks on the nuclear model calculations of the neutron capture cross sections are presented, on the basis of the optical model, statistical model and coupled channel calculation model. Calculation methods on the statistical model are discussed to obtain the total, elastic, inelastic scattering and capture cross sections consistently. The cross-section formulae with the level-width fluctuation and resonance interference are modified in order to conserve the sum of the partial cross sections. Example are shown on the cross sections of U-238. Effects of the competing process, that is the fission cross section, are also discussed.

---

\* Tokyo Institute of Technology

## 1. Introduction

There have been many kinds of the nuclear models available for the neutron cross-section calculations, in the energy region above resonance. The optical model<sup>1)</sup> is used to obtain the total cross section, shape elastic scattering cross section and total reaction cross section, and the statistical model<sup>2,3)</sup> is applied to the neutron capture, inelastic and compound elastic scattering cross-section calculations. Besides, we often use the direct and collective interaction models for the high energy neutron cross-section calculations. However, in the usual study of the nuclear physics, they are not necessarily used by taking account of their mutuality.

An aim of this work is to make the sum of partial cross sections equal the total cross section obtained from the optical model calculations, even if the partial cross sections are obtained by using different kinds of the nuclear model calculations. For the purpose of obtaining this equality, we have tried to modify the conventional neutron cross-section formulae in the framework of the statistical model calculations, from the view point of the neutron cross-section evaluation.

In section 2, conventional cross-section formulae will be reexamined from the view point of the above mentioned equality of the cross sections. Discussions will be given about the contributions of the competing processes, such as fission and (n,2n) reaction. In section 3, modified neutron cross-section formulae will be derived by taking account of the contributions from cascading process and the competing process. Correction factors of the resonance level-width fluctuation<sup>4,5,6,7)</sup> and of the repulsion effect<sup>5,6)</sup> will be introduced in our modified formulae of the cross sections. In this report, we will treat the cascading process in an approximate way. In section 4, we will show an example of the numerical calculation for U-238 cross section, and discuss the contributions of the resonance level-width fluctuation and resonance interference. In this report, we will try to unify the calculation methods of the neutron cross sections, in the framework of the statistical model calculation. Though this is a preliminary trial, it may be expected to develop a comprehensive and convenient method for nuclear cross-section calculations.

## 2. Conventional Cross-Section Formulae

Total cross section is one of the most characteristic quantities in the neutron induced reaction. It can be measured independently of partial neutron

cross sections whose sum must be equal to the total cross section. The similar situation holds in the theory. The total cross section can be obtained by the optical model calculation which provides shape elastic scattering cross section and total reaction cross section (formation cross section of the compound nucleus + direct reaction cross sections);

$$\sigma_{tot} = \sigma_{el.s} + \sigma_R = \sigma_{el.s} + \sigma_{el.c} + \sigma_{in} + \sigma_{n,\gamma} + \Delta\sigma, \quad (2.1)$$

where  $\Delta\sigma$  is the cross section of the competing process mentioned in the previous section. In general, partial cross sections  $\sigma_{el.c}$ ,  $\sigma_{in}$ ,  $\sigma_{n,\gamma}$  and  $\Delta\sigma$  in Eq.(2.1) are obtained by using the statistical model, direct and/or collective interaction models, and are not necessarily calculated by taking account of their mutuality, in the usual study of the nuclear physics.

From the view point of the neutron cross-section evaluation, it is desirable that the relation described in Eq.(2.1) is strictly satisfied in the nuclear model calculations. The neutron capture cross section, for instance, is calculated by using the following formula<sup>3)</sup>,

$$\sigma_{n,\gamma}(E_n) = \frac{\pi}{k_n^2} \sum_{J\pi j\ell} g^J \frac{\langle \overset{\circ}{T}_{njl}^{J\pi} \rangle \cdot \langle T_{\gamma 1}^{J\pi} \rangle}{\langle \overset{\circ}{T}^{J\pi} \rangle}, \quad (2.2)$$

in the framework of the conventional Hauser-Feshbach theory<sup>2)</sup>. In Eq.(2.2), a character "o" upon the neutron transmission coefficient  $\overset{\circ}{T}_{njl}^{J\pi}$  and the total transmission coefficient  $\overset{\circ}{T}^{J\pi}$  indicates the quantities obtained by the optical model calculations. Two kinds of the gamma-ray transmission coefficients are defined as follows<sup>8)</sup>,

$$\langle T_{\gamma 1}^{J\pi} \rangle = C_0^{J\pi} \int_{E_n}^{E_n+B_n} dE_\gamma E_\gamma^3 f_\gamma(E_\gamma) P_c(E_n+B_n-E_\gamma), \quad (2.3)$$

and

$$\langle T_{\gamma 2}^{J\pi} \rangle = C_0^{J\pi} \int_0^{E_n+B_n} dE_\gamma E_\gamma^3 f_\gamma(E_\gamma) P_c(E_n+B_n-E_\gamma), \quad (2.4)$$

respectively, and the total transmission coefficient  $\overset{\circ}{T}^{J\pi}$  includes only  $T_{\gamma 2}^{J\pi}$  ;

$$\overset{\circ}{T}^{J\pi} = \sum_{n'j'l'} \overset{\circ}{T}_{n'j'l'}^{J\pi} + T_{\gamma 2}^{J\pi} . \quad (2.5)$$

Descriptions of the normalization coefficient  $C_0^{J\pi}$  , profile function  $f_{\gamma}(E_{\gamma})$  and level density function  $\rho_c(U)$  will be given in later section.

Two quantities  $T_{\gamma 1}^{J\pi}$  and  $T_{\gamma 2}^{J\pi}$  correspond to the gamma-ray transition to the states below the neutron separation energy and to all the states available for the gamma-ray energy. We define a quantity which represents the difference between these two quantities;

$$\Delta T_{\gamma}^{J\pi} = \langle T_{\gamma 2}^{J\pi} \rangle - \langle T_{\gamma 1}^{J\pi} \rangle . \quad (2.6)$$

This corresponds also to the sum of the neutron and gamma-ray emissions through the cascading process from the compound nuclear states above the neutron separation energy. If this quantity  $\Delta T_{\gamma}^{J\pi}$  is not zero, the relation given in Eq.(2.1) is not satisfied formally, even in the energy region where  $\Delta O$  does not contribute. It is easily seen by looking at the formula for inelastic and compound elastic scattering cross sections;

$$\sigma_{n,n}(E_n) = \frac{\pi}{k_n^2} \sum_{J\pi j l j' l'} g^J \frac{\langle \overset{\circ}{T}_{n j l}^{J\pi} \rangle \cdot \langle \overset{\circ}{T}_{n' j' l'}^{J\pi} \rangle}{\langle \overset{\circ}{T}^{J\pi} \rangle} . \quad (2.7)$$

Summation of all the exit channels is not equal to the total reaction cross section;

$$\sigma_R(E_n) = \frac{\pi}{k_n^2} \sum_{J\pi j l} g^J \langle \overset{\circ}{T}_{n j l}^{J\pi} \rangle , \quad (2.8)$$

if  $\Delta T_{\gamma}^{J\pi} \neq 0$  . Therefore, we must treat the quantity  $\Delta T_{\gamma}^{J\pi}$  in a proper way for satisfying the equality mentioned in Eq.(2.1). In the next section, we will discuss this problem.

Moreover, we must consider the treatment of the competing process. In general, the cross section  $\Delta\sigma$  is able to include every partial cross section which we cannot calculate by our cross-section formulae. One of these partial cross sections may be the direct capture cross section<sup>8)</sup>, for instance. The total reaction cross section  $\sigma_R$  should include this partial cross section whose transmission coefficients are not included in our cross-section formulae, Eqs.(2.2) and (2.7). We assume here that the transmission coefficients for the competing process are proportional to the ratio;

$$\alpha = \Delta\sigma / \sigma_R, \quad (2.9)$$

and the total transmission coefficient with  $(J, \pi)$  is redefined as follows,

$$T^{J\pi} \equiv \overset{\circ}{T}^{J\pi} / (1 - \alpha). \quad (2.10)$$

This modified total transmission coefficient takes the place of  $\overset{\circ}{T}^{J\pi}$  in Eqs.(2.2) and (2.7). Thus, we are able to calculate the cross section including the contribution of the competing process.

We mentioned above that the partial cross section  $\Delta\sigma$  may be composed of every available partial cross section, if there is no contradiction among them. For practical purposes, some of them are the experimental data and the others may be the calculated values obtained by an appropriate nuclear model calculation. For example, we consider the direct capture cross section which is calculated by using the coupled channel theory<sup>9)</sup>. If we obtain the neutron transmission coefficients in Eqs.(2.2) and (2.7) by the use of the spherical optical model, our calculations would comprise some inconsistent components. From the view point of the consistent nuclear model calculations, it is desirable to carry out the calculations on the basis of the same fundamental nuclear model. Though the generalized optical model<sup>9,10)</sup> is very efficient for investigations of the nuclear physics, there are many problems to be solved in order to make use of the model effectively to the cross-section evaluation work. In this report, the spherical optical model is used as the basic model, but the essential points of our discussion will not be changed even in the case of the generalized optical model.

### 3. Modified Cross-Section Formulae

In the previous section, we mentioned that the sum of the partial cross sections is not equal to the total reaction cross section, in the framework of the conventional cross-section formulae. In this section, we derive the modified cross-section formulae, which take the place of Eqs.(2.2) and (2.7), by taking account of the quantity  $\Delta T_{\gamma}^{J\pi}$  given in Eq.(2.6). This quantity corresponds to the sum of the neutron and gamma-ray emission through the cascading process from the compound nuclear states above the neutron separation energy. The contribution of the cascading process to each exit channel should be estimated by using population probability<sup>7,11,12)</sup> of the intermediate states generated by the cascading process. In this report, however, we try to formulate this contribution in an approximate way.

We assume here that the contribution of the cascading process to each exit channel is proportional to the branching ratio;

$$\Delta T_{n'j'l'}^{J\pi} = \Delta T_{\gamma}^{J\pi} \times \frac{\langle \overset{\circ}{T}_{n'j'l'}^{J\pi} \rangle}{\langle \overset{\circ}{T}^{J\pi} \rangle}, \quad (3.1)$$

and

$$\Delta T_{\gamma_1}^{J\pi} = \Delta T_{\gamma}^{J\pi} \times \frac{\langle T_{\gamma_2}^{J\pi} \rangle}{\langle \overset{\circ}{T}^{J\pi} \rangle}. \quad (3.2)$$

Here, the denominators in Eqs.(3.1) and (3.2) are the original total transmission coefficients, but not the modified quantities, because the cross section  $\Delta \sigma$  is already given and the quantity  $\Delta T_{\gamma}^{J\pi}$  should be distributed among the neutron and gamma-ray channels. Using Eqs.(3.1) and (3.2), modified transmission coefficients are given for the neutron and gamma-ray channels respectively, as follows;

$$\langle T_{n'j'l'}^{J\pi} \rangle = \langle \overset{\circ}{T}_{n'j'l'}^{J\pi} \rangle + \Delta T_{n'j'l'}^{J\pi}, \quad (3.3)$$

and

$$\langle T_{\gamma}^{J\pi} \rangle = \langle T_{\gamma 1}^{J\pi} \rangle + \Delta T_{\gamma 1}^{J\pi} \quad (3.4)$$

It is easily seen that the relation given in Eq.(2.1) is satisfied by taking the modified quantities  $T^{J\pi}$ ,  $T_{n\gamma e}^{J\pi}$  and  $T_{\gamma}^{J\pi}$ , instead of the original quantities  $\overset{\circ}{T}^{J\pi}$ ,  $\overset{\circ}{T}_{n\gamma e}^{J\pi}$ , and  $T_{\gamma 1}^{J\pi}$  in Eqs. (2.2) and (2.7), respectively. Therefore, the cross-section formulae should be given as follows,

$$\sigma_{n,\gamma}(E_n) = \frac{\pi}{k_n^2} \sum_{\pi j l} g^J \frac{\langle \overset{\circ}{T}_{n j l}^{J\pi} \rangle \cdot \langle T_{\gamma}^{J\pi} \rangle}{\langle T^{J\pi} \rangle}, \quad (3.5)$$

and

$$\sigma_{n,n'}(E_n) = \frac{\pi}{k_n^2} \sum_{\pi j l j' l'} g^J \frac{\langle \overset{\circ}{T}_{n j l}^{J\pi} \rangle \cdot \langle T_{n' j' l'}^{J\pi} \rangle}{\langle T^{J\pi} \rangle}, \quad (3.6)$$

respectively, in the framework of the Hauser-Feshbach theory without resonance level-width fluctuation correction.

It may be believed that the properties of the resonance level-width fluctuation are not altered by the cascading process. Besides, the cross section  $\Delta\sigma$  is already given independently of the resonance level-width fluctuation correction. Therefore, the energy averages of the resonance contribution can be written for the neutron and gamma-ray channels as follows,

$$\left\langle \frac{\overset{\circ}{T}_{n j l}^{J\pi} \cdot T_{n' j' l'}^{J\pi}}{T^{J\pi}} \right\rangle = \frac{\langle \overset{\circ}{T}_{n j l}^{J\pi} \rangle \cdot \langle \overset{\circ}{T}_{n' j' l'}^{J\pi} \rangle}{\langle T^{J\pi} \rangle} S_{n j l; n' j' l'}^{J\pi} \left\{ 1 + \frac{\Delta T_{\gamma}^{J\pi}}{\langle \overset{\circ}{T}^{J\pi} \rangle} \right\}, \quad (3.7)$$

and

$$\begin{aligned} \left\langle \frac{\overset{\circ}{T}_{n j l}^{J\pi} \cdot T_{\gamma}^{J\pi}}{T^{J\pi}} \right\rangle &= \frac{\langle \overset{\circ}{T}_{n j l}^{J\pi} \rangle}{\langle T^{J\pi} \rangle} \left\{ \langle T_{\gamma 1}^{J\pi} \rangle \right. \\ &\quad \left. + \langle T_{\gamma 2}^{J\pi} \rangle \cdot \left[ \frac{\Delta T_{\gamma}^{J\pi}}{\langle \overset{\circ}{T}^{J\pi} \rangle} S_{n j l; \gamma 2}^{J\pi} - (1 - S_{n j l; \gamma 2}^{J\pi}) \right] \right\}, \end{aligned} \quad (3.8)$$

respectively, where the correction factors of the resonance level-width fluctuation  $S_{njl;c}^{JII}$  are calculated by using the original quantities only. Derivation of Eq.(3.8) is carried out by the use of an important relation for the transmission coefficients;

$$\sum_c \langle \dot{T}_c^{JII} \rangle (1 - S_{njl;c}^{JII}) = 0 \quad (3.9)$$

This relation is rewritten for the original quantities and for the modified quantities as follows,

$$\langle \dot{T}^{JII} \rangle = \sum_{n'j'l'} \langle \dot{T}_{n'j'l'}^{JII} \rangle S_{njl;n'j'l'}^{JII} + \langle T_{\gamma 2}^{JII} \rangle S_{njl;\gamma 2}^{JII}, \quad (3.10)$$

$$= \sum_{n'j'l'} \langle \dot{T}_{n'j'l'}^{JII} \rangle S_{njl;n'j'l'}^{JII} \left\{ 1 + \frac{\Delta T_{\gamma}^{JII}}{\langle \dot{T}^{JII} \rangle} \right\} + X, \quad (3.11)$$

respectively, where  $X$  is a quantity for the gamma-ray channel which should be expressed by the use of the modified quantities, and is given as follows,

$$X = \langle T_{\gamma 1}^{JII} \rangle + \langle T_{\gamma 2}^{JII} \rangle \left\{ (S_{njl;\gamma 2}^{JII} - 1) + \frac{\Delta T_{\gamma}^{JII}}{\langle \dot{T}^{JII} \rangle} \cdot S_{njl;\gamma 2}^{JII} \right\} \quad (3.12)$$

Our treatments mentioned above can be applied to the Moldauer theory<sup>5,6</sup>, whose transmission coefficients are given by the following equations,

$$\langle \dot{\Theta}_{njl}^{JII} \rangle - \frac{1}{4} Q^{JII} (\langle \Theta^{JII} \rangle) \cdot \langle \dot{\Theta}_{njl}^{JII} \rangle^2 = \langle \dot{T}_{njl}^{JII} \rangle, \quad (3.13)$$

for the neutron channel, and

$$\langle \dot{\Theta}_{\gamma i}^{JII} \rangle - \frac{1}{4} Q^{JII} (\langle \Theta^{JII} \rangle) \cdot \langle \dot{\Theta}_{\gamma i}^{JII} \rangle^2 = \langle T_{\gamma i}^{JII} \rangle, \quad (3.14)$$

for the gamma-ray channel, respectively. A quantity  $Q^{J\pi}$  represents the resonance interference effect<sup>5,6)</sup> and is a function of the total transmission coefficient given by the following formula

$$\langle \Theta^{J\pi} \rangle = \langle \dot{\Theta}^{J\pi} \rangle / (1-\alpha) = \left\{ \sum_{n'j'l'} \langle \dot{\Theta}_{n'j'l'}^{J\pi} \rangle + \langle \Theta_{\gamma 2}^{J\pi} \rangle \right\} / (1-\alpha). \quad (3.15)$$

The quantity  $\Delta T_{\gamma}^{J\pi}$  is replaced by a new quantity,

$$\Delta \Theta_{\gamma}^{J\pi} = \langle \Theta_{\gamma 2}^{J\pi} \rangle - \langle \Theta_{\gamma 1}^{J\pi} \rangle, \quad (3.16)$$

and the cross-section formulae are represented as follows,

$$\begin{aligned} \sigma_{n,\gamma}(E_n) = \frac{\pi}{k_n^2} \sum_{J\pi j l} g^J \frac{\langle \dot{\Theta}_{njl}^{J\pi} \rangle}{\langle \Theta^{J\pi} \rangle} \left\{ \langle \Theta_{\gamma 1}^{J\pi} \rangle \right. \\ \left. + \langle \Theta_{\gamma 2}^{J\pi} \rangle \cdot \left[ \frac{\Delta \Theta_{\gamma}^{J\pi}}{\langle \dot{\Theta}^{J\pi} \rangle} \cdot S_{njl;\gamma 2}^{J\pi} - (1 - S_{njl;\gamma 2}^{J\pi}) \right] \right\}, \end{aligned} \quad (3.17)$$

and

$$\begin{aligned} \sigma_{n,n'}(E_n) = \frac{\pi}{k_n^2} \sum_{J\pi j l j' l'} g^J \left\{ \frac{\langle \dot{\Theta}_{njl}^{J\pi} \rangle \cdot \langle \dot{\Theta}_{n'j'l'}^{J\pi} \rangle}{\langle \Theta^{J\pi} \rangle} S_{njl;n'j'l'}^{J\pi} \right. \\ \left. \times \left( 1 + \frac{\Delta \Theta_{\gamma}^{J\pi}}{\langle \dot{\Theta}^{J\pi} \rangle} \right) - \delta_{njl;n'j'l'} \frac{1}{4} (1-\alpha) Q^{J\pi} \langle \Theta^{J\pi} \rangle \cdot \langle \dot{\Theta}_{njl}^{J\pi} \rangle^2 \right\}, \end{aligned} \quad (3.18)$$

respectively. Explicit representation of the correction factors of the resonance level-width fluctuation is described as the following integral forms,

$$S_{njl;\gamma 2}^{J\pi} = \int_0^{\infty} dt \frac{\exp(-\langle \Theta_{\gamma 2}^{J\pi} \rangle \cdot t / \langle \dot{\Theta}^{J\pi} \rangle)}{\left( 1 + \frac{2}{\nu_n} \frac{\langle \dot{\Theta}_{njl}^{J\pi} \rangle}{\langle \dot{\Theta}^{J\pi} \rangle} t \right) \prod_{c \neq \gamma} \left( 1 + \frac{2}{\nu_c} \frac{\langle \dot{\Theta}_c^{J\pi} \rangle}{\langle \dot{\Theta}^{J\pi} \rangle} t \right)^{1/2}}, \quad (3.19)$$

for gamma-ray, and

$$S_{nje;nje}^{J\pi} = \int_0^\infty dt \frac{(1 + \frac{2}{\nu_n} \delta_{nje;nje}) \cdot \exp(-\langle \dot{H}_{\gamma 2}^{J\pi} \rangle t / \langle \dot{H}^{J\pi} \rangle)}{(1 + \frac{2}{\nu_n} \frac{\langle \dot{H}_{nje}^{J\pi} \rangle}{\langle \dot{H}^{J\pi} \rangle} t) \cdot (1 + \frac{2}{\nu_n} \frac{\langle \dot{H}_{n'je'}^{J\pi} \rangle}{\langle \dot{H}^{J\pi} \rangle} t) \cdot \prod_{c \neq n} (1 + \frac{2}{\nu_c} \frac{\langle \dot{H}_c^{J\pi} \rangle}{\langle \dot{H}^{J\pi} \rangle} t)^{1/2}} \quad (3.20)$$

for neutron, respectively.

In this section, we derived our modified cross-section formulae, Eqs.(3.17) and (3.18), for the neutron capture, inelastic and compound elastic scattering. Using Eqs.(3.9), (3.13), (3.14) and (3.15), it is easily seen that the relation in Eq.(2.1) is satisfied by these cross-section formulae. In the next section, we will confirm this result with numerical calculations.

#### 4. Example of Numerical Calculation

In Table 1, we show an example of the numerical calculations for U-238. Column 6 (Sum) is provided for the sum of the partial cross sections  $\sigma_{n,\gamma}$ ,  $\sigma_{el}$ ,  $\sigma_{in}$  and  $\Delta\sigma$ , and column 7 is for the total cross section obtained with the optical model calculation. Numerical values in col. 6 must be equal to the values in col. 7. Results show that the equality is apparently satisfied.

In this calculation, we adopted Kanda's evaluated values<sup>13)</sup> for the cross section  $\Delta\sigma$ , which is the fission cross section in this case. In this Table, we show the results for two examples. One is the calculation with the resonance level-width fluctuation correction and resonance interference effect, and the other is the calculation without the resonance interference effect. The results of the former are shown in the upper line for each energy block, and the results of the latter are in the lower line. The differences between these two are due to the resonance interference effect, and are small in the low energy region. In both cases, we normalized the neutron capture cross section to the value, 0.637 barns, at 10 keV, with the width of 5%. Therefore, these differences depend also on the difference of the normalization coefficient,  $C_0^{J\pi}$ , used in Eqs.(2.3) and (2.4). Precise comparison should be performed with the same normalization coefficient, but we do not discuss this problem in this report. The coefficient  $C_0^{J\pi}$  is given by using the observed gamma-ray width and level spacing;

$$C_0^{J\pi} = \left( \frac{2\pi T_\gamma^{J\pi}}{D_{J\pi}} \right)_{B_n} / \int_0^{B_n} dE_\gamma E_\gamma^3 f_\gamma(E_\gamma) \rho_c(B_n - E_\gamma), \quad (4.1)$$

where

$$\left( \frac{2\pi\Gamma_\gamma^{\text{th}}}{D_{\text{th}}} \right)_{B_n} = \frac{2J+1}{2(2I+1)} \frac{2\pi\Gamma_{\gamma,\text{obs.}}}{D_{\text{obs.}}} \quad (4.2)$$

It is also possible to use the theoretical values of  $\Gamma_\gamma^{\text{th}}$  and  $D_{\text{th}}$ , instead of the experimental data. In the calculation mentioned above, we did not use these data, but normalized the cross section directly.

As for the profile function  $f_\gamma(E_\gamma)$  used in Eqs.(2.3) and (2.4), there are two available types; Brink-Axel type<sup>7,14)</sup> and Lane-Lynn type<sup>8)</sup>. In this calculation, we adopted the Brink-Axel type tentatively;

$$f_\gamma(E_\gamma) = \frac{2\Gamma_R}{\pi} \frac{E_\gamma}{(E_\gamma^2 - E_R^2)^2 + (\Gamma_R E_\gamma)^2}, \quad (4.3)$$

with  $E_R = 13.6$  and  $\Gamma_R = 6.0$ . In the evaluation or analysis of the nuclear data, choice of the profile function as well as the values of the parameters should be carried out after careful investigations about their effects. In our preliminary investigation, there are little differences between the cross-section values with the Brink-Axel type and with the Lane-Lynn type.

In our calculation, we used the level density function of Gilbert-Cameron<sup>15)</sup> type. For the compound nucleus, we used the function without spin cut-off factor. Therefore, the level width of the gamma-ray channel is independent<sup>8)</sup> of the spin and parity of the compound nuclear state. The values of the parameters were taken from Gilbert-Cameron's recommendation, and the neutron separation energy was adopted from the table compiled by Wapstra and Gove<sup>16)</sup>.

For overlapping levels of the residual nucleus, we used the level density function with the spin cut-off factor as well as the distribution function of the parity which is defined as follows,

$$P_\pi(U) = \frac{N_\pi + 0.5 \exp[(U-E_0)/\Delta]}{1 + \exp[(U-E_0)/\Delta]}, \quad (4.4)$$

where  $N_{\pi}$  stands for the fraction of the discrete levels with parity  $\pi$ , and the parameters  $E_0$  and  $\Delta$  are given by the use of a joint energy  $E_x$ , at which the gas model and constant temperature model of the level density join smoothly, and an energy  $E_c$  above which the levels are assumed to be overlapping;

$$E_0 = (E_x + E_c)/2, \tag{4.5}$$

and

$$\Delta = |E_x - E_c|/8. \tag{4.6}$$

In Fig. 1, we show several kinds of the partial cross sections of U-238. The neutron capture cross section reveals two humps around 300 keV and 1.0 MeV. The former is due to the p-wave neutron capture and the latter is caused by the competition between the transmission coefficients for the gamma-ray and the inelastic neutron channels. The gamma-ray transmission coefficient increases rapidly above about 500 keV, and the transmission coefficients for the inelastic neutron channels, especially for the overlapping levels of the residual nucleus, become very large above about 1.0 MeV. Being due to this competition, the neutron capture cross section decreases with increasing the neutron incident energy, in the framework of the statistical model calculation. In general, the contribution of the direct and/or collective capture processes<sup>17~20)</sup> play a dominant role in the energy region above such energy as 1.0 MeV in this example. We tried to estimate the direct capture cross section for single particle E1 transition by using the adiabatic approximation of the coupled channel calculation<sup>9)</sup>;

$$\sigma_{n,\gamma}(E_n, J_\beta, K_\beta) = \frac{16}{9} \frac{\bar{e}^2}{\hbar k_n^2} \left(\frac{E_x}{\hbar c}\right)^3 \sum_J \left| \langle \Psi_{\beta J_\beta}^{K_\beta} \| m_e \| \Psi_{\alpha J} \rangle \right|^2, \tag{4.7}$$

where  $J_\beta$  and  $K_\beta$  are spin and K-quantum number of the bound state respectively, and

$$\begin{aligned}
 & \langle \Psi_{\beta J_{\beta}}^{K_{\beta}} \| \mathcal{M} \| \Psi_{\alpha J} \rangle \\
 &= \sum_{\bar{m}_j > 0} (1 - (-)^{J + \bar{m}_j}) \cdot \sum_{l j l' j'} (-)^{j' + \frac{1}{2}(l+l')} \frac{1}{2} (1 + (-)^{l+l'+1}) \cdot \sqrt{2j+1} \cdot (j j \frac{1}{2} - \frac{1}{2} | 1 0) \\
 & \times \{ (J 1 \bar{m}_j K_{\beta} - \bar{m}_j | J_{\beta} K_{\beta}) \cdot (j 1 \bar{m}_j K_{\beta} - \bar{m}_j | j' K_{\beta}) \quad (4.8) \\
 & + (-)^{j + \bar{m}_j} (J 1 - \bar{m}_j K_{\beta} + \bar{m}_j | J_{\beta} K_{\beta}) \cdot (j 1 - \bar{m}_j K_{\beta} + \bar{m}_j | j' K_{\beta}) \} \cdot \int R_{j l' K_{\beta}}^{\beta *}(r) \cdot R_{j l \bar{m}_j}^{\alpha}(r) \cdot r \cdot dr
 \end{aligned}$$

According to our preliminary calculation, the partial cross section for each single particle state was too small to be desired.

Finally, we show a comparison of the neutron capture cross sections obtained by the use of the Hauser-Feshbach's formulae, Eqs.(3.5) and (3.6), and Moldauer's formulae, Eqs.(3.17) and (3.18). In Fig. 2, we show two curves of the neutron capture cross section normalized at 10 keV. The curve with the Hauser-Feshbach's formulae reveals a rapid fall from several ten keV to hundred keV. This rapid fall is reduced in the curve of the Moldauer's formulae. The curve of the latter is apparently larger than the curve of the former, above about 50 keV. However, if we use the same coefficient  $C_{\circ}^{J\pi}$  mentioned in Eq.(4.1) for both curves, the situation of the two curves is upset. This is due to the effect of the level-width fluctuation, which moderates not only the variation but also the value of the neutron capture cross section.

### 5. Concluding Remarks

We derived the neutron cross-section formulae, by which we obtain the several partial cross section whose sum is equal to the total cross section calculated with the spherical optical model. The formulae are very useful for neutron cross-section evaluation work. Two quantities  $\Delta T_{\gamma}^{J\pi}$  and  $\Delta O$  play an important role in our cross-section formulae which represent the effects of the cascading and competing processes respectively. These two, however, are treated only approximately in our formulae presented in this report. It is necessary to look for the methods to obtain them reasonably, for the cross-section calculations. In particular, theoretical treatment of  $\Delta O$  is needed in order to improve our present nuclear model calculations. One possibility is to use the generalized optical model and to unify the statistical, direct and collective model calculations.

## References

1. H. Feshbach, C. E. Porter and V. F. Weisskopf; Phys. Rev. 96 (1954) 448
2. W. Hauser and H. Feshbach; Phys. Rev. 87 (1952) 366
3. B. Margolis; Phys. Rev. 88 (1952) 327
4. C. E. Porter and R. G. Thomas; Phys. Rev. 104 (1956) 483
5. P. A. Moldauer; Phys. Rev. 123 (1961) 968
6. P. A. Moldauer; Phys. Rev. 135 (1964) B642
7. J. E. Lynn; The Theory of Neutron Resonance Reactions, Oxford (1968)
8. A. M. Lane and J. E. Lynn; Nucl. Phys. 11 (1959) 646
9. T. Tamura; Rev. Mod. Phys. 37 (1965) 679
10. M. Kawai, A. K. Kerman and W. K. McVoy; Ann. Phys. 75 (1973) 156
11. E. S. Troubetzkoy; Phys. Rev. 122 (1961) 212
12. W. P. Poenitz; Z. Phys. 197 (1966) 262
13. Y. Kanda; Private Communication
14. P. Axel; Phys. Rev. 126 (1962) 671
15. A. Gilbert and A. G. W. Cameron; Can. J. Phys. 43 (1965) 1446
16. A. H. Wapstra and N. B. Gove; Nuclear Data Table A9 (1971) 265
17. C. F. Clement, A. M. Lane and J. R. Rook; Nucl. Phys. 66 (1965) 273
18. G. E. Brown; Nucl. Phys. 57 (1964) 339
19. G. Longo and F. Saporetti; Nucl. Phys. A127 (1969) 503
20. H. Kitazawa; Private Communication

## Table and Figure Caption

Table 1. Cross sections of U-238. "Sum" in col. 6 means the sum of  $\sigma_{n,\gamma}$ ,  $\sigma_{el}$ ,  $\sigma_{in}$  and  $\Delta\sigma$ . Values in col. 6 must be equal to the values in col. 7, which are the values of the total cross section calculated with the optical model.

Fig. 1. Partial cross sections of U-238. Cross sections of s-wave and p-wave neutron capture are also exhibited.

Fig. 2. Comparison of the neutron capture cross section obtained with Eqs.(3.5) and (3.17).

Table 1

	$\sigma_{n,\gamma}$ (b)	$\sigma_{el}$ (b)	$\sigma_{in}$ (b)	$\Delta\sigma$ (b)	Sum	$\sigma_{tot. opt.}$
1 keV	2.5511	24.929			27.4801	27.480
	2.5668	24.913			27.4798	"
10 keV	0.66142	15.705			16.3664	16.367
	0.66388	15.703			16.3669	"
100 keV	0.18283	11.273	0.38436		11.8402	11.840
	0.18353	11.281	0.37473		11.8393	"
800 keV	0.15408	5.5616	1.5820	0.003	7.30068	7.3007
	0.15274	5.7028	1.4422		7.30074	"
1 MeV	0.16573	5.0192	1.8546	0.022	7.06153	7.0615
	0.16231	5.1714	1.7058		7.06151	"
2 MeV	0.060607	4.3605	2.2546	0.528	7.20371	7.2037
	0.073002	4.4079	2.1948		7.20370	"

1st line : with fluctuation & interference.

2nd line : with fluctuation but without interference.

Normalization at 10 keV ,  $\sigma_{n,\gamma} = 0.637 \pm 5\%$

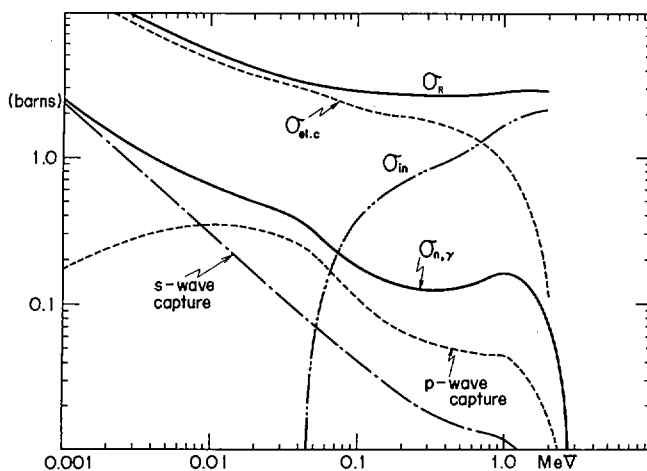


Fig. 1

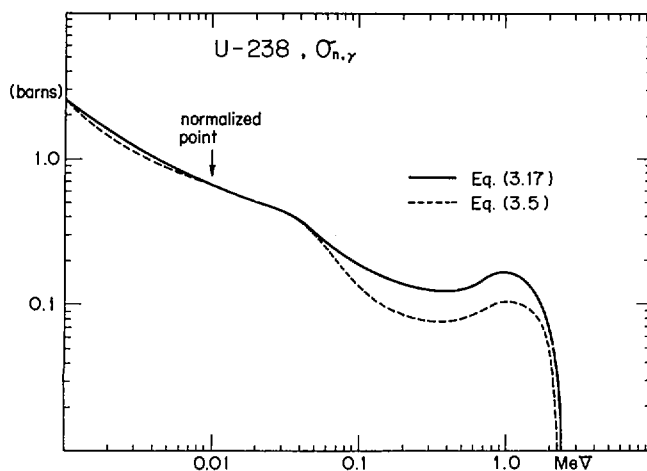


Fig. 2

DISCUSSION

H. E. JACKSON, JR.: How sensitive are your results to the use of the Brink Axel relationship for the transition strength?

S. IGARASI: I haven't investigated it in detail yet. As far as the cross-section calculation in the low energy region is concerned, there may be scarcely any difference between Brink-Axel form and Lane-Lynn form of the profile function.

## II-2. STATUS OF PREDICTIONS OF PHOTON STRENGTH FUNCTIONS BY GIANT DIPOLE RESONANCE AND VALENCE MODELS\*

H. E. Jackson  
Argonne National Laboratory, Argonne, Illinois 60439

The data available on the strength of radiative transitions from highly excited states in the threshold region are reviewed for nuclei from mass 50 to 250. Photon strength functions for E1 and M1 radiation resulting from measurements of threshold photoneutron spectra, individual neutron spectra, and average capture spectra are summarized. To date neither the single particle nor the giant dipole model has given an accurate description of  $\langle \Gamma(E1) \rangle / D$ . However, the precision of data on the magnitude and energy dependence of  $\langle \Gamma(E1) \rangle / D$  has improved and systematic trends are emerging. Evidence for the importance of single particle effects in the mass region  $A \approx 90$  are discussed briefly. Data parameterized in terms of the giant dipole prediction appears to be the most satisfactory basis for describing the systematics of  $\langle \Gamma(E1) \rangle / D$  in calculating and evaluating gamma-ray spectra and production cross sections. Data for the reaction  $^{181}\text{Ta}(n, x\gamma)$  are discussed. Use of the giant dipole model results in a major improvement in the comparison of calculated and measured spectra.

---

\* Work performed under the auspices of the U. S. Atomic Energy Commission.

## I. Introduction.

The purpose of this paper is to review our present knowledge of the strength of radiative transitions of highly-excited states in the threshold region. The topic is one which has been actively investigated in neutron and photonuclear physics for several decades. It is testimony to the difficulty in obtaining and interpreting accurate experimental estimates that even now our ideas are still in the formative stage. We will compare the growing body of data for dipole transitions which have been accumulated for a wide range of nuclei with the predictions of various simple models of radiative transitions. Our discussion will be restricted to the mass region, 50-250 where as a first approximation we can rely on the statistical model of highly excited states for a description of the properties of individual resonances. Under these assumptions individual radiation widths should be distributed according to the Porter-Thomas distribution. Resonance energies and spacings should be governed by well established laws such as the Wigner distribution. Variations in local averages of resonance in transition strength should be consistent with the random fluctuations in level density and width characteristic of these distributions. Under these conditions it is convenient to discuss the transition strength in terms of the photon strength functions for the various multipole types of transitions. For our discussion we define the strength function for multipole  $M_p$  as the dimensionless ratio of the average width to the mean spacing of states of the appropriate spin and parity:  $S(M_p) = \langle \Gamma_{\gamma i} \rangle / D$ . (1)

We expect the radiative strength corresponding to possible individual nuclear configuration to be spread over excitation regions large compared to the level spacing. In this case, any nuclear structure effects if important should manifest

themselves in variations in the strength function with energy and the mass.

## II. Single Particle Model.

The simplest and most widely used estimate of the photon strength function comes from the single-particle estimate of radiative transitions due to Weisskopf.<sup>1</sup> In this calculation a one-nucleon transition between bound single particle states is assumed. All wave functions are assumed to be constant within the nuclear radius and zero outside. The resulting estimates are

$$\begin{aligned} \langle \Gamma_{\gamma i}(E1) \rangle / D &= 6.8 \times 10^{-8} A^{2/3} E_{\gamma}^3 / D_0 \\ \langle \Gamma_{\gamma i}(M1) \rangle / D &= 2.1 \times 10^{-8} E_{\gamma}^3 / D_0 \\ \langle \Gamma_{\gamma i}(E2) \rangle / D &= 4.9 \times 10^{-14} A^{4/3} E_{\gamma}^5 / D_0 \end{aligned} \quad (2)$$

where  $D_0$  is customarily assumed to be a single particle spacing. The introduction of this level spacing has never been put on a sound theoretical basis, and over the years  $D_0$  has been treated as an empirical parameter which is adjusted to give the best fit to available data.

However, the single particle estimate for E1 can be more firmly established by using the connection between the strength function and the corresponding photon absorption cross section:

$$\langle \sigma_a \rangle = 2 \pi^2 \kappa^2 g \langle \Gamma_{\gamma i} \rangle / D \quad (3)$$

For E1 radiation, the absorption cross section can be constrained to satisfy the classical dipole sum rule:

$$\int_0^{\infty} \sigma_a \cdot dE = .060 NZ/A \text{ MeV barns} \quad (4)$$

It is reasonable in view of our knowledge of the systematics of the E1 giant dipole resonance to assume that the upper limit of the integration is approximately 40 MeV. Using the mass and energy dependence indicated by the Weisskopf expression in evaluating the sum rule leads to the relation:

$$\langle \Gamma_{\gamma i}(E1) \rangle / D = 8.8 \times 10^{-9} E^3 A^{2/3} \quad (5)$$

for a nucleus with  $A=160$ . This expression should be reasonable zeroth approximation to the E1 strength function.

Fig. 1 is a comparison of this single particle prediction with the data available on  $\langle \Gamma_{\gamma_i}(E1) \rangle / D$ . These data include results from measurements of average capture spectra, resonance capture spectra, and threshold photoneutron spectra. In compiling this data we required that the number of resonances studied in any measurement be sufficient to suppress the uncertainty imposed on the data by Porter-Thomas fluctuations. For this reason there are fewer data points than have been included in earlier compilations. The quantity plotted is actually the photon strength function divided by the energy and mass dependence of the single particle estimate. The solid line is the prediction based on the dipole sum rule. Clearly the latter predicts values much too large. If we arbitrarily decrease the single particle estimate by a factor of 3.5 we obtain the dotted curve which is in crude agreement with the data. However, the discrepancies for the lighter nuclei and the arbitrary character of the best normalization suggest that a more refined model is necessary.

### III. Giant Dipole Resonance.

Our knowledge of the systematics of the giant dipole resonance tell us that the single particle model with its uniform distribution of dipole strength is completely unrealistic. The situation is described in Fig. 2 for a nucleus of mass  $\approx 190$ . Here the single particle dipole matrix element is compared with the value implied by the empirically established Lorentzian approximation to the giant dipole resonance. The natural refinement first suggested by Brink<sup>2</sup> and implemented by Axel<sup>3</sup> was to use the systematics of

the giant dipole resonance in heavy nuclei to predict the strength function in the threshold region. Two assumptions are necessary. First, it is assumed that the dipole strength in the threshold region can be described by the low energy tail of the giant dipole resonance. This tail is then parameterized in terms of the classical Lorentzian shape that is used to fit the main part of the dipole resonance in the damped-harmonic oscillator model. The second assumption pertains to the relationship between radiative transitions in photon and neutron induced reactions. In  $(n, \gamma)$  reactions transitions to a range of final states occur while in the  $(\gamma, n)$  reaction the transition always corresponds to the inverse of the  $(n, \gamma)$  ground state transition. The relationship between photon strength functions for these two reactions is not evident. The usual assumption is the Brink Hypothesis, namely that each excited state has built on it the same giant dipole resonance as the ground state. This then establishes the equality of the strength functions as observed in the inverse reactions. This is indicated schematically in Fig. 3.

Following these assumptions Axel<sup>3</sup> has used parameterization of the giant dipole resonance that is applicable to a wide range of nuclei to develop a relationship for the photon strength function expected to be accurate in the threshold region:

$$\langle \Gamma_{\gamma 0} \rangle / D = 6.1 \times 10^{-15} E_{\gamma}^5 A^{8/3} . \quad (6)$$

$E_{\gamma}$  is in MeV.

In Fig. 4 we have presented a summary comparison of  $E1$  photon strength functions parameterized in terms of the giant dipole model with the predictions of Axel. The solid line is his prediction. The results are very interesting. As in the case of the single particle model the overall

agreement is poor. In the mass region between between 150 and 250 the giant dipole model badly overestimates the E1 strength. Perhaps we should not be surprised at this since only the order of 1% of the total E1 strength as given by the classical dipole sum rule is expected to occur below the threshold region. The Brink-Axel treatment may simply not be capable of describing such detail.

#### IV. Nuclear Structure Effects.

At the moment the best strength function estimate appears to be the "retarded" single particle value. This suggests that the radiative strength be attributed to some residual single particle strength in the threshold region. This possibility has been extensively discussed by Lynn<sup>4</sup> in developing his "Valence" approximation of radiative transitions. He observes that the giant dipole resonance is customarily attributed to the residual interaction between an excited core nucleon and the nucleons remaining in a closed shell. This interaction raises the energy of the shell-model excitation of the core nucleons to the giant resonance region. However, the effect should not be nearly as great for valence nucleons in partially filled shells. Consequently the energies of valence transitions should be much lower than those in the giant dipole resonance. Considerable support for this picture is found in the recent results from resonance-capture studies of the Brookhaven group in the mass region  $A = 90$  to  $100$ <sup>5</sup> where such valence effects are expected to be particularly strong.

A prime candidate for investigation of the valence model is the nucleus  $^{91}\text{Zr}$  which can be viewed as a single valence nucleon outside a spherical  $^{90}\text{Zr}$  core, as shown in Fig. 5. The ground state of  $^{91}\text{Zr}$  can be

approximated by a pure  $d_{5/2}$  orbital, which can be connected by an E1 transition to unbound  $p_{3/2}$  resonances. In the valence model, the transition would be between the  $3p_{3/2}$  and  $2d_{5/2}$  single particle states. Using the threshold photoneutron technique at Argonne<sup>6</sup> we have investigated the E1 strength for this nucleus. Because of the high level density we were able to resolve the structure only within 225 keV of threshold, and over such a small region of excitation we were not able to demonstrate the existence of any intermediate structure. However, the 35 observed  $p_{3/2}$  resonances represent a large enough sample for the study of the statistical properties of individual radiation widths. For these widths, using the valence approximation Lynn has established the relationship given in Fig. 5. The reduced width factors,  $\gamma_{\lambda}^2$  and  $\gamma_{\mu}^2$  measure the fractions of the appropriate single-particle states contained in the resonance and ground states of  $^{91}\text{Zr}$  respectively. As this equation indicates, the presence of a significant valence component in the mode of excitation will give rise to a correlation between  $\Gamma_{\gamma 0}$  and  $\gamma^2$ . This picture is strongly supported by the photoneutron data. The usual statistical analysis gives a value of the correlation coefficient between the radiation width and neutron width,  $\rho = 0.59$ . The correlation is clearly evident in the observed statistical distribution. The analysis of the individual widths was pursued under the assumption that the individual transition amplitudes are a sum of a valence term and a compound nucleus term.

$$\sqrt{\Gamma_{\gamma 0}^{\lambda}} \cong \sqrt{\Gamma_{\gamma 0}^{\lambda}}_{\text{cmpnd nuc.}} + b\gamma_{\lambda} \quad (7)$$

The results of this analysis are that the mean width for the valence component of  $\Gamma_{\gamma 0}$ ,  $b^2 \gamma^2 = 90$  meV out of an average total width of 150 meV. Using Lynn's approximation and the observed neutron widths we obtain an identical  $b^2 \gamma^2_{\text{predicted}} = 90$  meV. Such good agreement is probably fortuitous but the results do indicate that valence transitions account for a major portion of the E1 transition amplitude near threshold.

However, to date, the importance of such single particle effects has been clearly established only for nuclei with  $A \sim 90-100$  near the 3p peak in the neutron p-wave strength function. Such effects are also expected to be important in the mass regions  $A \sim 40-65$  and  $A \sim 40-180$  where the neutron interaction is dominated by the 3s and 4s peaks in the neutron strength function. Thus far, the evidence for valence effects in these regions is conflicting.

#### V. Energy Dependence of $\langle \Gamma_{\gamma i}(E1) \rangle / D$ .

One might hope to gain further insight into the behavior of the strength functions by studying their energy dependence. An extensive body of information,<sup>7</sup> particularly results from measurements from average capture spectra has been accumulated. A representative case is shown in Fig. 6 where the capture gamma-ray widths for Gd isotopes<sup>8</sup> are compared with the giant dipole resonance. The solid curve was calculated from the measured parameters for the giant dipole resonance, but the vertical scale has been adjusted to give the best fit with the data. The relative energy dependence is in good agreement with the prediction based on the giant resonance parameters, and clearly conflicts with the prediction of the single particle model. This agreement is typical of a wide range of nuclei and is a compelling reason

for not abandoning the Brink-Axel model in spite of its consistent overestimates of absolute values of  $\langle \Gamma_{\gamma i}(E1)/D \rangle$ .

The other aspect of the energy dependence which should be noted in this context is the evidence for a relatively localized but very dramatic variation in  $\langle \Gamma_{\gamma i}(E1)/D \rangle$  in the mass region Au-Pb. Bartholomew and co-workers in a recent review<sup>7</sup> report results of an extensive analysis of a wide range of data which establish that there is a sharp break in  $\langle \Gamma_{\gamma i}(E1) \rangle / D$  for nuclei in this mass range at about  $E_{\gamma} = 5$  MeV. Below this energy it appears that E1 transitions are severely inhibited.

Thus we find ourselves in something of a quandry as to how best to describe the electric dipole strength function. While the Brink-Axel model best describes the energy dependence, a somewhat retarded single particle estimate gives the more reasonable variation with atomic mass and better absolute values. I would suggest for the moment that we continue to rely on the giant dipole model. The accuracy of the data on E1 strength functions continues to improve. When existing data is parameterized in terms of this prediction, as in Fig. 4, the suggestion of a trend begins to emerge. Perhaps eventually the E1 strength function will be described satisfactorily in terms of a modified Brink-Axel model. In the meantime, the model does offer a convenient parameterization into which to cast the experimental data for use in the prediction and evaluation of gamma-ray production cross sections.

## VI. M1 Transitions.

Previous estimates<sup>9</sup> of the magnetic dipole strength function have been made by using Eq. 6 together with the observed ratio of the average widths for E1 and M1 transitions. Consequently the observation of structure in the E1 strength function or deviations from the Brink-Axel estimate, Eq. 2, will affect our estimates of the magnetic dipole strength function. If we restrict ourselves to measurements which establish absolute values, the information is indeed fragmentary. The results are shown in Fig. 7. For the most part the data are consistent with the earlier suggestion of Bollinger<sup>9</sup> that the photon strength function be approximated by  $18 \times 10^{-3}$ . This is roughly 10 to 20 times the single particle value. Strong evidence for enhancement above this value exists for the Pb isotopes, as a result of both electron scattering<sup>10</sup> and photoneutron measurements<sup>11</sup>. For <sup>207</sup>Pb the strength observed in the excitation region 7-8 MeV in the threshold photoneutron measurements are consistent with the existence of the giant M1 resonance resulting from the collective contributions of spin-flip transitions between the  $i_{13/2}$  and  $i_{11/2}$  neutron orbits and between the  $h_{11/2}$  and  $h_{9/2}$  proton orbits. There is also evidence for strong M1 transitions in the Ruthenium isotopes from recent resonance capture results of Chrien and co-workers<sup>12</sup> and evidence for an inhibition of M1 transitions in the Au-Ta region (see Fig. 7). However with the exception of the Pb isotopes, it has not been possible to establish a relationship between nuclear structure and observed values of the M1 strength function nor to justify the background value  $18 \times 10^{-3}$ , which characterizes many nuclei. A major objective of future work should be a systematic study of M1 strength over the periodic table and a search for significant departures from this background value.

## VII. Gamma Ray Production in $^{181}\text{Ta}$ ( $n, \gamma$ ).

I would like to finish by discussing briefly the application of data on photon strength functions to calculations of the gamma-ray production cross sections of  $^{181}\text{Ta}$ . It is clear from our discussion that for the present we must rely on the normalization and energy dependence of the photon strength function as measured for the same or neighboring nuclei in evaluating or predicting gamma-ray production cross sections. Fortunately measurements of average resonance capture have been made for Ta. Representative results<sup>13</sup> are shown in Fig. 8. The  $E^5$  energy dependence characteristic of the Brink-Axel model shown by the solid curves, is in accord with the spectra.

Unfortunately, to date, evaluations of gamma-ray production cross sections have been based on simple empirical evaporation models<sup>14</sup> whose relationship to more basic nuclear parameters remains obscure. However Bartholomew and co-workers<sup>7</sup> studied the implications of fast neutron gamma-ray production spectrum for  $^{181}\text{Ta}$  with regard to the photon strength function. Although it was not their intention, the analysis of such spectra in light of other more direct measurements of  $\langle \Gamma(E1) \rangle / D$  was already in a sense a data evaluation. They followed a fitting procedure which utilizes a dependence of level density on excitation energy adjusted to agree with values of the level spacing determined empirically just above the pairing gap ( $\sim 2$  MeV) and at threshold. A best fit to the data is obtained by varying the functional dependence of  $\langle \Gamma(E1) \rangle / D$ . Their results for 0.7 MeV neutrons are shown in Fig. 9 where it is compared with the calculated tail of the giant dipole resonance. The agreement with Brink-Axel hypothesis in this

case is excellent. However, the energy dependence  $E_\gamma < 2 \text{ MeV}$  must be excluded in their spectrum fitting procedure.

The statistical model evaporation codes under development by Gardner and co-workers<sup>15</sup> represent a much more ambitious attempt to calculate and evaluate gamma-ray production results. These routines calculate complete gamma-ray spectra as well as production cross sections. One of the principal difficulties to date has been that the calculated spectra do not show enough high energy gamma rays. Fig. 10 shows in the case of  $^{181}\text{Ta}$  the effect of replacing the usual Weisskopf estimate for E1 radiation by the Brink-Axel values. In addition, variations were made in the level density formula used. In this calculation, the full range of photon energies were fit. Although the results are still not satisfactory, the higher power energy dependence of the Brink-Axel model definitely does improve the fit into the experimental data. This work is in a continuing state of development, and I believe we can expect further improvement as our knowledge of the photon strength functions evolves and is applied to these calculations.

## REFERENCES

- <sup>1</sup> Blatt, J. M., Weisskopf, V. F., Theoretical Nuclear Physics, John Wiley & Sons, N. Y. (1952) and Wilkinson, D. H., Nuclear Spectroscopy, Part B (Ajzenberg-Selove, F., Ed.) Academic Press, N. Y. (1960) p. 852.
- <sup>2</sup> D. M. Brink, Doctoral Thesis, Oxford University (1955), unpublished.
- <sup>3</sup> P. Axel, Phys. Rev. 126, (1962) p. 671.
- <sup>4</sup> J. E. Lynn, The Theory of Neutron Resonances, Clarendon Press, Oxford (1968).
- <sup>5</sup> S. F. Mughabghab, in Proceedings of the Conference on the Study of Nuclear Structure with Neutrons, Budapest, 1972 (IUPAP, to be published).
- <sup>6</sup> R. E. Toohey and H. E. Jackson, Phys. Rev. C9, (1974) p. 346.
- <sup>7</sup> G. A. Bartholomew, E. D. Earle, A. J. Ferguson, J. W. Knowles, and M. A. Lone, Advances in Nuclear Physics 7, (Plenum Press, New York, 1974), p. 229.
- <sup>8</sup> L. M. Bollinger and G. E. Thomas, Phys. Rev. C2 (1970) p. 1951.
- <sup>9</sup> L. M. Bollinger, Proceedings of International Conference on Photonuclear Reactions and Applications, (USAEC Office of Information Services, Oak Ridge, 1973), p. 783.
- <sup>10</sup> L. Fagg, ref. 9, p. 663.
- <sup>11</sup> L. R. Medsker and H. E. Jackson, Phys. Rev. C9, (1974), p. 709.
- <sup>12</sup> K. Rimawii, J. B. Garg, R. E. Chrien, G. W. Cole, and O. A. Wasson, to be published.
- <sup>13</sup> L. M. Bollinger, J. R. Erskine, and G. E. Thomas, to be published.
- <sup>14</sup> R. J. Howerton, M. H. MacGregor, S. T. Perkins, UCRL-51306 (1972).
- <sup>15</sup> D. G. Gardner, private communication.
- <sup>16</sup> R. J. Carpenter, Argonne National Laboratory report ANL-6589 (1962).

## FIGURE CAPTIONS

- Fig. 1 Average Values of E1 reduced widths. The solid line is the prediction based on a normalization according to the dipole sum rule. The dotted line represents an arbitrary normalization.
- Fig. 2 Comparison of the square of the electric-dipole matrix element calculated from the single-particle estimate, dashed line, and an assumed Lorentz shape for the giant dipole resonance, solid curve (see reference 1).
- Fig. 3 Schematic representation of the Brink hypothesis. In the lower section the heavy horizontal arrows indicate the magnitude of the photon strength function,  $S$ ;
- Fig. 4 Average Values of the E1 transition strength. The solid curve is the prediction of the relationship due to Axel (ref. 3) given in eq. 6.
- Fig. 5 Schematic of the Valence Model of E1 transitions for  $^{91}\text{Zr}$ .
- Fig. 6 Relationship of the giant dipole resonance to the E1 widths (ref. 8).
- Fig. 7 Average Values of M1 reduced widths. The solid line is the empirical approximation suggested by Bollinger, (ref. 9).
- Fig. 8 Energy dependence of the average intensities of transitions to individual states in  $^{182}\text{Ta}$ . The dashed lines indicate the expected magnitude of Porter-Thomas fluctuations.
- Fig. 9 E1 reduced strength function for Ta according to Earle, Lane, and Bartholomew (ref. 7). The dotted curve represents the tail of the giant dipole resonance.
- Fig. 10 Calculated gamma-ray energy spectrum produced by 1 MeV neutrons on  $^{181}\text{Ta}$ , according to Gardner (ref. 15). Experimental data are indicated by open circles.

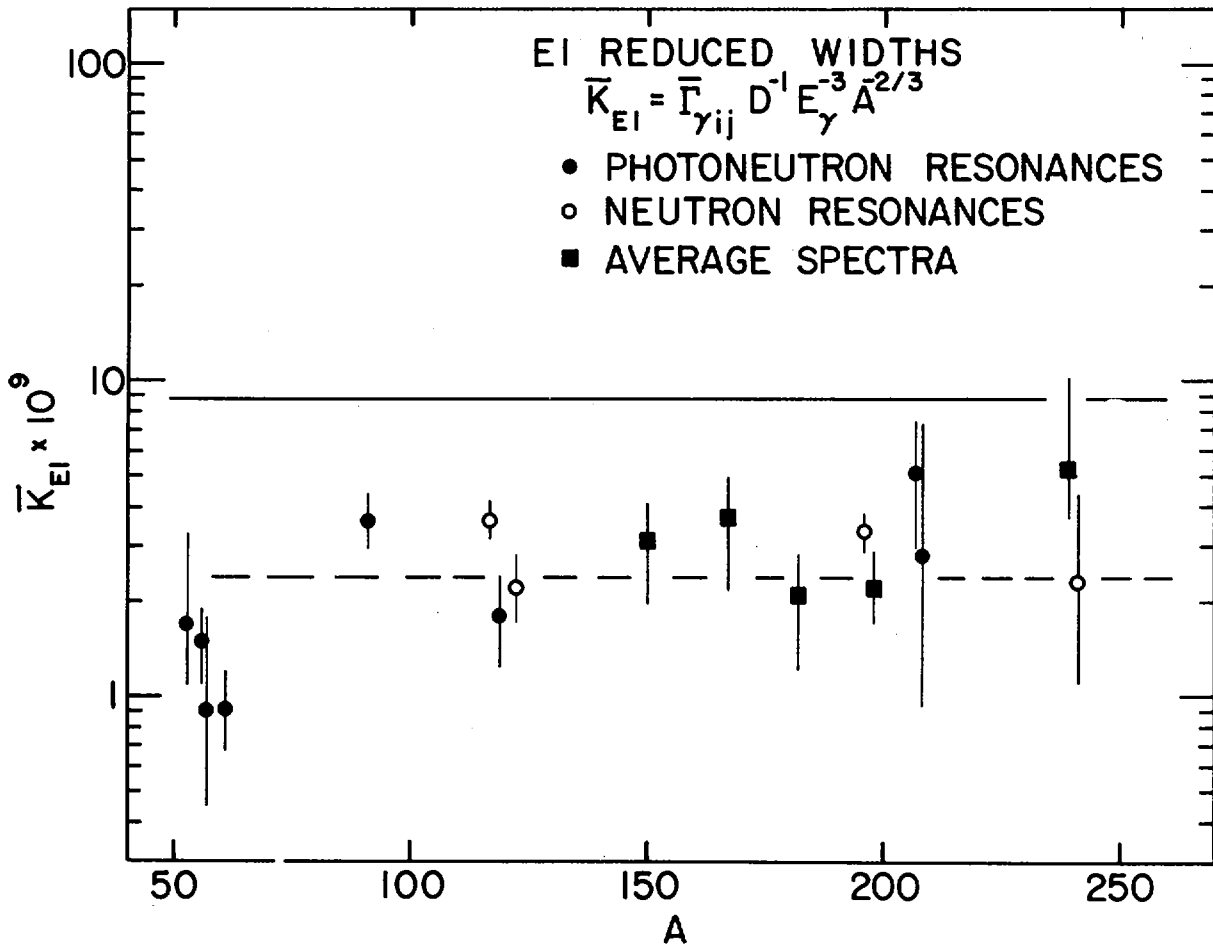


Fig. 1

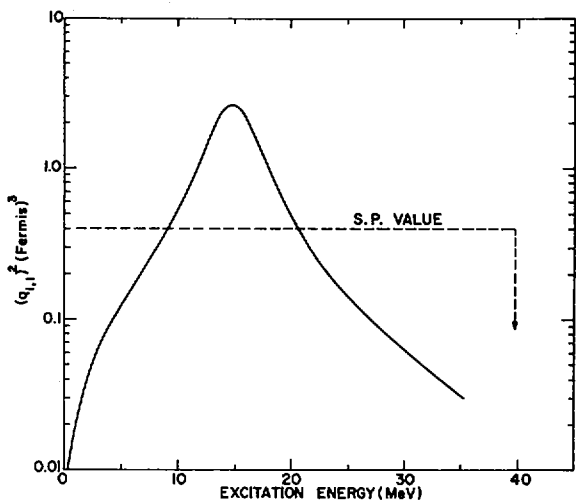


Fig. 2

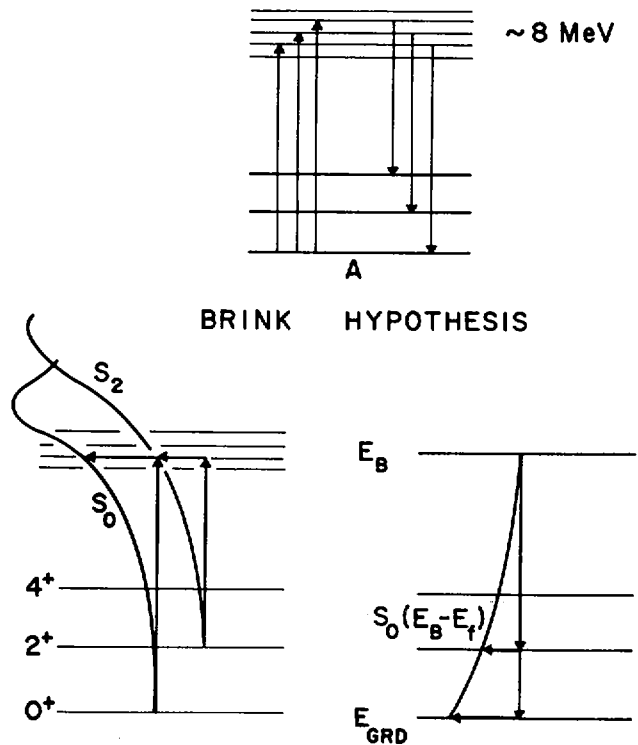


Fig. 3

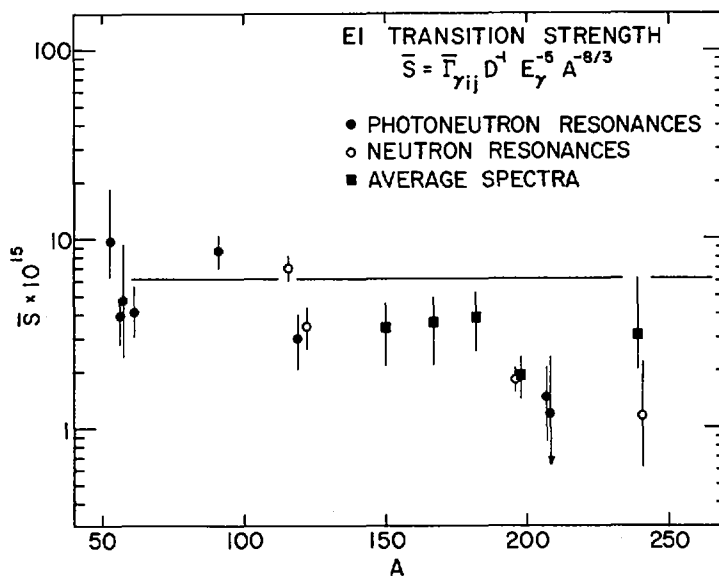


Fig. 4

VALENCE MODEL (LYNN)

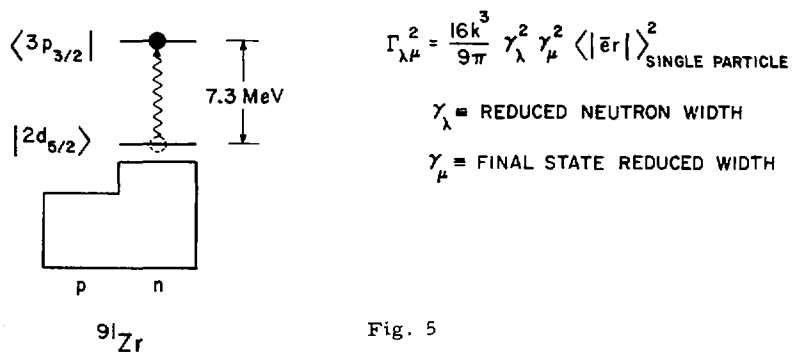


Fig. 5

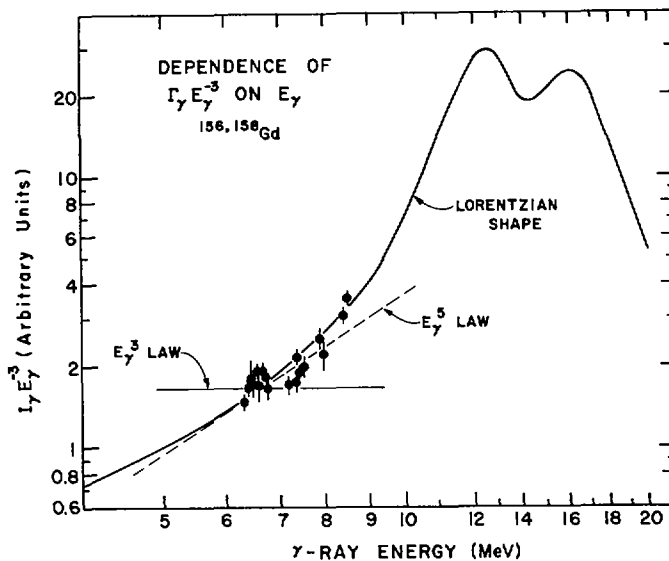


Fig. 6

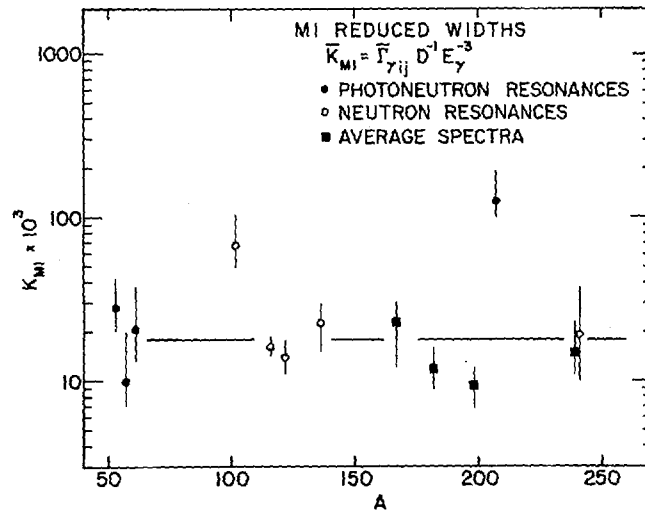


Fig. 7

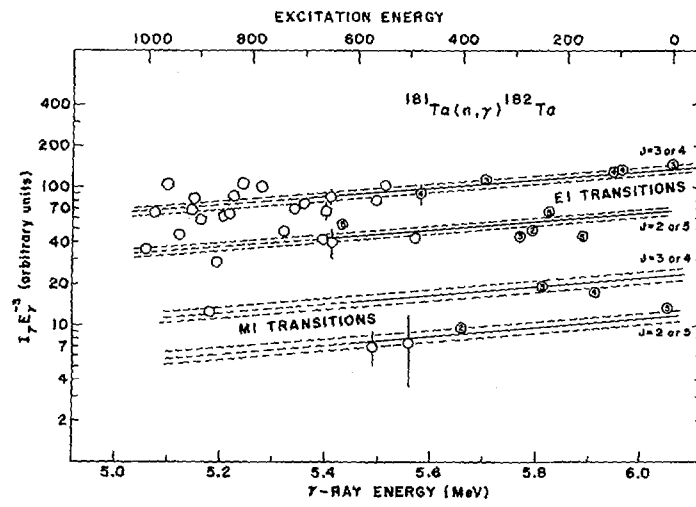


Fig. 8

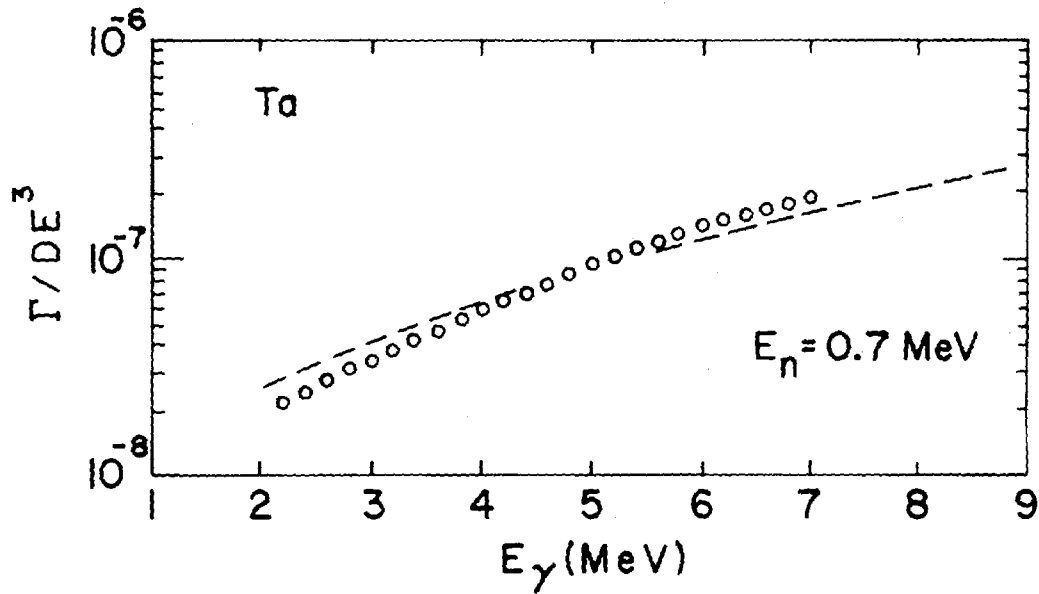


Fig. 9

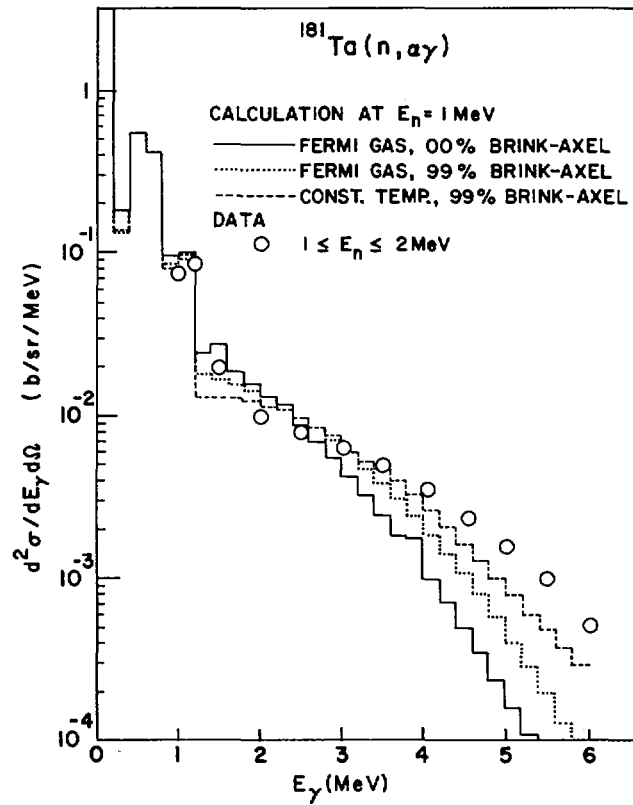


Fig. 10.

## DISCUSSION

R. E. CHRIEN: There has been considerable evidence for enhanced E-1 transition strength in the A=90 region. We have studied p-wave neutron capture and subsequent  $\gamma$ -decay in isotopes of Mo 92, 94, 96, 98 where the d5/2 shell is filling. These nuclides show strong E-1 strengths, considerably greater than predicted by either valence or giant dipole resonance models. Clearly the Brink hypothesis can only explain the photon strength function in some average sense. Considerable structure in photon strength is superposed on this giant resonance tail.

### II-3 Calculation of the Collective Radiative Capture Cross Sections for 5-20 MeV Neutrons

Hideo Kitazawa and Nobuhiro Yamamuro

Research Laboratory for Nuclear Reactors, Tokyo Institute  
of Technology, O-okayama, Meguroku, Tokyo, Japan

Abstract: A volume type particle-vibration coupling Hamiltonian in the collective radiative capture of fast neutrons is described in terms of the collective variables for density vibration. This Hamiltonian is compared with the ones of the surface and volume types, respectively given by Clement et al. and Longo and Saporetta. The closed neutron shell nuclei  $^{40}\text{Ca}$ ,  $^{88}\text{Sr}$ ,  $^{140}\text{Ce}$  and  $^{208}\text{Pb}$  are chosen for calculation of the capture cross section and capture  $\gamma$ -ray spectrum. The excitation curves for 5-20 MeV neutrons are calculated with these three Hamiltonians. Moreover the partial cross section for radiative capture to each neutron single particle state of  $^{209}\text{Pb}$  is obtained for 5-20 MeV neutrons, and the capture  $\gamma$ -ray spectra in  $^{40}\text{Ca}$ ,  $^{88}\text{Sr}$  and  $^{140}\text{Ce}$  for 14-MeV neutrons. Consequently it is concluded that in the giant dipole resonance energy region the profile of the capture  $\gamma$ -ray spectrum for the transitions to low lying states of a residual nucleus and the capture  $\gamma$ -ray yield are fairly well estimated by the collective capture model, using the volume coupling Hamiltonian and the reasonable isospin potential depth 90-130 MeV, with the exception of the rather small one for  $^{40}\text{Ca}$ . With the surface coupling Hamiltonian, however, a similar agreement between theory and experiment is obtained only when a much larger value than the experimentally predicted one is taken for the isospin potential depth.

## 1. Introduction

The radiative capture reactions by fast neutrons are interesting sources of information on the structure of the highly excited nuclear system. These reaction cross sections are indispensable nuclear data for design of a nuclear fusion reactor. Moreover, in the field of fast nuclear reactor technology there is the practical need for estimation of the  $\gamma$ -ray heating in the blanket of reactors. In this case it is necessary to obtain knowledge of the cross section and the  $\gamma$ -ray spectrum for the radiative neutron capture reaction, in the same manner as for fission and for inelastic scattering.

The radiative capture of low energy neutrons mainly takes place through the formation of a statistical compound nucleus. However, the statistical theory is unsatisfactory for understanding the mechanism of the radiative capture of neutrons with energies greater than about 5 MeV. The discrepancy between the theoretical and experimental results, generally speaking, is remarkable in the radiative capture reaction of 14-MeV neutrons by heavy nuclei. Lane and Lynn [1] suggested that the radiative capture of 14-MeV neutrons by heavy nuclei is dominated by a direct capture process. But, the calculation with this model gave a  $(p, \gamma)$  reaction cross section below 20 MeV that is too small by one order of magnitude [2]. To improve the situation a semi-direct and a collective capture model were proposed by Brown [3] and Clement et al. [4], respectively. The radiative capture cross section for 14-MeV neutrons of  $^{208}\text{Pb}$  has been calculated by these models [5]. The calculated cross section was smaller by a factor of 3 to 4 than the observed one. As a result it was considered that this discrepancy for the semi-direct capture model is due to the approximation in the schematic model and that the discrepancy for the collective capture model is due to the inadequacy of the particle-vibration coupling Hamiltonian of the surface type. On the other hand Longo and Saporetto [6] found an agreement between theory and experiment, using a volume coupling Hamiltonian.

In the present paper we give a volume type particle-vibration coupling Hamiltonian which is described in terms of the

collective variables for density vibration in the nuclear hydrodynamic model. This Hamiltonian is compared with the ones given by Clement et al. and Longo and Saporetti. Moreover the validity of the collective capture model is investigated for the radiative neutron capture reaction. The depth of the isospin dependent part of an optical potential, that is the strength of particle-vibration coupling, is also predicted from analyses of the capture  $\gamma$ -ray spectra for  $^{40}\text{Ca}$ ,  $^{88}\text{Sr}$ ,  $^{140}\text{Ce}$  and  $^{208}\text{Pb}$ .

2. Theoretical foundation

In the case of the target spin 0 we calculate the radiative neutron capture cross section and capture  $\gamma$ -ray spectrum by means of the direct and collective capture models. The direct capture process is an electric dipole radiative transition of an incident nucleon from its free state in the nucleon potential field to an unfilled single particle bound state of a target nucleus. In the collective capture process the incident nucleon and the target nucleus interact to give an intermediate state, in which the former is in a single particle bound state, while the latter is excited to its giant electric dipole state. The target nucleus then decays by an electric dipole radiation. The schematic interpretation for these processes is given in Fig. 1.

The matrix element of an electric dipole transition for the radiative capture process is given by

$$\langle T_{fi} = \psi_f | \epsilon^n | \tilde{\psi}_i^{(+)} \rangle + \frac{\langle \psi_f | \epsilon^t | \psi_{int} \rangle \langle \psi_{int} | H' | \tilde{\psi}_i^{(+)} \rangle}{\epsilon_{ij_i} - \epsilon_{fj_f} - E_R + \frac{1}{2} i \Gamma_R}, \quad (1)$$

where  $\tilde{\psi}_i^{(+)}$ ,  $\psi_{int}$  and  $\psi_f$  are the initial, intermediate and final state wave functions,  $E_R$  and  $\Gamma_R$  are the giant dipole resonance energy of a target nucleus and its width,  $\epsilon_{ij_i}$  and  $\epsilon_{fj_f}$  are the initial and final state energies of an incident neutron, and  $\epsilon^n$  and  $\epsilon^t$  are the incident neutron and target parts of an electric dipole operator. The particle-vibration coupling Hamiltonian  $H'$  couples the incident nucleon to the giant electric dipole state of the target nucleus. The first and second terms describe the direct and collective capture processes, respectively.

Clement et al. [4] have shown that the effective particle-vibration coupling Hamiltonian for the dipole mode which leaves the charge of the incident particle unchanged is given by

$$H' = \frac{3}{2\pi} \frac{NZ}{A} P^{10}_h(r) \frac{\mathbf{r} \cdot \boldsymbol{\eta}}{|\mathbf{r}|} \tau_3 \quad (2)$$

with

$$h(r) = \frac{\langle 1 | A_{1\mu}(r) | 0 \rangle}{\langle 1 | \alpha_{1\mu} | 0 \rangle}, \quad (3)$$

$$A_{1\mu}(r) = \int \rho Y_{1\mu}(\Omega) d\Omega, \quad (4)$$

$$\rho = \sum_i \tau_3 \delta(r-r_i), \quad (5)$$

where A, N and Z are the mass, neutron and proton numbers of the target nucleus,  $P^{10}$  is the strength of the isospin dependent two body force between the incident particle and the target nucleons,  $r$  and  $r_i$  are the position vectors of the incident particle and the target nucleons,  $\eta$  is the separation vector of the centroids of the neutron and proton systems, and  $\tau_3$  is the z-component of the isospin of an incident nucleon. The vectors  $|0\rangle$  and  $|1\rangle$  are the ground and giant dipole states of the target nucleus, and  $\alpha_{1\mu}$  are the collective coordinates. The function  $h(r)$  is the radial form factor of the coupling Hamiltonian and normalized as

$$\int h(r)r^3 dr = 1. \quad (6)$$

Using Eq. (2), Clement et al. [4] have introduced the particle-vibration coupling Hamiltonian of the surface type, hereafter referred to as "S", as follows:

$$H' = \left(\frac{v_1}{4}\right)^2 \frac{NZ}{A^2} \left(-\frac{df(r)}{dr}\right) \frac{r \cdot \eta}{|r|} \tau_3, \quad (7)$$

where  $v_1$  is the strength of particle vibration coupling and  $f(r)$  is the distribution function of the nucleon density. The coupling strength is related to the isospin dependent part of an optical potential, which is given by

$$V_1(r) = \frac{1}{2A} (\tau \cdot T) v_1 f(r), \quad (8)$$

where  $\tau$  and  $T$  are the incident nucleon and target isospins.

Here, we introduce a coupling Hamiltonian with a form factor of the volume type. In the hydrodynamic picture [7] the proton and neutron densities are given by

$$\rho_p = \bar{\rho}_p (1 + \delta), \quad (9)$$

$$\rho_n = \bar{\rho}_n (1 - \frac{Z}{N} \delta), \quad (10)$$

$$\bar{\rho} = \bar{\rho}_p + \bar{\rho}_n, \quad (11)$$

where  $\bar{\rho}_p$  and  $\bar{\rho}_n = (N/Z)\bar{\rho}_p$  are the proton and neutron equilibrium densities, and  $\delta$  is the fluctuating part of the density. The fluctuating density for a dipole mode is given by

$$\delta = \sum_{\mu} F_D j_1(k_D r) \alpha_{1\mu} Y_{1\mu}^*(\Omega) \quad (12)$$

with  $k_D = 2.0815/R$ , where  $F_D$  is the normalization constant,  $j_1(k_D r)$  is the spherical Bessel function,  $k_D$  is the wave number for the vibration of a dipole mode,  $R$  is the nuclear radius in fm, and  $\alpha_{1\mu}$  are the collective coordinates.

In Eq. (5), we approximate the nucleon density operator by the local isovector density

$$\rho = \rho_p - \rho_n. \quad (13)$$

Consequently the radial form factor is given by

$$h(r) = F_D \bar{\rho} j_1(k_D r) S(r), \quad (14)$$

where

$$S(r) = \begin{cases} 1 & r \leq R \\ 0 & r > R \end{cases}.$$

From Eqs. (2), (6) and (14), the volume coupling Hamiltonian, hereafter referred to as "V-1", is given by

$$H' = \left(\frac{v_1}{4}\right) 2 \frac{NZ}{A^2} K j_1(k_D r) S(r) \frac{\mathbf{r} \cdot \boldsymbol{\eta}}{|\mathbf{r}|^3} \quad (15)$$

with  $K = 9.931/R$ .

The dipole operators [4] are given by

$$\epsilon_{1\mu}^n = e_f r Y_{1\mu}(\Omega), \quad (16)$$

$$\epsilon_{1\mu}^t = \text{const.} + e \left( \frac{3}{4\pi} \right)^{\frac{1}{2}} \frac{NZ}{A} \eta_z, \quad (17)$$

where  $e_f$  is the effective charge ( $-Ze/A$  for a neutron,  $Ne/A$  for a proton). The sum-rule for the dipole operator[8] in the case when the transitions are concentrated in one state is given by

$$E_R \langle 1 | \eta_z | 0 \rangle^2 = \frac{A}{NZ} \frac{\hbar^2}{2M} (1 + 0.8x), \quad (18)$$

where  $x$  is the exchange force factor and taken to be 0.5.

On the other hand Longo and Saporetti[6] proposed the volume coupling Hamiltonian, hereafter referred to as "V-2", as follows:

$$H' = \left( \frac{3}{4\pi} \right)^{\frac{1}{2}} v_1 \frac{\pi}{A \langle r^2 \rangle} \text{rf}(r) \frac{\mathbf{r} \cdot \boldsymbol{\alpha}}{|\mathbf{r}|} \tau_3, \quad (19)$$

where  $\langle r^2 \rangle$  is the mean square distance of the nucleon's centre-of-mass from the nucleus' centre-of-mass. They calculated the matrix element between the ground and giant dipole states by using the non-energy weighted sum-rule

$$\langle 0 | \alpha^2 | 0 \rangle = \tilde{\alpha} \frac{A}{4\pi} \langle r^2 \rangle, \quad (20)$$

where  $\tilde{\alpha}$  is the reduction factor which takes into account the ground state correlation and estimated from the isospin splitting of the giant dipole resonance. In the next section we investigate on the validity of these coupling Hamiltonians S, V-1 and V-2.

## 3. Calculations and discussions

The closed neutron shell nuclei  $^{40}\text{Ca}$ ,  $^{88}\text{Sr}$ ,  $^{140}\text{Ce}$  and  $^{208}\text{Pb}$  are chosen for calculation of the capture cross section and capture  $\gamma$ -ray spectrum. The neutron single particle states in these nuclei are clear so that they are suitable for investigating the validity of the collective capture model. The initial state wave function is obtained with the optical potential

$$U(r) = -Vf(r) - iWg(r) - V_{so}h(r)(\ell \cdot \sigma), \quad (21)$$

where

$$f(r) = \left[ 1 + \exp\left(\frac{r-R}{a}\right) \right]^{-1},$$

$$g(r) = -4b \frac{d}{dr} \left[ 1 + \exp\left(\frac{r-R}{b}\right) \right]^{-1},$$

$$h(r) = -\lambda \pi^2 \frac{1}{r} \frac{d}{dr} f(r),$$

$$R = r_0 A^{\frac{1}{3}}.$$

The potential parameters  $V$ ,  $W$ ,  $V_{so}$ ,  $a$ ,  $b$  and  $r_0$  are taken from the work of Rosen et al. [9]. The final state wave function is obtained with the nucleon potential of the Wood-Saxon type

$$V(r) = -V_{n\ell j} f(r) - V_{so} h(r)(\ell \cdot \sigma), \quad (22)$$

where  $n$ ,  $\ell$  and  $j$  are the quantum numbers of a neutron single particle state. The radial dependence of the functions  $f(r)$  and  $h(r)$  are taken to be the same as in the optical potential  $U(r)$ . The depth of the central part of the nucleon potential is adjusted to give the observed value of the binding energy for the particular single particle state. The spin-orbit coupling potential is determined to give the experimentally obtained energy splitting of the centre of gravity of the neutron single particle levels  $j=\ell-1/2$  and  $j=\ell+1/2$ .

The giant dipole resonance energy and its width for the target nuclei are taken from the experiments of photo-nuclear reactions [10] and listed in Table 1. The resonance parameters of  $^{141}\text{Pr}$

are used for  $^{140}\text{Ce}$ . The reduction factors  $\tilde{\alpha}$  for  $^{88}\text{Sr}$ ,  $^{140}\text{Ce}$  and  $^{208}\text{Pb}$  are taken from the evaluation by Leonardi[11] and the one for  $^{40}\text{Ca}$  is calculated with the pure harmonic oscillator model.

### 3.1 $^{208}\text{Pb}(n,r)^{209}\text{Pb}$ reaction

The radiative capture cross sections of  $^{208}\text{Pb}$  for 5-20 MeV neutrons are calculated with three Hamiltonians V-1, V-2 and S. The spin-orbit coupling potential depth is determined from the energy splitting of the g-state. This value is taken to be 5.9 MeV for all final state wave functions. The characteristics of the neutron single particle states of  $^{209}\text{Pb}$  are taken from the study of the (d,p) reaction of  $^{208}\text{Pb}$ [12]. The spectroscopic factors of all states except for the  $j_{15/2}$  state are assumed 1.0. The one for the  $j_{15/2}$  state is taken to be 0.6.

The total and partial radiative capture cross sections are shown in Figs. 2-6. The solid, dashed and dot-dashed curves are calculated with the Hamiltonians V-1, V-2 and S, respectively. The calculated cross sections are compared with the observed ones[13,14] for 7-15 MeV neutrons. The isospin potential depth is so determined that the total capture cross section calculated for higher energy neutrons than the resonance energy agrees with the observed one. The quantities  $v_1$  are obtained to be 130 MeV for V-1, 110 MeV for V-2, and 240 MeV for S. It is not clear which radial form factor is the most suitable. However, the isospin potential depth obtained with the volume coupling Hamiltonian, V-1 or V-2, is consistent with the one predicted by Greenlees and Pyle[15]. It seems that the disagreement between the calculated and observed cross sections for 7-9 MeV neutrons should be removed by taking a contribution of the statistical process to this reaction into consideration.

### 3.2 $^{140}\text{Ce}(n,r)^{141}\text{Ce}$ reaction

The spin-orbit coupling potential depth is determined from the energy splitting of the p-state to be 10.3 MeV. The characteristics of the neutron single particle states of  $^{141}\text{Ce}$  are taken from the study of the (d,p) reaction of  $^{140}\text{Ce}$ [16]. The

spectroscopic factors of all states are assumed to be 1.0. The energy of the  $f_{5/2}$  state is calculated with the potential depth determined for the  $f_{7/2}$  state. Although the  $i_{13/2}$  state is not identified by the (d,p) experiment, it is included in the calculation; the state is probable in the experiment and expected by the shell model. The energy of the state is taken from the work of Rigaud et al.[17].

The capture  $\gamma$ -ray spectrum for  $^{140}\text{Ce}$  with 14-MeV neutrons and the excitation curve are shown in Figs. 7-8. The isospin potential depth is so determined that the observed capture  $\gamma$ -ray spectrum[17] for the transitions to low lying states of  $^{141}\text{Ce}$  agree with the one predicted by the theory. The quantities  $v_1$  are obtained to be 100 MeV for V-1, 90 MeV for V-2, and 190 MeV for S. A disagreement between theory and experiment is remarkable for the lower energy  $\gamma$ -ray spectrum. As reasons of this disagreement, there are three possibilities; firstly that is due to the contribution of the inelastic scattering  $\gamma$ -rays resulted in the energy broadening of  $\gamma$ -rays in a detector, secondly due to the contribution of other reaction mechanisms, and finally due to neglecting the highly excited single particle states.

### 3.3 $^{88}\text{Sr}(n,\gamma)^{89}\text{Sr}$ reaction

The spin-orbit coupling potential depth is determined from the splitting of the d-state to be 5.9 MeV. The characteristics of the neutron single particle states of  $^{89}\text{Sr}$  are taken from the study of the (d,p) reaction of  $^{88}\text{Sr}$ [18] and from the study of the (p,p) and (p,p') reactions of  $^{88}\text{Sr}$ [19]. The spectroscopic factors of all states are assumed to be 1.0. The  $h_{11/2}$  state is included in the calculation, though this state is not observed by the (d,p) reaction, as it is expected by the shell model. The energy of the state is taken from the work of Rigaud et al. [20]. The capture  $\gamma$ -ray spectrum for  $^{88}\text{Sr}$  with 14-MeV neutrons and the excitation curve are shown in Figs. 9-10. The isospin potential depths are 110 MeV for V-1, 100 MeV for V-2, and 250 MeV for S.

3.4  $^{40}\text{Ca}(n,\gamma)^{41}\text{Ca}$  reaction

The spin-orbit coupling potential depth is determined from the splitting of the p-state to be 7.5 MeV. The characteristics of the neutron single particle states of  $^{41}\text{Ca}$  are taken from the study of the (d,p) reaction of  $^{40}\text{Ca}$ [21]. The energy of the  $f_{5/2}$  state nearly agrees with the value predicted by using the energy splitting between the  $p_{3/2}$  and  $p_{1/2}$  states and by assuming the  $f_{7/2} - f_{5/2}$  splitting to be proportional to  $(2l+1)$ [22]. Since this state is difficult to observe by (d,p) experiments, it is probable that some weak  $f_{5/2}$  states are missed[21]. The spectroscopic factor of the  $f_{5/2}$  state is therefore assumed to be 1.0, even though it is observed to be 0.5. The  $g_{9/2}$  state is not clearly observed by the experiment. However, this state is expected by the experiment or by the shell model.

The capture  $\gamma$ -ray spectrum for  $^{40}\text{Ca}$  with 14-MeV neutrons and the excitation curve are shown in Figs. 11-12. The isospin potential depths are obtained to be 40 MeV for V-1, 35 MeV for V-2, and 80 MeV for S. A disagreement between theory and experiment is remarkable for higher excitation than about 3 MeV in  $^{41}\text{Ca}$ . From a preliminary calculation we obtained a result that this situation was fairly improved by including a contribution of the statistical process.

## 4. Concluding remarks

The depth of the isospin dependent potential for  $^{40}\text{Ca}$ ,  $^{88}\text{Sr}$ ,  $^{140}\text{Ce}$  and  $^{208}\text{Pb}$  has been obtained from the analysis of radiative neutron capture reactions by the collective capture model. The results are shown in Table 2. These quantities obtained with the volume coupling Hamiltonian are in the range of 90-130 MeV, except for the rather small one for  $^{40}\text{Ca}$ , and consistent with the values derived from different analyses. Consequently it is concluded that in the giant dipole resonance energy region the profile of the capture  $\gamma$ -ray spectrum for the transitions to low lying states of a residual nucleus and the capture  $\gamma$ -ray yield are fairly well estimated by the collective capture model and with the volume coupling Hamiltonian, V-1 or V-2. However, higher resolution measurements of capture  $\gamma$ -ray spectra are necessary for the detailed check of the radial dependence of the coupling Hamiltonian.

## References

- [1] A. M. Lane and J. E. Lynn, Nuclear Phys. 11 (1959) 646.
- [2] P. J. Daly, A. M. Lane and J. R. Rook, Nuclear Phys. 56 (1964) 331.
- [3] G. E. Brown, Nuclear Phys. 57 (1964) 339.
- [4] C. F. Clement, A. M. Lane and J. R. Rook, Nuclear Phys. 66 (1965) 273.
- [5] H. Kitazawa, JAERI-1228 (in Japanese); H. Kitazawa, S. Karashima, K. Koyama, K. Sakurada and N. Yamamuro, Bull. Tokyo Inst. Tech. 116 (1973) 11.
- [6] G. Longo and F. Saporetti, Physics Lett. 42B (1972) 17.
- [7] J. M. Eisenberg and W. Greiner, Nuclear Models, Vol. 1 (North-Holland Publ. Co., Amsterdam, 1970) Chap. 10.
- [8] J. S. Levinger and H. A. Bethe, Phys. Rev. 78 (1950) 115.
- [9] L. Rosen, J. G. Beery, A. S. Goldhaber and E. M. Auerbach, Ann. of Phys. 34 (1965) 96.
- [10] R. R. Harvery, J. T. Caldwell, R. L. Bramblett and S. C. Fultz, Phys. Rev. 136 (1964) B126; J. M. Wyckoff,

- B. Ziegler, H. W. Koch and R. Uhlig, Phys. Rev. 137 (1965) B576; A. Leptretre, H. Beil, R. Bergere, P. Carlos, A. Veyssiere and M. Sugawara, Nuclear Phys. A175 (1971) 609; P. F. Yergin and B. T. Fabricand, Phys. Rev. 104 (1956) 1334.
- [11] R. Leonardi, Phys. Rev. Letters 28 (1972) 836.
- [12] C. Ellegaard, J. Kantele and P. Vedelsby, Nuclear Phys. A129 (1969) 113.
- [13] I. Bergqvist, D. M. Drake and D. K. Mcdaniels, Nuclear Phys. A191 (1972) 641.
- [14] J. Csikai, G. Petö, M. Buczkó, Z. Miligy and N. A. Eissa, Nuclear Phys. A95 (1967) 229.
- [15] G. W. Greenlees and G. J. Pyle, Phys. Rev. 149 (1966) 836.
- [16] R. H. Fulmer, A. L. McCarthy and B. L. Cohen, Phys. Rev. 128, (1962) 1302.
- [17] F. Rigaud, J. L. Irigaray, G. Y. Petit, G. Longo and F. Saporetti, Nuclear Phys. A176 (1971) 545.
- [18] E. R. Cosman, H. A. Enge and A. Sperduto, Phys. Rev. 165 (1968) 1175.
- [19] E. R. Cosman, J. M. Joyce and S. M. Shafroth, Nuclear Phys. A108 (1968) 519.
- [20] F. Rigaud, J. Roturier, J. L. Irigaray, G. Y. Petit, G. Longo and F. Saporetti, Nuclear Phys. A154 (1970) 243.
- [21] T. A. Belote, A. Sperduto and W. W. Buechner, Phys. Rev. 139 (1965) B80.
- [22] B. L. Cohen, P. Mukherjee, R. H. Fulmer and A. L. McCarthy, Phys. Rev. 127 (1962) 1678.
- [23] F. Cvelbar and A. Hudoklin, Nuclear Phys. A159 (1970) 555.

## Table captions

- Table 1 Giant dipole resonance parameters and reduction factors used in calculations.
- Table 2 Depth of the isospin dependent part of an optical potential obtained with three Hamiltonians V-1, V-2 and S.

## Figure captions

- Fig. 1 Schematic interpretation for the direct and collective capture processes. The quantum numbers  $n$ ,  $\ell$  and  $j$  characterize the single particle state of a captured neutron.
- Fig. 2 Total cross section for the  $^{208}\text{Pb}(n,\gamma)^{209}\text{Pb}$  reaction. Experimental points of the closed circle are taken from the work of Bergqvist et al.[13]. These points are obtained by the spectrum method, that is by integrating  $\gamma$ -rays with energies higher than the incident neutron energy. Experimental points of the open circle are taken from the work of Csikai et al.[14] and obtained with the activation method. The solid, dashed and dot-dashed curves are calculated with the Hamiltonians V-1, V-2 and S, respectively.
- Fig. 3 Total cross section for the  $\gamma$ -ray transition to the  $g_{9/2}$  ground state of  $^{209}\text{Pb}$ . Experimental points are taken from the work of Bergqvist et al.[13]. The solid, dashed and dot-dashed curves are calculated with the Hamiltonians V-1, V-2 and S, respectively.
- Fig. 4 Total cross section for the  $\gamma$ -ray transition to the  $i_{11/2}$  state of  $^{209}\text{Pb}$ . Experimental points are taken from the work of Bergqvist et al.[13]. The solid, dashed and dot-dashed curves are calculated with the Hamiltonians V-1, V-2 and S, respectively.
- Fig. 5 Total cross section for the  $\gamma$ -ray transitions to the  $i_{15/2}$  and  $d_{5/2}$  states of  $^{209}\text{Pb}$ . Experimental points are taken from the work of Bergqvist et al.[13].

The solid, dashed and dot-dashed curves are calculated with the Hamiltonians V-1, V-2 and S, respectively.

- Fig. 6 Total cross section for the  $\gamma$ -ray transitions to the  $g_{7/2}$  and  $d_{3/2}$  states of  $^{209}\text{Pb}$ . Experimental points are taken from the work of Bergqvist et al.[13]. The solid, dashed and dot-dashed curves are calculated with the Hamiltonians V-1, V-2 and S, respectively.
- Fig. 7 Spectrum of  $\gamma$ -rays from the radiative capture of 14.06-MeV neutrons by  $^{140}\text{Ce}$ . Experimental points are taken from the work of Rigaud et al.[17]. The solid, dashed and dot-dashed curves are calculated with the Hamiltonians V-1, V-2 and S, respectively. The arrows indicate the centres of gravity of neutron single particle levels in  $^{141}\text{Ce}$ . Gauss distribution with FWHM=2 MeV is used as the response function of a  $\gamma$ -ray detector.
- Fig. 8 Total cross section for the  $^{140}\text{Ce}(n,\gamma)^{141}\text{Ce}$  reaction. An experimental point is taken from the work of Rigaud et al.[17]. The solid, dashed and dot-dashed curves are calculated with the Hamiltonians V-1, V-2 and S, respectively.
- Fig. 9 Spectrum of  $\gamma$ -rays from the radiative capture of 14.06-MeV neutrons by  $^{88}\text{Sr}$ . Experimental points are taken from the work of Rigaud et al.[20]. The solid, dashed and dot-dashed curves are calculated with the Hamiltonians V-1, V-2 and S, respectively. The arrows indicate the centres of gravity of neutron single particle levels in  $^{89}\text{Sr}$ . Gauss distribution with FWHM=2 MeV is used as the response function of a  $\gamma$ -ray detector.
- Fig. 10 Total cross section for the  $^{88}\text{Sr}(n,\gamma)^{89}\text{Sr}$  reaction. An experimental point is taken from the work of Rigaud et al.[20]. The solid, dashed and dot-dashed curves are calculated with the Hamiltonians V-1, V-2 and S, respectively.
- Fig. 11 Spectrum of  $\gamma$ -rays from the radiative capture of 14-MeV neutrons by  $^{40}\text{Ca}$ . Experimental points are taken from the work of Cvelbar and Hudoklin[23]. The solid, dashed and dot-dashed curves are calculated with the Hamiltonians V-1, V-2 and S, respectively. The arrows

indicate the centres of gravity of neutron single particle levels in  $^{41}\text{Ca}$ . Gauss distribution with FWHM=2 MeV is used as the response function of a  $\gamma$ -ray detector.

Fig. 12 Total cross section for the  $^{40}\text{Ca}(n,\gamma)^{41}\text{Ca}$  reaction. The solid, dashed and dot-dashed curves are calculated with the Hamiltonians V-1, V-2 and S, respectively.

Table 1

	$E_R$ (MeV)	$\Gamma_R$ (MeV)	$\bar{\alpha}$
$^{40}\text{Ca}$	19.8	4.50	0.50
$^{88}\text{Sr}$	16.7	4.20	0.35
$^{140}\text{Ce}$	15.4	3.90	0.27
$^{208}\text{Pb}$	13.6	3.78	0.24

Table 2

	$v_1$ (MeV)		
	V-1	V-2	S
$^{40}\text{Ca}$	40	35	80
$^{88}\text{Sr}$	110	100	250
$^{140}\text{Ce}$	100	90	190
$^{208}\text{Pb}$	130	110	240

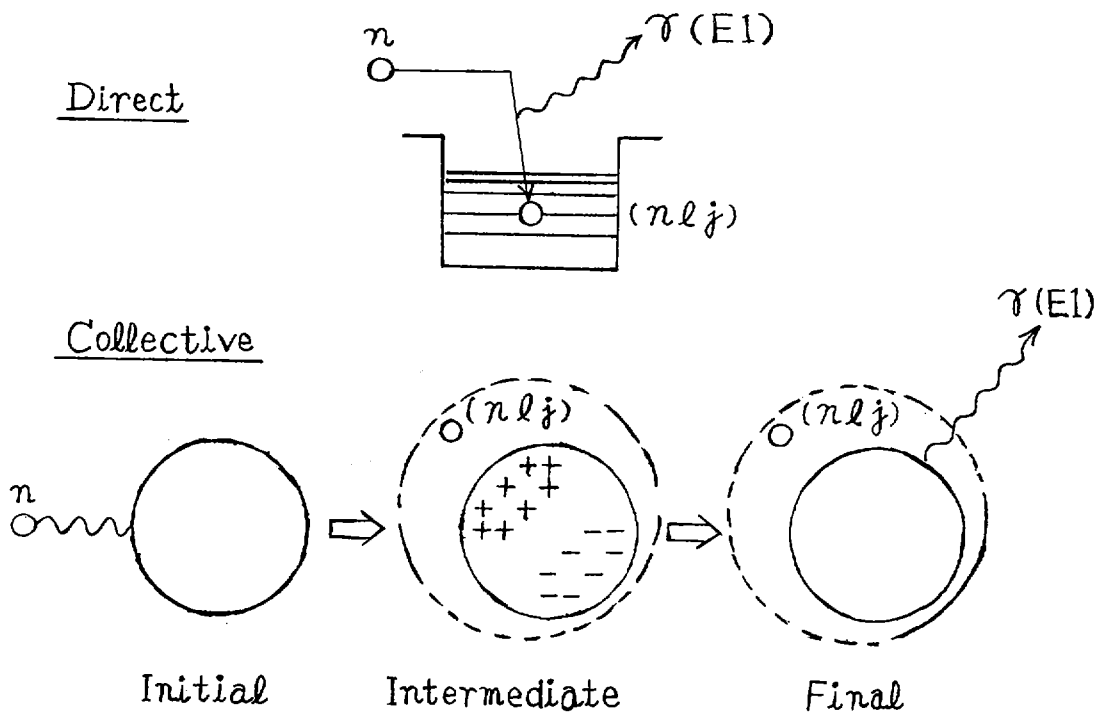


Fig. 1

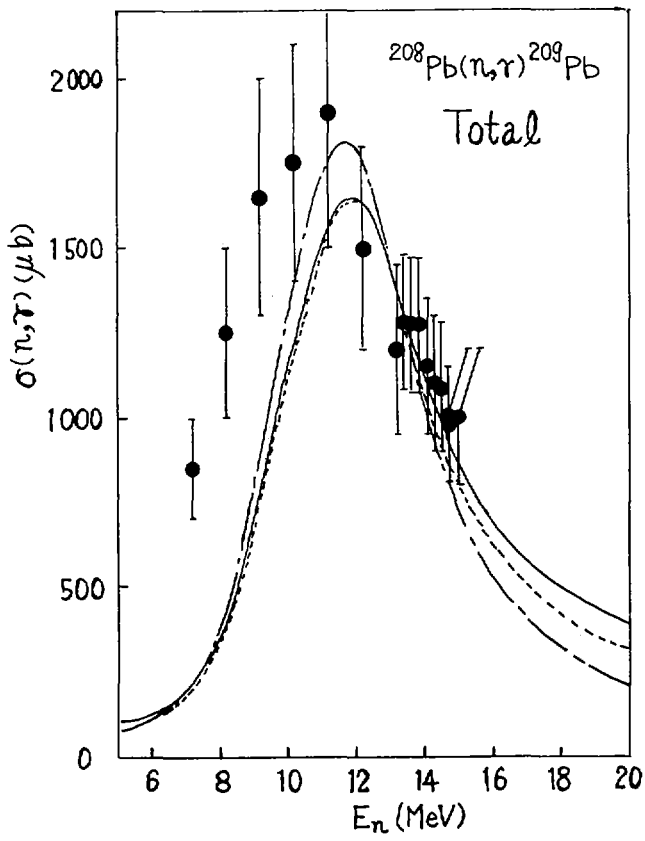


Fig. 2

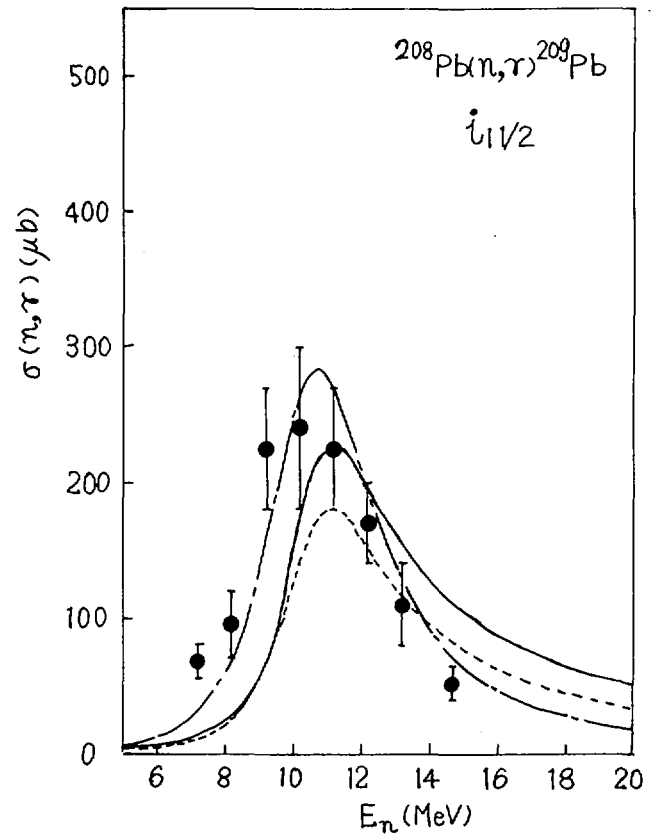


Fig. 4

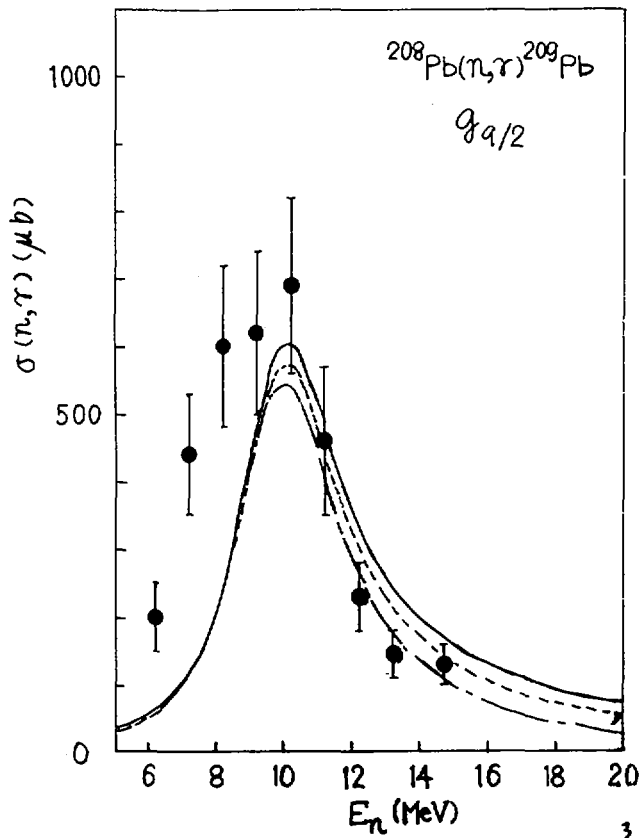


Fig. 3

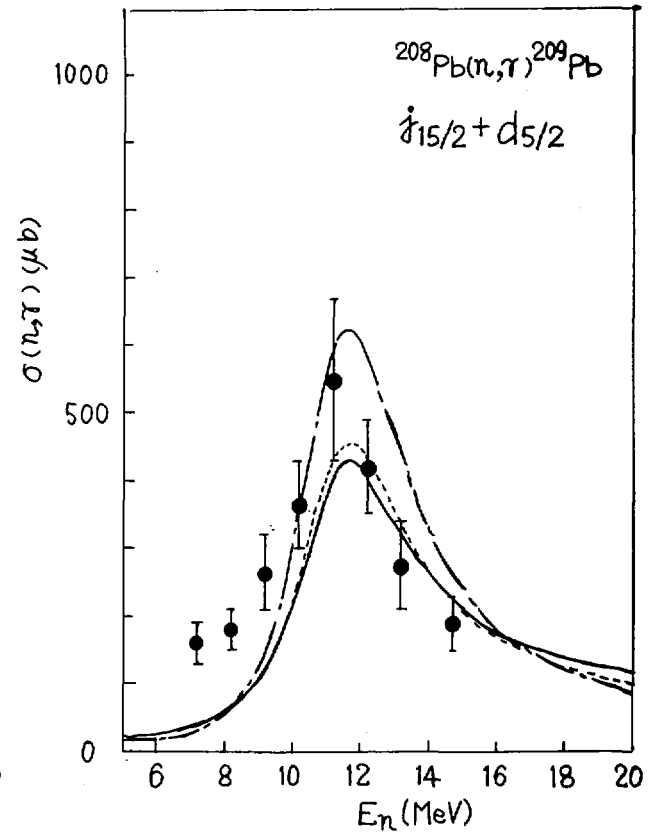


Fig. 5

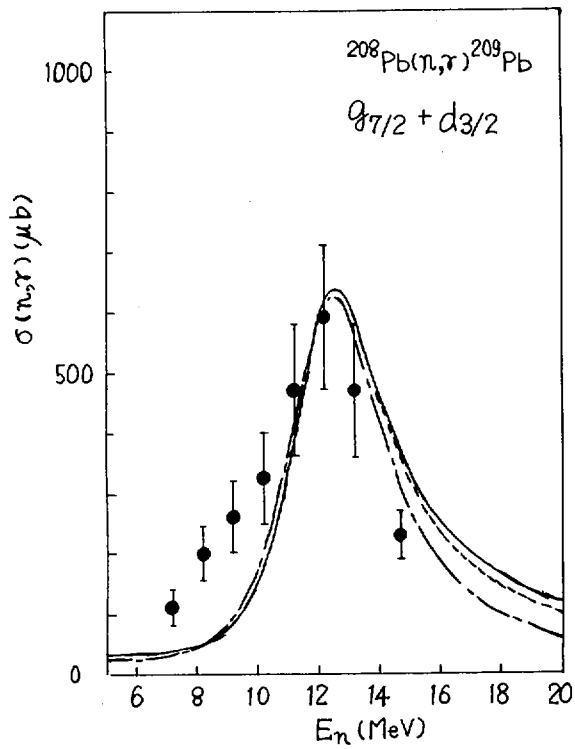


Fig. 6

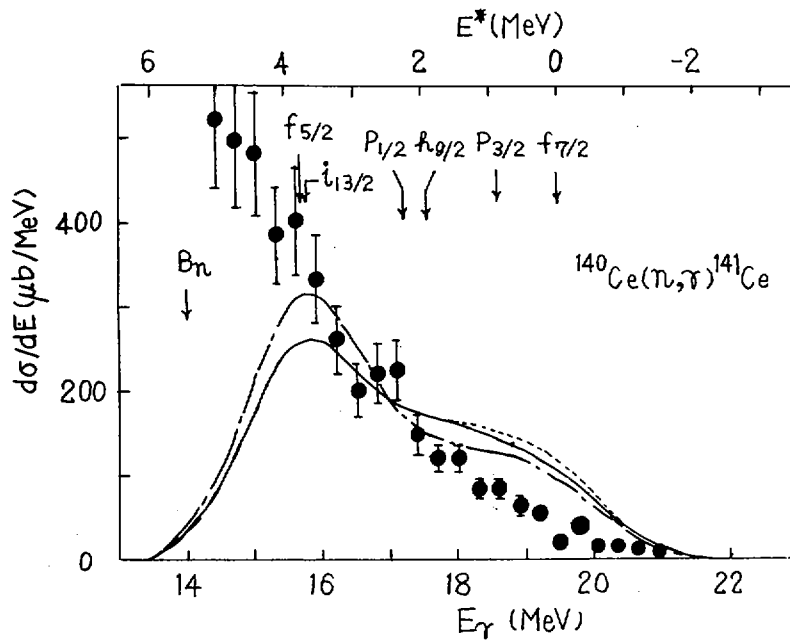


Fig. 7

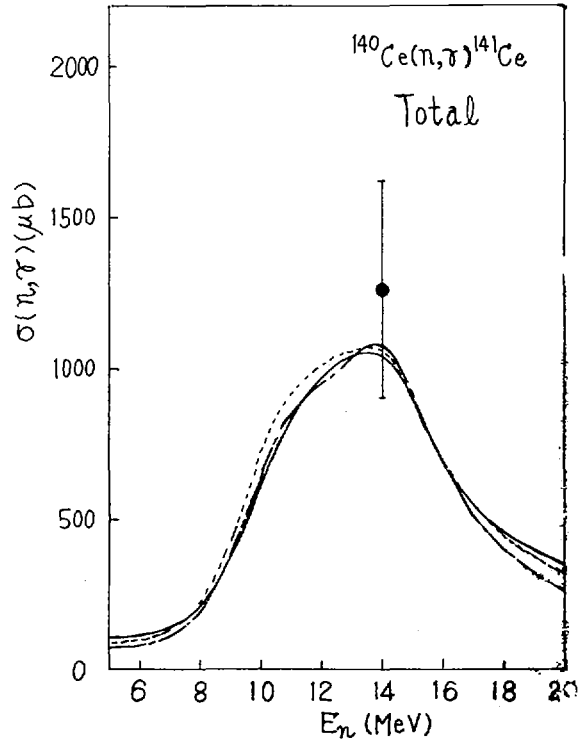


Fig. 8

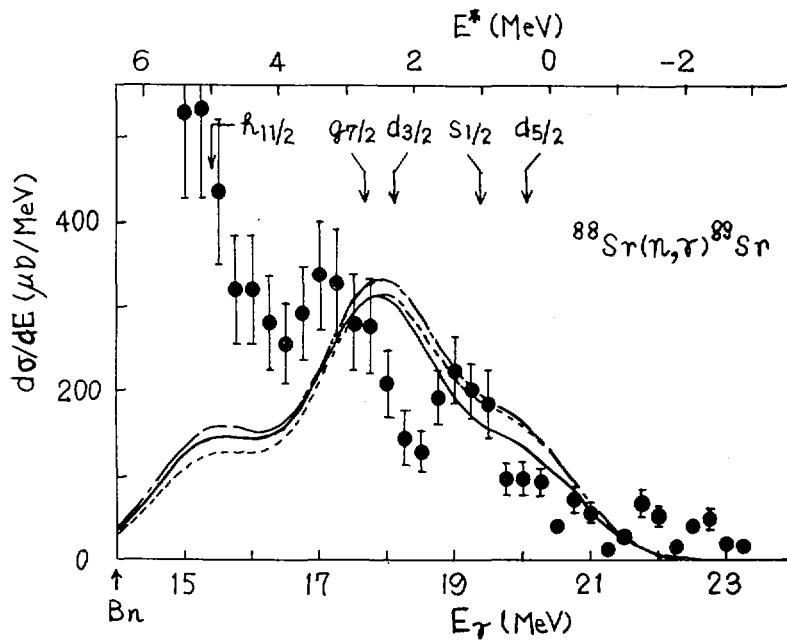


Fig. 9

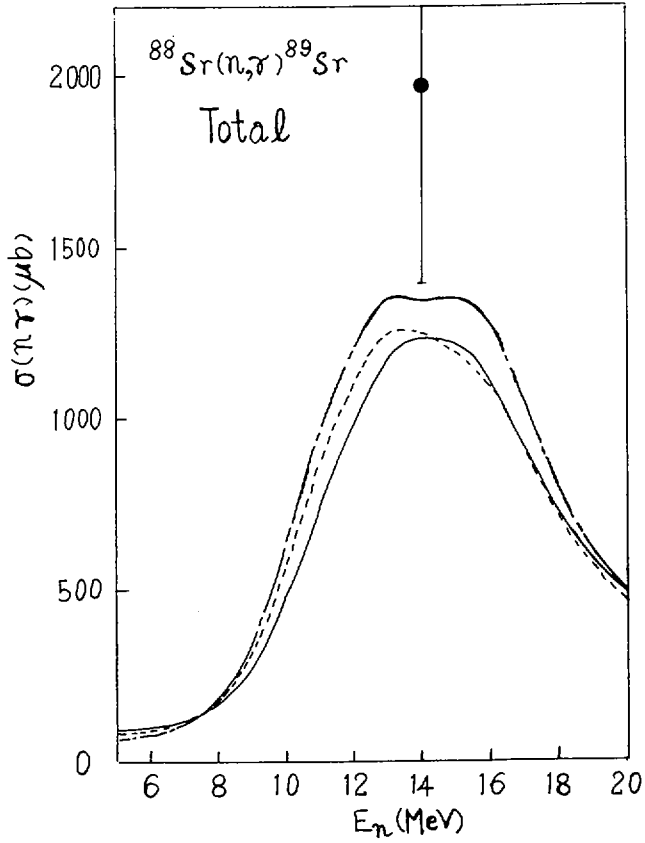


Fig. 10

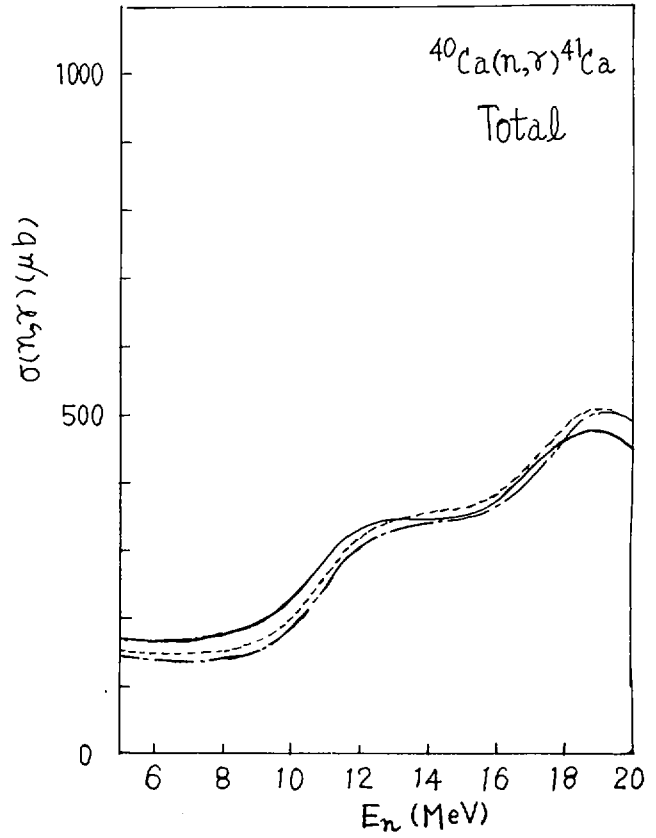


Fig. 12

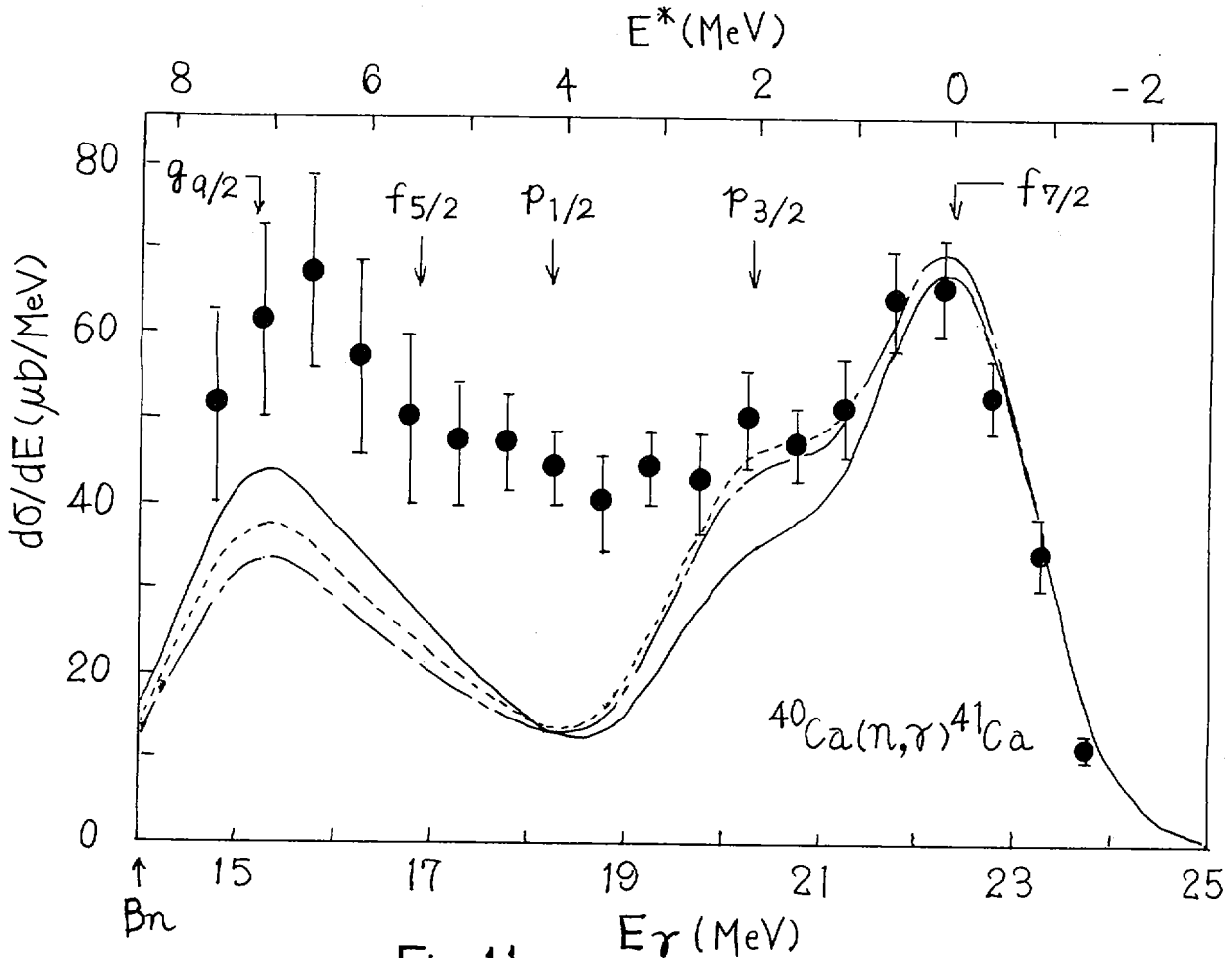


Fig. 11

DISCUSSION

R. E. CHRIEN: Does your calculation include the interference between collective and direct reaction mechanisms?

H. KITAZAWA: Yes.

III-1. Optical Model Analysis for  $^{56}\text{Fe}$ 

Hisao Yamakoshi

Ship Research Institute, Ministry of Transport, Japan

1. Introduction

Among optical potentials ever proposed, one may regard Engelbrecht-Fiedeldy's optical potential as a potential being applicable to more wider energy range than the Perey-Buck potential. (Hereafter, "E-F potential" will be referred to as abbreviation of Engelbrecht-Fiedeldy potential.) The E-F potential is based essentially on the non-local theory. The energy dependence of well depth parameters in the E-F potential is so determined as to give the consistent results with those obtained by Moldauer's local potential at low energy limit (zero energy), and to explain the behaviour of total cross section in high energy region (30 - 150 MeV) very well. Consequently, the E-F potential is supposedly applicable to analyses of total cross section and elastic scattering cross section over a wide energy range. As is shown in Table 1, this widness is characteristic to the E-F potential.

The E-F potential, however, still seems to be inadequate for explaining experimental data on polarization and angular distribution of elastic scattering of neutrons. It may be possible to say from Fig. 1\* that Rosen's potential and Becchetti-Greenlees's potential are superior to the E-F potential in explaining whole behaviour of experimental data on polarization for  $^{56}\text{Fe}$  at 24 MeV. From Fig. 2 for angular distribution of elastic scattering of neutrons from  $^{56}\text{Fe}$  at

---

\* All calculated curves fluctuate so violently around 25 degrees that detail of fluctuation is omitted in Fig. 1.

14.5 MeV, it may be also possible to say that at large scattering angle the E-F potential yields an angular distribution fluctuating too much around experimental data. The inadequacy suggests that there is a room for improving the E-F potential. In improving the situation, value of the radius parameter in the spin-orbit term of the E-F potential can be chosen independently of that in the volume term.

This recipe leads to new set of parameters plausible for explaining experimental data on angular distribution of elastic scattering and polarization for  $^{56}\text{Fe}$ , without harming applicability to the experimental data on neutron strength functions, total and elastic scattering cross section so much.

## 2. Potential Parameters

The E-F potential can be expressed as follows:

$$V(r) = -(V_0 + iW\phi)f_1(r) - iWsf_2(r) - V_{so}(\hbar/m\pi c)^2 (1/r) \left| df_1/dr \right| (\vec{\sigma} \cdot \vec{Q}),$$

where

$$f_1(r) = (1 + \exp((r - R_0)/a_1))^{-1},$$

$$f_2(r) = (4 \exp((r - R_s)/a_2)) / (1 + \exp((r - R_s)/a_2))^2,$$

$$V_0 = 46 - 0.25E \text{ (MeV)}, \quad W\phi = 0.125E - 4 \times 10^{-4} E^2 \text{ (MeV)},$$

$$W_s = 14 - 0.2E \text{ (MeV)}, \quad V_{so} = 0.7 \text{ (MeV)},$$

$$a_1 = 0.62 \text{ (fm)}, \quad a_2 = 0.5 \text{ (fm)},$$

$$R_0 = \bar{r}_0 A^{1/3} \quad \text{or} \quad R_0 = r_v + r_0 A^{1/3},$$

$$R_s = \bar{r}_s A^{1/3} \quad \text{or} \quad R_{so} = r_s + r_0 A^{1/3},$$

$$\bar{r}_0 = 1.317 \text{ (fm)} \quad \text{or} \quad r_v = 0.6 \text{ (fm)},$$

$$\bar{r}_s = 1.447 \text{ (fm)} \quad \text{or} \quad r_s = 1.1 \text{ (fm)}, \quad r_0 = 1.16 \text{ (fm)}.$$

In the present study, expression of the spin-orbit term is altered into the following expression:

$$-V_{so}(\hbar/m\pi c)^2 \cdot (1/r) \cdot |df_3/dr| \cdot (\vec{\sigma} \cdot \vec{r})$$

where

$$f_3(r) = (1 + \exp((r - R_{so})/a_3))^{-1},$$

$$R_{so} = \bar{r}_{so}^{1/3} \quad \text{or} \quad R_{so} = r_{so} + r_o A^{1/3},$$

According to preliminary parameter study, one can explain behaviour of experimental polarization data for  $^{56}\text{Fe}$  very well by choosing appropriate values for following parameters:

$$\bar{r}_{so}, a_2, V_{so}, \bar{r}_s \text{ and } \bar{r}_o$$

By taking account of results of preliminary parameter study and of values given by various authors, following range of values seems to be plausible:

$$1.317 \geq \bar{r}_{so} \geq 0.9, \quad 1.0 \geq a_2 \geq 0.1,$$

$$7 \geq V_{so} \geq 5, \quad 1.447 \geq \bar{r}_s \geq 1.332$$

$$1.317 \geq \bar{r}_o \geq 1.254,$$

### 3. Calculated Results

#### 3-A. Polarization of Scattered Neutrons at 24 MeV.

As a result of analysis at 24 MeV, it turned out that neutron polarization depends mainly on parameters  $\bar{r}_{so}$  and  $a_2$ . As is shown in Fig. 3. the peak of calculated curve around 30 degrees decreases once as the value of the parameter  $r_{so}$  decreases but again increases slowly. Judging from comparison of calculated curves with experimental results, desirable value of  $a_2$  is expected to be around 1.0.

Fig 4. shows that the valley around 50 degrees becomes shallower and the peak around 60 degrees becomes lower as the value of the parameter  $a$  decreases. Figures 5-1 to 5-3 shows

how changes the shape of polarization curve with changing the parameters  $V_{so}$ ,  $\bar{r}_o$  and  $\bar{r}_{so}$ . In general speaking, (1) the peak around 60 degrees becomes lower with the value of  $V_{so}$  decreases, (2) smaller value of  $\bar{r}_o$  makes the peaks around 30 degrees and 60 degrees higher, and the valley around 50 degrees shallower besides being shifted towards larger angles, and (3) as the value of  $\bar{r}_s$  decreases, the peaks around 30 degrees and 60 degrees become lower and the latter is shifted towards larger angle.

Taking account of above mentioned behaviour, it can be said that preferable parameter set is expected to be in the following region:

$$0.1 \leq a_2 \leq 0.5, \quad \bar{r}_{so} \cong 1.07, \quad V_{so} \cong 6, \\ 1.254 \leq \bar{r}_o \leq 1.286, \quad 1.332 \leq \bar{r}_s \leq 1.390.$$

### 3-B Neutron Strength Functions

Calculated neutron strength functions are shown in Table 2 together with used values of parameters. Strength functions  $S_{L,J}$  are calculated by the relation:<sup>(6)</sup>

$$S_{L,J} = (1 - (1 - T_{L,J})^{1/2}) / (\kappa \cdot V_L \cdot E^{1/2}). \quad (7)$$

where the quantity  $T_{L,J}$  is calculated by computer code ELLIESE-III. The quantity  $V_L$  is calculated by the following expression in terms of nuclear radius  $R$  multiplied by wave number  $K$  of incident neutron :  $KR$ .

$$V_L = P_L(KR) / KR \quad (8), (9)$$

where  $P$  is penetrability for L-wave neutrons, and

$$R = (1.23A^{1/3} + 0.8) \text{ fm},$$

$$K = 2.19685(A/A+1) E_n^{\frac{1}{2}}(\text{eV}) 10^{-3},$$

$$P_0 = 1,$$

$$P_1 = (KR)^2 / (1 + (KR)^2),$$

$$P_2 = (KR)^4 / (9 + 3(KR)^2 + (KR)^4),$$

Strength function averaged over J is calculated by the relation:

$$\langle S_L \rangle = (L \cdot S_{L,L-1} / 2 + (L+1) \cdot S_{L,L+1} / 2) / (2L+1).$$

As can be seen from Table 2, calculated S-wave strength function  $S_0$  is independent of values of parameters in the spin-orbit term, while calculated P-wave strength function  $S_1$  depends on values of parameters in spin-orbit term as well as in volume and surface terms.

Experimental value of S-wave neutron strength function for  $^{56}\text{Fe}$  is  $4 \times 10^{-4}$  <sup>(10)</sup>. Comparing this experimental data with the calculated value of S-wave strength function in Table 2, one can obtain following parameter region in which preferable parameter set for S-wave strength function may be found:

$$0.5 \leq a_2 \leq 0.7, \quad 1.254 \leq \bar{r}_0 \leq 1.317,$$

$$1.390 \leq \bar{r}_s \leq 1.447.$$

Experimental value of P-wave strength function for  $^{56}\text{Fe}$  is about  $1 \times 10^{-5}$  <sup>(11)</sup>. By comparing the experimental data on P-wave strength function with calculated value in Table 2, one can obtain following parameter region in which desirable parameter set for the P-wave strength function may be found:

$$0.5 \leq a_2 \leq 0.7, \quad \bar{r}_0 \cong 1.286, \quad \bar{r}_s \cong 1.390,$$

$$V_{so} \cong 6, \quad \bar{r}_{so} \cong 1.07.$$

On assumption that desirable parameter set for the P-wave strength function should be also found in the parameter region

for the S-wave strength function.

### 3-C. Angular Distributions of Elastic Scattering

By comparison of calculated angular distribution with experiment for <sup>(12) (15)</sup><sub>56</sub>Fe at 14.5 MeV, it can be said that value of parameter  $a_2$  must be about 0.7 (See Fig. 6-1 6-3). These figures seem to show that the choice of 0.7 for the parameter  $a$  is rather independent of any combination of values of parameters  $\bar{r}_o$ ,  $\bar{r}_s$  and  $V_{so}$ .

From Fig. 7 and Fig. 8, it can be said that preferable parameter set (for explaining angular distribution of elastic scattering at 14.5 MeV) is expected to be in the following region:

$$1.286 \leq \bar{r}_o \leq 1.317, \quad 5 \leq V_{so} \leq 6,$$

$$1.332 \leq \bar{r}_s \leq 1.390.$$

As is shown in Fig. 7, angular distribution of elastic scattering at 14.5 MeV is insensitive to the choice of the value for the parameter  $V_{so}$ . Since the value 6 is chosen for the parameter  $V_{so}$  as preferable value in explaining experimental polarization data at 24 MeV, one may also fix here the value 6 for the parameter  $V_{so}$ .

Fig. 9 shows angular distribution at 7.55 MeV. From figures 7, 8 and 9, one can expect that preferable parameter set in explaining the angular distributions of elastic scattering is :

$$\bar{r}_{so} \cong 1.317, \quad \bar{r}_s \cong 1.332, \quad V_{so} \cong 6,$$

$$a_2 \cong 0.7, \quad \bar{r}_{so} \cong 1.07.$$

3-D Total and Elastic Scattering Cross Sections

The calculated total and reaction cross sections at 14.5 MeV are given in Table 3 together with used values of the parameters. In Table 4, the calculated total and elastic scattering cross sections at 7.55 MeV are given. The calculated total elastic and inelastic scattering cross sections at 1.5 MeV are tabulated in Table 5.

At 14.5 MeV, experimental value by Kinney and Gwin is  $2.6^{(16)} \pm 0.05$  b for total cross section of  $^{56}\text{Fe}$ . Therefore, according to Table 3, preferable parameter set is expected to be in the following region:

$$\begin{aligned} \bar{r}_{so} &\simeq 1.07, & a_2 &\simeq 0.7, & \bar{r}_o &\simeq 1.317, \\ 1.332 &\leq \bar{r}_s \leq 1.390, & 5 &\leq V_{so} \leq 6. \end{aligned}$$

At 7.55 MeV, experimental value of  $3.5 \pm 0.04$  b is reported for total cross section by Kinney and Gwin. According to Table 4, preferable parameter set is expected to be in the following region:

$$\begin{aligned} \bar{r}_{so} & 1.07, & a_2 & 0.7, & \bar{r}_o & 1.317, \\ 1.390 & \bar{r}_s & 1.447, & 6 & V_{so} & 7. \end{aligned}$$

If Foster's data of  $3.3^{(17)}$  b is adopted in stead of Kinney and Gwin's data, preferable parameter set is expected to be in the following region:

$$\begin{aligned} \bar{r}_{so} &= 1.07, & a_2 &\simeq 0.7, & 1.286 &\leq \bar{r}_o \leq 1.317, \\ 1.332 &\leq \bar{r}_s \leq 1.447, & 5 &\leq V_{so} \leq 7. \end{aligned}$$

As to elastic scattering cross section at 7.55 MeV, experimental value of  $1.8 \pm 0.1$  b is reported by Holmqvist.<sup>(18)</sup>

Table 4 suggests that if the Holmqvist's data is taken into account, one should use more larger value to the parameter

$a_2$  than the value of 0.7.

As to total cross section at 1.5 MeV, available experimental data are those obtained by Carlson and Cerbone, Smith and Jones. These experimental data have fluctuation around the energy 1.5 MeV. Each author's experimental data is averaged over energy region from 1.0 MeV to 2.0 MeV to obtain averaged total cross section at 1.5 MeV. As an averaged value,  $(3.3 \pm 0.1)$ b may be deduced as total cross section at 1.5 MeV. Assuming the value 0.7 for  $a_2$  and the value 1.07 for  $\bar{r}_{so}$ , one can expect that preferable parameter set is in the following region:

$$1.286 \leq \bar{r}_o \leq 1.317, \quad 1.390 \leq \bar{r}_s \leq 1.447, \\ 6 \leq V_{so} \leq 7.$$

As to elastic scattering cross section at 1.5 MeV, experimental cross section is deduced from Gilboy's data at 3.0 MeV, 2.0 MeV and 1.0 MeV. Elastic scattering cross section at these energy points are  $(2.0 \pm 0.05)$  b,  $(2.24 \pm 0.05)$  b,  $(2.02 \pm 0.05)$  b respectively. From these data, experimental cross section at 1.5 MeV is deduced to be  $(2.12 \pm 0.11)$  b. The error of 0.11 b seems to be too large to select appropriate parameter set from Table 5. If experimental error is assumed to be 0.05 b, the value of the parameter  $r_s$  should be smaller than 1.447 fm obtained by E-F in the case of  $\bar{r}_o = 1.317$  and  $a_2 = 0.7$ . In the case of  $\bar{r}_o = 1.286$ , value of parameter  $\bar{r}_s$  should be smaller than 1.390. In the case of  $\bar{r}_o = 1.254$ , value of parameter  $\bar{r}_s$  could be equal to 1.332 at most. This tendency of the parameter  $\bar{r}_s$  seems to be contradicting with that found for other quantities. Thus, in this particular case of elastic

scattering cross section at 1.5 MeV, the value 0.5 seems to be more plausible for the parameter  $a$ , so far as it concerns with comparison between calculation and experiment.

### 3-E. Excitation Functions for Inelastic Scattering of Neutrons

Inelastic scattering cross section for the first excited level of  $^{56}\text{Fe}$  at 0.845 MeV by 1.5 MeV neutron is also tabulated in Table 5. In Fig. 10-1 and 10-2, excitation functions of inelastic scattering calculated for the first and second excited levels are compared with experimental data. <sup>(22)~(25)</sup>In these figures, calculated results with the E-F potential and with the most preferable parameter set are shown by broken lines and broken lines with dots, respectively. Here, the most preferable parameter set is as follows:

$$\begin{aligned} \bar{r}_0 &= 1.254, & \bar{r}_s &= 1.390, & V_{s0} &= 6, \\ a_2 &= 0.7, & \bar{r}_{s0} &= 1.07. \end{aligned}$$

### 3-F. (n,p), (n, $\alpha$ ) and (n,2n) Reaction Cross Sections at 14.5 MeV

The (n,p), (n, $\alpha$ ) and (n,2n) reaction cross sections through compound process are calculated at 14.5 MeV with the compound nucleus formation cross section or in Table 3. The cross section  $\sigma(n,x)$  is expressed as

$$\sigma(n,x)/\sigma_1 = \sum_i F_i,$$

where function  $F_i$  are given by

$$F_i = k g_i m_i \int_0^{E_{max}} E \sigma_i(E) W_i(U_i) dE,$$

$$W(U) = C \exp(2\sqrt{aU}).$$

In the above expressions, quantities  $\sigma_i(E)$ ,  $g_i$  and  $m_i$

are the inverse reaction cross sections, statistical weight factor determined by spin of emitted particle  $i$  and the reduced mass, respectively. The quantity  $W_i(U_i)$  is the level density of the residual nucleus at excitation energy  $U_i$  given by

$$U_i = E_n + Q(n, i) - E.$$

where  $E_n$  is the incident energy in center of mass system and  $Q(n, i)$  is the  $Q$ -value for the  $(n, i)$  reaction. The upper limit of the integration is the maximum energy available to the emitted particle  $i$  and is given by

$$E_{\max} = E_n + Q(n, i).$$

In performing the integration, energy dependence of the cross section  $\sigma_i(E)$  for charged particle emission is assumed to be:

$$\begin{aligned} \sigma_i(E) &= \sigma_0(1 - B_i/E) && \text{for } E > B_i, \\ &= 0 && \text{for } E < B_i. \end{aligned}$$

while for neutron emission, variation of the cross section  $\sigma_i(E)$  with energy is ignored. The quantity  $B_i$  in the above expression is effective coulomb barrier and is given by

$$B_i = k_i V_i, \tag{27}$$

where  $k_i$  is a coefficient varying with atomic number  $Z$ , and  $V_i$  is expressed as follows:

$$\begin{aligned} V_i &= 1.019(Z-1)/(A^{1/3} + 1) \quad (\text{MeV}), \quad \text{for } i = p, \\ &= 2.038(Z-2)/((A-3)^{1/3} + 4)^{1/3} \quad (\text{MeV}), \quad \text{for } i = \alpha. \end{aligned}$$

Integration gives following expressions for cross sections:

$$\begin{aligned} \sigma(n, p) / \sigma_r &= I_p e^{D_p/T} / (1 + I_p e^{D_p/T}), \\ D_p &= Q(n, p) + \delta_T - \delta_R - B_p, \\ I_p &= 1 - (1 + E_{mp}/T) e^{-E_{mp}}, \end{aligned}$$

$$\begin{aligned}
 E_{mp} &= E_n + Q(n,p) - B_p, \\
 \sigma(n,\alpha)/\sigma_r &= 2I_\alpha e^{D_\alpha/T} / (1 + I_p e^{D_p/T}), \\
 D_\alpha &= Q(n, \alpha) + \delta_T - \delta_R - B_\alpha, \\
 I_\alpha &= 1 - (1 + E_{m\alpha}/T) e^{-E_{m\alpha}/T}, \\
 E_{m\alpha} &= E_n + Q(n,\alpha) - B_\alpha, \\
 \sigma(n,2n)/\sigma_r &= (1 - (1 + (E_n - S_n)/T) e^{-(E_n - S_n)/T}) / (1 + I_p e^{D_p/T}),
 \end{aligned}$$

where  $S_n$  is neutron separation energy of target nucleus.

Using following values to various quantities in above expressions:

$$\begin{aligned}
 E_n &= 14.244 \text{ (MeV)}, & K_p &= 0.647, & (27) \\
 Q(n,p) &= -2.9191 \text{ (MeV)}, & K &= 0.881, & (28) \\
 Q(n, \alpha) &= 0.3220 \text{ (MeV)}, & \delta_T &= 1.54 + 1.27 \text{ (MeV)} & \text{for } (n,p) \text{ reaction} \\
 S_n &= 11.2027 \text{ (MeV)}, & \delta_R &= 0 \text{ (MeV)} & \\
 T &= 1.5833 \text{ (MeV)}, & \delta_T &= 1.54 + 1.27 \text{ (MeV)} & \text{for } (n,\alpha) \text{ reaction} \\
 & & \delta_R &= 1.35 + 1.30 \text{ (MeV)} &
 \end{aligned}
 \tag{30}$$

one obtains following results for branching ratios:

$$\begin{aligned}
 \sigma(n,p)/\sigma_r &= 0.09385, & \sigma(n,\alpha)/\sigma_r &= 0.01381, \\
 \sigma(n,2n)/\sigma_r &= 0.51729.
 \end{aligned}$$

Kinney has reported<sup>(16)</sup> that experimental value of total cross section for <sup>56</sup>Fe at 14.5 MeV is 2.6+0.05 b. As to experimental value of (n,p) reaction cross section for <sup>56</sup>Fe at 14.5 MeV, Kanda and Nakashima have deduced it to be 106+12 mb<sup>(31)</sup> by evaluation of existing experimental data.

Experimental value of elastic scattering cross section has been reported by Coon et al.<sup>(14)</sup> for natural iron at 14 MeV to be 1.14+0.06 b. From behaviour of elastic scattering cross section for iron around 14 MeV, one may expect quite the same value at 14.5 MeV. As to experimental value of (n,2n) reaction cross section for <sup>56</sup>Fe, Ashby et al. have reported<sup>(32)</sup> the value

0.5+0.04 b at 14 MeV. Judging the behaviour of (n,2n) reaction cross section for isotopes of Al and Cu, a more larger value is expected at 14.5 MeV.

By using obtained branching ratios and  $\sigma_r$  in Table 3, one can calculate (n,p), (n, $\alpha$ ) and (n,2n) reaction cross sections at 14.5 MeV.

Considering that values of (n,r), (n,d), (n,t) and (n,<sup>3</sup>He) reaction cross sections are negligibly small at 14.5 MeV, one can estimate inelastic scattering cross section  $\sigma_{in}$  by following approximation:

$$\sigma_{in} \cong \sigma_{tot} - \sigma_{el} - \sigma(n,p) - \sigma(n,\alpha) - \sigma(n,2n).$$

As to elastic scattering cross section, experimental value of 1.14+0.06 b seems to be fairly small in comparison with calculated result by using the E-F potential. This experimental value is in good agreement with those values for smaller value of  $r_0$  in Table 3. Experimental value of 106+12 mb for (n,p) reaction cross section corresponds to value of  $\sigma_r$  ranging from 1257 mb to 1002 mb. On taking account of this range of the cross section, one can see from Table 3 that preferable value of  $a_2$  is found to be in a region from 0.3 to 0.5.

The E-F potential yields following results:

$$\begin{aligned} \sigma_{tot} &= 2.6183 \text{ b.}, & \sigma_{el} &= 1.3171 \text{ b.}, & \sigma(n,p) &= 0.1221 \text{ b.}, \\ \sigma(n,\alpha) &= 13.8 \text{ mb.}, & \sigma(n,2n) &= 673.1 \text{ mb.}, & \sigma_{in} &= 492.2 \text{ mb.} \end{aligned}$$

while, one of preferable parameter sets:

$$\bar{r}_0 = 1.286, \quad \bar{r}_s = 1.390, \quad \bar{r}_{so} = 1.07,$$

$$V_{so} = 6, \quad a_2 = 0.7.$$

gives following results:

$$\begin{aligned} \sigma_{tot} &= 2.5337 \text{ b.}, & \sigma_{el} &= 1.1844 \text{ b.}, & \sigma(n,p) &= 0.1226 \text{ b.}, \\ \sigma(n,\alpha) &= 18.6 \text{ mb.}, & \sigma(n,2n) &= 698.0 \text{ mb.}, & \sigma_{in} &= 472.4 \text{ mb.} \end{aligned}$$

By comparing these results for the two parameter sets with experimental values, it can be said that the latter parameter set yields fairly good agreement with experimental results and that one can use the parameter set in stead of the E-F set.

#### 4. Discussion

From comparison between experiment and calculation for angular distribution of elastic scattering at 14.5 MeV, the value 0.7 seems to be more suitable for the parameter  $a_2$ , although the value 0.5 has been used in the E-F potential. This is also supported by S-wave strength function and total cross section. Experimental data on polarization at 24 MeV seems to insist on some value at most 0.5. But assignment of the value 0.7 is possible by choosing values of other parameters properly.

So far as one uses penetrabilities for square well potential, experimental P-wave strength function requires quite a large value for channel radius parameter, as large as 20 percent more than 1.25 fm. (8)

Elastic scattering cross section measured by Coon et al. at 14 MeV seems to be rather small. From experimental data at 14 MeV and 14.5 MeV for  $\sigma(n,p)$  and  $\sigma(n,2n)$  preferable parameter region cannot be found except the parameter  $a_2$ . This is due to large experimental error for these cross sections.

As a final conclusion, the most preferable parameter set for <sup>56</sup>Fe is determined to be

$$\begin{aligned} \bar{r}_{so} &= 1.07, & \bar{r}_s &= 1.390, & \bar{r}_o &= 1.286, \\ a_2 &= 0.7, & V_{so} &= 6. \end{aligned}$$

on balance of contradicting requirements to parameter set deduced

from experimental data except for that on inelastic scattering.

The cross section of total inelastic scattering at 14 MeV has been reported as  $1113+149$  mb by Fujita et al.<sup>(33)</sup> while the present calculation gives  $470\sim 490$  mb. However, it seems to be not clear whether the experimental value includes contributions not only from inelastic scattering but also from (n,2n) reaction. If the experimental value is considered to be the cross section for neutron emission, present calculation seems to give rather consistent result.

As to calculated excitation curves on  $^{56}\text{Fe}$ , it seems that the most preferable parameter set explains experimental data fairly well as a whole, although there is a tendency of slight over estimation of excitation function in low energy region from 0.845 to about 2.0 MeV. This tendency may be relieved by taking account of the Moldauer effect.

#### Acknowledgement

The author is grateful to Dr. R. Nakasima for his useful suggestions discussion on calculation of branching ratios in addition to encouragement.

Reference.

- ( 1 ) Ann. of Phys., 42, 262, (1967), Engelbrecht C.A and Fiedeldy H.
- ( 2 ) Nucl. Phys., 32, 353, (1962), Perey F. and Buck B.
- ( 3 ) Nucl. Phys., 47, 65, (1963), Moldauer P.A.
- ( 4 ) Ann. of Phys., 34, 96, (1965), Rosen L.P., Beery J.G., Goldhaber A.S. and Auerbach E.H.
- ( 5 ) Phys. Rev., 182, 1190, (1969), Becchetti F.D. Jr. and Greenlees G.W.
- ( 6 ) Nucl. Science Eng., 52, 461, (1973), Goldsmith M.
- ( 7 ) JAERI-1224, (1972), Igarasi S.
- ( 8 ) Theoretical Nuclear Physics, 361, (1952), Blatt. J.M and Weisskopf V.F., John Wiley & Sons, New York.
- ( 9 ) BNL-50274 (T-601), D-16, (1970), Drake M.K.
- (10) Ann. of Phys., 10,455, (1960), Bilpuch E.G., Weston L.W. and Newson H.W.
- (11) Phys. Rev., 178, 1746, (1969), Hockenbury R.W., Bartolome Z.M., Tatarczuk J.R., Moyer W.R. and Block R.C.
- (12) Phys. Rev., 101, 648, (1956), Elliot J.O.
- (13) Doklay Akademii Nauk, 113, 533, (1957), Kahletskii
- (14) Phys. Rev., 111, 250, (1958), Coon J.H., Davis R.W. Felthausen H.E. and Nicodemus D.E.
- (15) Phys. Rev., 110, 160, (1958), Anderson J.D., Gardner C.C., Nakad M.P. and Wong C.
- (16) ORNL-TM-2052, (1968), Kinney W.E. and Gwin E.R.
- (17) HW-73116, (1963), Foster C.G. and Glasgow D.W.
- (18) AB Atomenergi, 366, (1969), Holmqvist B. and Wiedeling T.

- (19) Nucl. Sci. Eng., 42, 28, (1970), Carlson A.D. and Cerbone R.J.
- (20) ANL-6792, (1963), Smith A.B.
- (21) Phys. Rev., 110, 466, (1958), Weil J. L.
- (22) Nucl. Phys., 64, 130, (1965), Gilboy W.B. and Towle J.H.
- (23) Nucl. Phys., 51, 353, (1963), Bonazzola G.C., Bressani T.B., Brovetto P., Chiavassa E. and Demochelli R.
- (24) Nucl. Sci. Eng., 19, 431, (1964), Hopkins J.C. and Silbert M.G.
- (25) EAN(J), 3, 18, (1966), Tsukada K.
- (26) Geola Inst. Tech., Wingston L.W. (1970)
- (27) Phys. Rev., 116, 683, (1959), Dostrovsky I., Fraenkel Z. and Friedlander G.,
- (28) Nuclear Data, p.429, (1966(A2))
- (29) Nuclear Data Tables, 9, No. 4 - 5, (1971), Wapstra A. H. and Gove N. B.
- (30) Can. Jour. Phys., 43, 1446, (1965), Gilbert A. and Cameron A. G. W.
- (31) JAERI - 1207, (1972), Kanda Y. and Nakasima R.
- (32) Phys. Rev., 111, 616, (1958), Ashby V. J., Catron H. C. and Newkirk L. L.,
- (33) Jour. Nucl. Sci. Tech., 9, 301, (1972), Fujita I. Sonoda M., Kawase A. Wakuta Y., Tawara H., Hyakutake M. and Iwatani K.
- (34) Rev. Mod. Phys., 1097, Oct., (1964), Moldauer P. A.

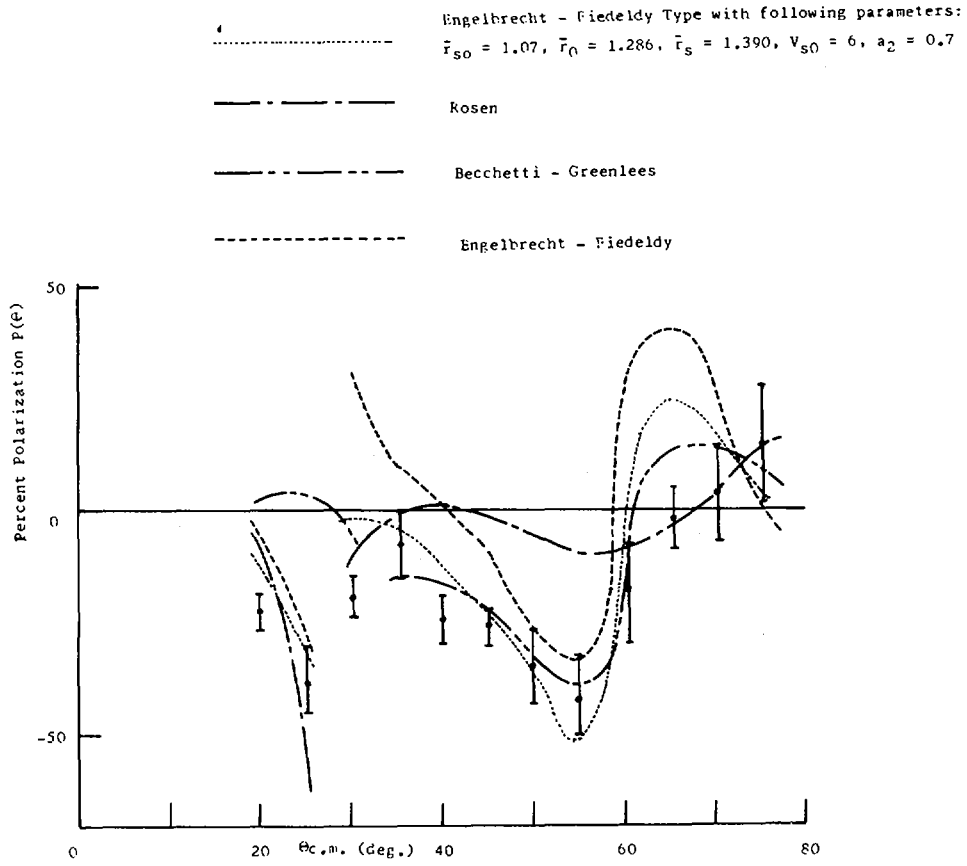


Fig. 1 Percent Polarization at 24 MeV

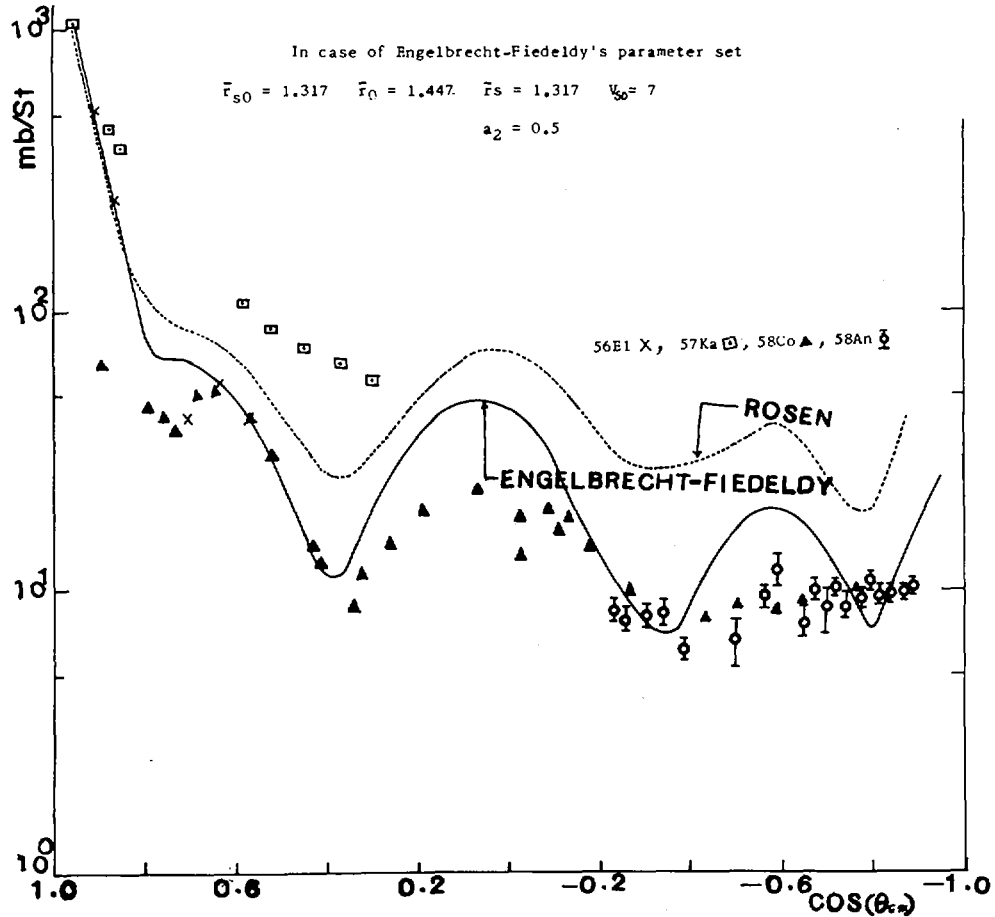


Fig. 2 Differential Elastic Scattering Cross Section at 14.5 MeV

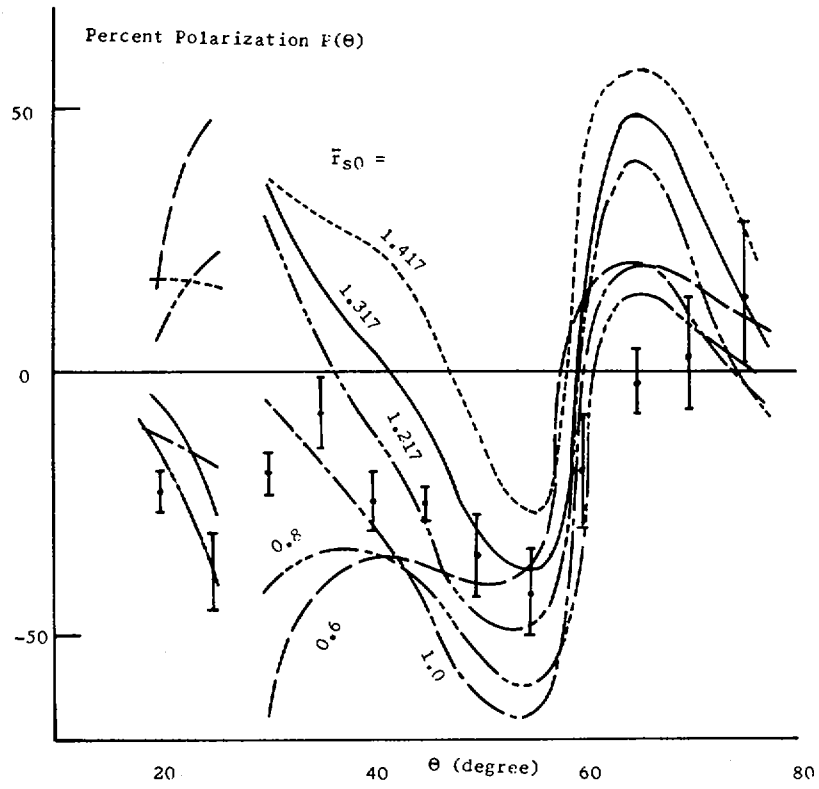


Fig. 3  $\bar{r}_{s0}$  Dependence of Percent Polarization

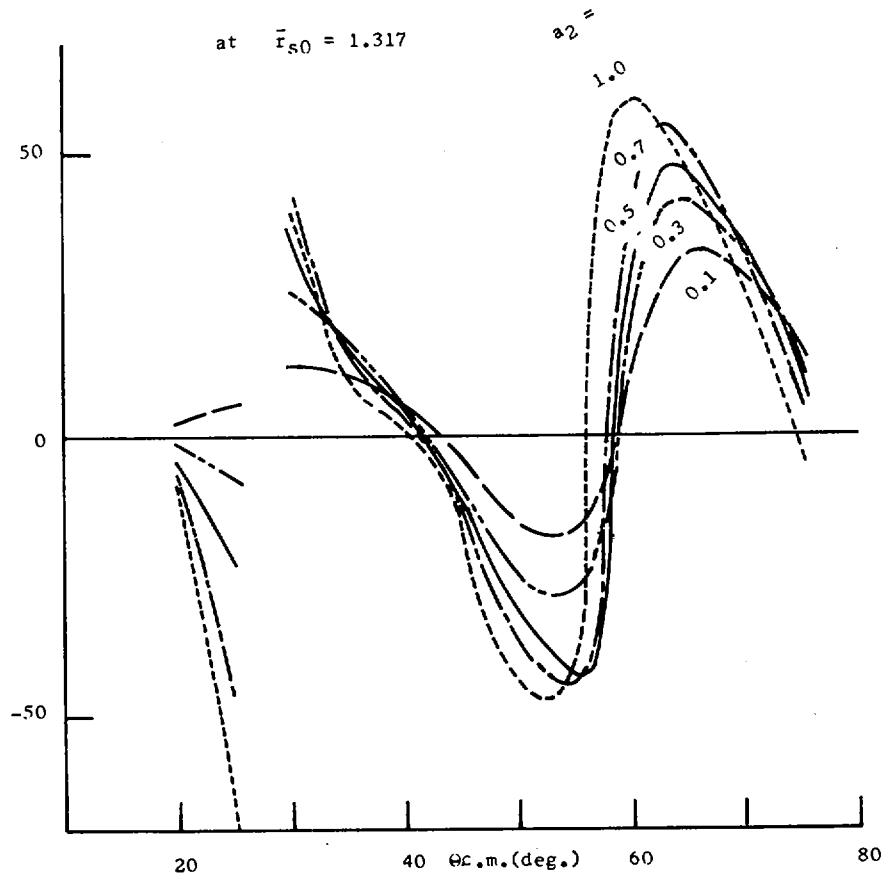


Fig. 4  $a_2$  Dependence of Percent Polarization

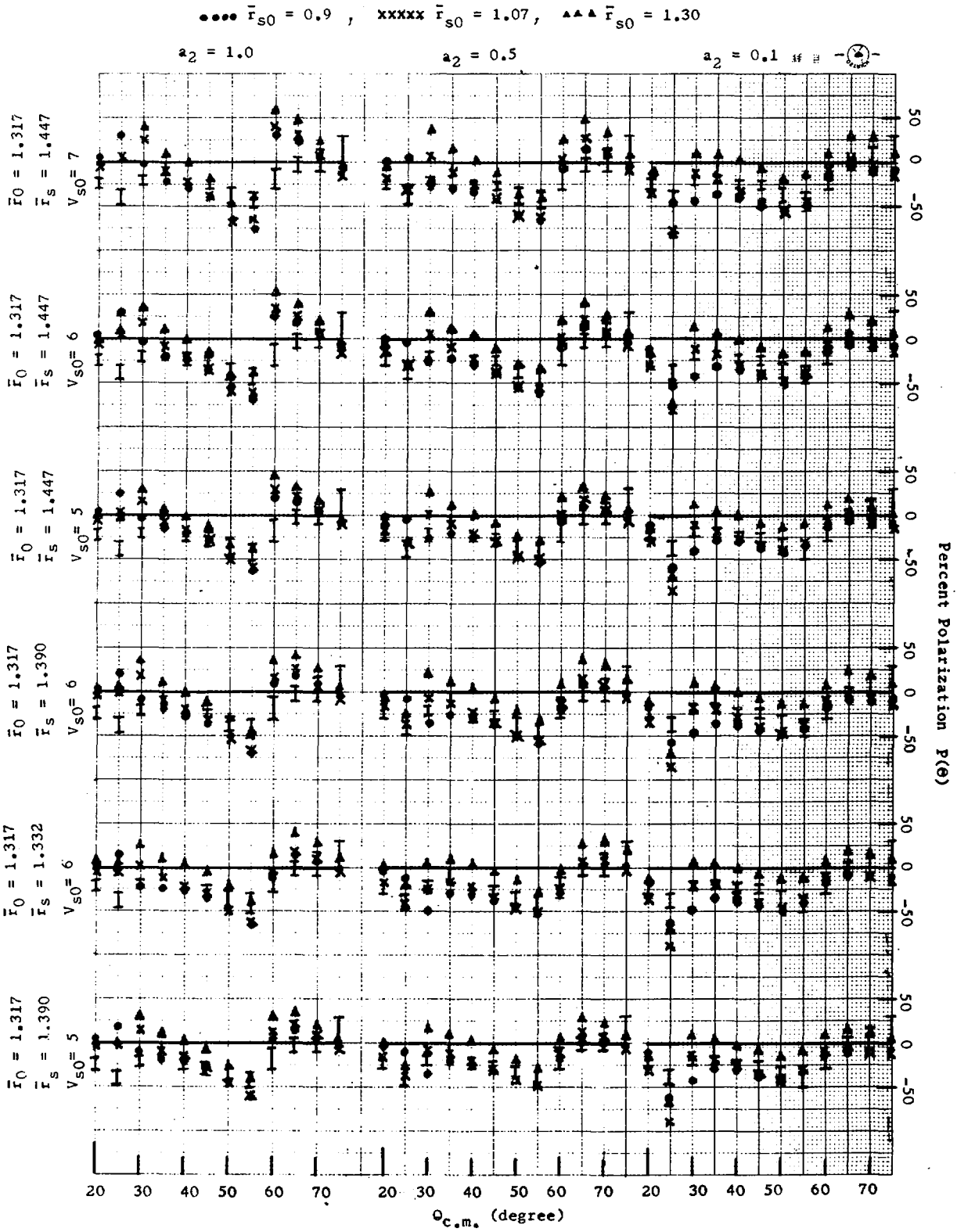


Fig. 5-1

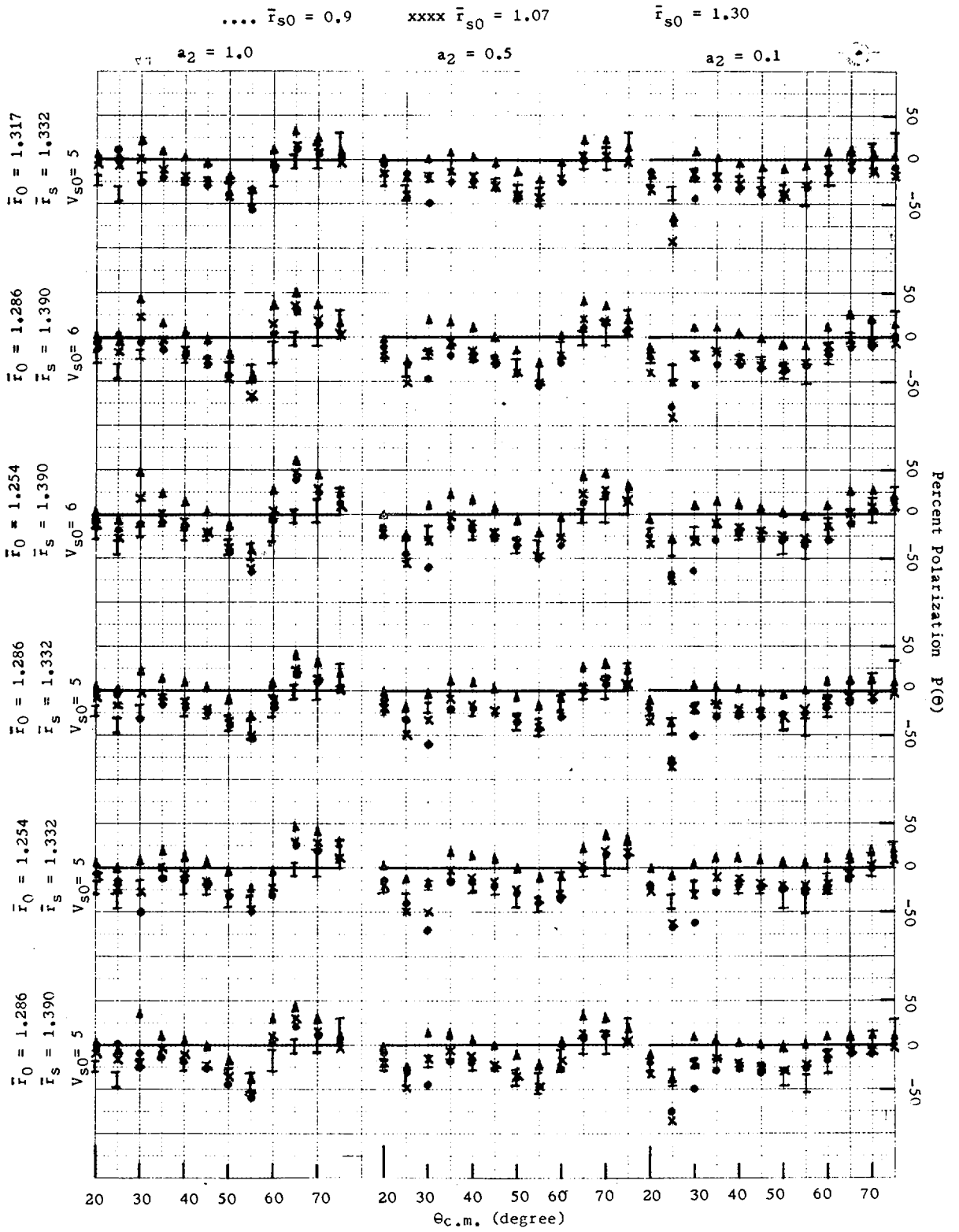


Fig. 5-2

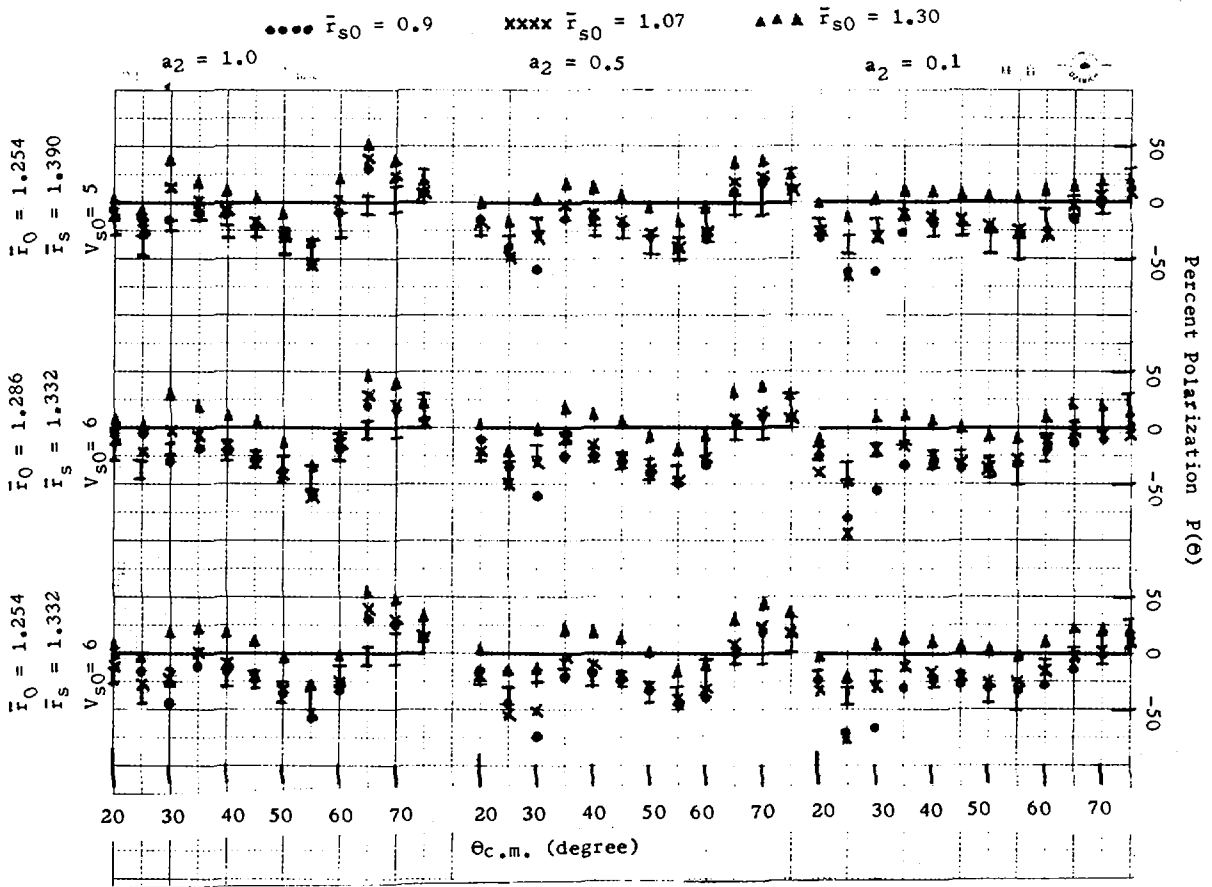
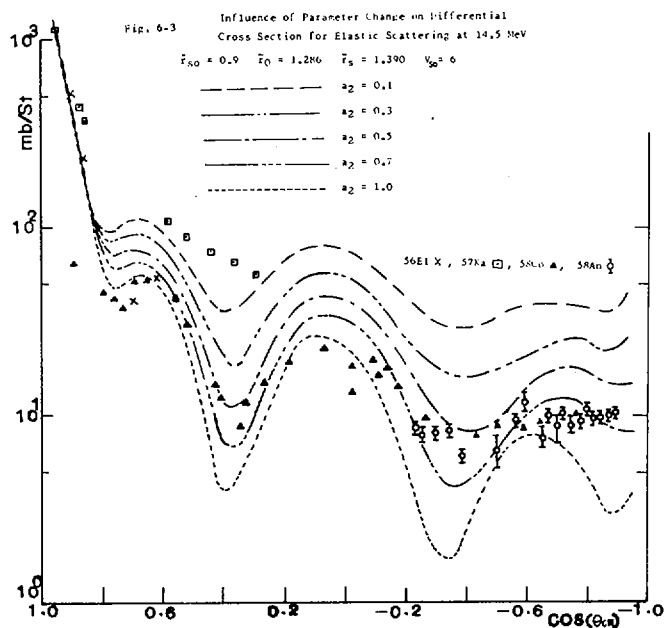
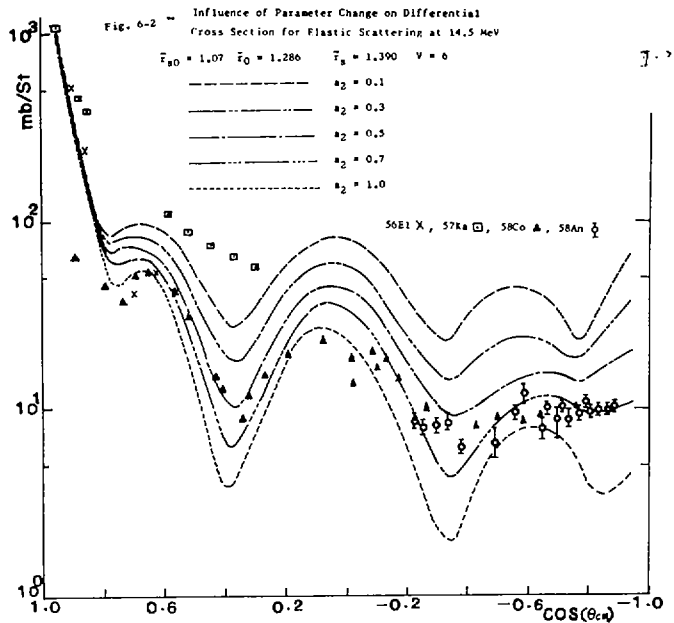
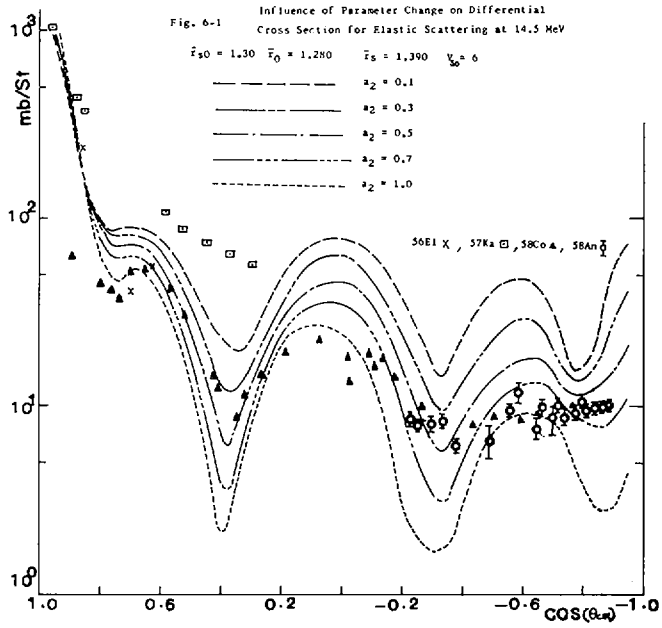
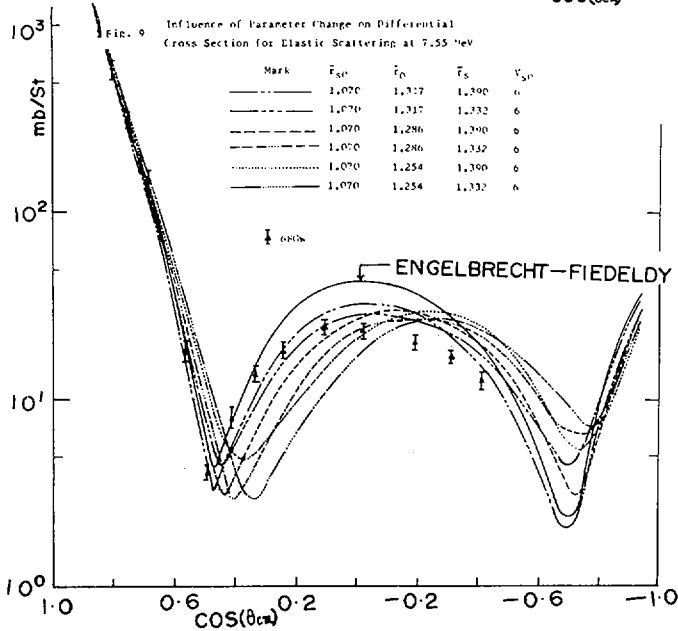
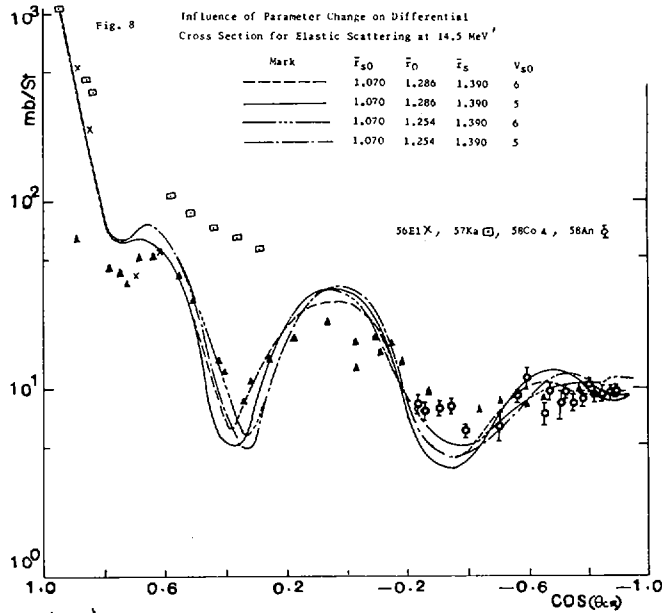
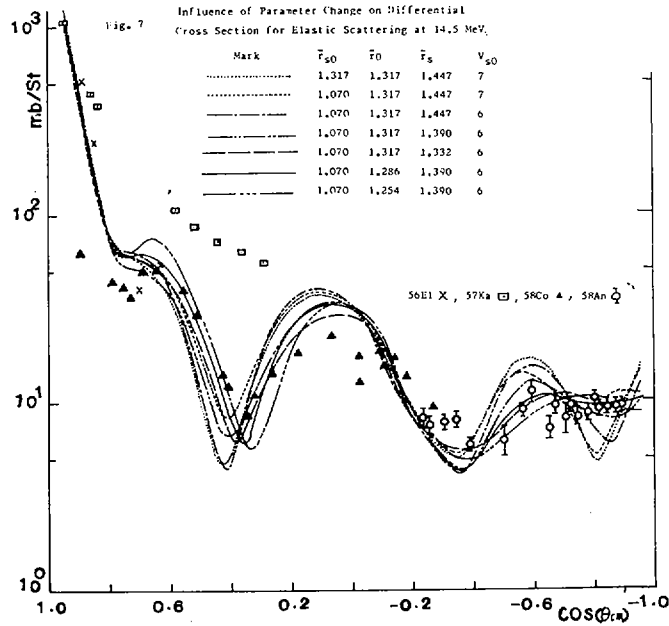


Fig. 5-3





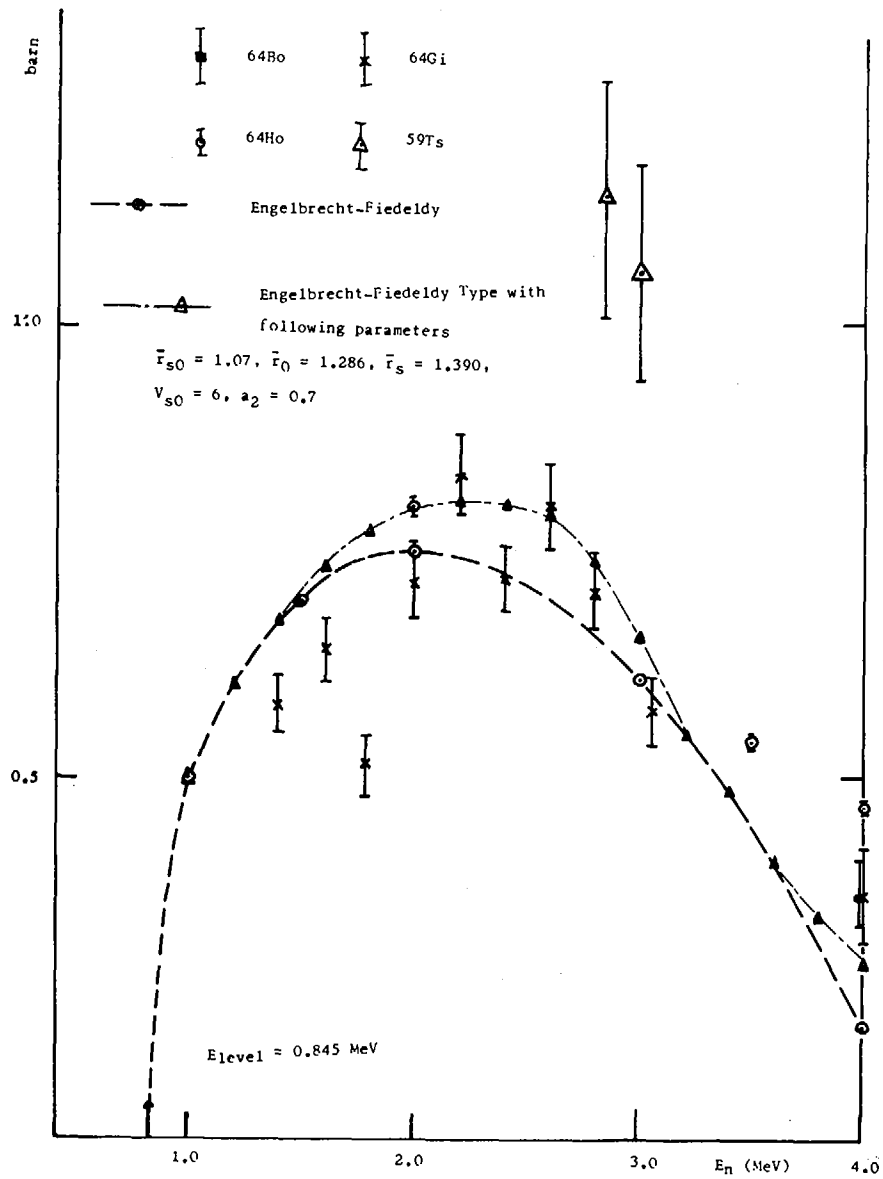


Fig. 10-1 Excitation Curve for the First Level of  $^{56}\text{Fe}$

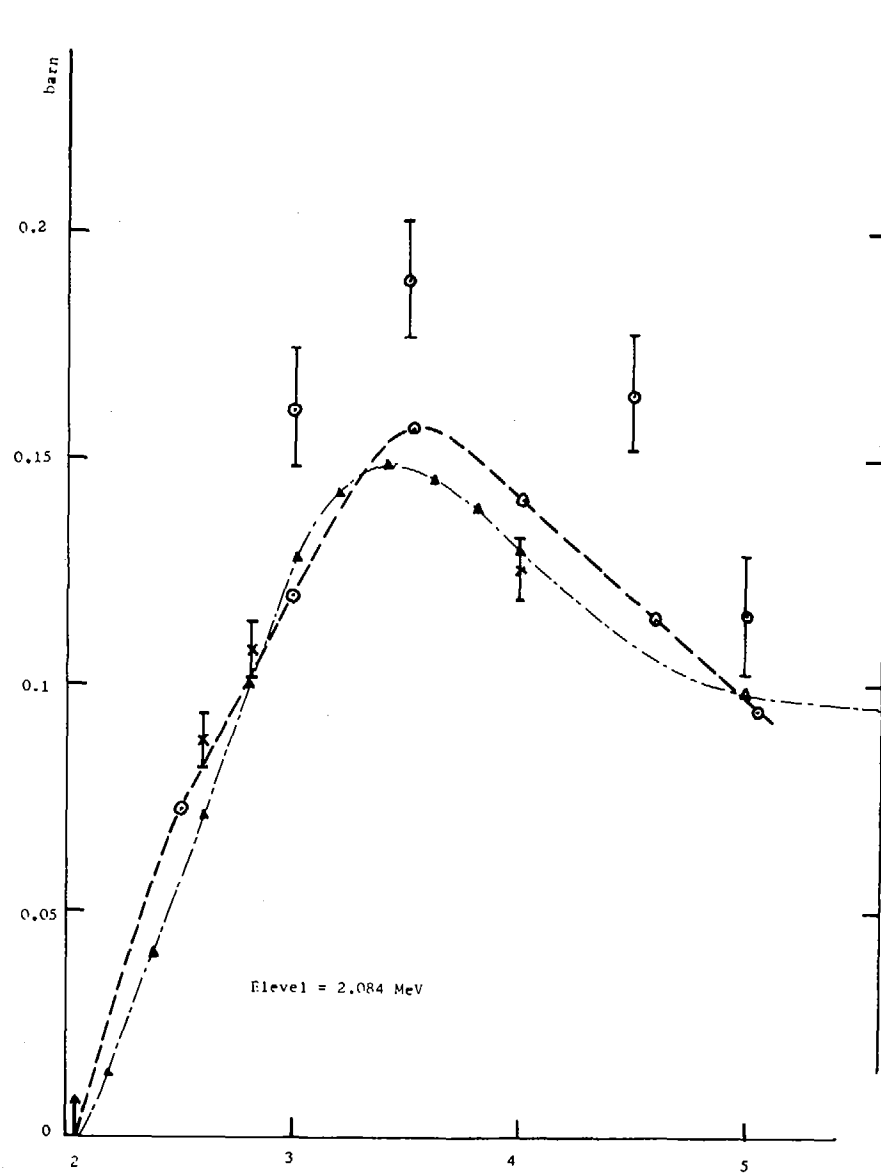


Fig. 10-2 Excitation Curve for the Second Level of  $^{56}\text{Fe}$

Table 1 Comparison of Potentials and Potential Parameters

Authors Applicable Energy	Rosen et al 4 MeV ~ 24 MeV	Engelbrecht - Fiedeldy 0 MeV ~ 150 MeV	Bjorklund Fernbach 14 MeV	Auerbach Moor 0.98 MeV ~ 4 MeV	Becchetti- Greenlees 0.5 MeV ~ 50 MeV
Optical Parameter					
Volume Part					
$V_0$ (MeV)	49.3 - 0.33 E	46.0 - 0.25 E	50.0	46.9	56.3 - 0.32 E - 24.0 (N - Z)/A
$U_0$ (MeV)		0.125 E - 4x10 <sup>-4</sup> E <sup>2</sup>			0.22 E - 1.56 or 0.0 (either larger one)
$r_0$ (Fermi)	1.25	1.16	1.25	1.28	{ 1.17 (Real Part), 1.26 (Imag. Part)
$r_1$ (Fermi)*		0.6 } $\bar{r}_0 = 1.317$			
$a_1$ (fermi)	0.65	0.62	0.65	0.55	0.75 (Real Part) , 0.58 (Imag. Part)
Surface Part					
$W_0$ (MeV)	5.75	14 - 0.2 E	9.5	14.8	13.0 - 0.25 E - 12(N - Z)/A or 0.0
$r_0$ (Fermi)	1.25	1.16	1.25	1.28	1.26
$r_2$ (Fermi)*		1.1 } $\bar{r}_s = 1.447$			
$a_2$ (Fermi)	0.70	0.5	0.98	1.0	0.58
Spin-Orbit Part					
$V_{so}$ (MeV)	5.5	7	7	5.1	6.2
$r_{so}$ (Fermi)	1.25	1.317 ( $\bar{r}_{so}$ )	1.25	1.28	1.01
$a_{so}$ (Fermi)	0.65	0.62	0.65	0.55	0.75
Comment for the Surface Term	Diff. Wood-Saxon	Gaussian	Gaussian	Gaussian	Diff. Wood-Saxon

\*  $R \equiv r_k + r_0 A^{1/3}$  where, k = 1,2

$R = r_0 A^{1/3}$

table 2-1 Strength Functions Estimated at 10 eV

$H_0$	$H_s$	V	$H_{SO}$	$a_2 = 0.1$	$a_2 = 0.3$	$a_2 = 0.5$	$a_2 = 0.7$	$a_2 = 1.0$	
1.317	1.447	7	1.317	$S_0$	$6.199 \times 10^{-4}$	$5.800 \times 10^{-4}$	$4.191 \times 10^{-4}$	$3.200 \times 10^{-4}$	$2.382 \times 10^{-4}$
				$S_1^+$	$1.526 \times 10^{-7}$	$4.225 \times 10^{-6}$	$1.810 \times 10^{-5}$	$4.401 \times 10^{-5}$	$1.060 \times 10^{-5}$
				$S_1^-$	$1.697 \times 10^{-6}$	$6.213 \times 10^{-6}$	$1.886 \times 10^{-5}$	$4.072 \times 10^{-5}$	$8.704 \times 10^{-5}$
				$S_1$	$6.674 \times 10^{-7}$	$4.888 \times 10^{-6}$	$1.835 \times 10^{-5}$	$4.291 \times 10^{-5}$	$9.967 \times 10^{-5}$
1.317	1.447	7	1.070	$S_0$	$6.199 \times 10^{-4}$	$5.800 \times 10^{-4}$	$4.191 \times 10^{-4}$	$3.200 \times 10^{-4}$	$2.382 \times 10^{-4}$
				$S_1^+$	$5.711 \times 10^{-8}$	$4.118 \times 10^{-6}$	$1.784 \times 10^{-5}$	$4.379 \times 10^{-5}$	$9.942 \times 10^{-5}$
				$S_1^-$	$2.925 \times 10^{-6}$	$8.488 \times 10^{-6}$	$2.207 \times 10^{-5}$	$4.422 \times 10^{-5}$	$8.960 \times 10^{-5}$
				$S_1$	$1.013 \times 10^{-6}$	$5.575 \times 10^{-6}$	$1.925 \times 10^{-5}$	$4.393 \times 10^{-5}$	$9.615 \times 10^{-5}$
1.317	1.447	6	1.070	$S_0$	$6.199 \times 10^{-4}$	$5.800 \times 10^{-4}$	$4.191 \times 10^{-4}$	$3.200 \times 10^{-4}$	$2.382 \times 10^{-4}$
				$S_1^+$	$8.151 \times 10^{-8}$	$4.081 \times 10^{-6}$	$1.771 \times 10^{-5}$	$4.338 \times 10^{-5}$	$9.860 \times 10^{-5}$
				$S_1^-$	$2.419 \times 10^{-6}$	$7.615 \times 10^{-6}$	$2.104 \times 10^{-5}$	$4.335 \times 10^{-5}$	$8.971 \times 10^{-5}$
				$S_1$	$8.607 \times 10^{-7}$	$5.259 \times 10^{-6}$	$1.882 \times 10^{-5}$	$4.337 \times 10^{-5}$	$9.564 \times 10^{-5}$
1.317	1.447	5	1.070	$S_0$	$6.199 \times 10^{-4}$	$5.800 \times 10^{-4}$	$4.191 \times 10^{-4}$	$3.200 \times 10^{-4}$	$2.382 \times 10^{-4}$
				$S_1^+$	$1.148 \times 10^{-7}$	$4.075 \times 10^{-6}$	$1.759 \times 10^{-5}$	$4.294 \times 10^{-5}$	$9.765 \times 10^{-5}$
				$S_1^-$	$1.934 \times 10^{-6}$	$6.807 \times 10^{-6}$	$2.004 \times 10^{-5}$	$4.268 \times 10^{-5}$	$8.993 \times 10^{-5}$
				$S_1$	$7.212 \times 10^{-7}$	$4.986 \times 10^{-6}$	$1.841 \times 10^{-5}$	$4.285 \times 10^{-5}$	$9.508 \times 10^{-5}$
1.317	1.390	6	1.070	$S_0$	$4.618 \times 10^{-4}$	$6.612 \times 10^{-4}$	$5.129 \times 10^{-4}$	$3.929 \times 10^{-4}$	$2.820 \times 10^{-4}$
				$S_1^+$	$2.390 \times 10^{-6}$	$8.372 \times 10^{-6}$	$2.288 \times 10^{-5}$	$4.643 \times 10^{-5}$	$9.339 \times 10^{-5}$
				$S_1^-$	$6.501 \times 10^{-6}$	$1.786 \times 10^{-5}$	$3.433 \times 10^{-5}$	$5.499 \times 10^{-5}$	$9.276 \times 10^{-5}$
				$S_1$	$3.760 \times 10^{-6}$	$1.153 \times 10^{-5}$	$2.670 \times 10^{-5}$	$4.928 \times 10^{-5}$	$9.318 \times 10^{-5}$
1.317	1.332	6	1.070	$S_0$	$2.562 \times 10^{-4}$	$7.076 \times 10^{-4}$	$6.337 \times 10^{-4}$	$4.976 \times 10^{-4}$	$3.438 \times 10^{-4}$
				$S_1^+$	$5.262 \times 10^{-6}$	$1.977 \times 10^{-5}$	$3.733 \times 10^{-5}$	$5.893 \times 10^{-5}$	$9.649 \times 10^{-5}$
				$S_1^-$	$9.098 \times 10^{-6}$	$3.305 \times 10^{-5}$	$5.341 \times 10^{-5}$	$7.231 \times 10^{-5}$	$1.010 \times 10^{-4}$
				$S_1$	$6.541 \times 10^{-6}$	$2.420 \times 10^{-5}$	$4.269 \times 10^{-5}$	$6.339 \times 10^{-5}$	$9.799 \times 10^{-5}$
1.317	1.390	5	1.070	$S_0$	$4.618 \times 10^{-4}$	$6.612 \times 10^{-4}$	$5.129 \times 10^{-4}$	$3.929 \times 10^{-4}$	$2.820 \times 10^{-4}$
				$S_1^+$	$2.543 \times 10^{-6}$	$8.687 \times 10^{-6}$	$2.329 \times 10^{-5}$	$4.664 \times 10^{-4}$	$9.303 \times 10^{-5}$
				$S_1^-$	$5.879 \times 10^{-6}$	$1.642 \times 10^{-5}$	$3.255 \times 10^{-5}$	$5.344 \times 10^{-5}$	$9.228 \times 10^{-5}$
				$S_1$	$3.655 \times 10^{-6}$	$1.126 \times 10^{-5}$	$2.638 \times 10^{-5}$	$4.891 \times 10^{-5}$	$9.278 \times 10^{-5}$
1.317	1.332	5	1.070	$S_0$	$2.5615 \times 10^{-4}$	$7.076 \times 10^{-4}$	$6.337 \times 10^{-4}$	$4.976 \times 10^{-4}$	$3.438 \times 10^{-4}$
				$S_1^+$	$5.436 \times 10^{-6}$	$2.034 \times 10^{-5}$	$3.809 \times 10^{-5}$	$5.935 \times 10^{-5}$	$9.648 \times 10^{-5}$
				$S_1^-$	$8.553 \times 10^{-6}$	$3.124 \times 10^{-5}$	$5.113 \times 10^{-5}$	$7.034 \times 10^{-5}$	$9.997 \times 10^{-5}$
				$S_1$	$6.475 \times 10^{-6}$	$2.397 \times 10^{-5}$	$4.244 \times 10^{-5}$	$6.301 \times 10^{-5}$	$9.764 \times 10^{-5}$

Table 2-2 Strength Functions Estimated at 10 eV

$r_0$	$r_s$	V	$r_{so}$	$a_2 = 0.1$	$a_2 = 0.3$	$a_2 = 0.5$	$a_2 = 0.7$	$a_2 = 1.0$	
1.286	1.390	6	1.070	$S_0$	$2.959 \times 10^{-3}$	$9.218 \times 10^{-4}$	$5.657 \times 10^{-4}$	$4.079 \times 10^{-4}$	$2.873 \times 10^{-4}$
				$S_1^+$	$2.505 \times 10^{-6}$	$1.057 \times 10^{-5}$	$2.453 \times 10^{-5}$	$4.530 \times 10^{-5}$	$8.637 \times 10^{-5}$
				$S_1^-$	$6.350 \times 10^{-6}$	$2.398 \times 10^{-5}$	$4.129 \times 10^{-5}$	$6.000 \times 10^{-5}$	$9.214 \times 10^{-5}$
				$S_1$	$3.787 \times 10^{-6}$	$1.504 \times 10^{-6}$	$1.504 \times 10^{-5}$	$3.011 \times 10^{-5}$	$8.829 \times 10^{-5}$
1.254	1.390	6	1.070	$S_0$	$8.503 \times 10^{-4}$	$7.014 \times 10^{-4}$	$4.906 \times 10^{-4}$	$3.753 \times 10^{-4}$	$2.775 \times 10^{-4}$
				$S_1^+$	$5.447 \times 10^{-6}$	$1.498 \times 10^{-5}$	$2.952 \times 10^{-5}$	$4.842 \times 10^{-5}$	$8.417 \times 10^{-5}$
				$S_1^-$	$1.364 \times 10^{-5}$	$3.508 \times 10^{-5}$	$5.504 \times 10^{-5}$	$7.190 \times 10^{-5}$	$9.746 \times 10^{-5}$
				$S_1$	$8.178 \times 10^{-6}$	$2.168 \times 10^{-5}$	$3.803 \times 10^{-5}$	$5.625 \times 10^{-5}$	$8.859 \times 10^{-5}$
1.286	1.332	5	1.070	$S_0$	$3.220 \times 10^{-3}$	$1.305 \times 10^{-3}$	$7.822 \times 10^{-4}$	$5.386 \times 10^{-4}$	$3.514 \times 10^{-4}$
				$S_1^+$	$4.684 \times 10^{-6}$	$2.351 \times 10^{-5}$	$4.084 \times 10^{-5}$	$5.964 \times 10^{-5}$	$9.132 \times 10^{-5}$
				$S_1^-$	$7.964 \times 10^{-6}$	$3.755 \times 10^{-5}$	$5.827 \times 10^{-5}$	$7.556 \times 10^{-5}$	$9.941 \times 10^{-5}$
				$S_1$	$5.777 \times 10^{-6}$	$2.819 \times 10^{-5}$	$4.665 \times 10^{-5}$	$6.495 \times 10^{-5}$	$9.402 \times 10^{-5}$
1.254	1.332	5	1.070	$S_0$	$5.357 \times 10^{-4}$	$8.236 \times 10^{-4}$	$6.205 \times 10^{-4}$	$4.710 \times 10^{-4}$	$3.302 \times 10^{-4}$
				$S_1^+$	$8.404 \times 10^{-6}$	$2.938 \times 10^{-5}$	$4.753 \times 10^{-5}$	$6.466 \times 10^{-5}$	$9.089 \times 10^{-5}$
				$S_1^-$	$1.425 \times 10^{-5}$	$4.921 \times 10^{-5}$	$7.176 \times 10^{-5}$	$8.621 \times 10^{-5}$	$1.047 \times 10^{-4}$
				$S_1$	$1.035 \times 10^{-5}$	$3.599 \times 10^{-5}$	$5.561 \times 10^{-5}$	$7.184 \times 10^{-5}$	$9.549 \times 10^{-5}$
1.286	1.390	5	1.070	$S_0$	$2.959 \times 10^{-3}$	$9.218 \times 10^{-4}$	$5.657 \times 10^{-4}$	$4.079 \times 10^{-4}$	$2.873 \times 10^{-4}$
				$S_1^+$	$2.653 \times 10^{-6}$	$1.108 \times 10^{-5}$	$2.521 \times 10^{-5}$	$4.584 \times 10^{-5}$	$8.646 \times 10^{-5}$
				$S_1^-$	$5.820 \times 10^{-6}$	$2.194 \times 10^{-5}$	$3.881 \times 10^{-5}$	$5.776 \times 10^{-5}$	$9.094 \times 10^{-5}$
				$S_1$	$3.709 \times 10^{-6}$	$1.470 \times 10^{-5}$	$2.974 \times 10^{-5}$	$4.981 \times 10^{-5}$	$8.795 \times 10^{-5}$
1.254	1.390	5	1.070	$S_0$	$8.503 \times 10^{-4}$	$7.014 \times 10^{-4}$	$4.906 \times 10^{-4}$	$3.753 \times 10^{-4}$	$2.775 \times 10^{-4}$
				$S_1^+$	$5.731 \times 10^{-6}$	$1.568 \times 10^{-5}$	$3.052 \times 10^{-5}$	$4.927 \times 10^{-5}$	$8.454 \times 10^{-5}$
				$S_1^-$	$1.240 \times 10^{-5}$	$3.209 \times 10^{-5}$	$5.124 \times 10^{-5}$	$6.832 \times 10^{-5}$	$9.527 \times 10^{-5}$
				$S_1$	$7.954 \times 10^{-6}$	$6.345 \times 10^{-5}$	$3.743 \times 10^{-5}$	$5.569 \times 10^{-5}$	$8.812 \times 10^{-5}$
1.254	1.332	6	1.070	$S_0$	$5.357 \times 10^{-4}$	$8.236 \times 10^{-4}$	$6.205 \times 10^{-4}$	$4.710 \times 10^{-4}$	$3.302 \times 10^{-4}$
				$S_1^+$	$8.095 \times 10^{-6}$	$2.266 \times 10^{-5}$	$4.634 \times 10^{-5}$	$6.324 \times 10^{-5}$	$9.021 \times 10^{-5}$
				$S_1^-$	$1.533 \times 10^{-5}$	$3.987 \times 10^{-5}$	$7.581 \times 10^{-5}$	$8.999 \times 10^{-5}$	$1.068 \times 10^{-4}$
				$S_1$	$1.051 \times 10^{-5}$	$2.840 \times 10^{-5}$	$5.516 \times 10^{-5}$	$7.216 \times 10^{-5}$	$9.574 \times 10^{-5}$

Table 3, Total, Elastic and Reaction Cross Sections at 14.5 MeV ( in mb )

$\bar{I}_0$	$\bar{I}_s$	$V_{so}$	$\bar{I}_{so}$	$a_2 = 0.1$	$a_2 = 0.3$	$a_2 = 0.5$	$a_2 = 0.7$	$a_2 = 1.0$
1.317	1.447	7	1.07	$\sigma_t$ $2.493 \times 10^3$	$2.564 \times 10^3$	$2.618 \times 10^3$	$2.706 \times 10^3$	$2.899 \times 10^3$
				$\sigma_{e1}$ $1.563 \times 10^3$	$1.383 \times 10^3$	$1.317 \times 10^3$	$1.301 \times 10^3$	$1.335 \times 10^3$
				$\sigma_r$ $0.930 \times 10^3$	$1.181 \times 10^3$	$1.301 \times 10^3$	$1.405 \times 10^3$	$1.565 \times 10^3$
1.317	1.447	7	1.07	$\sigma_t$ $2.580 \times 10^3$	$2.620 \times 10^3$	$2.673 \times 10^3$	$2.755 \times 10^3$	$2.983 \times 10^3$
				$\sigma_{e1}$ $1.677 \times 10^3$	$1.458 \times 10^3$	$1.376 \times 10^3$	$1.348 \times 10^3$	$1.369 \times 10^3$
				$\sigma_r$ $0.903 \times 10^3$	$1.163 \times 10^3$	$1.297 \times 10^3$	$1.407 \times 10^3$	$1.569 \times 10^3$
1.317	1.447	6	1.07	$\sigma_t$ $2.582 \times 10^3$	$2.608 \times 10^3$	$2.659 \times 10^3$	$2.743 \times 10^3$	$2.928 \times 10^3$
				$\sigma_{e1}$ $1.674 \times 10^3$	$1.446 \times 10^3$	$1.363 \times 10^3$	$1.336 \times 10^3$	$1.359 \times 10^3$
				$\sigma_r$ $0.908 \times 10^3$	$1.162 \times 10^3$	$1.297 \times 10^3$	$1.407 \times 10^3$	$1.570 \times 10^3$
1.317	1.447	5	1.07	$\sigma_t$ $2.588 \times 10^3$	$2.603 \times 10^3$	$2.650 \times 10^3$	$2.733 \times 10^3$	$2.920 \times 10^3$
				$\sigma_{e1}$ $1.675 \times 10^3$	$1.439 \times 10^3$	$1.352 \times 10^3$	$1.325 \times 10^3$	$1.349 \times 10^3$
				$\sigma_r$ $0.914 \times 10^3$	$1.164 \times 10^3$	$1.298 \times 10^3$	$1.408 \times 10^3$	$1.571 \times 10^3$
1.317	1.390	6	1.07	$\sigma_t$ $2.572 \times 10^3$	$2.550 \times 10^3$	$2.575 \times 10^3$	$2.640 \times 10^3$	$2.808 \times 10^3$
				$\sigma_{e1}$ $1.716 \times 10^3$	$1.406 \times 10^3$	$1.299 \times 10^3$	$1.258 \times 10^3$	$1.276 \times 10^3$
				$\sigma_r$ $0.856 \times 10^3$	$1.144 \times 10^3$	$1.276 \times 10^3$	$1.382 \times 10^3$	$1.532 \times 10^3$
1.317	1.332	6	1.07	$\sigma_t$ $2.568 \times 10^3$	$2.509 \times 10^3$	$2.512 \times 10^3$	$2.652 \times 10^3$	$2.712 \times 10^3$
				$\sigma_{e1}$ $1.728 \times 10^3$	$1.379 \times 10^3$	$1.251 \times 10^3$	$1.197 \times 10^3$	$1.206 \times 10^3$
				$\sigma_r$ $0.840 \times 10^3$	$1.131 \times 10^3$	$1.261 \times 10^3$	$1.365 \times 10^3$	$1.506 \times 10^3$
1.317	1.390	5	1.07	$\sigma_t$ $2.580 \times 10^3$	$2.554 \times 10^3$	$2.565 \times 10^3$	$2.630 \times 10^3$	$2.799 \times 10^3$
				$\sigma_{e1}$ $1.716 \times 10^3$	$1.397 \times 10^3$	$1.289 \times 10^3$	$1.248 \times 10^3$	$1.267 \times 10^3$
				$\sigma_r$ $0.846 \times 10^3$	$1.147 \times 10^3$	$1.277 \times 10^3$	$1.382 \times 10^3$	$1.533 \times 10^3$
1.317	1.332	5	1.07	$\sigma_t$ $2.577 \times 10^3$	$2.503 \times 10^3$	$2.504 \times 10^3$	$2.553 \times 10^3$	$2.704 \times 10^3$
				$\sigma_{e1}$ $1.728 \times 10^3$	$1.368 \times 10^3$	$1.241 \times 10^3$	$1.187 \times 10^3$	$1.198 \times 10^3$
				$\sigma_r$ $0.849 \times 10^3$	$1.135 \times 10^3$	$1.263 \times 10^3$	$1.366 \times 10^3$	$1.506 \times 10^3$
1.286	1.390	6	1.07	$\sigma_t$ $2.323 \times 10^3$	$2.387 \times 10^3$	$2.449 \times 10^3$	$2.534 \times 10^3$	$2.718 \times 10^3$
				$\sigma_{e1}$ $1.430 \times 10^3$	$1.286 \times 10^3$	$1.209 \times 10^3$	$1.184 \times 10^3$	$1.216 \times 10^3$
				$\sigma_r$ $0.893 \times 10^3$	$1.102 \times 10^3$	$1.241 \times 10^3$	$1.349 \times 10^3$	$1.502 \times 10^3$
1.254	1.390	6	1.07	$\sigma_t$ $2.150 \times 10^3$	$2.284 \times 10^3$	$2.360 \times 10^3$	$2.452 \times 10^3$	$2.644 \times 10^3$
				$\sigma_{e1}$ $1.377 \times 10^3$	$1.202 \times 10^3$	$1.140 \times 10^3$	$1.126 \times 10^3$	$1.167 \times 10^3$
				$\sigma_r$ $0.773 \times 10^3$	$1.082 \times 10^3$	$1.220 \times 10^3$	$1.326 \times 10^3$	$1.447 \times 10^3$

Table 3 ( continued )

$r_0$	$r_s$	$V_{so}$	$r_{so}$	$a_2 = 0.1$	$a_2 = 0.3$	$a_2 = 0.5$	$a_2 = 0.7$	$a_2 = 1.0$
1.286	1.332	5	1.07	$\sigma_t$ $2.350 \times 10^3$	$2.353 \times 10^3$	$2.357 \times 10^3$	$2.437 \times 10^3$	$2.602 \times 10^3$
				$\sigma_{e1}$ $1.486 \times 10^3$	$1.250 \times 10^3$	$1.145 \times 10^3$	$1.107 \times 10^3$	$1.132 \times 10^3$
				$\sigma_r$ $0.864 \times 10^3$	$1.103 \times 10^3$	$1.230 \times 10^3$	$1.330 \times 10^3$	$1.470 \times 10^3$
1.254	1.332	5	1.07	$\sigma_t$ $2.206 \times 10^3$	$2.241 \times 10^3$	$2.274 \times 10^3$	$2.343 \times 10^3$	$2.518 \times 10^3$
				$\sigma_{e1}$ $1.420 \times 10^3$	$1.159 \times 10^3$	$1.070 \times 10^3$	$1.043 \times 10^3$	$1.079 \times 10^3$
				$\sigma_r$ $0.786 \times 10^3$	$1.082 \times 10^3$	$1.203 \times 10^3$	$1.300 \times 10^3$	$1.439 \times 10^3$
1.286	1.390	5	1.07	$\sigma_t$ $2.371 \times 10^3$	$2.407 \times 10^3$	$2.453 \times 10^3$	$2.531 \times 10^3$	$2.713 \times 10^3$
				$\sigma_{e1}$ $1.452 \times 10^3$	$1.288 \times 10^3$	$1.204 \times 10^3$	$1.178 \times 10^3$	$1.210 \times 10^3$
				$\sigma_r$ $0.919 \times 10^3$	$1.119 \times 10^3$	$1.249 \times 10^3$	$1.353 \times 10^3$	$1.503 \times 10^3$
1.254	1.390	5	1.07	$\sigma_t$ $2.223 \times 10^3$	$2.310 \times 10^3$	$2.368 \times 10^3$	$2.452 \times 10^3$	$2.642 \times 10^3$
				$\sigma_{e1}$ $1.417 \times 10^3$	$1.206 \times 10^3$	$1.137 \times 10^3$	$1.122 \times 10^3$	$1.163 \times 10^3$
				$\sigma_r$ $0.806 \times 10^3$	$1.104 \times 10^3$	$1.231 \times 10^3$	$1.331 \times 10^3$	$1.479 \times 10^3$
1.286	1.332	6	1.07	$\sigma_t$ $2.293 \times 10^3$	$2.334 \times 10^3$	$2.370 \times 10^3$	$2.438 \times 10^3$	$2.606 \times 10^3$
				$\sigma_{e1}$ $1.458 \times 10^3$	$1.248 \times 10^3$	$1.150 \times 10^3$	$1.113 \times 10^3$	$1.138 \times 10^3$
				$\sigma_r$ $0.835 \times 10^3$	$1.085 \times 10^3$	$1.220 \times 10^3$	$1.325 \times 10^3$	$1.468 \times 10^3$
1.254	1.332	6	1.07	$\sigma_t$ $2.130 \times 10^3$	$2.215 \times 10^3$	$2.264 \times 10^3$	$2.340 \times 10^3$	$2.519 \times 10^3$
				$\sigma_{e1}$ $1.378 \times 10^3$	$1.155 \times 10^3$	$1.072 \times 10^3$	$1.046 \times 10^3$	$1.083 \times 10^3$
				$\sigma_r$ $0.752 \times 10^3$	$1.060 \times 10^3$	$1.191 \times 10^3$	$1.293 \times 10^3$	$1.436 \times 10^3$

Table 4. Total and Elastic Cross Sections at 7.55 MeV ( in barns)

$r_0^1$	$r_s^1$	$V_{s0}$	$r_{s0}^1$	$a_2=0.1$	$a_2=0.3$	$a_2=0.5$	$a_2=0.7$	$a_2=1.0$
1.317	1.317	7	1.317	$\sigma_t$ 3.967	3.759	3.613	3.558	3.611
	1.447		1.317	$\sigma_{el}$ 2.871	2.506	2.232	2.071	1.965
1.317	1.447	7	1.070	$\sigma_t$ 4.031	3.801	3.642	3.578	3.625
	1.447		1.070	$\sigma_{el}$ 2.895	2.518	2.235	2.069	1.962
1.317	1.447	6	1.070	$\sigma_t$ 3.966	3.759	3.618	3.564	3.618
	1.447		1.070	$\sigma_{el}$ 2.857	2.497	2.224	2.063	1.960
1.317	1.447	5	1.070	$\sigma_t$ 3.867	3.711	3.591	3.549	3.610
	1.447		1.070	$\sigma_{el}$ 2.818	2.478	2.215	2.059	1.958
1.317	1.390	6	1.070	$\sigma_t$ 3.917	3.694	3.539	3.474	3.510
	1.390		1.070	$\sigma_{el}$ 2.865	2.488	2.196	2.012	1.885
1.317	1.332	6	1.070	$\sigma_t$ 3.940	3.656	3.493	3.419	3.435
	1.332		1.070	$\sigma_{el}$ 2.953	2.499	2.189	1.983	1.830
1.317	1.390	5	1.070	$\sigma_t$ 3.820	3.646	3.515	3.462	3.505
	1.390		1.070	$\sigma_{el}$ 2.825	2.468	2.186	2.007	1.883
1.317	1.332	5	1.070	$\sigma_t$ 3.829	3.605	3.467	3.406	3.430
	1.332		1.070	$\sigma_{el}$ 2.906	2.476	2.177	1.976	1.826
1.286	1.390	6	1.070	$\sigma_t$ 3.698	3.526	3.398	3.353	3.416
	1.390		1.070	$\sigma_{el}$ 2.848	2.348	2.087	1.931	1.829
1.254	1.390	6	1.070	$\sigma_t$ 3.547	3.355	3.240	3.221	3.316
	1.390		1.070	$\sigma_{el}$ 2.553	2.192	1.964	1.839	1.767
1.286	1.332	5	1.070	$\sigma_t$ 3.547	3.392	3.285	3.250	3.311
	1.332		1.070	$\sigma_{el}$ 2.849	2.307	2.040	1.871	1.756
1.254	1.332	5	1.070	$\sigma_t$ 3.434	3.230	3.118	3.100	3.192
	1.332		1.070	$\sigma_{el}$ 2.568	2.145	1.902	1.764	1.683
1.286	1.390	5	1.070	$\sigma_t$ 3.553	3.454	3.365	3.338	3.410
	1.390		1.070	$\sigma_{el}$ 2.783	2.325	2.076	1.925	1.826
1.254	1.390	5	1.070	$\sigma_t$ 3.444	3.307	3.219	3.211	3.312
	1.390		1.070	$\sigma_{el}$ 2.513	2.178	1.957	1.834	1.764
1.286	1.332	6	1.070	$\sigma_t$ 3.698	3.462	3.319	3.267	3.318
	1.332		1.070	$\sigma_{el}$ 2.921	2.332	2.053	1.880	1.761
1.254	1.332	6	1.070	$\sigma_t$ 3.545	3.275	3.140	3.112	3.198
	1.332		1.070	$\sigma_{el}$ 2.617	2.161	1.911	1.771	1.687

Table 5-1 Total, Elastic and Inelastic Cross Sections at 1.5 MeV (in barns)

		$a_2 = 0.1$	$a_2 = 0.3$	$a_2 = 0.5$	$a_2 = 0.7$	$a_2 = 1.0$
1.317	1.317	$\sigma_t$ 3.9942	3.3989	3.2823	3.3554	3.6911
		$\sigma_{el}$ 2.9980	2.1957	2.1296	2.2002	2.4446
		$\sigma_{in}$ 0.5416	0.7172	0.6745	0.6633	0.7086
1.317	1.447	$\sigma_t$ 4.2174	3.4747	3.3206	3.3778	3.7025
		$\sigma_{el}$ 3.1736	2.2381	2.1492	2.2118	2.4513
		$\sigma_{in}$ 0.5849	0.7376	0.6842	0.6685	0.7107
1.317	1.447	$\sigma_t$ 4.2645	3.5086	3.3340	3.3827	3.7029
		$\sigma_{el}$ 3.1961	2.2532	2.1547	2.2135	2.4509
		$\sigma_{in}$ 0.6272	0.7538	0.6907	0.6714	0.7115
1.317	1.447	$\sigma_t$ 4.2548	3.5371	3.3448	3.3866	3.7038
		$\sigma_{el}$ 3.1730	2.2652	2.1590	2.2148	2.4508
		$\sigma_{in}$ 0.6720	0.7687	0.6963	0.6739	0.7125
1.317	1.390	$\sigma_t$ 4.4360	3.5532	3.3388	3.3540	3.5964
		$\sigma_{el}$ 3.4743	2.2497	2.0924	2.1154	2.3161
		$\sigma_{in}$ 0.5309	0.7840	0.7347	0.7107	0.7288
1.317	1.332	$\sigma_t$ 4.4881	3.6941	3.4451	3.3952	3.5543
		$\sigma_{el}$ 3.5505	2.3178	2.0793	2.0493	2.2027
		$\sigma_{in}$ 0.4885	0.8189	0.8035	0.7800	0.7717
1.317	1.390	$\sigma_t$ 4.3868	3.5821	3.3522	3.3499	3.5976
		$\sigma_{el}$ 3.4151	2.2616	2.0982	2.1178	2.3168
		$\sigma_{in}$ 0.5818	0.8003	0.7411	0.7129	0.7294
1.317	1.332	$\sigma_t$ 4.4280	3.7238	3.4615	3.4032	3.5564
		$\sigma_{el}$ 3.4783	2.3290	2.0866	2.0534	2.2044
		$\sigma_{in}$ 0.5435	0.8375	0.8109	0.7830	0.7721
1.286	1.390	$\sigma_t$ 4.2888	3.6700	3.4208	3.4047	3.6194
		$\sigma_{el}$ 2.9564	2.2720	2.1474	2.1808	2.3668
		$\sigma_{in}$ 0.8337	0.8270	0.7433	0.7035	0.7106
1.254	1.390	$\sigma_t$ 4.7804	3.6143	3.4387	3.4457	3.6476
		$\sigma_{el}$ 3.5863	2.2811	2.2116	2.2587	2.4299
		$\sigma_{in}$ 0.5503	0.7588	0.7030	0.6752	0.6876
1.286	1.332	$\sigma_t$ 4.7834	3.8355	3.5057	3.4314	3.5655
		$\sigma_{el}$ 3.5265	2.3268	2.0962	2.0830	2.2397
		$\sigma_{in}$ 0.7887	0.8806	0.8202	0.7762	0.7533

Table 5-1 (continued)

$r_0$	$r_s$	$V_{SO}$	$r_{SO}$	$a_2 = 0.1$	$a_2 = 0.3$	$a_2 = 0.5$	$a_2 = 0.7$	$a_2 = 1.0$
1.254	1.332	5	1.07	$\sigma_t$ 4.8458	3.6583	3.4424	3.4191	3.5704
				$\sigma_{e1}$ 3.6927	2.2597	2.1086	2.1263	2.2881
				$\sigma_{in}$ 0.4702	0.7789	0.7586	0.7337	0.7230
1.286	1.390	5	1.07	$\sigma_t$ 4.5845	3.7305	3.4418	3.4142	3.6226
				$\sigma_{e1}$ 3.1561	2.3015	2.1565	2.1852	2.3686
				$\sigma_{in}$ 0.8721	0.8440	0.7507	0.7070	0.7117
1.254	1.390	5	1.07	$\sigma_t$ 4.8260	3.6452	3.4537	3.4533	3.6506
				$\sigma_{e1}$ 3.6116	2.2937	2.2177	2.2623	2.4316
				$\sigma_{in}$ 0.5510	0.7682	0.7083	0.6777	0.6882
1.286	1.332	6	1.07	$\sigma_t$ 4.3638	3.5749	2.3765	3.4184	3.5614
				$\sigma_{e1}$ 3.2147	2.2849	2.0825	2.0767	2.3373
				$\sigma_{in}$ 0.7509	0.8612	0.8114	0.7723	0.7523

## DISCUSSION

P. RIBON: The problem of uniqueness of parameters is a very frequent problem in nuclear data evaluation. In the conclusions of your abstract, you expose that you obtained several parameters sets providing satisfactory explanation of experimental data. Can you comment about the origin of these different sets, and how it would be possible to select the best one.

H. YAMAKOSHI: Prior to answer the question, the following may be mentioned in order to note on criteria imposed on calculated nuclear data to check if a given set of parameter values is plausible or not. The criteria in this study consists of experimental data for following items: Angle dependence of percent polarization at 24 MeV, total and elastic cross sections at 14.5 MeV, 7.55 MeV and 1.5 MeV, angle dependence of elastic differential cross section at 14.5 MeV, 7.55 MeV and 1.5 MeV, neutron strength functions for s-wave and p-wave and excitation curves for inelastic neutron scattering up to third level.

Now, cause of existence of several plausible parameter sets can be ascribed to following two reasons. (A) Experimental data for each item has uncertainty in its value because of experimental error. (B) For monotonic change in value of a parameter arbitrarily chosen in parameter space, experimental data in some items persist that value of the parameter in certain range can explain experiments well, while experimental data in another group of items persist that value of the parameter in quite other range can explain experimental data well. This sort of inconsistency is one of the causes of the possibility of existence of several plausible parameter sets.

As a significant example, just take  $a_2$  dependence. In accordance with increase of  $a_2$  value from 0.1 to 1.0, calculated s-wave strength function has a tendency of decreasing from value far larger than experimental value to value smaller than experimental value. This situation suggests that possible  $a_2$  value lies between 0.5 and 0.7, while comparison between calculated and experimental data for angular distribution of differential elastic scattering at 14.5 MeV suggests that possible  $a_2$  value is between 0.7 and 1.0. Similar discussion for total cross section at 7.55 MeV yields that possible  $a_2$  value is between 0.3 to 0.5, while for total cross section at 14.5 MeV, possible  $a_2$  value is between 0.7 and 1.0. Besides, p-wave strength function suggests that possible  $a_2$  value is between 0.1 and 0.5.

As a whole, judging from experimental error for each item, it is possible to say that the most plausible value of  $a_2$  is around 0.5. One cannot also beat the case that the most plausible value of  $a_2$  is around 0.7. One confronts to similar situations for other parameters.

Thus, it is possible to say that there are several recommendable parameter sets for  $^{56}\text{Fe}$  calculation in addition to the set shown in the text. The most plausible parameter set should be chosen from more global view point. That is, the most plausible parameter set should explain experimental data on the average over medium weight nucleus region. Even if a parameter set explains experimental data for  $^{56}\text{Fe}$ , it is not always true that the parameter set can explain experimental data for other nucleus well.

## III-2. OPTICAL MODEL CALCULATIONS

AT

RENSSELAER POLYTECHNIC INSTITUTE\*

Jose' M. Sierra and Paul J. Turinsky#  
 Department of Nuclear Engineering  
 Rensselaer Polytechnic Institute  
 Troy, New York, USA 12181

## ABSTRACT

Experimental evidence of deep minima in the p-wave neutron strength function about mass numbers 55 and 160 has been studied via optical model calculation. By employing a spherical optical model with an angular momentum dependent ( $\ell$ ) imaginary potential strength ( $W^{(\ell)}$ ), a global optical model parameter set has been determined which accurately predicts the s and p-wave neutron strength functions and potential scattering radius over mass numbers 40-240. Extension of the angular momentum dependent optical potential to coupled-channel calculations treating  $0^+ - 2^+$  collective state coupling, improved the agreement between prediction and experimental data. The values  $W^{(0)} = 12 \text{ MeV}$  and  $W^{(1)} = 1.5 \text{ MeV}$  employed in the calculations indicate that p-wave neutrons effectively interact less weakly than s-wave neutrons with the target nucleus.

---

\* Research supported by the USAEC under Contract AT(11-1)-3058.

#Present Address: Senior Engineer, Westinghouse Electric Corporation  
 Nuclear Center, Box 355  
 Pittsburgh, Pennsylvania, USA 15230

## I. INTRODUCTION

High resolution neutron interaction experiments have made available p-wave neutron strength function ( $S_1$ ) values, in addition to refined s-wave neutron strength function ( $S_0$ ) and potential scattering radii ( $R'$ ) values, as a function of mass number (A). Experiments conducted at the RPI Linear Accelerator Laboratory<sup>(1)</sup> and other facilities revealed strong minima in  $S_1$ , where at A=55 and 160 values of  $\approx 4 \times 10^{-6}$  and  $\approx 1 \times 10^{-5}$  were observed, respectively.

This new data on  $S_1$  has regenerated an interest in the ability of optical model calculations to simultaneously accurately predict  $S_0$ ,  $S_1$  and  $R'$  versus mass number A from 40 to 240. Previous work performed by Perey-Buck,<sup>(2)</sup> Moldauer,<sup>(3)</sup> and by others<sup>(4-5)</sup> on obtaining a global optical model parameter set was biased towards simultaneous fits to  $S_0$  and  $R'$  versus A, since scarce data existed on  $S_1$  values. With interesting  $S_1$  data available, we have attempted to obtain a global optical model parameter set with as few additional free parameters that also accurately predicts  $S_1$  versus A, in addition to  $S_0$  and  $R'$ .

## II. ANGULAR MOMENTUM INDEPENDENT OPTICAL MODEL

Restricting our discussion to low energy neutron interactions, the basis of optical model calculations is that the interaction of the incident neutron and target nucleus can be modeled by a complex central potential, hence, the optical model Schrödinger's equation becomes

$$-\frac{\hbar^2}{2m} \nabla^2 \Psi(\vec{r}) + V_{Op}(|\vec{r}|) \Psi(\vec{r}) = E \Psi(\vec{r}) \quad (1)$$

where

$$V_{Op}(|\vec{r}|) = V_{Real}(|\vec{r}|) + i V_{Imag}(|\vec{r}|). \quad (2)$$

Physically the real potential accounts for shape elastic scattering; whereas, the imaginary potential accounts for excitations of the target nucleus which would generally remove the incident neutron from its entrance channel and lead to resonance behavior. Hence, the magnitude of  $V_{Imag}(|\vec{r}|)$  can be interpreted as the entrance channel removal interaction strength exerted between the incident neutron and the target nucleus.

Noting the simplicity of the Hamiltonian operator in Eq. (1), the incident neutron's wave function  $\Psi(\vec{r})$  is easily numerically determined. We have employed the ABACUS II computer-code<sup>(6)</sup> for the numerical determination of  $\Psi(\vec{r})$ . Once having determined this wave function, the energy averaged neutron total, shape elastic and removal cross sections can be computed. Alternately, the neutron strength function and potential scattering radius values can be evaluated, where as usual, we define the angular momentum dependent  $(\ell)$  strength function by

$$S_l = \frac{1}{2l+1} \sum_J \frac{g_J \langle \Gamma_l^J \rangle}{\sqrt{E} V_l \langle D^J \rangle} \quad (3)$$

and potential scattering radii by

$$R' = \lim_{E \rightarrow 0} \left( \frac{\langle \sigma_{se} \rangle}{4\pi} \right)^{\frac{1}{2}} \quad (4)$$

with

$$V_l = P_l / kR \quad (5)$$

$g_J = (2J+1)/2$  ... statistical spin factor,

$P_l$  ... neutron penetration factor for  $l$ -waves,

$k$  ... neutron wave number,

$R$  ... channel radius,

$\langle \Gamma_l^J \rangle$  ... average neutron total width for angular momentum  $l$  and total momentum  $J$ ,

$\langle D^J \rangle$  ... average resonance spacing for total momentum  $J$ ,

$\langle \sigma_{se} \rangle$  ... shape elastic neutron cross section

It is recognized that the potential scattering radii can be associated with hard sphere elastic scattering interaction; whereas, the strength function indicates the target nucleus strength to enter into resonance reactions with either s or p-wave incident neutrons.

Having defined  $S_0, S_1$  and  $R'$  and indicated they can be obtained from the model systems wave function,  $\Psi(\vec{r})$ , we now consider the construction of the optical potential,  $V_{op}(|\vec{r}|)$ . As usual, we express  $V_{op}(|\vec{r}|)$  as the sum of the potential well and spin-orbit real terms plus an imaginary term, hence

$$V_{op}(|\vec{r}|) = -V_{Re} f(|\vec{r}|, a_{Re}, R) - V_{so} \frac{\hbar^2}{4\pi} \vec{\sigma} \cdot \vec{l} \frac{1}{r} \left| \frac{df(|\vec{r}|, a_{so}, R)}{dr} \right| - 4i W a_{Im} g(|\vec{r}|, a_{Im}, R+b). \quad (6)$$

The real form function,  $f$ , has generally been chosen to reflect the target nucleus nucleon density via the Saxon-Wood's form

$$f(|\vec{r}|, a, R) = \left[ 1 + \exp\left(\frac{r-R}{a}\right) \right]^{-1} \quad (7)$$

which we have also employed.

By contrast, several imaginary form functions,  $g$ , have been employed in the past, in particular Moldauer employed a shifted Gaussian form given by

$$g(|\vec{r}|, a_{Im}, R+b) = \frac{1}{4a_{Im}} \exp\left[-\left(\frac{r-R-b}{a_{Im}}\right)^2\right] \quad (8)$$

and Perey-Buck, ourselves and others have used the Saxon-Wood's derivative form

$$g(|\vec{r}|, a_{Im}, R+b) = \left| \frac{df(r, a_{Im}, R+b)}{dr} \right| \quad (9)$$

where  $R=r_0 A^{1/3}$ . It will be noted that the only quantum number dependence of the chosen optical potential is contained in the spin-orbit potential via  $(\vec{\sigma} \cdot \vec{l})$ . Theoretical calculations <sup>(7-8)</sup> do indicate considerably more quantum number dependence, but to minimize the number of unknown optical parameters to be determined there is a strong incentive to ignore this fact. We refer to the proposed potential as the angular momentum independent spherical optical potential.

Having specified the angular momentum independent optical model form, we have attempted to determine a global optical model parameter set which simultaneously predicts values of  $S_0$ ,  $S_1$ , and  $R'$  over the mass number range  $A=40-240$  consistent with experimental values. We were particularly interested in predicting the recently observed deep minima in  $S_1$  about  $A=55$  and  $160$ . Table I presents the optical parameter set we thus determined and contrasts our set to optical parameter sets proposed by Perey-Buck and Moldauer.

It should be recalled that both of the previous works were primarily concerned with predicting  $S_0$  and  $R'$ , since little data on  $S_1$  was then available. In Figures (1-3) values of  $S_0$ ,  $S_1$ , and  $R'$  versus mass number  $A$  are presented respectively, as calculated by Perey-Buck, Moldauer and our work and experimentally determined. Moldauer predicts  $S_0$  very accurately; whereas, our work underpredicts the  $S_0$  minima due to our heavy bias on accurately predicting  $S_1$ . Figure (2) reveals that indeed we have improved upon former works in predicting  $S_1$  versus  $A$ , particularly in the deep  $S_1$  minima. It is quite surprising that Moldauer's work predicted the deep  $S_1$  minima about  $A=55$  before any strong supporting experimental evidence. Finally, Figure (3) clearly illustrates the trouble we encountered in accurately predicting  $R'$  in conjunction with  $S_0$  and  $S_1$ . With considerable effort expended on obtaining a global optical parameter set that simultaneously predicts  $S_0$ ,  $S_1$ , and  $R'$  versus  $A$  and the poor results indicated in Figures (1-3), we concluded that the employed angular momentum independent spherical optical model was inadequate.

### III. ANGULAR MOMENTUM DEPENDENT OPTICAL MODEL

Concluding that an angular momentum dependent spherical optical model was required, we have attempted to construct such a model with a minimum of additional unknown optical parameters. With bound state calculations indicating only a weak dependence [other than spin-orbit force] of the real potential,  $V_{\text{Real}}(\vec{r})$ , on the bound state particle angular momentum, we chose to place the total angular momentum dependence of the optical potential on the imaginary term,  $V_{\text{Imag}}(\vec{r})$ .

To minimize the additional number of optical parameters introduced, angular momentum dependence was restricted to the potential strength, hence

$$V_{\text{Imag}}(i\vec{r}) = -4W^{(l)}a_{\text{Im}} \left| \frac{df(|\vec{r}|, a_{\text{Im}}, R+b)}{dr} \right|. \quad (10)$$

Theoretical derivations<sup>(7-8)</sup> of the optical potential indicate angular momentum dependence, but little information exists to support the form we have assumed.

The proposed angular momentum dependent spherical optical potential was then employed to obtain an associated set of global optical parameters which would simultaneously predict  $S_0$ ,  $S_1$ , and  $R'$  from  $A=40-240$ . Table II presents the values we obtained, and contrasts them (Table I) to optical parameter values obtained by Perey-Buck and Moldauer. It is noted that our real potential employs a smaller diffuseness length,  $a_{\text{Re}}$ , implying a sharper nucleon surface. In contrast to previous work which has chosen to restrict  $a_{\text{So}}=a_{\text{Re}}$ , we have chosen  $a_{\text{So}}=a_{\text{Im}}$ . The imaginary potential shape employed by Moldauer and our work were found very similar, even though different imaginary form functions,  $g$ , were employed. Most interestingly, we determined  $W^{(0)}=12 \text{ MeV}$  and  $W^{(1)}=1.5 \text{ MeV}$ . The optimum value of  $W^{(1)}$  to employ was found not very uniquely specified, but all acceptable values of  $W^{(1)}$  were considerably smaller than  $W^{(0)}$ . We conclude from the large magnitude of  $(W^{(0)}/W^{(1)})$  that s-wave neutrons effectively interact with the target nucleus much stronger than p-wave neutrons. A theoretical derivation of the optical potential in a (2 particle-1-hole) basis is underway to determine whether a simple mechanism for this behavior can be identified.

Values of  $S_0$ ,  $S_1$ , and  $R'$  versus mass number  $A$  are presented in Figures(4-6) using the angular momentum dependent spherical optical model. The simultaneous fit to these three quantities is very accurate over a majority of the mass number range. As illustrated, calculations using the ABACUS II computer code were performed at three different neutron energies, revealing the care that should be exercised in interpreting the adequacy of the fit in the energy sensitive strength function peaks. For certain mass number ranges where either  $S_0$  or  $S_1$  reach maxima or minima, agreement between prediction and data is less adequate. Following the work of Perey-Buck<sup>(2)</sup> we attributed this disagreement to be due to the presence of low lying collective target nucleus states which could easily be excited by the incident neutron. With our spherical optical model not modeling such collective state excitations, we extended our angular momentum dependent optical model to coupled-channel calculations anticipating improved agreement in predicted and measured  $S_0$ ,  $S_1$ , and  $R'$  values.

Briefly reviewing the basis of coupled-channel calculations and employing the notation of Tamura<sup>(9)</sup>, the coupled-channel model Schrödinger equation is given by

$$\left[ q_H - \frac{\hbar^2}{2m} \nabla_{\vec{r}}^2 + V_{op}(\vec{r}) \right] \Psi(\vec{r}, \vec{\xi}) = E \Psi(\vec{r}, \vec{\xi}) \quad (11)$$

where  $\vec{r}$  denotes the incident neutron coordinates and  $\vec{R}$  the collective target nucleus coordinates. Now the collective target nucleus wave function,  $\Phi_{I_n M_n}$  satisfies the Hamiltonian

$$\mathcal{H}_T[\Phi_{I_n M_n}] = \omega_n \Phi_{I_n M_n} \quad (12)$$

for intrinsic momentum  $I_n$  and projection  $M_n$  for energy state  $n$ . The solution of the collective state Hamiltonian equation is well known for vibrator and rotator states and totally specified by the excitation energy,  $\omega_n$ , and deformation parameter,  $\beta$ , associated with each state. Thus by expanding the total system wave function,  $\Psi$ , in the collective state basis, Eq. (11) can be numerically solved, from which energy averaged cross sections,  $S_0$ ,  $S_1$ , and  $R'$  values can be determined. The JUPITER computer code<sup>(9)</sup> was used for these calculations. We recognize that  $S_0$ ,  $S_1$ , and  $R'$  values are not only sensitive to the optical parameter set employed, but also the parameters specifying the collective states. In our calculations, the collective state parameters are not free to choose but set to values determined in fitting other data (electromagnetic transition strengths, etc.).

Restricting our coupled-channel calculations to  $0^+ - 2^+$  target nucleus collective states,  $S_0$ ,  $S_1$ , and  $R'$  were computed employing the angular momentum dependent optical parameter set previously given in Table II. The excellent results are presented in Figures (4-6). Both the vibrator state splitting of the  $S_0$  peak about  $A=150$  and minima filling about  $A=100$  and  $240$  are accurately predicted.

Figure (5) illustrates the excellent prediction of the deep  $S_1$  minima, where the presence of vibrator states is noted to fill the  $S_1$  minima about  $A=160$  which does not contradict the existing data. Of particular interest is the  $S_1$  peak about  $A=100$ . Contradicting experimental evidence as to whether this  $S_1$  peak is split has once again appeared.<sup>(10)</sup> Both our spherical and collective optical model calculations do predict splitting. To help understand the mechanism of this splitting, in Figure (7) the  $p^{1/2}$  and  $p^{3/2}$  strength functions are presented as calculated by the spherical and collective angular momentum dependent optical model. The spherical optical model results indicate that the split  $S_1$  peaks about  $A=100$  can be uniquely associated with either the  $p^{1/2}$  or  $p^{3/2}$  states, hence caused by the spin-orbit force. However, when the presence of collective states is modeled via coupled-channel calculations, no such unique identification is possible. Finally, the scarce data on the potential scattering radii is seen in Figure (6) to be accurately fitted via coupled-channel calculations employing the angular momentum dependent optical model.

Having demonstrated that a set of global optical parameters exists for the proposed angular momentum dependent optical model that accurately predicts  $S_0$ ,  $S_1$ , and  $R'$  from  $A=40-240$ , we have employed this model to also compute the energy averaged total neutron cross section. Indeed from a practical viewpoint, we are most interested in obtaining a model that accurately predicts cross sections for use in reactor physics calculations. Figure (8) contrasts predictions of the total neutron cross section energy averaged about 100 keV, obtained by Perey-Buck and our work for both the spherical and collective models. Our work predicts considerably more structure than Perey-Buck's work, which the data weakly supports.

Both models fail to correctly predict the total cross section peak about  $A=150$ , caused by the split  $S_0$  peak. To study the energy sensitivity of our model, the energy averaged total neutron cross section was calculated and contrasted to experimental data in Figure (9) at 30, 100 and 300 keV. As in the previous figure, the data has considerable scatter but does indicate the expected trend of increased total cross section peaks with decreasing neutron energy due to single particle binding. The previously discussed total cross section peak about  $A=150$  is noted to be quite energy sensitive in our calculations, hence difficult to accurately predict. Scatter of data does not enable us to make a firm statement as to the adequacy of our angular momentum optical model in computing the energy averaged total neutron cross section, but we can conclude that general trends are adequately predicted.

#### IV CONCLUSION

Our work has indicated that an angular momentum ( $l$ ) dependent optical model employing a global optical parameter set is required to simultaneously and accurately predict  $S_0$ ,  $S_1$ , and  $R'$  versus mass numbers  $A=40-240$ . We have chosen the angular momentum dependence of the optical model to be totally contained in the strength of the imaginary potential,  $W^{(l)}$  [other than spin orbit force]. Extending this model to coupled-channel calculations, the fine structure of  $S_0$ ,  $S_1$ , and  $R'$  have been accurately predicted. The large magnitude of  $(W^{(l)}/W^{(0)})$  obtained in this work indicates that s-wave neutrons effectively interact much stronger than p-wave neutrons with the target nucleus. Theoretical calculations employing a (2 particle-1 hole) basis are in progress to possibly determine the mechanism of this interaction strength phenomena <sup>(8)</sup>

REFERENCES:

1. R. W. Hockenbury, et. al., Phys. Rev. 178, 1746 (1969).
2. B. Buck and F. Perey, Phys. Rev. Letters 8, 444 (1962).
3. P. A. Moldauer, Nuclear Physics 47, 65 (1963).
4. A. P. Jain, Nuclear Physics 50, 157 (1964).
5. T. K. Kreuger and B. Margolis, Nuclear Physics 28, 578 (1961).
6. E. H. Auerbach, et. al., Report KAPL-3020 (1958).
7. A. M. Lane, Phys. Letters 33B, 274 (1970)
8. J. Sierra and P. J. Turinsky, RPI Linear Accelerator Project Progress Report, January-March, 1973, 31, COO-3058-34.
9. T. Tamura, Rev. Mod. Phys. 37, 679 (1965).
10. H. S. Camarda, Phys. Rev. C, 9, 28 (1974).

FIGURE CAPTIONS:

- Figure (1) The s-wave neutron strength function as calculated by the angular momentum independent spherical optical model.
- Figure (2) The p-wave neutron strength function as calculated by the angular momentum independent spherical optical model.
- Figure (3) The potential scattering radius as calculated by the angular momentum independent spherical optical model.
- Figure (4) The s-wave neutron strength function as calculated by both the angular momentum dependent spherical and collective state optical model.
- Figure (5) The p-wave neutron strength function as calculated by both the angular momentum dependent spherical and collective state optical model.
- Figure (6) The potential scattering radius as calculated by both the angular momentum dependent spherical and collective state optical model.
- Figure (7) The  $p^{1/2}$  and  $p^{3/2}$  neutron strength functions as calculated by both the angular momentum dependent spherical and collective state optical model.
- Figure (8) The energy averaged total neutron cross section at 100 keV as calculated by both an angular momentum independent (Perey-Buck) and dependent (RPI) spherical and collective state optical model.
- Figure (9) The energy averaged total neutron cross section at 30, 100 and 300 keV as calculated by both the angular momentum dependent spherical and collective state optical model.

TABLE CAPTIONS

- Table (I) The angular momentum independent optical parameter sets employed by Perey-Buck, Moldauer, and ourselves used to obtain results shown in Figures (1-3).
- Table (II) The angular momentum dependent optical parameter set we employed to obtain results shown in Figures (4-9).

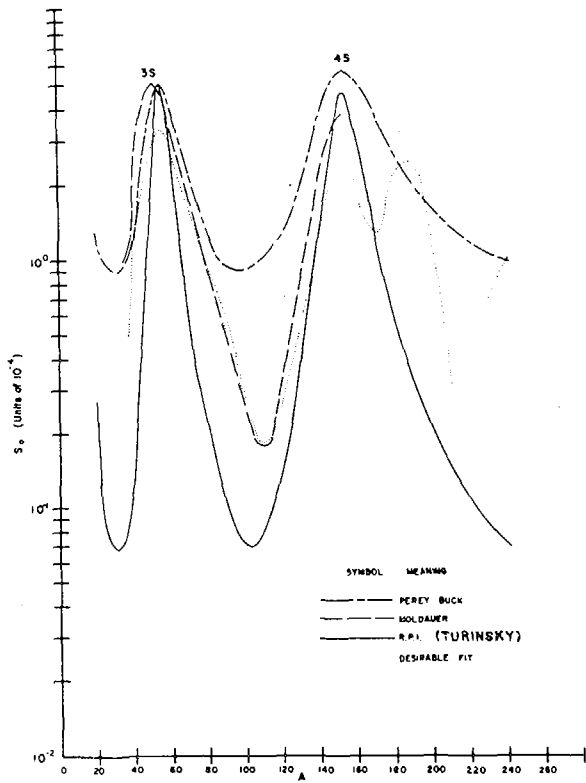


FIG. 1

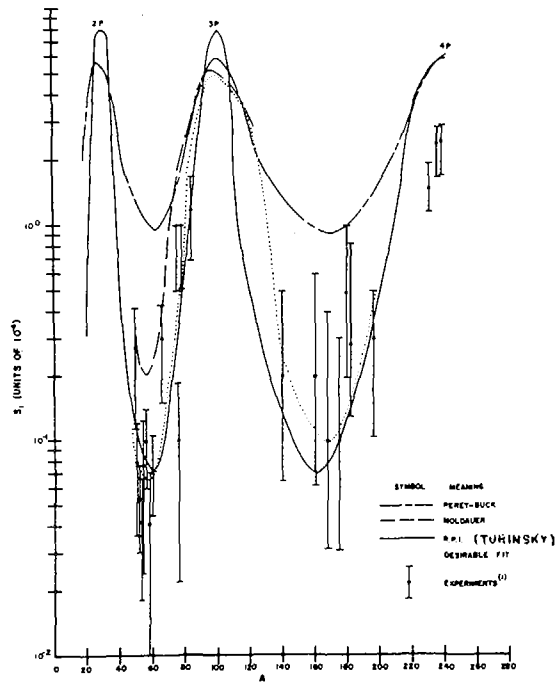


FIG. 2

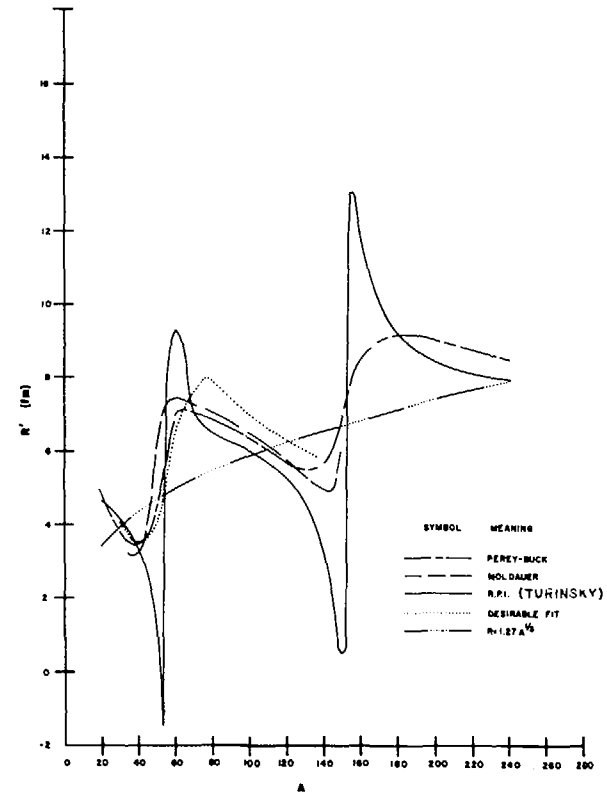


FIG. 3

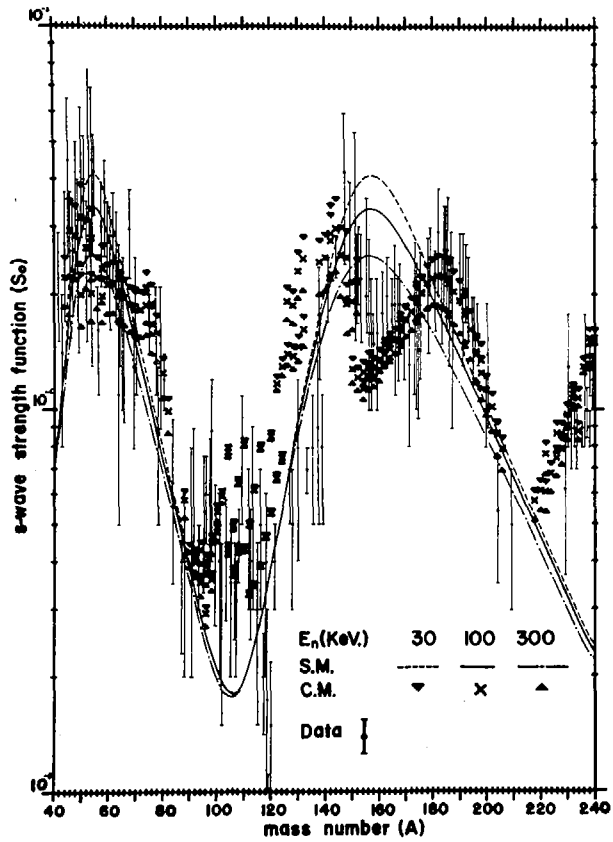


FIG. 4

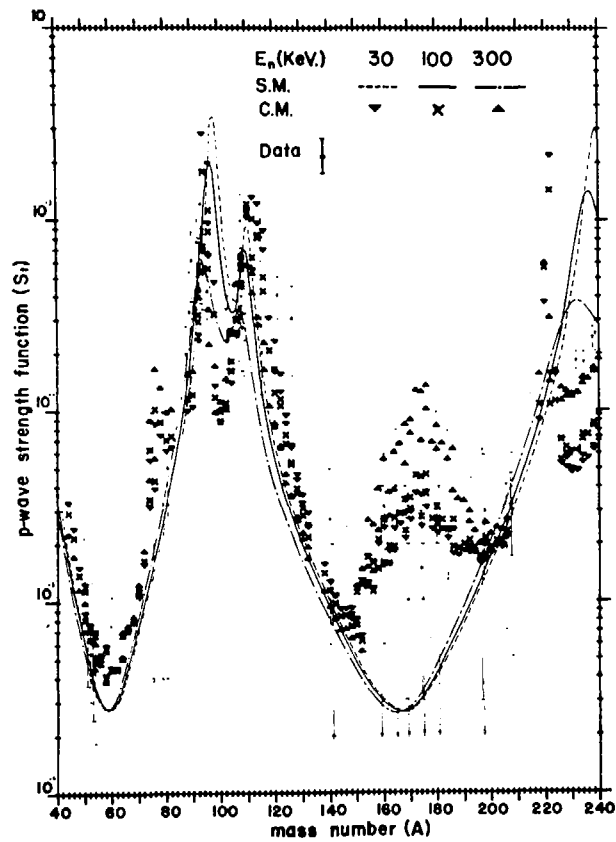


FIG. 5

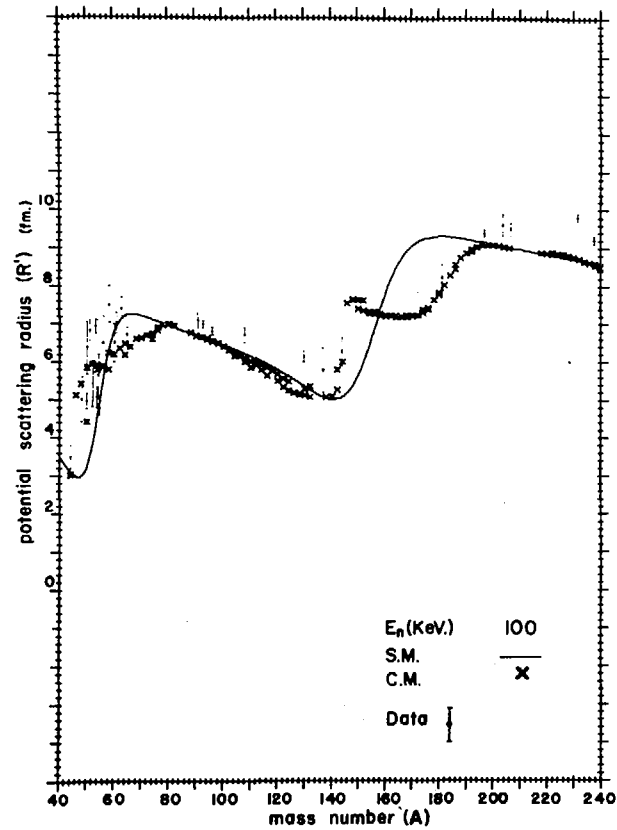


FIG. 6

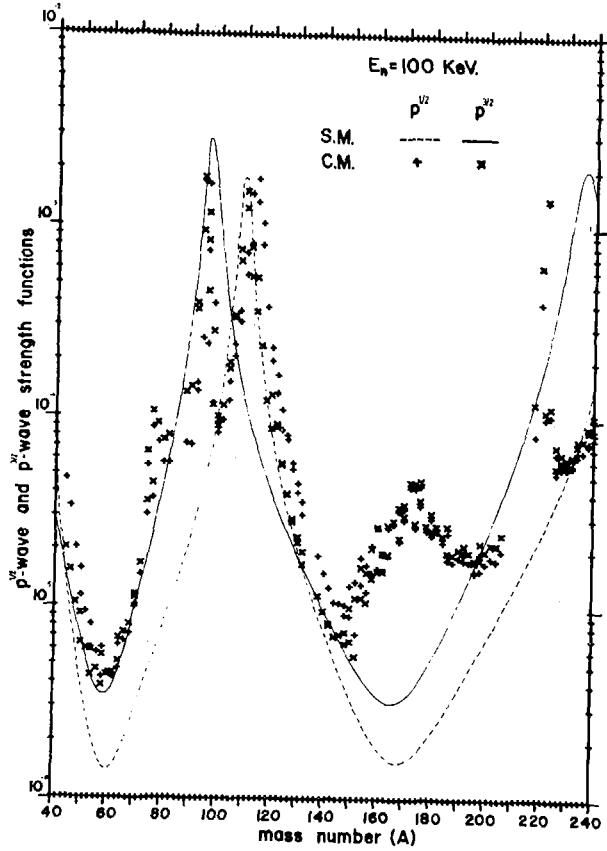


FIG. 7

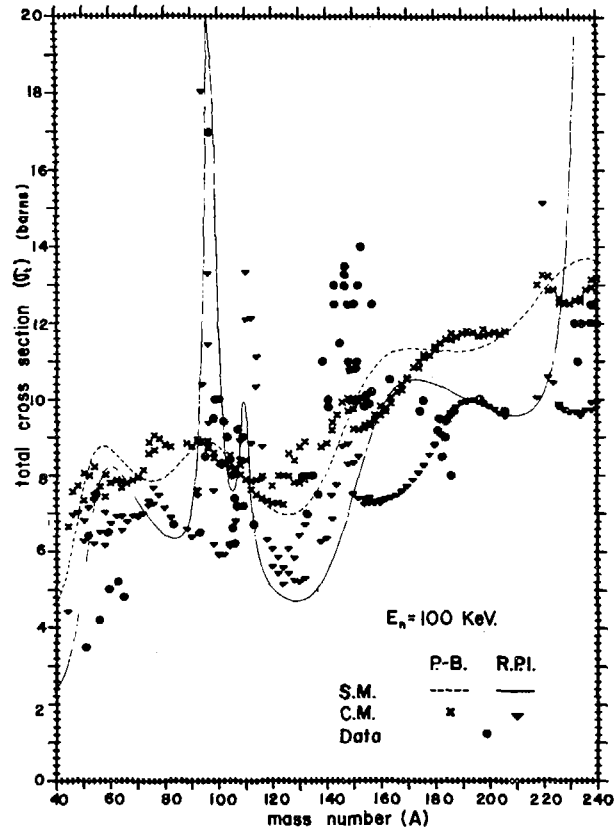


FIG. 8

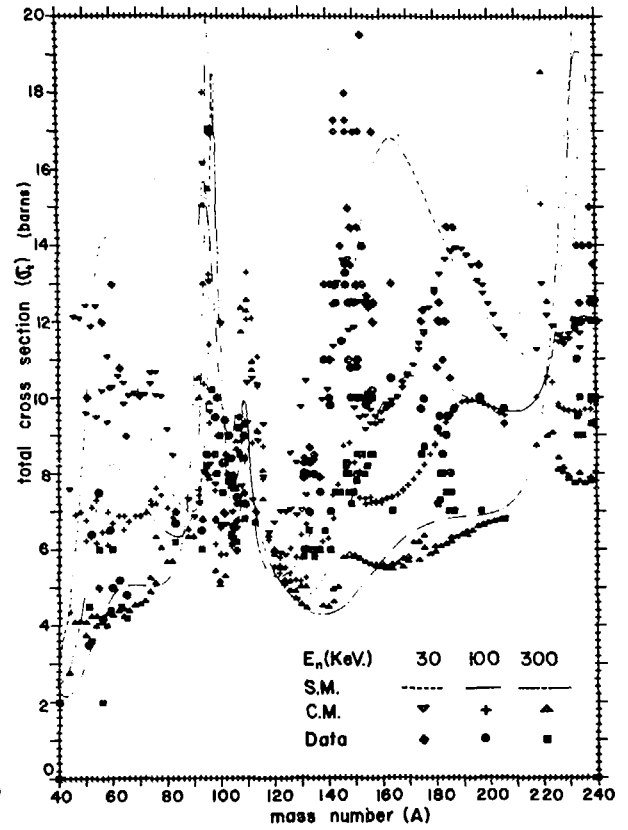


FIG. 9

TABLE I

UNITS: POTENTIAL-MeV, LENGTH-fm

PEREY-BUCK PARAMETERS

$V_{Re} = 48$	$a_{Re} = 0.65$	$R = 1.27A^{1/3}$
$V_{So} = 6$	$a_{So} = 0.65$	
$W = 11$	$a_{Im} = 0.47$	$b = 0.00$

MOLDAUER PARAMETERS

$V_{Re} = 46$	$a_{Re} = 0.62$	$R = 1.16A^{1/3} + 0.6$
$V_{So} = 7$	$a_{So} = 0.62$	
$W = 14$	$a_{Im} = 0.50$	$b = 0.50$

RPI PARAMETERS

$V_{Re} = 52$	$a_{Re} = 0.40$	$R = 1.27A^{1/3}$
$V_{So} = 6$	$a_{So} = 0.65$	
$W = 4$	$a_{Im} = 0.25$	$b = 0.00$

TABLE II

UNITS: POTENTIAL-MeV, LENGTH-fm

$V_{Re} = 47$	$a_{Re} = 0.52$	$R = 1.30A^{1/3}$
$V_{So} = 6$	$a_{So} = 0.23$	
$W^{(b)} = 12$	$a_{Im} = 0.23$	$b = 0.30$
$W^{(l)} = 1.5$		

DISCUSSION

P. RIBON: By increasing slightly the number of adjusted parameters, you have been able to improve the fit to data that you have considered; but do you know which are the consequences for other data such as polarization?

R. BLOCK: No, we do not as yet. As I mentioned in this talk, this study had a limited objective of fitting  $S_0$ ,  $S_1$  and  $R'$  data. No comparisons have been made with polarization data.

### III-3. Analysis of Neutron Cross Sections Using the Coupled-Channel Theory

Shigeya TANAKA

Japan Atomic Energy Research Institute  
Tokai-mura, Naka-gun, Ibaraki-ken

Abstract: Fast neutron total and scattering cross sections calculated with the coupled-channel theory and the spherical optical model are compared with experimental data. The optical-potential parameters used in both the calculations were obtained from comparison of calculations with scattering data for  $^{209}\text{Bi}$ .

The calculations for total cross sections were made for thirty-five nuclides from  $^{23}\text{Na}$  to  $^{239}\text{Pu}$  in the energy range of 0.25 to 15 MeV, and good results were obtained with the coupled-channel calculations. The comparisons of the calculations with the elastic data for about twenty nuclides were made at incident energies of 8 and 14 MeV. In general, the coupled-channel calculations at 8 MeV have given better agreements with the experimental data than the spherical optical-model calculations. At 14 MeV, differences between both the calculations were small. The analysis was also made for the elastic and inelastic scattering by several nuclei such as Fe, Ni,  $^{120}\text{Sn}$ , Pu in the low energy region, and good results have been given by the coupled-channel calculations.

Thus, it is demonstrated that the coupled-channel calculations with one set of the optical parameters well reproduce the total and scattering cross sections over a wide energy and mass region.

#### 1. Introduction

So far many authors have made optical-model analyses for neutron cross sections and proposed optical potentials<sup>1)</sup> which well reproduce the neutron cross sections for a wide energy and mass region. Almost all of those analyses were based on the spherical optical model. Accordingly, those authors did not make predictions or analyses of cross sections for largely deformed nuclei, in which couplings between the states in the ground band are strong. Cross sections for vibrational nuclei, in which couplings between the ground states and the excited states are of medium strength, have usually been calculated in the framework of the spherical optical model, assuming that the effect of couplings on the cross sections is negligible. This assumption,

however, is not always true. Therefore, it will be worthwhile to make a systematic analysis for neutron cross sections over a wide energy and mass region under a condition that the coupling effect is always taken into account in the calculations.

This report aims at a presentation of an optical potential for coupled-channel calculations, which well reproduces neutron cross sections over a wide energy and mass region.

We have already reported<sup>2)</sup> that the angular distributions of elastic neutrons for rare-earth nuclei such as <sup>139</sup>La, <sup>141</sup>Pr, Gd, Fr calculated with the coupled-channel theory fit the experimental data better than those calculated with the spherical optical model. Potential parameters used in those calculations were obtained from the comparison of the spherical optical-model calculations with experimental values for neutron scattering by <sup>209</sup>Bi. The present analysis also starts from the comparison with the <sup>209</sup>Bi data.

## 2. Optical Potential

In the coupled-channel calculation the following potential was used:

$$V(r, \theta, \phi) = -V \frac{1}{1 + \exp[(r-R)/a]} - 4iW \frac{\exp[(r-R)/b]}{\{1 + \exp[(r-R)/b]\}^2} - V_{so} (\vec{\sigma} \cdot \vec{1}) \chi_{\pi}^2 \frac{1}{ar} \frac{\exp[(r-R_0)/a]}{\{1 + \exp[(r-R_0)/a]\}^2},$$

where

$$R = R_0 \{1 + \sum_{\lambda} \beta_{\lambda} Y_{\lambda 0}(\theta)\} \quad \text{for rotational,}$$

$$R = R_0 \{1 + \sum_{\lambda \mu} \alpha_{\lambda \mu} Y_{\lambda \mu}(\theta, \phi)\},$$

$$\alpha_{\lambda \mu} = \beta_{\lambda} \frac{1}{\sqrt{2\lambda+1}} \left( b_{\lambda \mu} + (-)^{\mu} b_{\lambda - \mu}^* \right) \quad \text{for vibrational.}$$

The potential parameters were obtained according to the following procedure:

(1) By using the spherical optical model, the depth parameters  $V$  and  $W$  were searched so that the calculated results were fitted to the elastic data for <sup>209</sup>Bi, and the energy dependence of  $V$  and  $W$  was obtained; while other optical parameters were fixed to some reasonable values. Open circles in Fig. 1 show the values thus obtained. In this figure it is seen that the energy dependence of  $V$  is obviously represented by a straight line. The energy dependence of  $W$

is not so clear. In the present analysis, however, we adopted  $W=2.55\sqrt{E}$ . Crosses are values of Tomita et al.<sup>3)</sup> which were obtained from analysis of  $^{207}\text{Pb}$  data. These values support the present curve for W.

(2) In order to make the potential applicable to a wide mass region, charge symmetry term  $24(N-Z)/A$  was accounted for V. Charge symmetry term for W was not considered in the present analysis, because of its uncertainty in the strength.

(3) The value of coupling parameter taken from published bibliography<sup>4)</sup> or other papers (ref. a, c-h in Table 1 and 2) were used in the coupled-channel calculations.

All the calculated results, i.e. both the coupled-channel and the spherical optical-model calculations, shown hereafter are based on an optical potential with the parameter values thus adopted; i.e.

$$V = 51.85 - 0.33E - 24(N-Z)/A \quad (\text{MeV}), \quad a = 0.65 \quad (\text{fm}),$$

$$W = 2.55\sqrt{E} \quad (\text{MeV}), \quad b = 0.48 \quad (\text{fm}),$$

$$V_{so} = 7.0 \quad (\text{MeV}),$$

$$R_0 = r_0 A^{1/3}, \quad r_0 = 1.25 \quad (\text{fm}).$$

In the present analysis, the coupled-channel calculations were carried out with complex coupling using the code JUPITOR-1<sup>5)</sup> and the rest of calculations using the codes STAX2<sup>6)</sup> and ELIESE3<sup>7)</sup>.

Table 1 shows coupling modes, etc. used in the coupled-channel calculations. In the column of the coupling mode, "rot." stands for rotational, "vibr." for vibrational and "W.C." for weak coupling. Brackets mean average with respect to isotopes. Most nuclides were treated as vibrational. The weak coupling model was applied to odd nuclei such as  $^{27}\text{Al}$ ,  $^{55}\text{Mn}$ , etc., although this application is not appropriate. Calculated results for these nuclei will be shown by dash-dot curves in the figures shown hereafter. Table 2 also shows the coupling modes, etc. for heavier nuclei.

### 3. Analysis for the Total Cross Sections

Foster and Glasgow<sup>8)</sup> have measured the total cross sections for a number of nuclei ranging from H to  $^{239}\text{Pu}$  in the energy range of 2.5 to 15 MeV. Of those data, typical thirty-five nuclei from  $^{23}\text{Na}$  to  $^{239}\text{Pu}$  were chosen in

the present analysis. In order to extend the energy range downwards, the data in the energy range from 0.25 to 2.5 MeV were cited from BNL 325 and its Supplements<sup>9)</sup>. In the following figures from Fig. 2 to Fig. 5, the former data are represented by thick crooked curves and the latter by dashed thick curves. Thin solid and dash-dot curves represent the coupled-channel calculations, and thin dashed curves the spherical optical-model calculations.

Fig. 2 shows the total cross sections from  $^{23}\text{Na}$  to Ni. Large differences between the two kinds of calculations are seen in the low energy region, the region below about 3 MeV, and in almost all cases, the results of coupled-channel calculations give values closer to the experimental data than the spherical ones.

Fig. 3 shows the cross sections for heavier nuclei from Cu to In. The same as the case of Fig. 2 may be said of the fitness. In Fig. 4, agreement of the coupled-channel calculations with the experimental data is fairly good for Sn, Sb,  $^{139}\text{La}$  and  $^{141}\text{Pr}$  even in the low energy region of 1 to 3 MeV. For the total cross sections of largely deformed nuclei such as Gd, Fr, Hf, Ta, W, there appear large differences between the two kinds of curves not only in the low energy region but also in the energy region of 5 to 12 MeV, and, as may be expected, the solid curves give far better agreement with the data than the dashed curves.

The cross sections for actinide nuclei are shown in Fig. 5. For these nuclei, agreement between the coupled-channel calculations and the experimental data is not always good. In the energy region higher than 7 MeV, good agreement was obtained, but in the lower energy region the coupled-channel calculation does not reproduce the experimental maxima and minima. However, this is very much improved by using smaller values of the deformation parameters than those in Table 2. For example, the solid curve for plutonium was calculated using  $\beta_2=0.28$ , but by changing this value to 0.22, as Benzi et al.<sup>10)</sup> used in Helsinki Conf., good fit to the experimental data is obtained. The smaller values of the deformation parameters are supported by the recent Coulomb excitation experiment done by Bermis, Jr. et al.<sup>11)</sup> They reported  $\beta_2=0.223$  and 0.233 for  $^{238}\text{Pu}$  and  $^{240}\text{Pu}$ , respectively, which were calculated on the basis of a deformed Woods-Saxon potential model. As will be shown afterwards, the same thing may be said of angular distributions of the elastic scattering.

#### 4. Scattering Cross Sections at 8 and 14 MeV

Measurement of the elastic scattering cross sections has been made extensively at 8 MeV by Holmqvist and Wiedling<sup>12)</sup> and at 14 MeV by various

experimenters. On the other hand, analysis at such energies is rather straightforward, because contribution of the compound elastic is negligible.

The analysis at 8 MeV is shown in Figs. 6 - 8. Circles are data of Holmqvist and Wiedling<sup>12)</sup>, crosses JAERI data<sup>13)</sup>, and triangles Kentucky data<sup>14)</sup>. Solid and dash-dot curves represent the coupled-channel calculations. The curves shown by dash-dot denote such that the weak coupling model was used in the calculation, notwithstanding that the application of this model is not appropriate. Dashed curves represent the spherical optical-model calculations. From Figs. 6 and 7 we can see that, if the couplings are appropriately taken into account, the coupled-channel calculation results in good fit to the experimental data. For example, we see in Fig. 7 that the solid curves for Ni, Cu and Zn rather well fit to the data, whereas the dash-dot curves for  $^{59}\text{Co}$  and  $^{75}\text{As}$  do not.

In the case of rotational nuclei such as Hf,  $^{181}\text{Ta}$  in Fig. 8, agreement of the solid curves with the data are not so good at backward angles, though fairly good agreement is obtained at the rest of angles. A little smaller value of  $\beta_2$ , within its ambiguity might improve the fitness, as it is the case for  $^{239}\text{Pu}$ . This case will be shown later.

Fig. 9 shows the elastic cross sections at 14 MeV. Comparisons with the experimental data<sup>15)</sup> are made for many nuclei, but the differences between the two kinds of calculations are too small to select which calculation gives better fitting to the experimental data.

##### 5. Analysis for Several Nuclei in Low Energy Region

We have seen in the figures of the total cross sections that there are large differences between the coupled-channel and the spherical optical-model calculations in the low energy region, i.e. the region lower than 3 or 4 MeV. Therefore, the analysis of the scattering cross sections in this energy region will be of more interest. In this region we have to take the compound process into account and must be careful about fluctuation of the cross sections. The analysis in this energy region has been made for several nuclei such as Fe, Ni, Zn,  $^{120}\text{Sn}$ , Gd, Pu, etc. Results of some of them are mentioned in the following.

Fig. 10 shows the analysis for iron. Closed circles are JAERI data<sup>16)</sup>. The compound elastic scattering was calculated by using the Moldauer theory<sup>17)</sup>, in which seven excited levels up to 3.12 MeV in  $^{56}\text{Fe}$  were taken into account, and the results were added to both the calculations. As may be expected, both

the calculations lead to considerably different values each other, and the coupled-channel calculations show very good agreement with the experimental data. In the figure of inelastic scattering for the 0.85 MeV level, the dashed curves represent Moldauer calculation, and solid curves Moldauer calculation plus the coupled-channel calculation. The solid curves well agree with the data at the higher energies, but at the lower three energies they show large deviations from the data. Intermediate structures with width of 0.2 MeV, however, have been reported at 1.6 and 2.05 MeV<sup>18)</sup>. The measurement was made with an energy spread of 0.09 MeV. Therefore, the deviations at 1.71 and 2.01 MeV are consistent with the presence of the intermediate structures. The deviation at 1.37 MeV may also be due to fluctuation of the cross section.

In case the spherical optical model was used in the analysis, what parameter values would be obtained? Circles and triangles in Fig. 11 are the values of  $V$  and  $W$ , respectively, searched with the spherical optical model so as to be fitted to the solid curves in Fig. 10 (a), <sup>etc.</sup> i.e. to the values calculated with the coupled-channel theory. In the calculation,  $r_0$  was changed to 1.25 fm to improve the fitness. Therefore, the circles in the figure approximately satisfy the rule of  $Vr_0^2 = \text{const}$ . A remarkable feature is the large values of  $W$ . They scatter in a region from 8 to 11 MeV. They lead to somewhat larger values of the compound inelastic cross sections than the original values of  $W$  do.

Fig. 12 shows the scattering cross sections of nickel. Closed circles are JAERI data<sup>16)</sup>. The compound cross sections were estimated by taking into account six excited levels assumed in a "nucleus" averaged with respect to <sup>58</sup>Ni and <sup>60</sup>Ni in the Moldauer calculation. Both the elastic and inelastic results calculated by taking into account the coupling between the ground and first  $2^+$  levels show far better agreement than the case without the coupling.

Fig. 13 shows the scattering cross sections of <sup>120</sup>Sn. Closed circles are JAERI data<sup>15)</sup>. Twenty-one excited levels up to an excitation energy 3.07 MeV were taken into account in the Moldauer calculation. As may be expected, the effect of the coupling on the elastic and inelastic cross sections is not large, but still the results with the coupling show better agreement with the elastic and first  $2^+$  inelastic data.

Fig. 14 shows the elastic cross sections of <sup>239</sup>Pu. The experimental data shown by circles are of Koppola and Knitter<sup>19)</sup>. Argonne data<sup>20)</sup> are shown by triangles. The experimental values contain the inelastic cross sec-

tions for low-lying levels. Accordingly, the solid lines also contain the contribution of the direct inelastic scattering from the three lowest-lying levels. As mentioned in the discussion for the total cross section of plutonium, the deformation parameter  $\beta_2$  was taken to be 0.22. Agreement with the experimental data is fairly good. The value of  $\beta_2=0.28$ , which is close to the values for  $^{238}\text{Pu}$  and  $^{240}\text{Pu}$  in a bibliography<sup>4)</sup>, resulted only in a poor agreement with the data. The same thing may be said of the analysis for gadolinium (the result is not shown here). The value of  $\beta_2$  taken from the bibliography<sup>4)</sup> is 0.34, but  $\beta_2=0.30$  or a little smaller value gave better results.

For a largely deformed nucleus one has to change the value of  $r_0$ , if the volume of nuclear matter is to be held constant. For example,  $r_0$  for a nucleus of a prolate deformation with  $\beta_2=0.30$  should be changed from 1.25 to 1.24, where 1.25 is for the spherical nucleus, and a nucleus with  $\beta_2=0.34$ ,  $r_0$  should be changed to 1.23. We considered these changes for the analysis of Gd, Pu, etc., and the changes of the  $r_0$  values showed a little improvement for the fitness. Use of the smaller values of  $\beta_2$  was, however, still needed to obtain good agreement.

## 6. Conclusion

In conclusion, the coupled-channel calculations using the one set of the optical parameters well reproduce the total and scattering cross sections over a fairly wide energy and mass region, except for extremely low energy region and extremely light nuclei. For largely deformed nuclei, use of a little smaller values of deformation parameter, which are consistent with the values obtained from a recent Coulomb excitation experiment<sup>11)</sup>, gives good fit to the experimental data.

## References

- 1) F. Perey and B. Buck, Nucl. Phys. 32 (1962) 353, P.A. Moldauer, Nucl. Phys. 47 (1963) 65, D. Wilmore and P.E. Hodgson, Nucl. Phys. 55 (1964) 673, L. Rosen, J.G. Beery, A.S. Goldhaber and E.M. Auerbach, Ann. Phys. (U.S.A.) 34 (1965) 96, C.A. Engelbrecht and H. Fiedeldey, Ann. Phys. (U.S.A.) 42 (1967) 262, F.D. Becchetti, Jr. and G.W. Greenlees, Phys. Rev. 182 (1969) 1190, etc.
- 2) S. Tanaka, Y. Tomita, K. Ideno and S. Kikuchi, Nucl. Phys. A179 (1972) 513.
- 3) Y. Tomita, S. Tanaka and M. Maruyama, JAERI-M 5418 (1973).
- 4) P.H. Stelson and L. Grodzins, Nuclear Data A1 (1965) 21.
- 5) A version prepared by M. Wakai, S. Igarasi, O. Mikoshiba and S. Yamaji, JAERI memo 3833 (1969) (unpublished) from the original code by T. Tamura, ORNL-4152 (1967) (unpublished).
- 6) Y. Tomita, JAERI 1191 (1970).
- 7) S. Igarasi, JAERI 1224 (1972).
- 8) D.G. Foster, Jr. and D.W. Glasgow, Phys. Rev. C3 (1971) 576, D.W. Glasgow and D.G. Foster, Jr., Phys. Rev. C3 (1971) 604.
- 9) D.J. Hughes and R.B. Schwartz, BNL 325 (1958), M.G. Goldberg, S.F. Mughab, B.A. Magurno and V.M. May, BNL 325, 2nd Edition, Supplement No. 2 (1966).
- 10) V. Benzi, L. Zuffi, M. Coppola and H.H. Knitter, Nuclear Data for Reactors, IAEA, Vienna (1970) Vol. II, p.863.
- 11) C.E. Bermis, Jr., F.K. McGowan, J.L.C. Ford, Jr., W.T. Milner, P.H. Stelson and R.L. Robinson, Phys. Rev. C8 (1973) 1466.
- 12) B. Holmqvist and T. Wiedling, Nuclear Data for Reactors, IAEA, Vienna (1970) Vol. II, p. 341.
- 13) S. Tanaka, K. Tsukada, M. Maruyama and Y. Tomita, Nuclear Data for Reactors, IAEA, Vienna (1970) Vol. II, p. 317, For molybdenum data, S. Tanaka and Y. Yamanouti, to be published.
- 14) J.D. Rober and J.D. Brandenberger, Phys. Rev. 163 (1967) 1077.
- 15) cited from D.I. Garber, L.G. Strömberg, M.D. Goldberg, D.E. Cullen and V.M. May, BNL 400, 3rd Edition (1970), except for Fe and Bi data. For iron data, M. Matoba et al. Private communication. For bismuth data, M. Matoba, M. Hyakutake, H. Tawara, K. Tsuji, H. Hasuyama, S. Matsuki, A. Katase and M. Sonoda, Nucl. Phys. A204 (1973) 129.
- 16) K. Tsukada, S. Tanaka, Y. Tomita and M. Maruyama, Nucl. Phys. A125 (1969) 641. For  $^{120}\text{Sn}$ , S. Tanaka, Y. Tomita, Y. Yamanouti and K. Ideno, Contributed Paper to "Conf. on Nucl. Structure with Neutrons", Budapest, p. 148

- (1972).
- 17) P.A. Moldauer, Phys. Rev. 135 (1964) B642.
  - 18) Y. Tomita, K. Tsukada, M. Maruyama and S. Tanaka, Nuclear Data for Reactors, IAEA, Vienna (1970) Vol. II, p. 301.
  - 19) M. Coppola and H.H. Knitter, Z. Physik 232 (1970) 286.
  - 20) A.B. Smith, private communication (1972).

## References for Table 1 and 2

- a) V. Fasoli, D. Tonido, G. Gabo and V. Benzi, Nucl. Phys. A125 (1969) 227.
- b) trial value
- c) from (p,p') average value in Table 8 by G. Bruce, J.C. Faivre, H. Farragi and A. Bussiere, Nucl. Phys. A146 (1970) 312.
- d) *ibid.*
- e) *ibid.*
- f) B. Holmqvist, T. Wiedling, V. Benzi and L. Zuffi, Nucl. Phys. A150 (1970) 105.
- g) R.P. Sharma, Nucl. Phys. A145 (1970) 312.
- h) F. Hinterlieger, G. Mairle, U. Schmidt-Rohr, G.J. Wagner and P. Turek, Nucl. Phys. A115 (1968) 570.
- i) average of the values for  $^{234}\text{U}$  and  $^{236}\text{U}$  in ref. 4).

## Figure captions

- Fig. 1. Energy dependence of the potential depths. Open circles and crosses are the values obtained from parameter search using  $^{209}\text{Bi}$  data<sup>2)</sup> and  $^{207}\text{Pb}$  data<sup>3)</sup>, respectively.
- Fig. 2. Comparison between the experimental and calculated total cross sections. Thick solid curves are the data of Foster and Glasgow<sup>8)</sup> and thick dotted curves are the data cited from BNL 325 and its Supplements<sup>9)</sup>. Thin solid and dash-dot curves represent the coupled-channel calculations, and thin dashed curves the spherical optical-model calculations.
- Fig. 6. Comparison between the experimental and calculated cross sections for elastic scattering at 8 MeV. Circles are the data of Holmqvist and Wiedling<sup>12)</sup>, crosses JAERI data<sup>13)</sup>, and triangles Kentucky data<sup>14)</sup>. Solid and dash-dot curves represent the coupled-channel calculations, and dashed curves the spherical optical-model calculations.
- Fig. 8. Comparison between the experimental and calculated scattering cross sections at 14 MeV. The experimental data<sup>15)</sup> are shown by various symbols. Solid curves represent the coupled-channel calculations and dashed curves the spherical optical-model calculations.
- Fig. 9. Comparison between the experimental and calculated cross sections for elastic (a) and inelastic (b) scattering by iron. Closed circles are JAERI data<sup>16)</sup>. Solid and dashed curves for the elastic scattering are cross sections calculated with the coupled-channel theory and the spherical optical model, respectively. The compound elastic cross sections were added to both the calculated results. The dashed curves for the inelastic scattering

are those calculated with the Moldauer theory. The solid curves represent the summed values of the coupled-channel and the Moldauer calculations.

- Fig. 11. Energy dependence of the potential depths for  $^{56}\text{Fe}$ . Circles and triangles are the values searched with the spherical optical model so as to be fitted to the values calculated with the coupled-channel theory.
- Fig. 12. Comparison between the experimental and calculated cross sections for elastic (a) and inelastic (b) scattering by nickel. Points and curves have the same meaning as in Fig. 10.
- Fig. 13. Comparison between the experimental and calculated cross sections for elastic (a) and inelastic (b) scattering by  $^{120}\text{Sn}$ . Points and curves have the same meaning as in Fig. 10.
- Fig. 14. Comparison between the experimental and calculated cross sections for elastic scattering by  $^{239}\text{Pu}$ . Open and closed circles are the data of Koppola and Knitter<sup>19)</sup>, and triangles Argonne data<sup>20)</sup>. Solid curves represent the coupled-channel calculations and dashed curves the spherical optical-model calculations.

Table 1

	Coupling mode	Coupled states	$\beta_2$	$\beta_3$
<sup>23</sup> Na	<sup>23</sup> Na rot.	$3/2^+ - 5/2^+ - 7/2^+$	0.45 <sup>a)</sup>	
<sup>27</sup> Al	( <sup>28</sup> Si+p) W.C. rot.	$5/2^+ - (1/2^+ \sim 9/2^+)$	0.40	
Si	<sup>28</sup> Si rot.	$0^+ - 2^+$	0.40	
S	<sup>32</sup> S vibr.	$0^+ - 2^+$	0.37	0.10 <sup>b)</sup>
Ca	<sup>40</sup> Ca vibr. trial	$0^+ - 3^-$		0.32 <sup>c)</sup>
<sup>51</sup> V	—	—		
<sup>52</sup> Cr	<sup>52</sup> Cr vibr.	$0^+ - 2^+ - 3^-$	0.23	0.17 <sup>d)</sup>
<sup>55</sup> Mn	( <sup>56</sup> Fe+ph) W.C. vibr. trial	$5/2^- - (1/2^- \sim 9/2^-)$	0.23	
Fe	<sup>56</sup> Fe vibr.	$0^+ - 2^+ - 3^-$	0.23	0.20 <sup>e)</sup>
<sup>58</sup> Co	( <sup>60</sup> Ni+ph) W.C. vibr.	$7/2^- - (3/2^- \sim 11/2^-)$	0.211	
Ni	( <sup>58,60</sup> Ni) vibr.	$0^+ - 2^+$	0.194	
Cu	( <sup>62</sup> Ni+p) W.C. vibr. } ( <sup>64</sup> Ni+p) W.C. vibr. }	$3/2^- - (1/2^- \sim 7/2^-)$ $3/2^- - (1/2^- \sim 7/2^-)$	0.193 0.192	
Zn	( <sup>64,66,68</sup> Zn) vibr.	$0^+ - 2^+$	0.23	
<sup>75</sup> As	( <sup>74</sup> Ge+p) W.C. vibr.	$3/2^- - (1/2^- \sim 7/2^-)$	0.290	
Sr	<sup>88</sup> Sr W.C. vibr.	$0^+ - 2^+$	0.140	
<sup>93</sup> Nb	( <sup>92</sup> Zr+p) W.C. vibr.	$9/2^+ - (5/2^+ \sim 13/2^+)$	0.11	
Mo	( <sup>92,94,96,100</sup> Mo) vibr.	$0^+ - 2^+$	0.153	
<sup>103</sup> Rh	( <sup>102</sup> Ru+p) W.C. vibr.	$1/2^- - (3/2^-, 5/2^-)$	0.264	

Table 2

	Coupling mode	Coupled states	$\beta_2$	$\beta_3$
Cd	( <sup>110-116</sup> Cd, even) vibr.	$0^+ - 2^+$	0.19	
In	( <sup>116</sup> Sn+ph) W.C. vibr.	$9/2^+ - (5/2^+ \sim 13/2^+)$	0.113	
Sn	( <sup>112-124</sup> Sn, even) vibr.	$0^+ - 2^+$	0.113	
Sb	( <sup>120</sup> Sn+p) } W.C. vibr. ( <sup>122</sup> Sn+p) }	$5/2^+ - (1/2^+ \sim 9/2^+)$ $7/2^+ - (3/2^+ \sim 11/2^+)$	0.112 0.118	
<sup>139</sup> La	( <sup>138</sup> Ba+p) W.C. vibr.	$7/2^+ - (3/2^+ \sim 11/2^+)$	0.120	
<sup>141</sup> Pr	( <sup>140</sup> Ce+p) W.C. vibr.	$5/2^+ - (1/2^+ \sim 9/2^+)$	0.104	
Gd	(Gd, even) rot.	$0^+ - 2^+ - 4^+ - 6^+$	0.34	
Er	(Er, even) rot.	$0^+ - 2^+ - 4^+ - 6^+$	0.34	
Hf	(Hf, even) rot.	$0^+ - 2^+ - 4^+$	0.27	
<sup>181</sup> Ta	<sup>181</sup> Ta rot.	$7/2^+ - 9/2^+ - 11/2^+ - 13/2^+ - 15/2^+$	0.26 <sup>f)</sup>	
<sup>182</sup> W	<sup>182</sup> W rot.	$0^+ - 2^+ - 4^+ - 6^+$	0.25	
<sup>197</sup> Au	( <sup>198</sup> Hg+ph) W.C. vibr.	$3/2^+ - (1/2^+ \sim 7/2^+)$	0.109 <sup>g)</sup>	
<sup>209</sup> Bi	( <sup>208</sup> Pb+p) W.C. vibr.	$9/2^- - (3/2^- \sim 15/2^-)$		0.10 <sup>h)</sup>
<sup>232</sup> Th	<sup>232</sup> Th rot.	$0^+ - 2^+ - 4^+ - 6^+$	0.267	
<sup>235</sup> U	<sup>235</sup> U rot.	$7/2^- - 9/2^- - 11/2^- - 13/2^- - 15/2^-$	0.27 <sup>i)</sup>	
<sup>238</sup> U	<sup>238</sup> U rot.	$0^+ - 2^+ - 4^+ - 6^+$	0.277	
Pu	<sup>239</sup> Pu rot.	$1/2^+ - 3/2^+ - 5/2^+ - 7/2^+ - 9/2^+$	0.28	

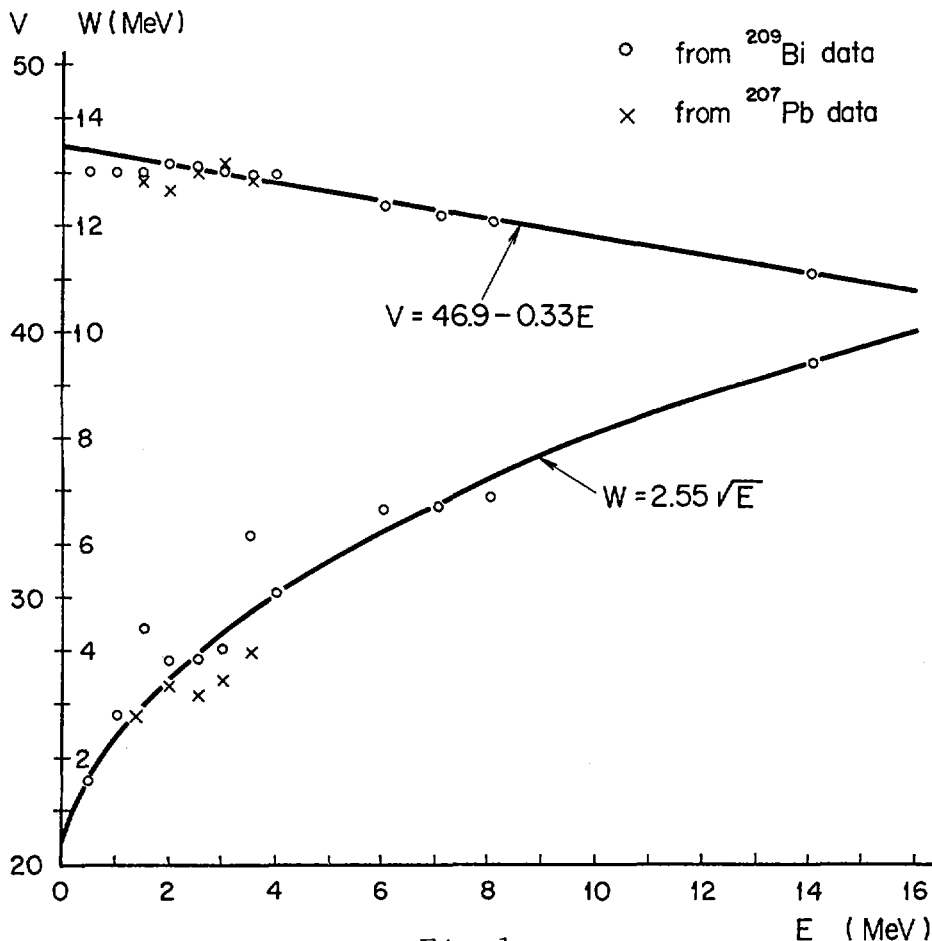


Fig. 1

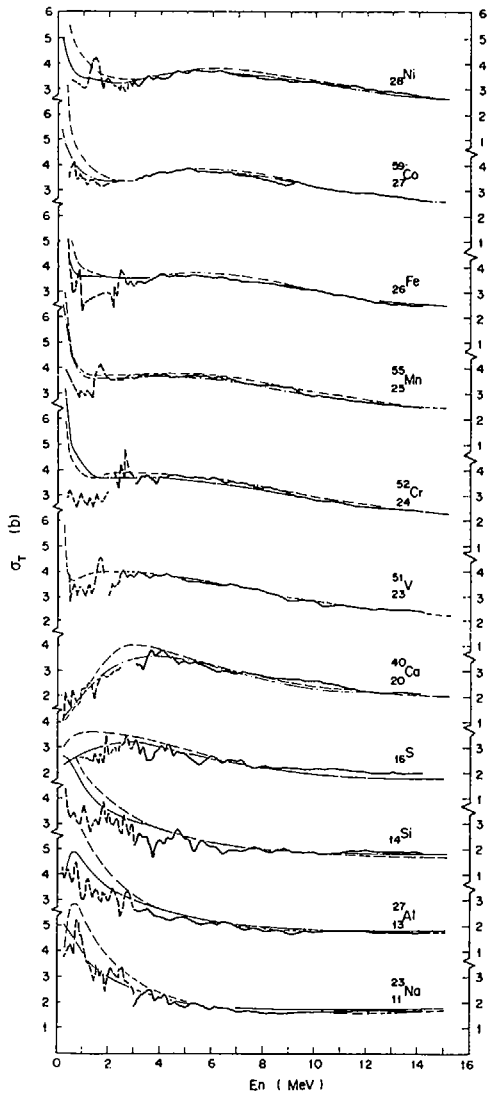


Fig 2

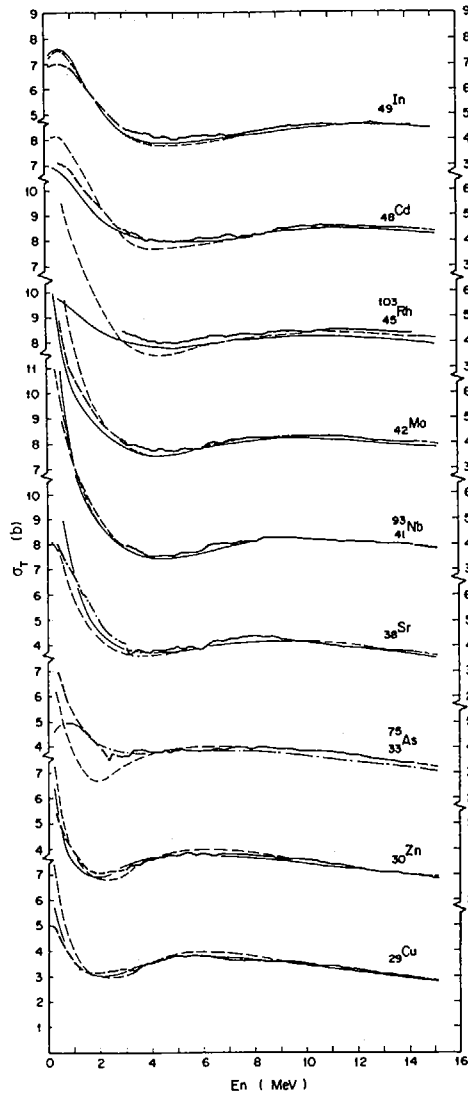


Fig 3

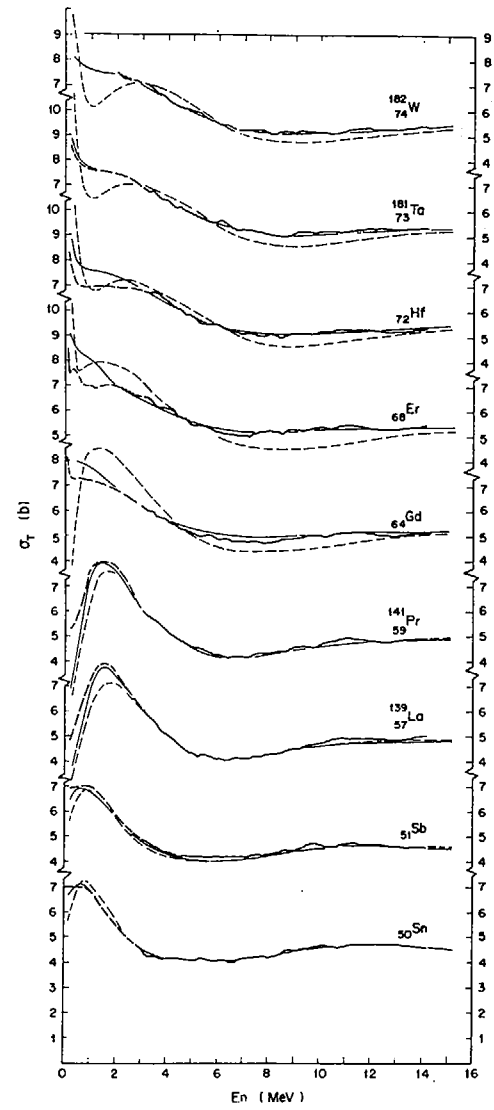


Fig 4

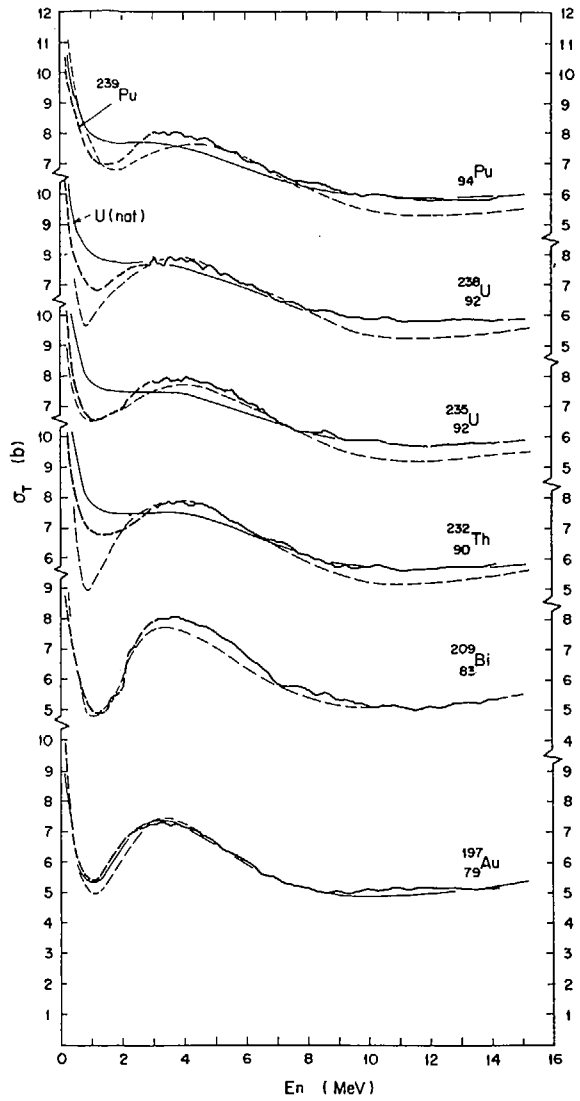


Fig. 5

Fig 5

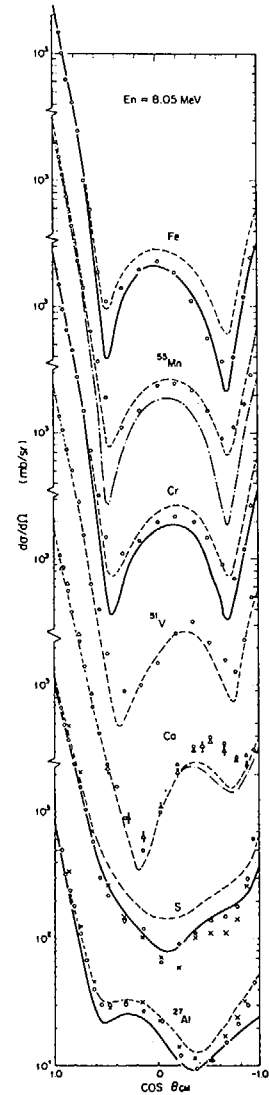


Fig. 6

Fig 6

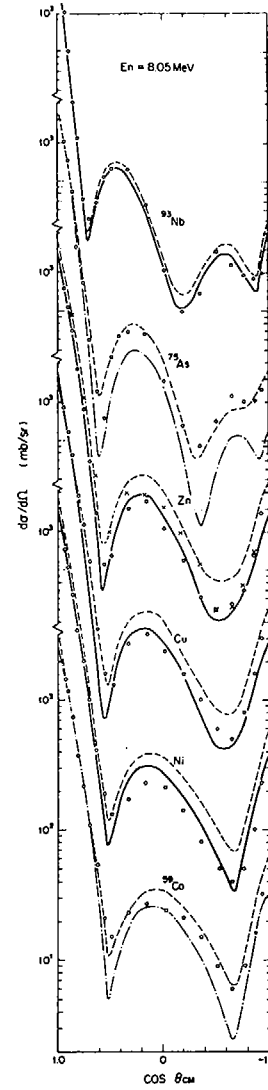
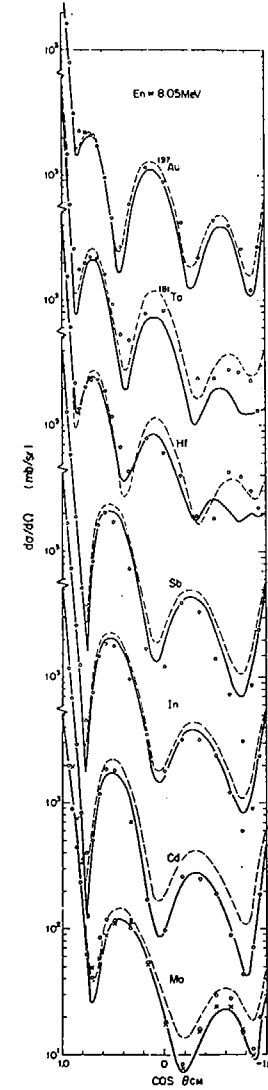


Fig. 7

Fig 7



Fig

Fig 8

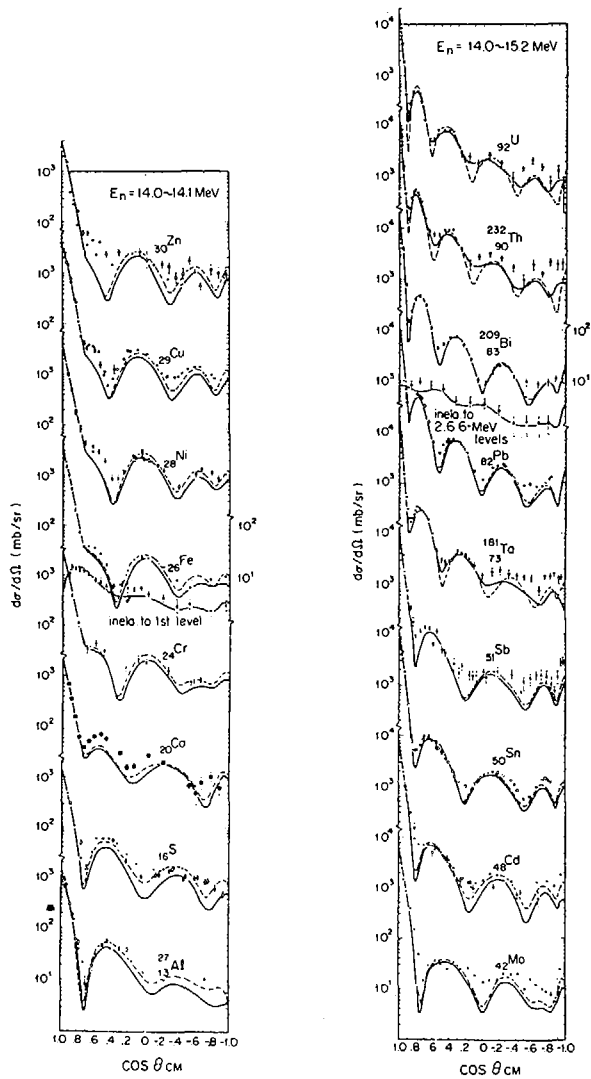


Fig.9

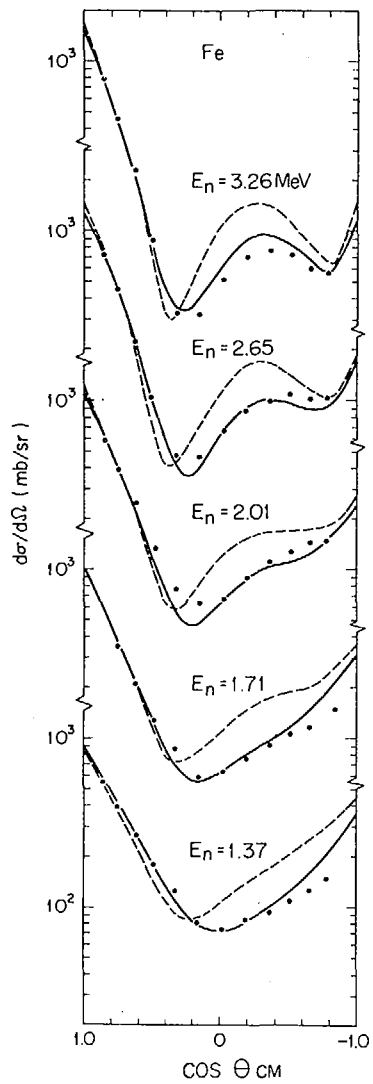


Fig.10 (a)

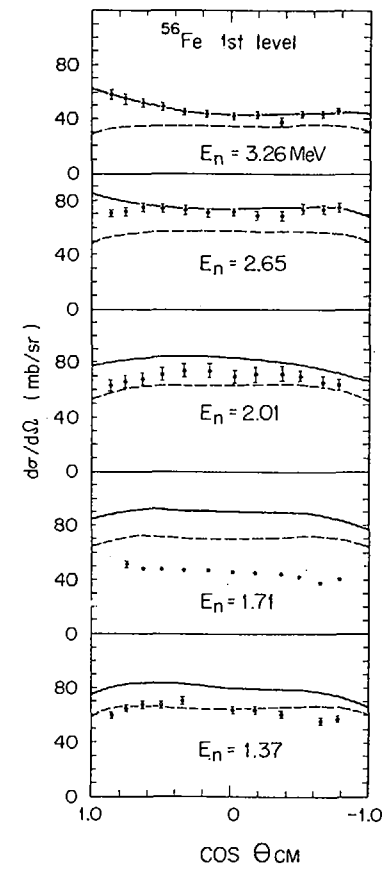


Fig.10 (b)

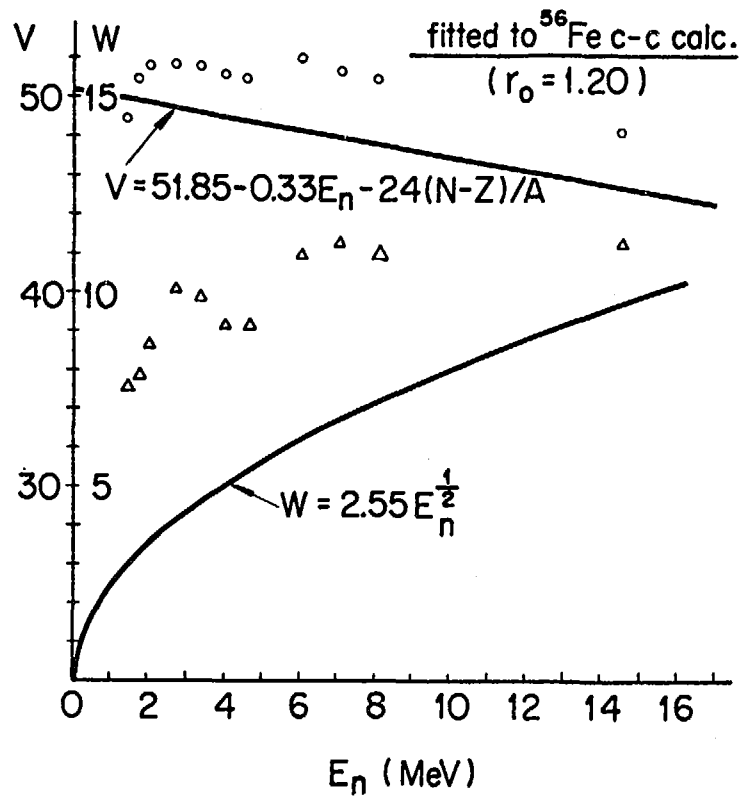


Fig. 11

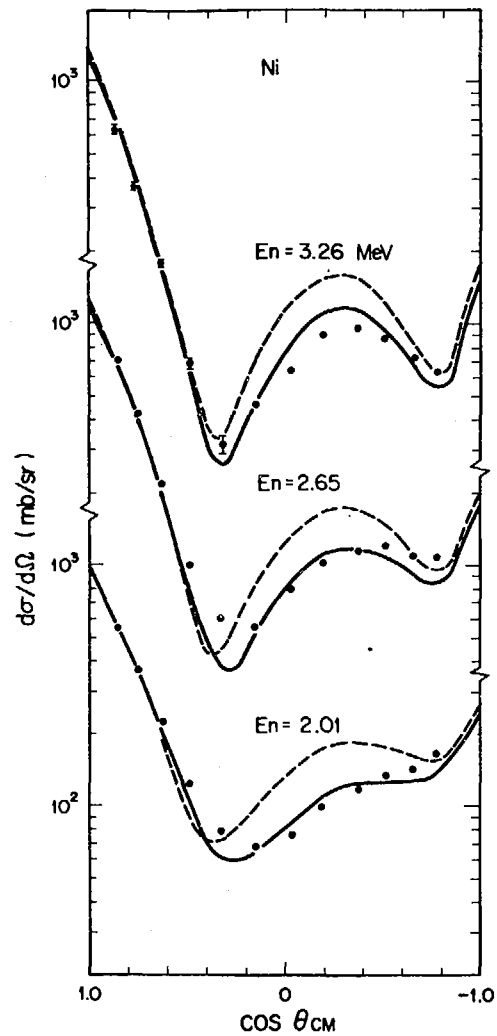


Fig. 12 (a)

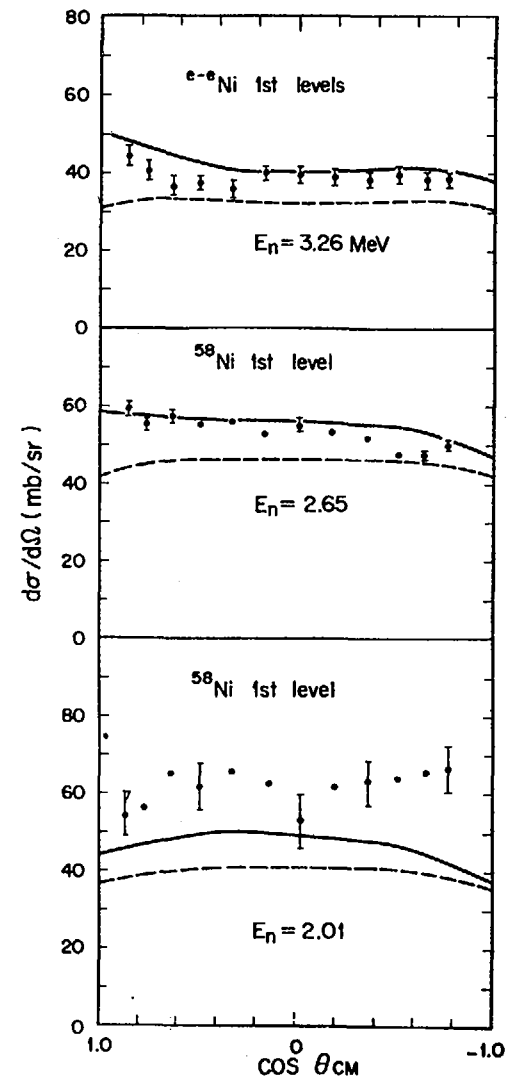


Fig. 12 (b)

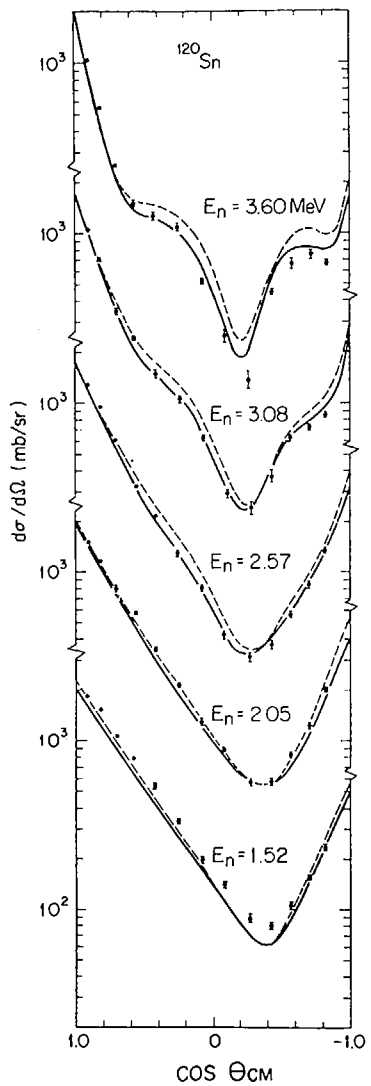


Fig.13 (a)

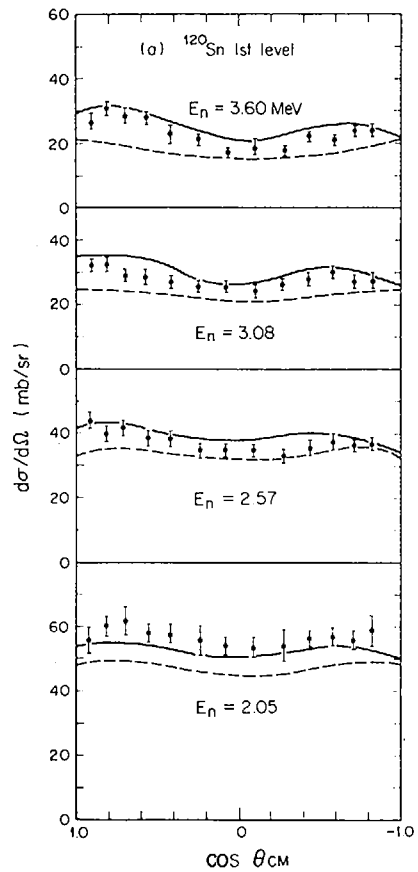


Fig.13 (b)

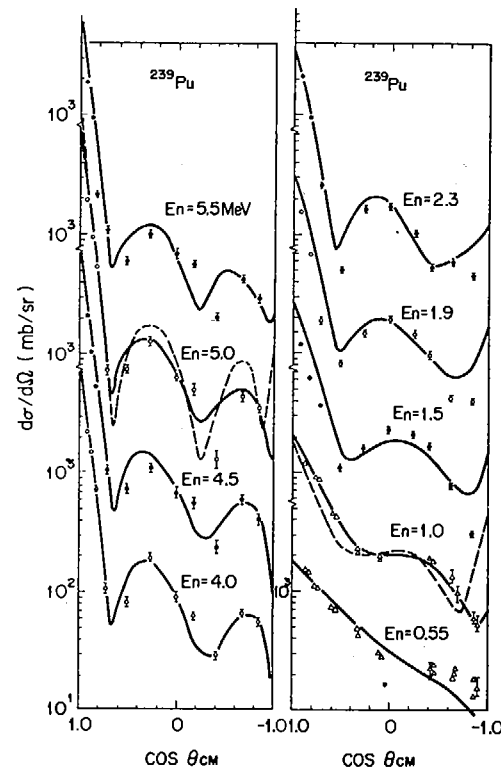
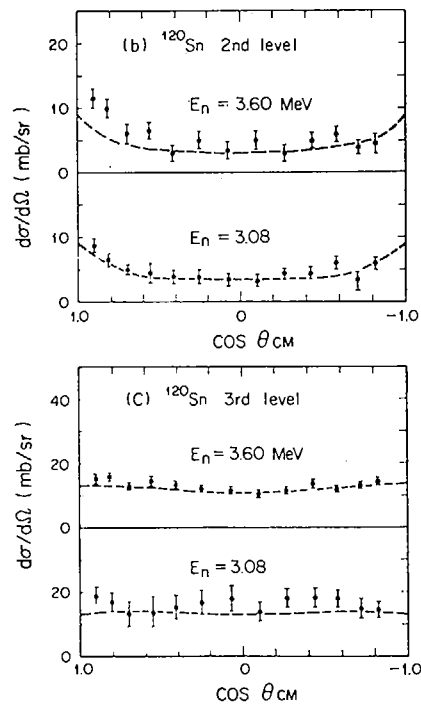


Fig.14

## DISCUSSION

K. NISHIMURA: Your coupled-channel calculation does not show the good fit for actinide nuclei. Do you have any specific reason for it?

S. TANAKA: By using a little smaller value than that taken from other bibliography for coupling parameter, the present potential can well reproduce the experimental data. For example, the value was changed from 0.28 to 0.22 so that the coupled-channel calculations gave good fit to the experimental data, Dr. Harada commented that the value 0.22 is not unreasonable.

S. W. CIERJACKS: Have you applied the coupled channel method to the interpretation of cross sections above 15 MeV? At Karlsruhe we have observed in the analysis of total neutron cross sections quite severe deviations of experiments from theory. These are normally explained in terms of onset of volume absorption. Can this be accounted for in the coupled channel model by inclusion of a volume absorption term or perhaps by changing the coupling strength systematically with increasing energy?

S. TANAKA: I have only few experiences on the application of the coupled-channel model in the energy range above 15 MeV. Once I tried parameter search for  $^{209}\text{Bi}$  elastic data at 24 MeV, and had to include a volume absorption term in the potential, I remember. I don't think that the large differences between the coupled-channel calculations and the experimental data above 15 MeV can be accounted for by the coupled-channel calculations using my parameter values.

R. C. BLOCK: Have you calculated the strength functions with your potential?

S. TANAKA: Not yet calculated. So I don't insist that the present parameter set is applicable to the very low energy region.

III-4. OPTICAL MODEL ANALYSIS OF NEUTRON CROSS SECTIONS  
AND STRENGTH FUNCTIONS

C.M. Newstead

Physics Department, Combustion Engineering, Inc.  
Windsor, Connecticut

and

Institut für Angewandte Kernphysik  
Kernforschungszentrum Karlsruhe

and

S. Cierjacks

Institut für Angewandte Kernphysik  
Kernforschungszentrum Karlsruhe

ABSTRACT

Current problems met in the attempt to interpret fast neutron total cross sections with spherical and coupled channels optical model calculations are discussed. The energy dependence of the real and imaginary potential strengths is considered and progress in fitting neutron total cross sections over a wide energy range is discussed. Fluctuations in the strength of the imaginary potential are investigated in terms of the s- and p-wave neutron strength function. The role of strength function systematics in aiding study of the optical potential is developed. The implications of energy and mass dependences of the optical potential for neutron data predictions are outlined.

## INTRODUCTION

The optical model has been remarkably successful in describing a variety of nuclear reactions encompassing a wide energy range. In recent years a number of global potentials have been proposed each of which has particular merits in describing the gross features of particular sets of reactions. To assess the validity of the several forms of the optical model and the various potentials for the actual evaluation of nuclear data one is concerned not with a global description but rather with the extent of the departure from it. By comparison of the optical model predictions with accurately measured cross sections we can hope to learn in what way and perhaps even why the potentials depart from their global trends. In an attempt to investigate these variations we have: 1) compared the predictions of the model with neutron total cross sections over a wide energy range to study the energy dependence of the optical potential strength and 2) considered the accuracy of the model in predicting s- and p-wave neutron strength functions for a number of nuclei to both obtain information concerning the strength of the potential at low energy and its variation with mass number. It is hoped that this and similar studies may serve as some guide to evaluators faced with the problem of choosing a potential suitable for a particular mass and energy range.

## TOTAL CROSS SECTION ANALYSIS

Theoretically the total neutron cross section constitutes a remarkable and constantly varying mixture of elastic and inelastic partial cross sections. From an experimental standpoint the total cross section can be measured absolutely with high precision. Thus analysis of the variation of the total cross section with energy provides a useful tool for study of the optical potential.

In what follows we present the results of a series of total cross section measurements carried out at the Karlsruhe cyclotron and their analysis in terms of the spherical non-local optical model potential of Perey and Buck. We then attempt to understand the observed departures from this global description in terms of simple physical considerations.

Total neutron cross sections for a variety of spherical and vibrational nuclei ranging from calcium to bismuth were measured with a nominal resolution of 0.04 nsec/m in the energy range 0.5 to 40 MeV with the fast neutron time-of-flight spectrometer of the Karlsruhe isochronous cyclotron. For the present study these high resolution results were averaged with a sliding energy width of 500 keV. The resulting average cross sections are plotted in figure 1 and compared to the predictions of the spherical non-local optical model of Perey and Buck<sup>1)</sup>. We note that below 3 MeV and above approximately 20 MeV the agreement between theory and experiment rapidly deteriorates.

In a previous investigation carried out with moderate energy resolution in the energy range 2.5 to 15 MeV, Foster and Glasgow<sup>2)</sup> measured the neutron total cross section of a number of nuclei ranging from hydrogen to plutonium. Comparing their data with the predictions of the spherical non-local potential of Perey and Buck they found better than 3 % agreement for the 46 spherical or vibrational nuclei included in their study as illustrated in figure 2 for the case of various  $1f_{7/2}$  shell nuclei while agreement was only within 17 % for the 19 deformed nuclei considered in their study as illustrated in figure 3 for various  $1h_{9/2}$  and  $2f_{7/2}$  shell nuclei.

This latter result is clearly to be expected and serves to illustrate the utility of coupled channels calculations for rotational nuclei. The former result was considered an additional triumph for the Perey-Buck model. It certainly must be regarded as an achievement since the potential was originally derived from fitting only the elastic angular distribution for 7 and 14.5 MeV neutrons on lead although the resulting potential was then compared to angular distributions and reaction cross sections for a number of nuclei at 4.1, 7- 14.5 and 24 MeV and found to give an adequate description. The remarkable success of this simple potential is most probably due to its non-locality or put another way to the fact that the local representation has a built-in energy dependence.

The present study demonstrates that the Perey-Buck potential is inadequate to describe the upper and lower regions of the extended energy range. We note that above 20 MeV an increase in the strength of the imaginary potential would yield better agreement. While this is partly a matter of ener-

gy dependence of the surface peaked absorption it is primarily due to the onset of volume absorption. The Perey-Buck potential does not include a volume absorption term. While this is perfectly justified at the energies considered in their analysis because of the inhibiting effects of the Pauli principle which dictates surface absorption at low energy, it becomes increasingly inadequate at the higher energies considered here. Of course we cannot uniquely determine the ratio of surface to volume absorption and its variation with energy from our total cross section analysis but rather can only infer the need to increase the strength of the imaginary term.

It would appear that agreement between prediction and measurement could be obtained below 3 MeV by reducing the strength of the surface peaked absorption. This is reasonably theoretically since there are less channels available for excitation at low energy. Thus in the simplest possible terms the imaginary potential may be thought of as being given by the product of an average interaction matrix element and the density of states available for interaction. When this density is low so is the imaginary potential strength.

Recently evidence for the reduction of the imaginary potential strength at low neutron energy has been forthcoming from several different sources. In the latter part of this paper evidence from neutron strength function analysis will be given. Evidence is also available from analysis of both neutron scattering and the (p,n) interaction on lead.

Fu and Perey<sup>3)</sup> have carried out an extensive analysis of elastic and inelastic reactions for the lead isotopes. They find it necessary to reduce the strength of the surface peaked absorption at low energy to correctly describe inelastic scattering while preserving agreement for elastic scattering. Fu and Perey employ the strengths  $V = 47.0 - 0.25 E_n$  MeV and  $W = 3.5 + 0.43 E_n$  eV. This is to be compared with the equivalent local representation of the non-local potential of Perey-Buck which has been determined by Hodgson and Wilmore<sup>4)</sup> to be given by  $W = 47.01 - 0.267 E_n - 0.00118 E_n^2$  MeV and  $W = 9.52 - 0.053 E_n$  MeV. We note that these two parameterizations of the energy dependence agree well in the vicinity of 14 MeV where the Perey-Buck analysis was predominately biased by the experi-

mental results.

Smith and co-workers<sup>5)</sup> have found both positive and negative energy dependent coefficients for the imaginary strength depending on the nuclei being analyzed. This may in part be due to compensation for the use of the spherical model to describe deformed or highly vibrational nuclei.

Additional evidence for the reduction of imaginary strength at low energy comes from the study of the total proton decay of isobaric analogue states near threshold. Hoffmann and Coker<sup>6)</sup> have suggested that the sharp drop in the  $(p,n)$   $\tilde{p}$  excitation function near threshold can be described by such a reduction. It should be noted, however, that there are a number of difficulties in both the measurement and interpretation of these excitation functions.

The energy dependence of the central or isospin independent optical potential ( $V_0$  and  $W_0$ ) is intimately connected with the energy dependence of the isospin dependent optical potential or so-called Lane potential ( $V_1$  and  $W_1$ ). The energy dependence of the complex Lane potential as obtained from analysis of  $(n,n)$ ,  $(p,p)$ , and  $(p,n)$  reactions from a few MeV up to 100 MeV has been previously discussed<sup>7)</sup>. This analysis tends to support Rook's<sup>8)</sup> theoretical calculations for the energy dependence of  $V_0$  and  $V_1$  carried out using the Bruckner - Bethe G-matrix and the reference spectrum method of Bethe.

Isospin effects may be of importance when the optical potential is used to evaluate cross sections for chains of isotopes. Perhaps the best way to determine the strength and energy dependence of the complex Lane potential is the comparison of proton and neutron scattering at a number of different energies. The role of isospin in increasing absorption for protons as a function of increasing asymmetry (and decreasing it in the same manner for neutrons) is illustrated in figure 4 and provides the signature of the isospin component.

Unfortunately neutron angular distributions of quality comparable with their proton counterparts are not generally available because of the experi-

mental difficulties involved in such measurements. To further our study of isospin strengths a series of high resolution differential excitation functions at ten different angles are currently planned for measurement at the Karlsruhe cyclotron to complement the total cross section work. It is recognized that the study of chains of separated isotopes will be of particular value here.

#### STRENGTH FUNCTION ANALYSIS

Nuclear data requirements for reactors tend to be concerned with the lower neutron energy region (if one excludes fusion and material damage requirements) while our knowledge of the optical potential tends to be based on measurements and calculations carried out in large measure at higher energies. In this respect study of neutron strength function systematics are particularly valuable since the strength function is intimately related to the strength of the optical potential at low energy. Since the strength function is measured for particular waves one also is spared some of the ambiguity inherent in averaging over many partial waves as is necessary at higher energies.

In recent years improvements in time-of-flight spectrometry and strength function analysis techniques have greatly increased our knowledge of accurate strength function values. In particular use of cyclotron based high resolution fast neutron spectrometers has permitted us to obtain strength functions for light nuclei and higher partial waves<sup>9)</sup> while the employment of the "sharp spike capture technique" by Block and co-workers at RPI<sup>10)</sup> has led to the measurement of strength functions in deep minima. In addition the average analysis technique as developed at Harwell<sup>11)</sup> and Saclay<sup>12)</sup> has led to the accurate determination of s-, p- and d-wave strength functions by the sampling of a large number of resonances and elimination of the necessity of individual resonance parity assignment.

Analysis of these new results by coupled channel optical model calculations has led to several interesting conclusions. It has been found that the deep s- and p-wave strength function minima can be simultaneously described by the same optical potential<sup>13)</sup>. The results of the calculation

are given in table 1 and figure 5 where comparison is made with the experimental values. The important point here is that the strength of the surface peaked absorption must be reduced in comparison to the value normally employed for higher energy scattering. It will be recognized that this tends to substantiate the conclusion reached in the total cross section discussion given above. It is interesting in this respect to compare the strength function predictions of the Perey-Buck spherical non-local potential with strength function measurements. This comparison is given in figure 6. We note that the Perey-Buck predictions tend to be larger than the measured values in the minima and smaller than experiments in the maxima. This is consistent with our supposition that the Perey-Buck imaginary strength ( $W = 9.5\text{MeV}$ ) is too strong for the low energy region. (Note that in the maxima reduction of  $W$  results in increase of  $S_0$ .) We note that the imaginary strengths given in table 1 are considerably less than 9.5 MeV.

Sometime ago Moldauer<sup>14)</sup> proposed an optical potential which gave good agreement with the s-wave neutron strength functions for the mass 100 region and also provided a good description of neutron scattering near 1 MeV. In a series of investigations Smith and co-workers<sup>5)</sup> have verified the utility of the Moldauer potential for the description of low energy neutron interactions. The essential characteristics of the Moldauer potential are the reduction in width of the surface peaked absorption and the translation of the location of the absorptive band by a small amount outside the nuclear half-way radius. One can regard this as a way of reducing the imaginary potential strength rather than having any deeper physical significance associated with diffuseness or polarization of the nuclear matter distributions. Such an interpretation would be consistent with the interpretation of our study. It should be mentioned that the RPI group has proposed an explanation of the deep strength function minima based upon the optical potential being different for s- and p-waves. While this is acceptable theoretically it would not appear to substantiate the trend found in the total cross section analysis.

It does seem that particularly at low energy (because of the availability of states argument) the optical potential fluctuates with mass number as can be seen from table 1. In extensive scattering studies carried out at 8 MeV Holmqvist and Wiedling<sup>15)</sup> have also found fluctuations in the strength of the potential as illustrated in figure 7.

Thus it is clear that evaluators must give some thought to the variation of the strength of the potential when attempting to make accurate assessments of neutron cross sections. Clearly at the lower energies involved in most nuclear data evaluations nuclear structure effects play an important role in modulating the global optical potential.

#### REFERENCES

- 1/ F. G. Perey, B. Buck; Nucl. Phys. 32 (1962) 353
- 2/ D. Foster, D. Glasgow; Phys. Rev. C3 (1971) 576  
and D. Glasgow, D. Foster; Phys. Rev. C3 (1971) 604
- 3/ C. Y. Fu, F. G. Perey; Report, ORNL-4765 (1972)
- 4/ D. Wilmore, P. E. Hodgson; Nucl. Phys. 55 (1964) 673
- 5/ A. B. Smith, in "New Developments in Reactor Physics and Shielding" CONF-720 901, Vol. 2 (1972) p. 1063 and references therein.
- 6/ G. W. Hoffmann, W. R. Coker; Phys. Rev. Lett. 29 (1973) 227
- 7/ C. M. Newstead; Bull. Am. Phys. Soc. 18 (1973) 547  
and Proc. Int. Conf. on Nuclear Physics, Munich, North Holland Publishing Company, Vol. 1 (1973), p. 366
- 8/ H. R. Kidwai, J. R. Rook; Nucl. Phys. A169 (1971) 417,  
and J. R. Rook; Nucl. Phys. to be published
- 9/ S. Cierjacks; Proc. II. All-Union Conf. on Neutron Physics, Kiev, Vol. 2, (1973), p. 307 and references therein.
- 10/ R. G. Stieglitz, R. W. Hockenbury, R. C. Block; Nucl. Phys. A163 (1971) 592 and references therein.
- 11/ C. A. Uttley, C. M. Newstead, K. Diment; in "Nuclear Data for Reactors", IAEA Vienna, Vol. 1 (1966) 165

- 12/ C. M. Newstead, J. Delaroche, B. Cauvin; in "Statistical Properties of Nuclei", Plenum Press, New York (1972), p. 367
- 13/ C. M. Newstead; Europhysics Study Conf. on Intermediate Processes in Nuclear Reactions, Plitvice (1973)
- 14/ P. A. Moldauer; Nucl. Phys. 47 (1963) 65
- 15/ B. Holmqvist, T. Wiedling; in "Nuclear Data for Reactors", IAEA Vienna, Vol. 2 (1970) 341

## FIGURE CAPTIONS

- Fig. 1 Karlsruhe neutron total cross sections versus energy for nuclei ranging from  $^{40}\text{Ca}$  to  $^{209}\text{Bi}$  compared to predictions of Perey-Buck spherical non-local optical model.
- Fig. 2 Battelle neutron total cross sections versus energy for various  $1f_{7/2}$  nuclei (with the exception of  $^{44}\text{Ca}$ ) compared to predictions of Perey-Buck spherical non-local optical model<sup>2)</sup>.
- Fig. 3 Battelle neutron total cross sections versus energy for various  $1h_{9/2}$  and  $2f_{7/2}$  nuclei compared to predictions of Perey-Buck spherical non-local optical model<sup>2)</sup>.
- Fig. 4 Contrast between neutron and proton imaginary potentials versus asymmetry  $e$  when the optical potential has an isospin dependent strength  $W_1$ . A similar effect occurs for the isospin dependent real potential.
- Fig. 5 Comparison between experimental and theoretical values of the s- and p-wave neutron strength functions versus mass number. The solid curves are the Buck and Perey collective model predictions while the symbols + indicate the coupled channels calculations of the present study whose parameters are given in table 1.
- Fig. 6 S-wave neutron strength functions predicted by the Perey-Buck spherical non-local optical model compared to experimental values. This comparison suggests that the Perey-Buck imaginary potential strength should be reduced at low neutron energy. It is understood that the spherical model is inadequate to describe the splitting of the 4 S size resonance.<sup>1)</sup>
- Fig. 7 Optical model parameters (strength and geometry) versus mass number as obtained from a study of 8 MeV neutron elastic scattering. The open circles are the result of a five parameter analysis. The solid circles are the result of a two parameter (U and W) analysis with the other parameters held fixed at average values.<sup>15)</sup>

Table 1 Comparison of theoretical and experimental results for the s- and p-Wave strength functions

TARGET	V	W	$\beta_2$	$s_0^{th}$	$s_1^{th}$	$s_0^{exp.}$	$s_1^{exp.}$
$^{35}_{Cl}$	51.04	0.9	0.0	0.15	1.15	$0.08^{+0.07}$	$1.65^{+0.55}$
$^{37}_{Cl}$	48.38	0.9	0.0	0.13	2.07	$0.12^{+0.09}$	$2.87^{+1.06}$
$^{39}_K$	48.00	2.5	0.0	0.41	2.40	$0.37^{+0.23}$	$2.71^{+0.82}$
$^{40}_{Ca}$	53.50	1.5	$\beta_2=0.00$	2.16	0.31	$2.56^{+1.20}$ $-0.58$	$0.25^{+0.12}$ $-0.06$
$^{50}_{Cr}$	51.11	1.12	$\beta_3=0.36$ 0.22	1.94	0.27	$2.18^{+0.75}$	$0.264^{+0.152}$
$^{52}_{Cr}$	50.40	0.8	0.17	2.06	0.15	$2.10^{+1.05}$	$0.053^{+0.023}$
$^{54}_{Cr}$	49.60	0.44	0.17	0.89	0.076	$1.79^{+1.03}$	$0.042^{+0.024}$
$^{89}_Y$	48.97	3.6	0.0	0.44	3.92	$0.39^{+0.27}$ $-0.12$	$4.4^{+2.0}$ $-1.2$
$^{93}_{Nb}$	49.15	1.35	0.0	0.15	5.18	$0.17^{+0.06}$	$5.16^{+0.24}$
$^{98}_{Mo}$	48.42	6.2	0.168	0.77	7.21	$0.42^{+0.25}$	$6.8^{+0.5}$
$^{100}_{Mo}$	47.90	4.0	0.253	0.74	4.43	$0.55^{+0.30}$	$4.6^{+0.5}$
$^{103}_{RH}$	48.91	3.3	0.264	0.40	5.06	$0.40^{+0.05}$ $-0.08$	$5.07^{+0.53}$ $-0.29$
$^{135}_{Ba}$	47.59	4.0	0.150	1.01	1.60	$1.0^{+0.3}$	
$^{137}_{Ba}$	47.22	1.82	0.130	0.50	0.84	$0.33^{+0.17}$	
$^{139}_{La}$	47.30	2.12	0.130	0.71	0.83	$0.70^{+0.20}$ $-0.14$	$0.70^{+0.3}$ $-0.2$
$^{141}_{Pr}$	47.81	4.00	0.110	1.73		$2.04^{+0.47}$ $-0.35$	
$^{165}_{Ho}$	47.5	3.00	0.30	1.82	1.61	$1.66^{+0.24}$	$1.63^{+0.25}$
$^{209}_{Bi}$	46.5	1.5	$\beta_2=0.00$ $\beta_3=0.20$	0.50	0.29	$0.65^{+0.39}$ $-0.17$	$0.25^{+0.09}$ $-0.05$

Geometry set for all calculations:  $r_0 = 1.25 f$ ,  $a = 0.65 f$ ,  $b = 0.47 f$ . Potentials strengths in MeV.  $S_0$  and  $S_1$  in units of  $10^{-4}$ .

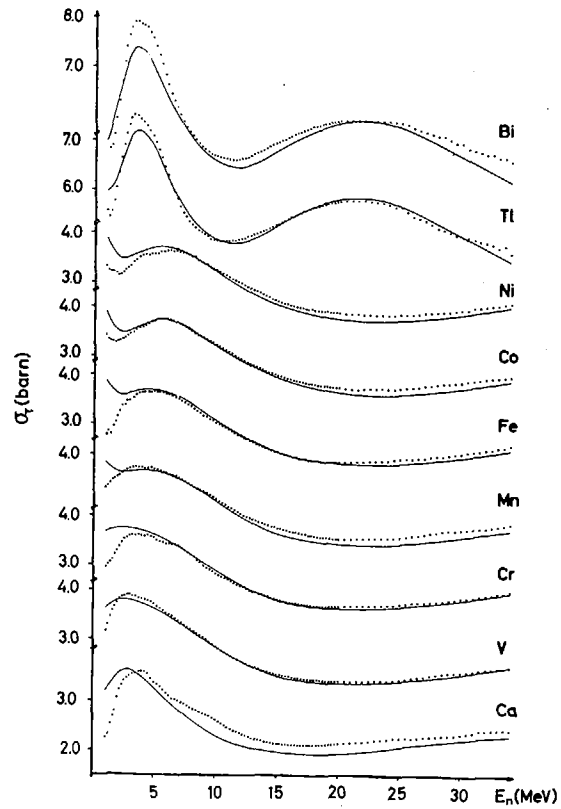


Fig.1

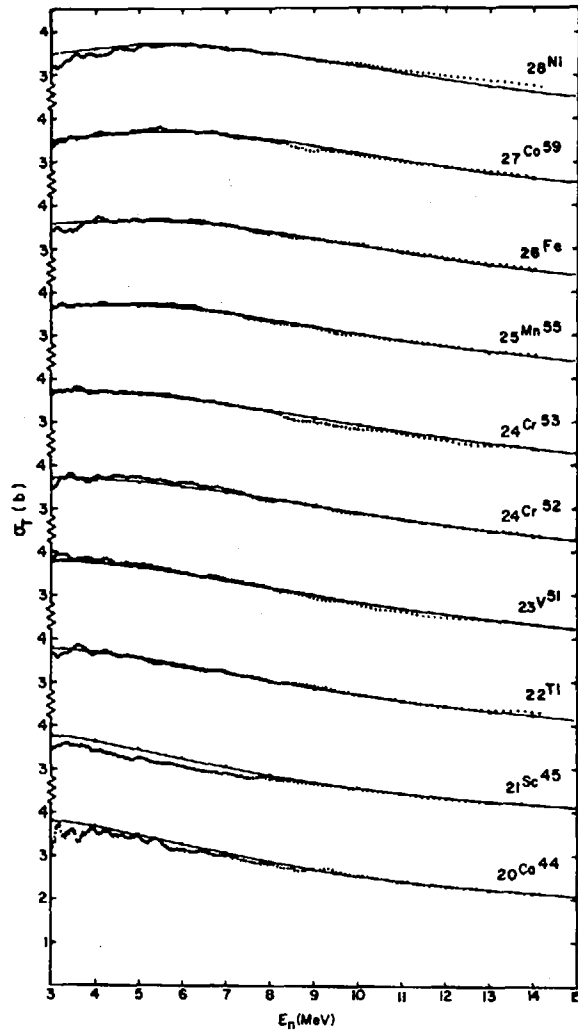


Fig.2

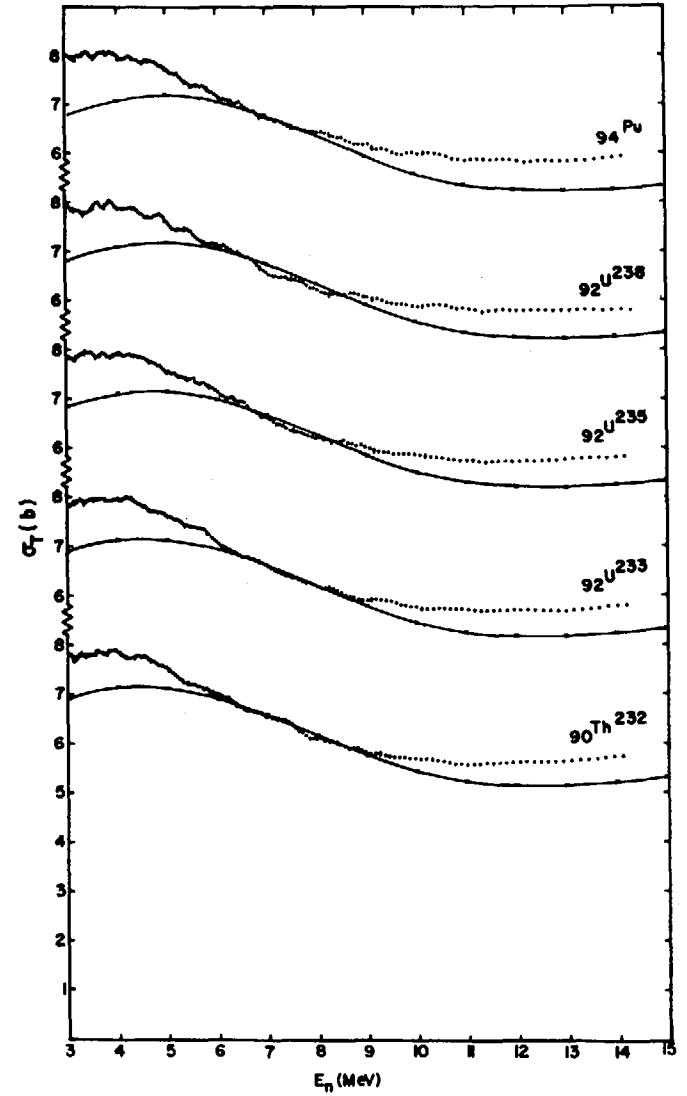


Fig.3

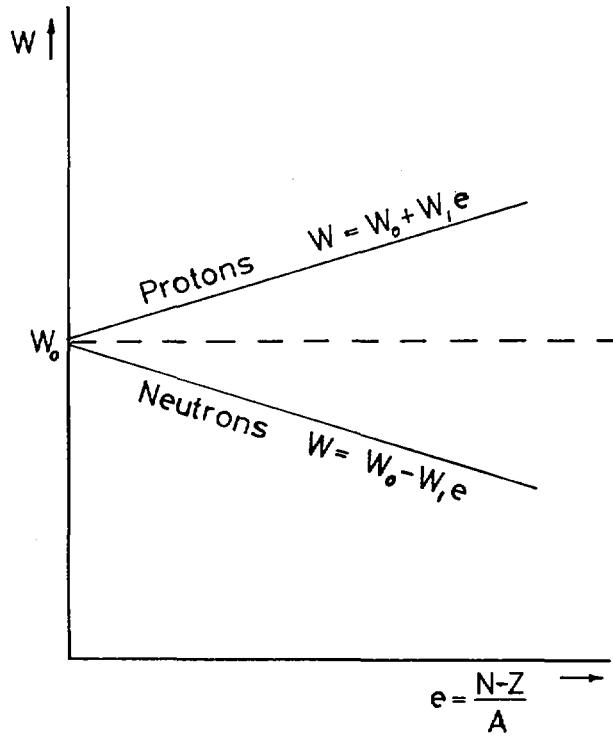


Fig. 4

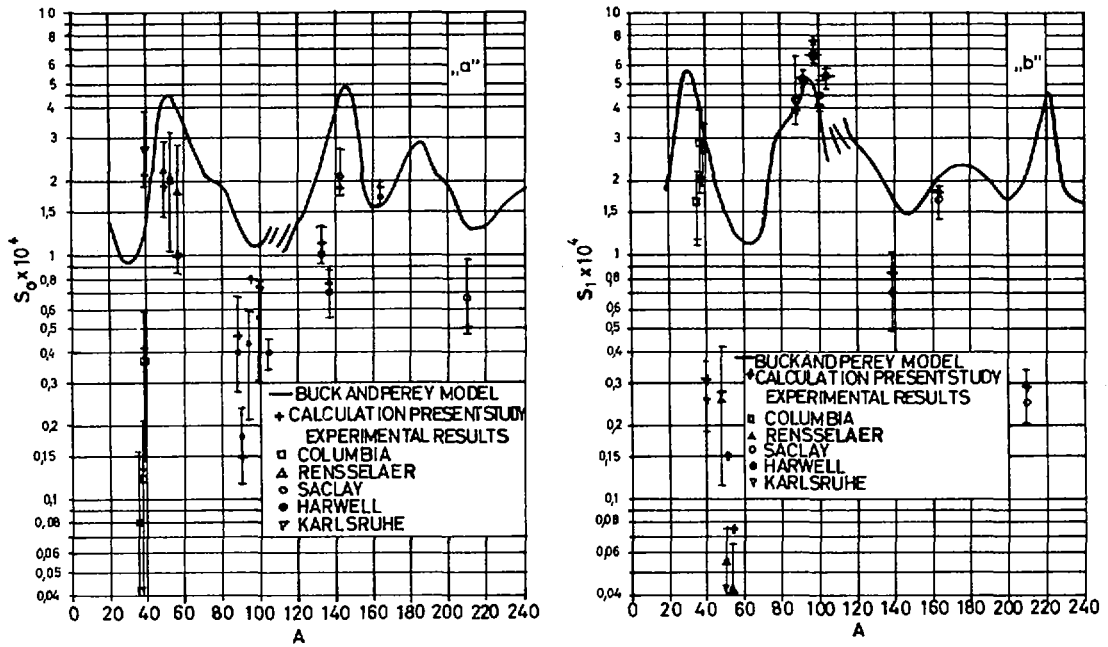


Fig. 5

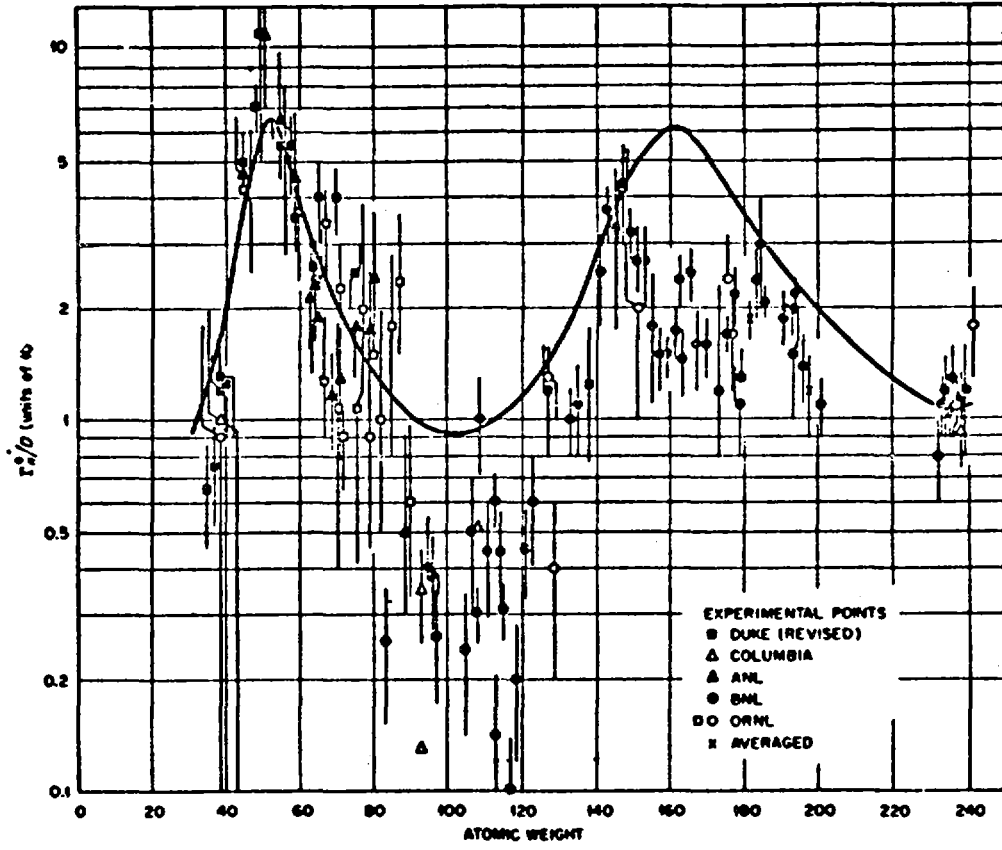


Fig.6

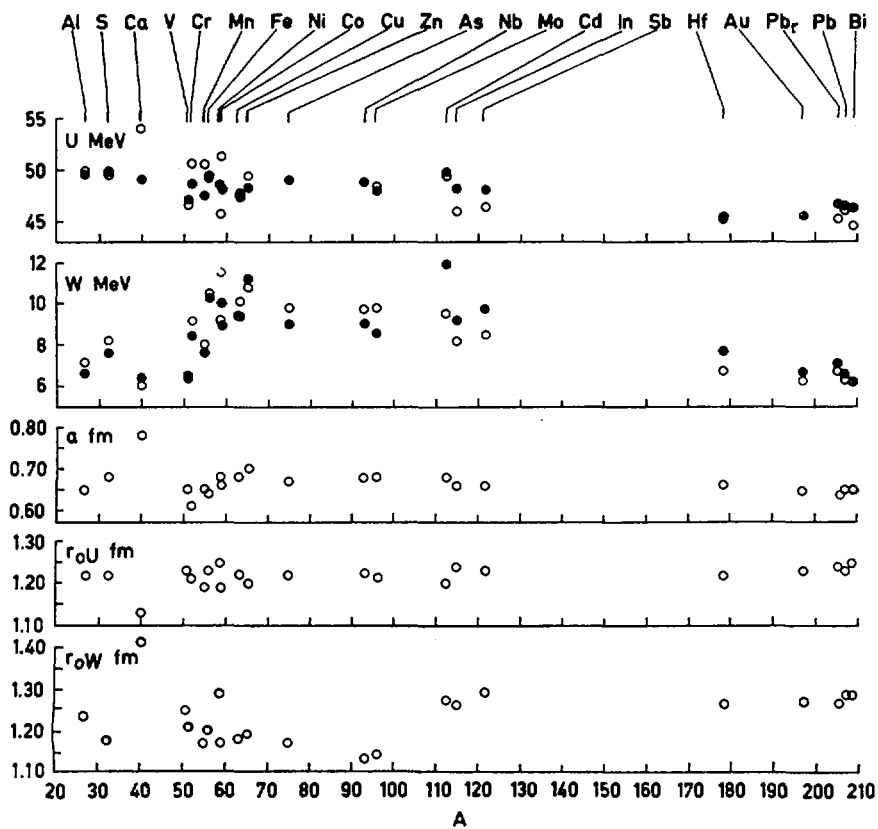


Fig.7

## DISCUSSION

R. C. BLOCK: At RPI, Turinsky et al. showed that a "simple" (i.e. non  $l$ -dependent imaginary potentials) optical model could produce deep  $S_0$  and  $S_1$  minima. However, when attempting to fit  $R'$ , the "simple" potential did not work. Thus, to fit  $S_0$ ,  $S_1$  and  $R'$  requires more than a "simple" potential --- can you comment on the Karlsruhe work with regard to fitting  $R'$ ?

S. W. CIERJACKS: It is, of course, possible to adjust the parameters of simple optical potentials to fit the deep  $S_0$  and  $S_1$  minima. The crucial problem is, however, whether you can simultaneously reproduce minima, maxima and the widths of size resonances for the strength functions with one consistent potential. That this is possible, has been demonstrated to some extent by the work of Newstead and collaborators. I am not aware of investigations to fit potential scattering radii,  $R'$ , additionally.

IV-1. Evaluation of Neutron Elastic and  
Inelastic Scattering of Cr and Ni  
Isotopes Using Coupled-Channel Calculations

by

A. Prince and M. R. Bhat  
National Neutron Cross Section Center  
Brookhaven National Laboratory  
Upton, New York 11973

March 1974

1. Introduction

Evaluation of the neutron and gamma production cross section data have been carried out for the ENDF/B-IV data library. The high energy elastic and inelastic scattering data from the vibrational states of the even-even isotopes of Cr and Ni were analyzed in terms of coupled channel calculations. The results of these are presented in this paper. A detailed discussion of the complete evaluation will be published soon.

## 2. Chromium (A. Prince)

As part of the evaluation effort for natural chromium, it was necessary to analyze the neutron angular distributions for the various isotopes ( $^{50,52,53,54}\text{Cr}$ ). Most of the experimental data exists only for Cr(nat) and  $^{52}\text{Cr}$ , therefore as part of the investigation it was necessary to carry out model type calculations and make comparisons with the available experimental data. Special emphasis was placed on  $^{52}\text{Cr}$  and  $^{53}\text{Cr}$  since their abundances of 83.79% and 9.5% make them the major contributors to the cross sections of Cr(nat).

Optical model calculations using a modified coupled-channel code JUPITOR<sup>(1,2)</sup> were carried out to determine the total, shape elastic, reaction and direct inelastic cross sections. The compound nucleus contributions were analyzed with the code COMNUC.<sup>(3)</sup>

The optical model parameters were derived<sup>(4)</sup> by a method similar to that of Greenlees et al.,<sup>(5,6)</sup> Bolsterli et al.<sup>(7)</sup>

The number of excitations used to calculate the inelastic cross sections are given in Table I.

Table I

<u>Isotope</u>	<u># Levels</u>	<u>Energy of highest level (MeV)</u>
Cr-50	10	4.7
Cr-52	24	7.9
Cr-53	15	4.0
Cr-54	11	3.8

The low lying levels were assumed to be vibrational thus the collective inelastic excitations were calculated assuming  $0 - 2^+$ ,  $0 - 2^+ - 3^-$ ,  $0 - 2^+ - 4^+$

type coupling. The higher states are weakly coupled to the ground state so their contributions were assumed to be negligible.

The inconsistency between the Hauser-Feshbach calculations of the inelastic scattering and the coupled-channel calculations were removed by introducing a reduction factor R given by

$$R = \frac{\sigma_{\text{expt}'1} - \sigma_{\text{DI}}}{\sigma_{\text{expt}'1}}$$

where it has been assumed that the difference between the experimental inelastic cross section and the direct inelastic cross section is the true compound inelastic cross section.

The comparison between the calculations and experimental data is given in Figures 1 through 5.

Fig. 1 Shows the comparison between the compound differential inelastic and the direct differential inelastic scattering cross sections of the 1.434(2<sup>+</sup>) MeV level in <sup>52</sup>Cr. The sum of these producing the total inelastic. The experimental data is that of Kinney and Perey.<sup>(8)</sup> Note the symmetry about 90° in the compound process as compared to the high forward peaking in the direct process.

Fig. 2 Depicts the 2.369(4<sup>+</sup>) level excitation at E<sub>n</sub> = 8.56 MeV. Both compound and direct components have been taken into account.

Fig. 3 The differential elastic cross section is given by

$$\frac{d\sigma_{\text{el}}}{d\Omega} = \frac{d\sigma_{\text{SE}}}{d\Omega} + \frac{d\sigma_{\text{CE}}}{d\Omega}$$

the shape elastic ( $\sigma_{\text{SE}}$ ) was calculated from JPIX and the compound elastic ( $\sigma_{\text{CE}}$ ) was calculated from the statistical model code COMNUC.

Fig. 4 Shows the high degree of anisotropy in the inelastic scattering which is assumed to be due primarily to the direct excitation of these levels. The coupled-channel calculations while producing a satisfactory shape, slightly

underestimated the magnitude of the cross section by about 20%. The solid curves have been normalized to the experimental data. It should be mentioned that the experimental data of Stelson et al.<sup>(9)</sup> is for Cr(nat) which means that the low lying level contains a contribution for the 1.3 ( $5/2^-$ ) MeV level in  $^{53}\text{Cr}$ .

Fig. 5 Compares the coupled channel calculation with experimental data<sup>(9)</sup> at 14.0 MeV. Here the compound elastic cross section was zero, thus all the contribution is derived from the potential scattering.

## 2. Nickel (M. R. Bhat)

The following evaluation of the experimental data available on the even-even isotopes  $^{58, 60, 62, 64}\text{Ni}$  and the related calculations were carried out in connection with the ENDF/B-IV data library. There are extensive data on the inelastic cross section of the first excited  $2^+$  state in  $^{58}\text{Ni}$  at 1.454 MeV and in  $^{60}\text{Ni}$  at 1.333 MeV along with differential angular distributions. A continuous curve showing the excitation function for these levels could be drawn through the experimental data from threshold to about 8.56 MeV and joined smoothly to the results of coupled channel calculations above this energy. It is reasonable to assume that the compound nuclear contributions are essentially negligible at and above 9.0 MeV incident neutron energy and that the observed cross section is entirely due to direct interaction. Below this energy the compound nuclear and direct interaction cross sections were added to account for both the total magnitude of the inelastic cross section as well as the differential angular distributions.

The compound nuclear cross sections were calculated using the code COMMNUC-I<sup>(3)</sup> and the coupled channel calculations were done using JPIXR<sup>(2)</sup> which is a modified version of JUPITOR-1<sup>(1)</sup>. The optical model parameters used in the calculations were determined by fitting experimental differential elastic data in the energy range 0.2 to 14.0 MeV.<sup>(10)</sup> In these calculations all the discrete energy levels below 3.5 MeV excitation with known spins and parities were used and it was assumed that the levels above 3.5 MeV could be described by a continuum. However, in the coupled channel calculations, the  $3^-$  level at about 4 MeV was explicitly taken into account as it is strongly coupled to the ground state. The coupling

parameters used in these calculations are from the literature<sup>(9,11,12)</sup> were obtained from an analysis of (n,n'), ( $\alpha,\alpha'$ ) and (p,p') reactions. Because of the large computer time involved in the coupled channel calculations, only three states viz., the ground state, the first excited  $2^+$  state and either the  $3^-$  or one of the two phonon states were coupled at a time. At those energies where the compound nuclear contributions were significant, the direct interaction contribution was subtracted from the evaluated total inelastic cross section and the differential inelastic distributions from the compound nuclear processes normalized to this value. This was then added to the angular distribution given by the coupled channel calculations for comparison with experimental data. In case the evaluated inelastic cross section differed from the integrated inelastic cross section of a particular data set the differential angular distribution was further normalized to this value. The results of such calculations are shown in Figs. 6-12. In these are shown the data of Boschung and Lindow<sup>(13)</sup> for  $^{58,60}\text{Ni}$  and the data of Kinney and Perey<sup>(14)</sup> on  $^{60}\text{Ni}$ . In addition are shown the elastic scattering data at 14.0 MeV<sup>(15,9,16)</sup> and the inelastic scattering to the first excited state in the nickel isotopes. Kammerdiener<sup>(16,17)</sup> also obtains a value of  $39.5 \pm 2.8$  mb for the inelastic scattering to the first excited states in Ni. This agrees with the data of Stelson et al.<sup>(9)</sup> as well as the results of the present calculations.

References

1. T. Tamura, ORNL-4152 (1967).
2. C. J. Slavik, KAPL-M-7079 (1971).
3. C. L. Dunford, AI-AEC-12931.
4. A. Prince, BNL (to be published).
5. G. W. Greenlees et al., Phys. Rev. 171 (1968) 1115.
6. G. W. Greenlees et al., Phys. Rev. C1 (1970) 1145.
7. M. Bolsterli et al., Phys. Rev. C5 (1972) 1050.
8. W. E. Kinney, ORNL-4806, Jan. 1974.
9. P. H. Stelson et al., Nucl. Phys. 68 (1965) 97.
10. C. R. Lubitz, private communication (1973).
11. Nuclear Data Sheets B3 (1970).
12. T. Tamura, Prog. Theor. Phys. Supplement 37/38 (1966) 383.
13. P. Boschung, J. T. Lindow and E. F. Shrader, Nucl. Phys. A161 (1971) 593.
14. W. E. Kinney and F. G. Perey, ONRL-4807 (1974).
15. R. L. Clarke and W. G. Gross, Nucl. Phys. A95 (1967) 320.
16. J. L. Kammerdiener, UCRL-51232 (1972).
17. L. F. Hansen, private communication (1973).

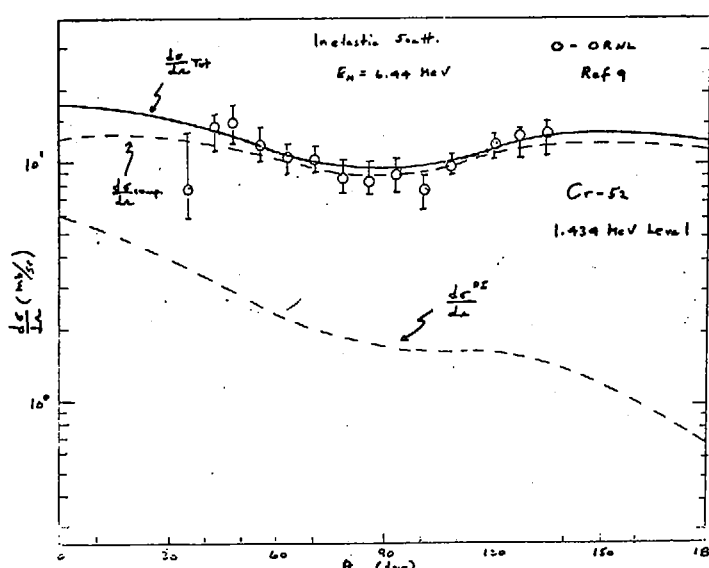


Fig. 1

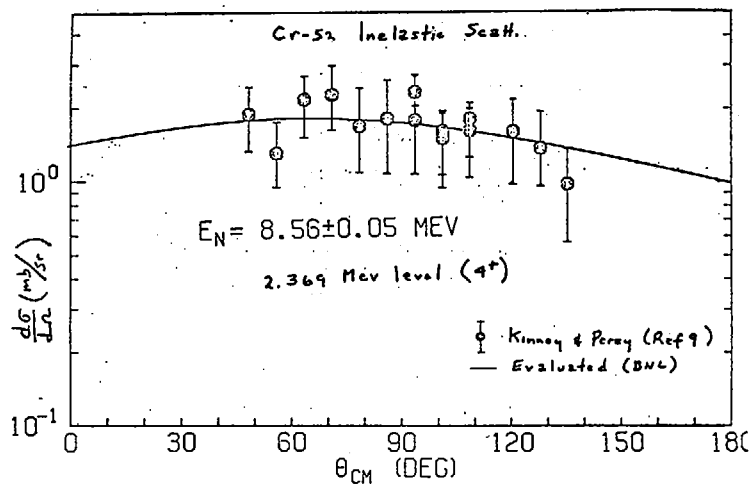


Fig. 2

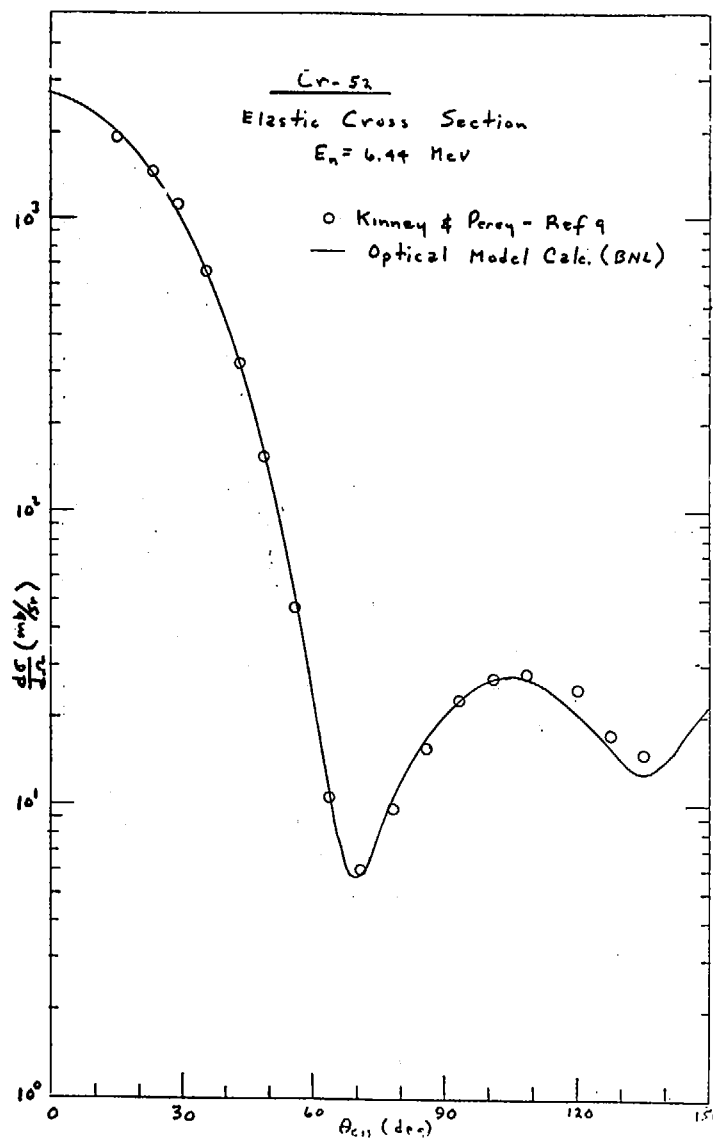


Fig. 3

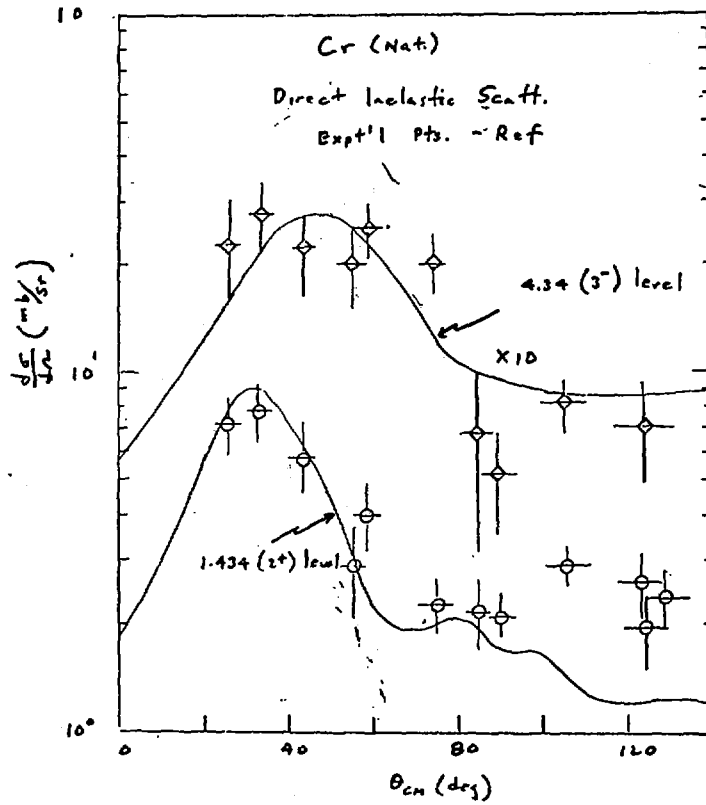


Fig. 4

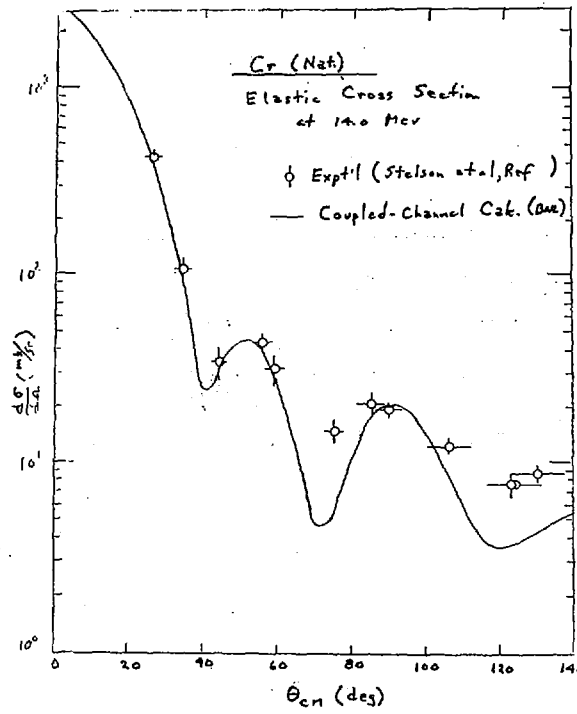


Fig. 5

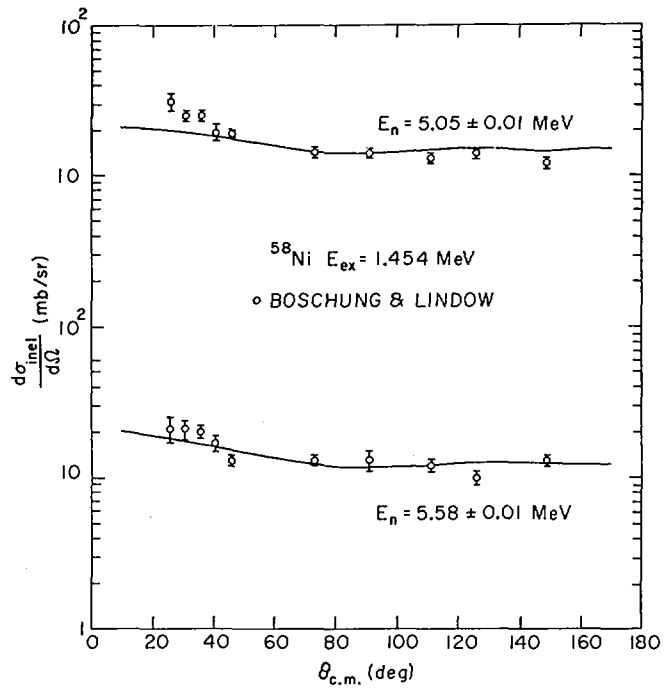


Fig 6

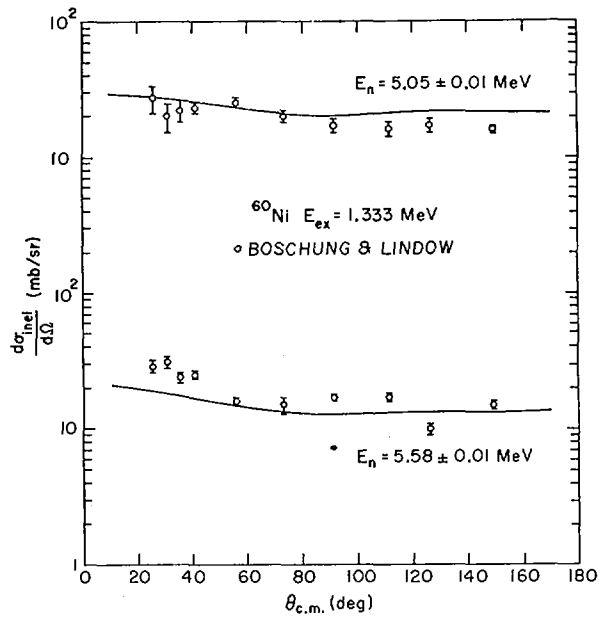


Fig 7

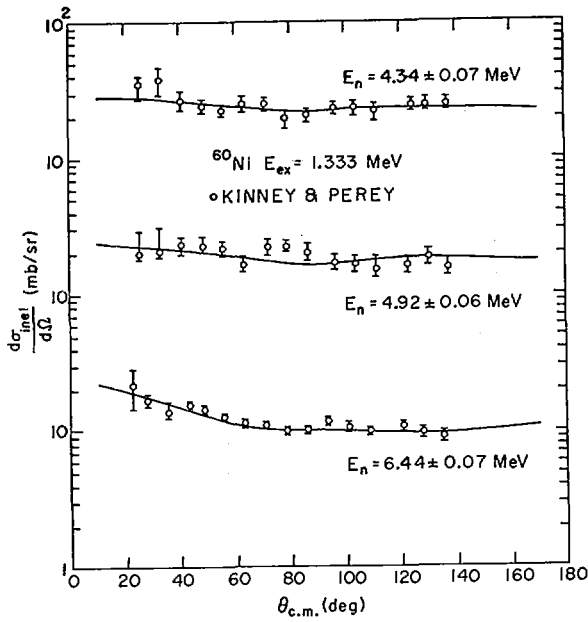


Fig. 8

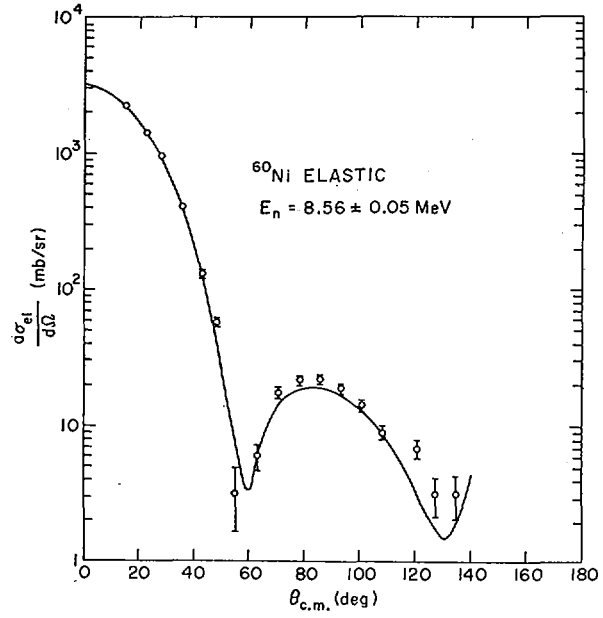


Fig. 10

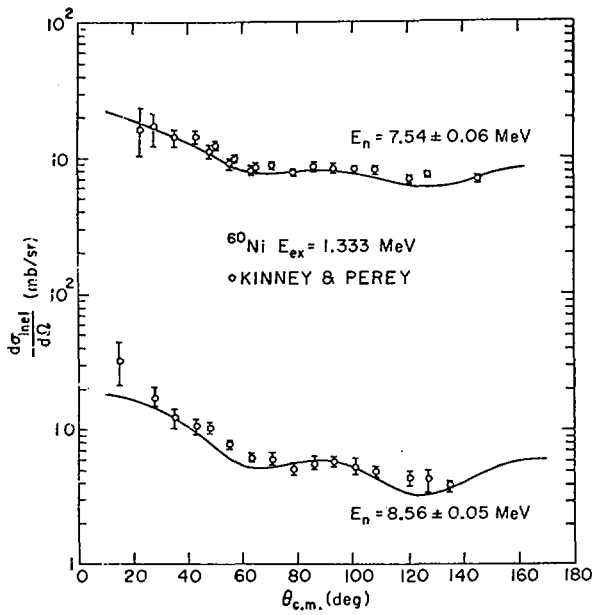


Fig. 9

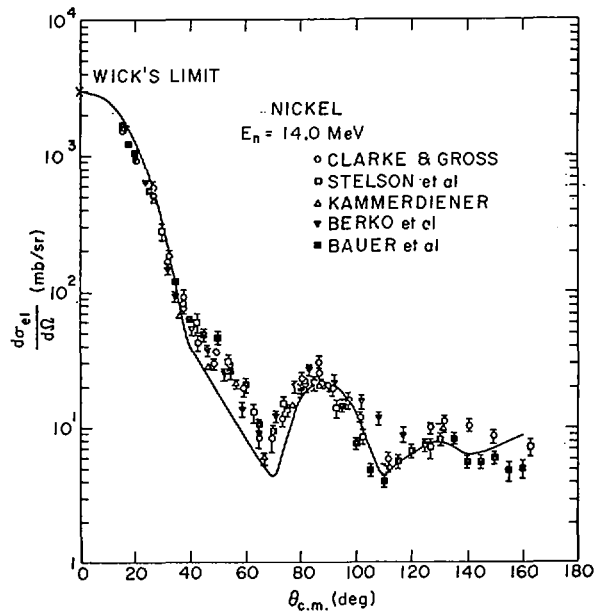


Fig. 11

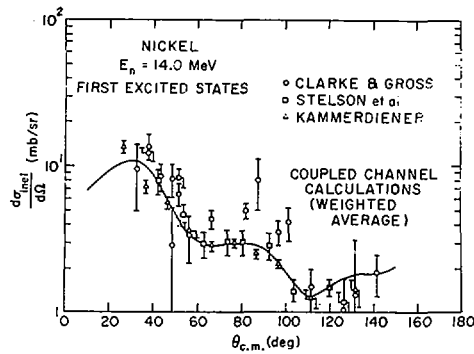


Fig. 12

DISCUSSION

S. TANAKA: In your talk on Prince and Bhat's work, what optical parameters did they use?

R. E. CHRIEN: I don't know. The optical parameters in Bhat's work were determined by fitting experimental differential elastic data in the energy range 0.2 to 14 MeV.

IV-2. The Effect of Gamma Ray Strength Function on the  
Neutron Capture and Gamma Ray Production Cross Section  
of Manganese and Europium

Hiroshi Takahashi

National Neutron Cross Section Center  
Brookhaven National Laboratory, Upton, New York 11973, U.S.A.\*  
(\*Present Address: Research Laboratory of Nuclear Reactor  
Tokyo Institute of Technology)

Abstract

To calculate the high energy neutron gamma ray production cross section of manganese, the ORNL measurements for iron were analyzed by changing the functional form of the gamma ray strength function. The  $E_\gamma^2$  dependence of the  $\gamma$ -ray strength function used by Axel in the region of 7 MeV, gives better agreement with the overall experimental spectra than the energy-independent form of the Blatt-Weiskopf single particle formula. The analysis was carried out by using the statistical model code GROGI-3 with the Greenlees and Fernandez optical potential parameters for neutron, proton, and  $\alpha$ -particles. Also, the yrast levels which affect the shape of the gamma-ray spectrum in the region of high and low energies, are taken into account. The neutron capture cross sections of manganese calculated by using the Axel formula are larger than the experimental values for neutron energies above 1 MeV. This result and the marked structure in the measured gamma ray production cross section indicates that the overall gamma ray strength function varies as  $E_\gamma^2$ . In addition to this, Cook's level density parameters for  $^{55}\text{Mn}$  used in these calculations were tested by comparing the calculated neutron emission spectrum with the experimental results. The agreement is good.

The analysis of the neutron capture cross section for Europium-151 and 153 isotopes indicates that there is less structure in the gamma ray strength function than for the light element manganese. The analysis also indicates that the neutron capture cross sections between 100 keV and 1.5 MeV in ENDF/B-II are too small by a factor of 2 to 3.

1. Gamma ray production cross section of Fe.

Since there are no experimental data on Mn it was decided to test the general validity of the evaporation - cascade model used in these calculations by comparison with the Fe ORNL data<sup>(1)</sup>. These measurements were analyzed by changing the functional form of the gamma ray strength function. The gamma-ray strength function is defined here as Eq. (1)<sup>(2)</sup>

$$f_{i \lambda X L}^J(E_\gamma) = \frac{\bar{\Gamma}_{\gamma i \lambda X L}^J}{E_\gamma^{2L+1}} \rho_J(E_\lambda) \quad (1)$$

where  $\bar{\Gamma}_{\gamma i \lambda X L}^J$  is the  $\gamma$ -ray partial width averaged over states  $\lambda$  of a given spin and parity (denoted together by J) in the neighborhood of  $E_\lambda$ ,  $\rho(E_\lambda)$  is the average level density for such states and  $E_\gamma^{2L+1}$  is the energy dependence for multiplicity L.

In the single particle approximation of Blatt, Weiskopf,<sup>(3)</sup> this strength function is energy independent. But it was pointed out by Brink<sup>(4)</sup> and emphasized by Axel<sup>(5)</sup> that a more realistic energy dependence of the E1 transition probability could be expressed by

$$f_{o \lambda E 1}^{\rightarrow} = K \frac{\Gamma_G E_\gamma}{(E_\gamma^2 - E_G^2)^2 + \Gamma_G^2 E_\gamma^2} \quad (2)$$

where K is constant for any particular nucleus and the quotient, involving the width  $\Gamma_G$  and energy  $E_G$  of the electric giant dipole resonance are derived from the classical Lorentz line. Figure 1 shows this function for Gd. This figure is taken from L. Bollinger's paper<sup>(6)</sup>. Axel has shown that the radiative width should vary approximately as  $E_\gamma^5$  in the region of 7 MeV. That is, the E1  $\gamma$ -ray strength function varies as  $E_\gamma^2$ .

To study the effect of the  $\gamma$ -ray strength functional form on the  $\gamma$ -ray production cross section, the statistical nucleus evaporation model code GROGI-III<sup>(7)</sup> was used to analyze the recent experimental results for iron. The analysis was carried out for <sup>56</sup>Fe isotope which has an abundance of 91.7% in natural Fe. The GROGI-III code replaces the details of nuclear level excitation by a continuum of levels, so that the strong structure shown in the experimental results are smoothed out and only the overall shape of the  $\gamma$ -ray spectrum is calculated. This code also handles yrast levels which are important in the calculation of the competition between neutron and radiative emissions from the high spin compound states. The effect of the yrast level on the  $\gamma$ -ray spectrum will be discussed later. As regards radiative transitions, this code handles only the dipole and quadrupole emissions. No distinction between electric and magnetic transitions is made because the excitation level density as defined in this code does not specify parity. The functional forms of the dipole and quadrupole  $\gamma$ -ray strength functions used in this code are energy independent in the single particle approximation. The code was therefore modified to take into account the  $E_\gamma^2$  dependence of the  $\gamma$ -ray strength function. The normalization of the radiative width was carried out so that its value was equal to the experimental measurement at the neutron binding energy. The optical potential parameters used in the transmission calculations of neutron, proton and  $\alpha$ -particles are respectively the ones obtained by Greenlees et al<sup>(9)</sup> and Fernandez<sup>(10)</sup>.

Figs. 2-5 show the  $\gamma$ -ray production cross sections calculated with the energy independent and  $E_\gamma^2$  functional form of the gamma-ray strength function, and the ORNL experimental results. These indicate that the cross sections calculated by using the  $\gamma$ -ray strength function of  $E_\gamma^2$  dependence are

closer to the experimental results than the ones calculated by the energy independent  $\gamma$ -ray strength function. As indicated above, since a continuum of excitation levels were used in these calculations they do not show any structure. It was pointed out by Thomas and Grover<sup>(11)</sup> that the yrast level affects very much the  $\gamma$ -ray production cross section and the averaged energy for fast fission  $\gamma$ -rays. The author<sup>(12)</sup> showed the effect of the yrast level on the  $\gamma$ -ray spectrum. To study this effect, figure 5 compares the  $\gamma$ -ray spectra which are respectively calculated with and without the consideration of yrast levels. The inclusion of the yrast level increases the high energy  $\gamma$ -rays and decreases the low energy  $\gamma$ -rays.

In this calculation, the yrast levels for low spin states were determined from the Horen et al.<sup>(13)</sup> level scheme and the ones for the high spin states were calculated by using the approximate expression of Eq. (3)<sup>(8)</sup>

$$E_J = (J + \frac{1}{2})^2 / 2 I + \delta \quad (3)$$

where J is spin, I represents the effective nuclear moments, and  $\delta$  is the pairing energy. From the analysis of the experiment for iron, it was found that the overall  $\gamma$ -ray production cross section could be calculated by using the  $E_\gamma^2$  dependent  $\gamma$ -ray strength function. Hence, the  $^{55}\text{Mn}$  calculations were carried out in the same way as for  $^{56}\text{Fe}$  using the  $E_\gamma^2$  dependent  $\gamma$ -ray strength function and the results put in the ENDF/B-IV (preliminary)<sup>(14)</sup> data files.

## 2. Neutron capture cross section of $^{55}\text{Mn}$ .

The neutron capture cross section of  $^{55}\text{Mn}$  was calculated by using the Hauser-Feshbach statistical model code COMNUC-3<sup>(15)</sup> with Axel's  $\gamma$ -ray strength function of Eq. (2). The discrete excitation levels were taken

from Horen et al.'s data and the continuum level parameters were taken from Cook's data<sup>(16)</sup> in the Cameron Gilbert formula<sup>(17)</sup>.

Figure 7 shows the comparison between the calculated neutron capture cross section and several experimental results. The calculated curve is quite similar to the one calculated by Devbenko<sup>(18)</sup>.

The calculated neutron capture cross section deviates from the experimental values above 1.5 MeV. To get the smaller capture cross section, the  $\gamma$ -ray strength function should be small or the competitive cross section such as inelastic should be large. However, the calculated discrete level excitation functions show good agreement with the experimental values. Furthermore, the calculated neutron emission spectrum for 7 MeV neutron also shows the good agreement with experiment so that the level density parameter used for the continuum level must be correct. Thus, to get the smaller neutron capture cross section, the  $\gamma$ -ray strength function should be smaller. In the light nuclei, the  $\gamma$ -ray strength function is not so smooth as shown in Fig. 1 but has some structure. This might give a smaller cross section above 1 MeV neutron energy. The neutron capture cross section from 0.1 MeV to 2.5 MeV in ENDF/B-IV (preliminary) data was evaluated mostly from the experimental data, but the small structure due to the opening of the inelastic neutron channel were taken into account by the results of the COMNUC-III calculations. The cross sections between 2.5 MeV and 10 MeV are evaluated from the Menlove et al.<sup>(19)</sup> data and the ones from 10 MeV to 20 MeV were based on the Longo-Saporetti<sup>(20)</sup> semi-direct process calculation.

### 3. The neutron capture cross section of $^{151}\text{Eu}$ and $^{153}\text{Eu}$ .

Figures 9 and 10 show the neutron capture cross sections of  $^{151}\text{Eu}$  and  $^{153}\text{Eu}$  respectively. Both ENDF/B-II data of  $^{151}\text{Eu}$  and  $^{153}\text{Eu}$  from 160 keV to 2.5 MeV are taken from the activation cross section of  $^{152}\text{Eu}$  9.3 h metastable state<sup>(21)</sup>, and the cross section for  $^{152}\text{Eu}$ -ground states is neglected. To evaluate the cross section, the COMNUC-III calculation was carried out in the same manner as in the case of  $^{55}\text{Mn}$ . The normalization of the capture cross section was carried out so that the calculated capture cross sections for both isotopes equal the Konks et al.<sup>(22)</sup> experimental data. The solid lines from 100 keV to 3 MeV are the values calculated by COMNUC-III code. These are larger than the ENDF/B-II data by a factor of 2 to 3. Recently, Harker<sup>(23)</sup> made the integral measurement by using the hard spectrum of CFRMF facility. The measured values are shown in the figures with the values calculated by using the flux obtained by Harker. The agreement between experimental and calculated values is excellent. The isomeric branching ratio obtained by Harker's integral measurements also confirms that the higher cross section of COMNUC-III calculation between 160 keV and 2.5 MeV is reasonable. In this calculation, the Axel's  $\gamma$ -ray strength function formula was used. The effect of the functional form on the capture cross section in low energy neutron energy range from 1 keV to 100 keV, is small and the calculation shows a straight line. The Konks et al. data indicates that there are small fluctuations in the capture cross section, but this must be due to the fluctuation of level density, etc. Therefore, the normalization of  $\gamma$ -ray strength function, which directly affects the capture cross section, should be done with care. Recent Czirr's<sup>(24)</sup> and Hockenbury's<sup>(25)</sup> preliminary experimental data around

10 keV neutron energy shows a little higher value than the Konks data, but we took the Konks experimental data as the ENDF/B-IV evaluated data from the consideration of Harker's integral experimental data and the COMNUC-III calculations. Above 2.5 MeV, the ENDF/B-IV data was evaluated by using the GROGI calculation and the direct semi-direct process estimates.

#### References

1. J. K. Dickens et al. Nucl. Sci. & Eng. 50, 311 (1973).
2. G. A. Bartholomew et al. Preprint "Advances in Nuclear Physics" Feb. 1973.
3. J. M. Blatt and V. F. Weisskopf. Theoretical Nucl. Phys. John Wiley and Sons, New York (1952).
4. D. M. Brink. Doctoral Thesis, Oxford University (1955).
5. P. Axel. Phys. Rev. 126, 671 (1962).
6. L. Bollinger in Proc. of International Symposium on Nuclear Structure, Dubna, Oct. 13-16, 1970. AED-CONF-70-364-002.
7. H. Takahashi. GROGI-III, Modified from GROGI-2 (8) (1972).
8. J. Gilat. BNL-50246 (T-580) (1969).
9. F. Becchetti and G. Greenlees. Phys. Rev. 182, 1190 (1969).
10. F. Fernandez. Phys. Rev. 180, 140 (1968).
11. T. D. Thomas and J. R. Grover. Phys. Rev. 159, 980 (1967).
12. H. Takahashi. Nucl. Sci. & Eng. 51, 296 (1973).

13. D. J. Horen et al. To be published in Nuclear Data Table.
14. H. Takahashi. To be published as ENDF/B-IV data.
15. C. Dunford. Private communication (COMNUC-3 code) (1971).
16. J. Cook, H. Ferguson and A. Musgrove. Australian Atomic Energy Commission AAEC/TM-392 (1967).
17. A. Gilbert and Cameron. Can. J. Phys. 43, 1446 (1965).
18. A. G. Dovbenko et al. J. of Atomic Energy 26, 67 (1969).
19. H. O. Menlove et al. Phys. Rev. 163, 1299 (1967).
20. G. Longo and F. Saporetti. Nucl. Phys. A127, 503 (1969).
21. A. E. Johnsrud, M. G. Silbert and H. H. Barshall. Phys. Rev. 116, 927 (1959).
22. V. A. Konks, Yu, I. Fenin. Dubna 64, 100 (1964).
23. Y. D. Harker. Private communication (1973).
24. J. B. Czirr. UCRL-50804 (1970).
25. R. Hockenbury et al. Private communication. Dec. 1973.

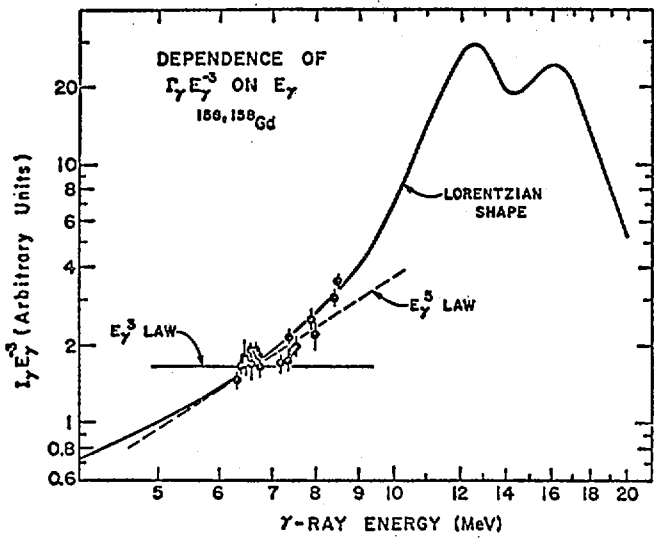


Fig. 1

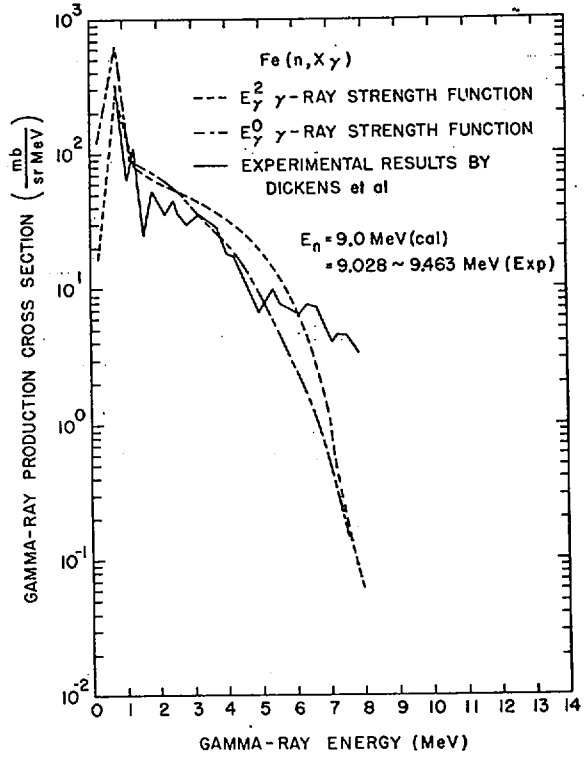


Fig. 3

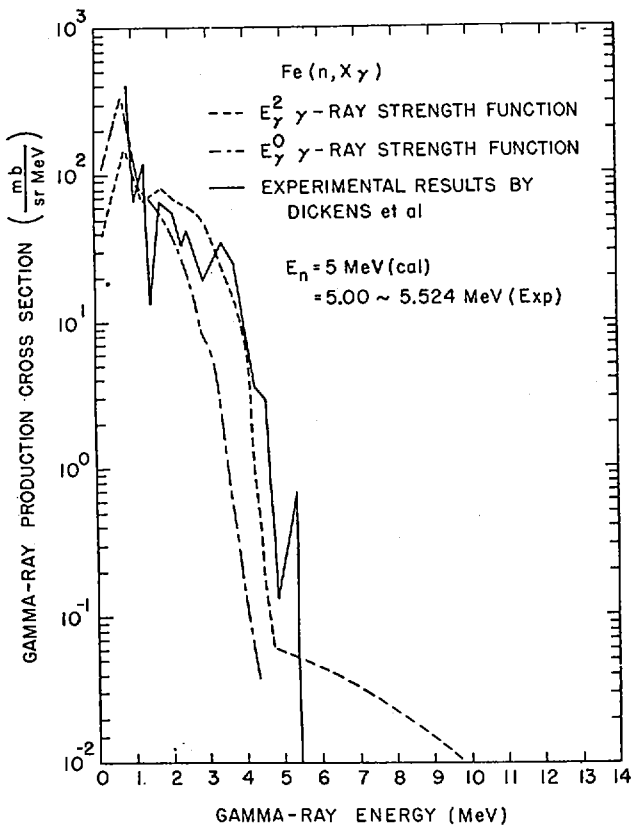


Fig. 2

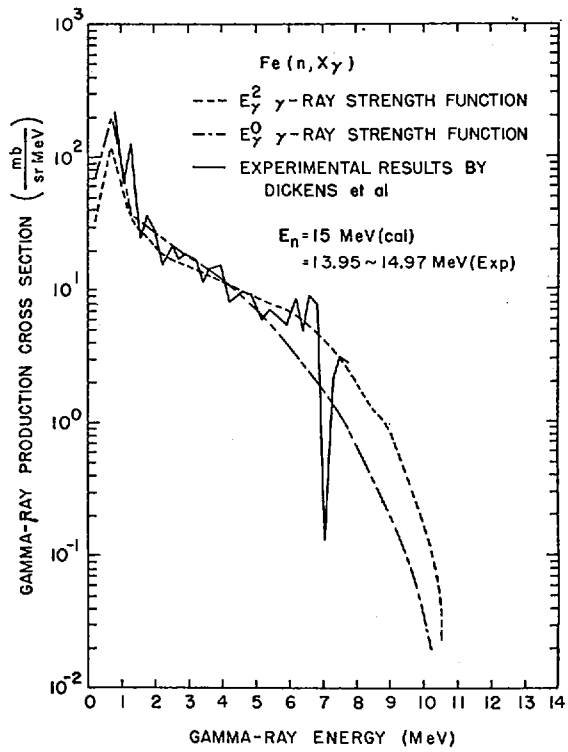


Fig. 4

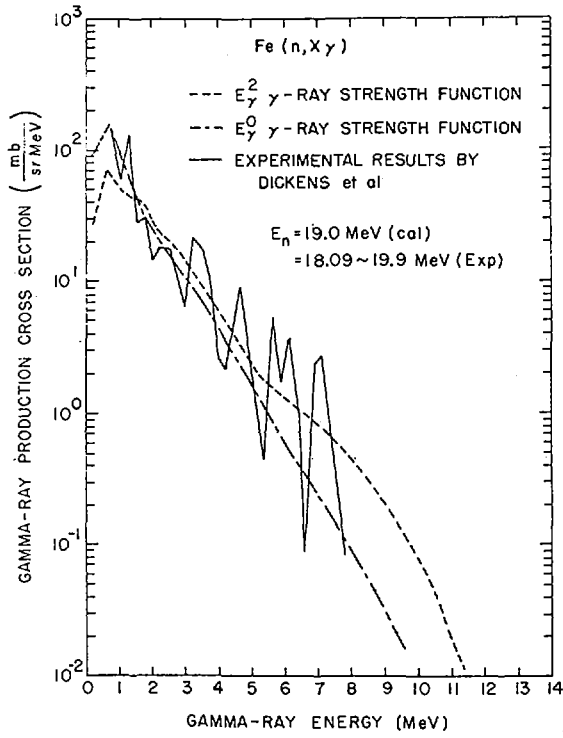


Fig. 5

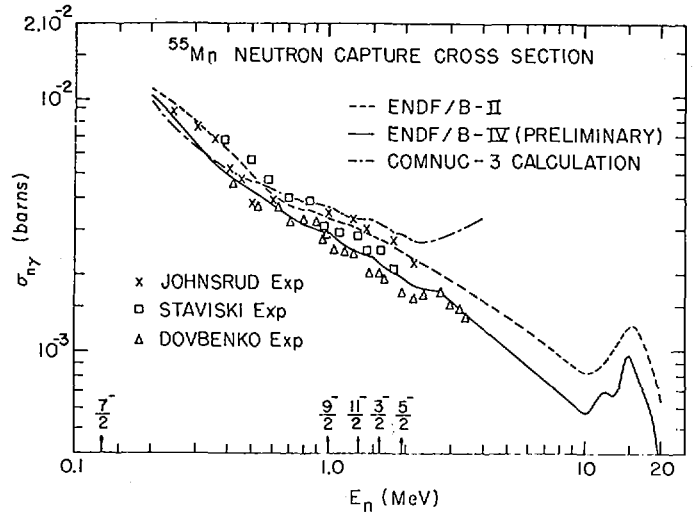


Fig. 7

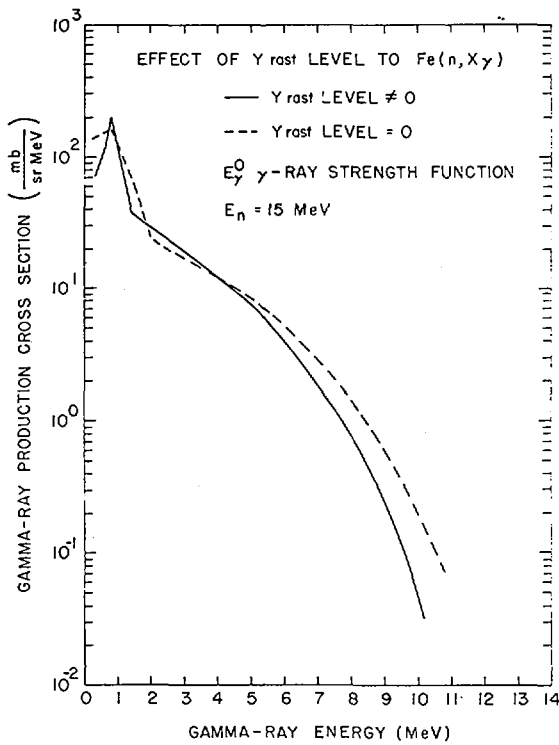


Fig. 6

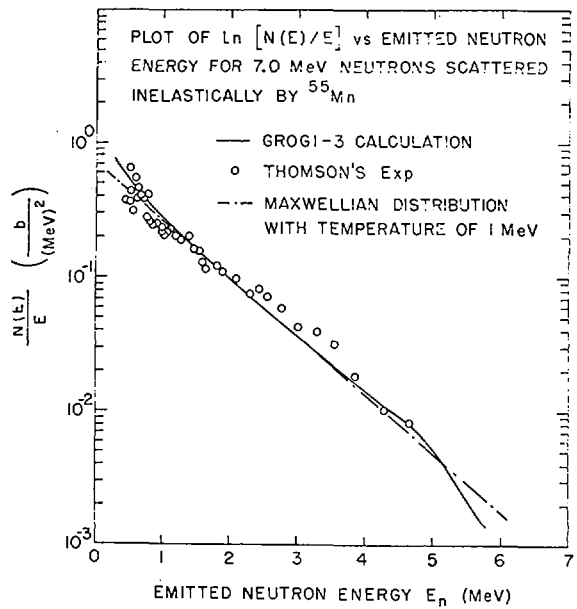


Fig. 8

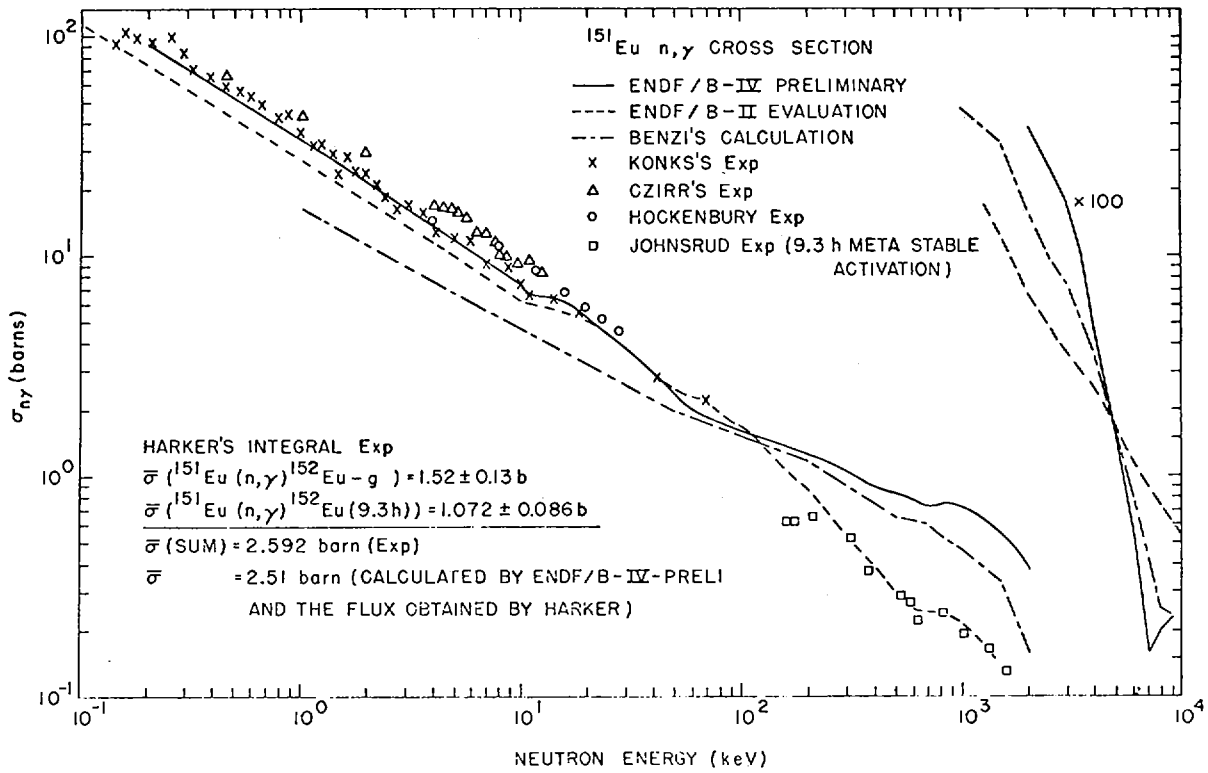


Fig. 9

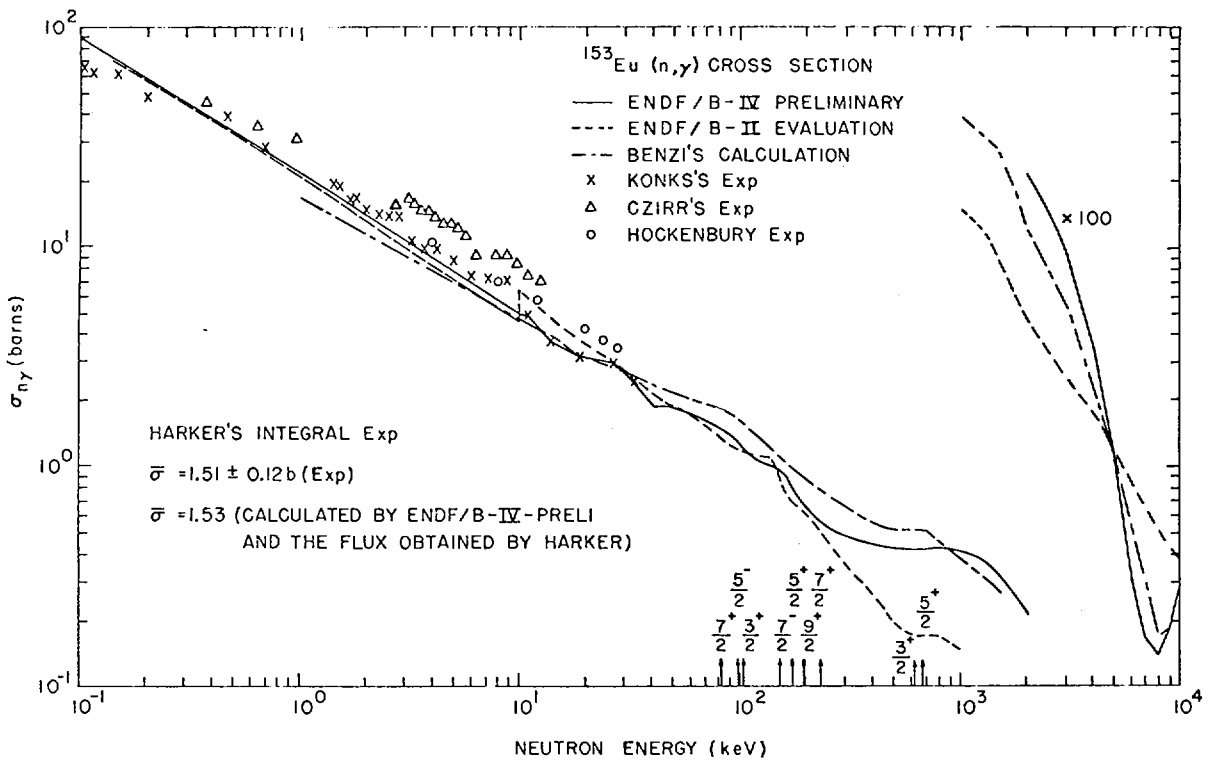


Fig. 10

## DISCUSSION

H. E. JACKSON, Jr.: I know of data on the photoabsorption cross sections for Mn and V from the Lawrence Livermore Laboratory which show strong structure in the threshold region. So it is not surprising that the results for Mn suggest structure in the photon strength function.

R. E. CHRIEN: We have seen evidence for a "pygmy" E-1 resonance in Mo 92-94-96-98 peaking near 7 MeV. The experiment was done with a 24 keV neutron beam with a FWHM of 2 keV.

IV-3. Models, Measurements and Evaluation<sup>\*†</sup>

by

P. Guenther, P. Moldauer and A. Smith

Argonne National Laboratory

Argonne, Illinois, USA.

ABSTRACT

A unified program of physical measurements and theoretical calculations for the provision of evaluated neutron data in the continuum region is outlined. The basic theoretical concepts are the optical, coupled-channel and statistical R-matrix models. The complementary measurement program provides the essential experimental foundation consisting primarily of neutron total and scattering cross sections. The integrated use of experiment and theory to provide evaluated data sets is discussed inclusive of: 1) average total and elastic scattering cross sections and the optical and coupled-channel models, 2) inelastic neutron scattering cross sections and the statistical and direct-reaction models, and 3) resonance statistics and fluctuations. The importance of physical concepts is emphasized throughout.

---

\*This work supported by the U. S. Atomic Energy Commission.

†Some of the contents are of a preliminary nature and subject to change.

I. Average Neutron Total and Elastic Scattering Cross Sections and the Optical Model

The basic tool for the interpretation, extrapolation and evaluation of fast neutron cross sections is the optical model (1) and its generalization, the rotational and vibrational coupled-channel model (2). The basic relation of these models to nuclear forces and experimental observables is schematically illustrated in Fig. 1.

--- The data that are most basically related to these models are the average total and elastic scattering cross sections.

The average total cross section is always directly specified by the optical or coupled-channel models. These models also provide shape elastic and direct inelastic cross sections. At low energies where few inelastic channels are open these calculated cross sections must be supplemented by compound-nucleus contributions which can be estimated by methods discussed in Section II, below. In addition, neutron strength function data may be used for determination of the model parameters and the behavior of the fluctuating cross sections at lower energies can provide additional information as discussed in Section III, below.

The present work is a physically integrated approach to model determination based upon complimentary measured total and elastic scattering cross sections in the energy range 0.1 to 6.0 MeV and above with the objective of providing comprehensive evaluated neutron data sets. The comparison of measured and calculated results reveals information about the variation of model parameters from nuclide-to-nuclide including the magnitude of the  $(N-Z)/A$  dependent term, the energy dependence of model parameters and the effect of ellipsoidal deformation. The results are of value

in the prediction and extrapolation of cross sections, as inputs to the calculation of inelastic cross sections and in the study of cross section fluctuations. The application of models to inelastic scattering are discussed in Section II. Section III deals with fluctuations and their implications on the selection of optical and coupled-channel parameters.

The experimental average total cross section foundation is obtained by measurements (3 to 9) with the objective of assuring the

---- precise experimental values essential to the formation of the model and evaluation.

The experimental resolution is good but not a goal in itself. Fig. 2 illustrates the type of results obtained for nickel together with the corresponding measured elastic scattering values and evaluated total cross section. The latter is derived from high-resolution values reported primarily by Perey et al. (10) and Cierjacks et al. (11), normalized where necessary to the present experimental values. The model parameters are chosen so as to describe the observed average total cross sections to within a few percent from 0.1 to 20 MeV. The adjustments include the six optical model parameters and the deformation,  $\beta_2$ . The energy dependence of the parameters is a free variable but the results are generally consistent with that reported by Engelbrecht and Fiedeldey (12). The characteristically good agreement between measured and calculated total cross sections is illustrated in Fig. 3.

---- The potentials are specific to the given nuclide and not necessarily of a general nature.

The model parameters fluctuate from nuclide-to-nuclide reflecting real differences in the total cross sections. For example, the iron and nickel models differ appreciably due

primarily to the 15-20% differences between iron and nickel average total cross sections in the region 1 to 3 MeV.

The total-cross-section based model parameters are subsequently adjusted to fit the measured elastic scattering angular distributions  
---- the measurement of which is an essential part of this effort.

At low energies the measurements are made with sufficient resolution to define the intermediate structure and at higher energies with broader resolutions (3 to 9). The iron and niobium results of Fig. 4 illustrate this experimental foundation. They are extended to higher energies using values reported in the literature (e.g. by Perey et al. (13) and by Holmqvist and Wiedling (14)).

The model adjustments emphasize elastic scattering at energies  $\sim 5$  MeV where the compound-elastic contribution can be reasonably well determined. The adjustments were constrained to give a continued good agreement with the observed average total cross sections. Below 1-2 MeV the pronounced fluctuations in cross sections of lighter nuclei can preclude the determination of a well defined average elastic angular distribution. Above approximately 6-8 MeV the angular distributions are primarily due to shape-scattering but compound-nucleus and other processes (e.g. pre-compound processes) remain contributing factors particularly in the minima which are very sensitive to model parameter choice. Some of these physical aspects are illustrated by the examples of Fig. 5. A simple spherical potential is suitable for cobalt in the few MeV range. Above 3 MeV the calculation of compound elastic contributions becomes uncertain, yet the measured values fall between the limits of shape-elastic and shape-elastic+compound-elastic calculations. The same trends occur in nickel. However, the first few excited states are known to be two-phonon vibrational levels

(15) and thus the calculations are based upon the coupled-channel model, coupling the ground and first excited states in a vibrational interaction.

---- The effect of coupling on the elastic distributions can be large, 50% or more at some angles and energies.

Fissile, fertile and many fission product nuclei are rotational-deformed and precise measurement of their scattering cross sections is difficult. Theoretical extrapolation is often necessary and the coupled-channel model is a suitable mechanism. Such a model has been experimentally validated in the case of W-186 and subsequently utilized in the evaluation of the scattering cross section of U-238.

The energy intervals of the ground-state rotational band of W-186 are about twice those of U-238 (15). As a consequence, W-186 scattering cross sections can be well resolved at few-MeV energies in a manner not technically feasible in the case of U-238. The total and scattering cross sections of W-186 were measured to  $\sim 4$  MeV and used to deduce the parameters of a coupled-channel model. The suitability of the model is illustrated in Fig. 6. The overall best agreement with measurements was obtained with an ellipsoidal deformation of  $\beta_2 \sim 0.2$ . This value is smaller than that deduced from charge-sensitive studies (e.g. coulomb excitation (16)) with possible theoretical implications.

With minor adjustments the above W-186 model also describes the U-238 average total cross sections over the range 0.1 to 20 MeV and the elastic angular distributions to 8 MeV. The latter comparisons included inelastic scattering components consistent with the various experimental resolutions employed in the measurements. The majority of the elastic angular distributions were measured especially for this interpretation and evaluation and the experimental resolutions

are reasonably well known. Representative comparisons of measured and calculated elastic angular distributions are shown in Fig. 7. Generally the measured values fall between the two limits: 1) shape-elastic+direct-elastic and 2) shape-elastic+compound-elastic+compound-inelastic+direct-inelastic. The discrepancies between measurement and calculation are generally no larger than between experiments and systematic uncertainties tend to be concentrated near the cross section minima where the unresolved contributions from inelastic scattering are largest, the data most uncertain, and the contribution to the angle-integrated cross sections least.

The angle-integrated elastic scattering cross sections deduced from the model interpretation of experiment are summarized in Fig. 8. The results lead to

---- evaluated U-238 elastic scattering cross sections differing from ENDF/B (17), particularly in the range 1-3 MeV.

No physical explanation of the latter's lower values could be identified. The present evaluated elastic cross sections imply the total inelastic scattering cross sections shown in Fig. 9.

---- These results are consistent with those subsequently deduced from discrete excitation functions but are 10-20% lower than the maximum of the ENDF/B evaluation.

Such a reduction in the inelastic scattering cross section of U-238 has been indicated from the analysis of some integral experiments. This U-238 example illustrates the importance of precise evaluation of total and elastic scattering cross sections with their consequent implication of non-elastic and inelastic scattering cross sections.

It is attractive to employ the optical model for broad extrapolations in mass, energy and charge and this is widely done. Fundamental considerations lead to generality at the expense of simplicity (18). The non-locality of the nuclear

force implies an energy dependence of the potential (19). Iso-spin considerations lead to an  $(N-Z)/A$  dependence (20) and shell dependent terms have been proposed (21). The resulting "global" optical potentials have not been extensively verified in a neutron context.

--- Therefore the generality of the optical potential was quantitatively examined for neutron induced processes in the region of  $A=100$ .

This is the mass region of many fission products whose evaluation is often based upon model extrapolations. The potential can be written in the form (22).

$$V_{\text{real}} = V_0 - BE - (N-Z)/A \times C \quad (1)$$

$$W_{\text{imag}} = W_0 - DE - (N-Z)/A \times E$$

The constants are usually determined from comparisons of measured and calculated charged-particle induced processes. An example is the work of Becchetti and Greenlees (22) from which the values  $V_0 = 56.3$  MeV,  $B=0.32$ ,  $C=24$  MeV,  $W_0 = 13$  MeV,  $D=0.25$  and  $E=12$  MeV are obtained. These values of  $B$  and  $D$  are consistent with those of other authors (12).  $C$  and  $E$  are more uncertain even with respect to sign (1,20). In any event, these parameters and Eq. 1 lead to appreciable variations of the potential even for rather small mass and energy shifts.

We have studied a comprehensive set of measured total and scattering cross sections of the isotopes Mo-92, -96, -98 and -100 extending from a few hundred keV to 4 MeV. The measurements were made in such a manner as to best identify the mass dependence. The total cross sections were determined with accuracies of  $\sim 5\%$  and the differential scattering measurements made with sufficient detail to assure a good data

base in both energy and angle and to avoid isolated energy dependent fluctuations. The energy range was chosen to be reasonably consistent with a knowledge of all exit channels. Some impression of the scope of this experimental foundation is given in Fig. 10.

The analysis was based upon a six parameter Xi-square fit to the measured elastic angular distributions (real and imaginary strengths, radii and diffusenesses). The potential form consisted of Woods-Saxon real, Gaussian-surface imaginary and Thomas spin-orbit terms. The compound-elastic contributions were calculated using the Hauser-Feshbach formula with width fluctuation corrections. The overall agreement between experiment and calculation using a fixed potential is illustrated in Fig. 10. Careful "tuning" of parameters from this general base lead to several conclusions.

---- The real potential strength decreased with increasing mass at each energy.

The effect was very small but consistent with the constant "C" of Eq. 1. The parameter "B" giving the energy dependence tends to be smaller than 0.32 of Ref. 22.

---- The results were not sensitive to small variations in  $W_{\text{imag}}$  given in Eq. 1.

There was a small tendency toward decreasing imaginary radius with increasing energy. This may be a first step toward the volume absorption known to exist at higher energies.

We conclude that there is

---- a small  $(N-Z)/A$  dependence of the real potential for neutron processes in the mass-energy region  $A=100$ ,  $E \lesssim 4.0$  MeV consistent with that observed in charged-particle studies (22).

The magnitude of the effect is only slightly greater than the experimental uncertainties. Further, it is possible that the

effect is mitigated by some other potential dependence (e.g. shell effects).

The model parameters derived here in general do not agree well with those deduced from high energy elastic scattering cross sections ( $E > 6$  MeV). The manner of the transition of the parameters from the low to high energy region will present an interesting topic for further study.

The above optical and coupled-channel models provide a good method for the energy extrapolation of total cross sections in the absence of definitive experimental information. They are directly employed in the angle and energy extrapolation of elastic cross sections for evaluation, where such extrapolation is always necessary to some degree. The models can also be used for extrapolating into unmeasured regions (e.g. fission products) but only with reduced reliability as detailed variations of the model parameters from nuclide to nuclide are still uncertain.

## II. Inelastic Neutron Scattering

Optical and coupled-channel parameters determined through the fitting of neutron total and elastic-scattering cross sections can be applied to the  
--- calculation of average inelastic neutron scattering cross sections by means of the Hauser-Feshbach formula (23).

Where spins and parities of inelastic levels are known comparisons of the Hauser-Feshbach predictions with observed excitation functions can provide additional confirmation of the optical and coupled-channel model parameters. Where they are unknown level spins and parities can be determined either precisely or within limits.

Precise application of the models for the interpretation and evaluation of inelastic neutron scattering data ----- requires modifications of the conventional Hauser-Feshbach formula.

They are the width fluctuation and resonance interference corrections (24). The latter is important at higher energies where the excitation of individual levels generally becomes difficult to resolve. The width fluctuation correction enhances the average cross sections for reactions in which the entrance and exit channel fluctuations are correlated, with a corresponding reduction of reactions without such correlation. One example is the reduction of the cross section for the excitation of the first few levels near threshold. This reduction can approach a factor of 1/2 in the case of the first 2+ level of an even isotope. A second example is the enhancement of compound-elastic scattering which may approach a factor of three when a large number of exit channels are open. The latter can be important in the determination of optical model parameters from elastic scattering cross sections (see Section I, above). Finally, ----- the theory predicts an enhancement of inelastic cross sections for levels that are strongly coupled to the ground state.

This is the result of both the direct cross section due to channel coupling and the correlation enhancement of the compound-inelastic cross sections. Theoretical and numerical studies are now in progress which will define more accurately the application of these corrections to the Hauser-Feshbach formula. The use of a number of these concepts to the interpretation and evaluation of inelastic neutron scattering cross sections is outlined in the following paragraphs.

The simplest example is the use of the spherical optical model and the Hauser-Feshbach formula in the interpretation and evaluation of inelastic neutron scattering from cobalt.

The measured values, the calculated results and the evaluation are summarized in Fig. 11. The theory guides the evaluation near threshold. However, the range of applicability is narrow with increasing uncertainty above  $\sim 3$  MeV due to unknown exit channels. The uncertainties are such as to make detailed interpretation unrewarding. Even in the well defined range the calculations are sensitive to  $J^\pi$  as indicated by the two sets of calculations based upon alternate spectroscopic schemes (15). Neither is in detailed agreement with experiment but the calculations do resolve  $J^\pi$  ambiguities. For example, the 1.19 MeV state is  $9/2^-$  rather than the alternate  $5/2^-$  allowed by charged particle studies. This assignment as well as similar ones support a spectroscopic scheme consistent with the concept of a proton hole in the  $f_{7/2}$  shell strongly coupled to the spherical core with associated collective bands in the manner of Mottelson and Nilsson (27).

--- Thus even this rather simple approach can give structure information not otherwise easily available.

--- However, the evaluation remains primarily based upon experimental information.

Indeed, undue reliance on the model can lead to erroneous results. For example, Fig. 12 compares the present experimentally based evaluation (curve A) with ENDF/B (curve B) based primarily upon model calculations. While the thresholds are very similar the magnitudes of the prominent components can differ by a factor of two or more.

The effects of channel-coupling and the width fluctuation correction are evident in inelastic scattering from nickel. The first few excited states of the predominant even isotopes are vibrational levels. Results of calculations based upon both spherical and coupled-channel models are compared with experimental results in Fig. 13. At these

energies the spherical and coupled-channel (ellipsoidal) results do not appreciably differ. However, the direct contribution increases with energy amounting to  $\sim 40$  mb for the excitation of the first  $2+$  state at 14 MeV; consistent with experimental observations of Kammerdiener (25). Below 3 MeV some of the cross sections calculated with the Hauser-Feshbach formula are appreciably larger than the experimental values (e.g. the excitation of the  $2+$ , 1.45 MeV state in Ni-58). In these instances the experimental results themselves vary considerably probably reflecting actual fluctuations very similar to those commonly observed in the excitation of the 346 keV state in iron. It is a region where the fluctuation correction should be large and, indeed, it reduced the Hauser-Feshbach result by approximately a factor of two as indicated by the WFC curve of Fig. 13.

--- When fluctuation corrected the calculation provides a good extrapolation of measured values into the experimentally difficult threshold region.

The fissile and fertile nuclei as well as many fission product nuclei are ellipsoidally deformed with rotational level spectra (15). The members of the ground state energy bands of these nuclei are strongly coupled to the ground state with a resulting enhancement of the cross section for excitation of these levels by inelastic neutron scattering. An example is provided by the scattering to the first several excited states in W-186 which is shown in Fig. 6. The spherical model calculations ( $\beta_2 = 0$ ) are seen to be low by about a factor of three, while coupled channel calculations with spheroidal deformation parameters  $\beta_2$  in the range of 0.2 - 0.3 provide good agreement with the observed cross sections. The influence of the deformation

is clearly of great importance. In this case the inelastic calculations are consistent with the value of  $\beta_2 \sim 0.25$ , deduced from the elastic scattering cross sections.

---- The W-186 study establishes the importance of a coupled-channel model for application to the experimentally more uncertain inelastic scattering in U-238. At low energies the model can be used to extrapolate the discrete level excitation cross sections of U-238 but it becomes less reliable at higher energies where the level structure is uncertain or unknown. For example, the excitation of the first excited state (2+, 45 keV) can be experimentally resolved to 1.2 MeV (7). The direct component of the inelastic cross sections for this first excited state is computed to remain large up to several MeV as indicated by the dotted curve in Fig. 15. At  $\sim 3.0$  MeV this cross section is several times the value given in the ENDF/B evaluation. At low energies the excitation function for the first excited state in  $U^{238}$  exhibits the effects of both direct coupling and width fluctuations. A definitive evaluation in this region requires a calculation including those effects. In this region there is a large discrepancy between experimental values and  
 ---- extrapolation to threshold using theory provides an essential guide to evaluation.

### III. Resonances and Fluctuations

The high resolutions now technically available provide details of the resonances or fluctuations up to relatively high energies. The optical and coupled-channel models can also be applied to the calculation of the statistical properties of these fluctuations. The average reaction amplitudes provided by these models determine the average R-matrix parameters  $R^\infty$  and  $\langle \gamma_{\mu e}, \gamma_{\mu d} \rangle / D$ . The resonance spacings  $D$  are determined from resonance neutron data and the  $\gamma_{\mu e}$  are assumed to be normally distributed with zero means.

This information suffices to construct a numerical statistical reaction amplitude. From this, fluctuating cross sections are computed whose statistical properties are then compared with the measured high resolution data. This statistical comparison permits a further "fine tuning" of the optical or coupled-channel model parameters. It also permits the statistical prediction of cross section fluctuations from poor resolution data. Finally, the method is used for better definition of parameters that determine width fluctuation and resonance interference corrections to the Hauser-Feshbach formula. This is done by averaging the statistically generated cross sections and comparing these averages with the predictions of the formula.

The above computational procedures have been incorporated into a computer program STASIG (26). A random number generator is used to select the R-matrix parameters in accordance with optical and statistical model. The statistical cross sections are calculated, averaged with a resolution function equivalent to that of the experiments and compared with the measured values. Such statistical comparisons can be made either qualitatively by visual comparisons of the curves or quantitatively by comparisons of auto-correlation functions, cross section distribution functions, etc. The internal consistency of the calculations is verified by averaging the statistical total cross section over large energy intervals and comparing these averages with cross sections obtained from the optical model employed in the input to the calculations.

The total and inelastic scattering cross sections of the even isotopes of titanium were calculated using the above methods with both spherical and ellipsoidal models and compared with the measured values obtained in the

complementary experimental effort (8). The measured and calculated total cross sections are compared in Fig. 16.

---- Both qualitatively and quantitatively the ellipsoidal calculation agrees better with the measurement, particularly with respect to the cross section extrema and the grouping of resonances, as well as with regard to the auto-correlation function.

Similar comparisons of measured and calculated cross sections for the excitation of the 984 keV state of Ti-48 are shown in Fig. 17.

---- The ellipsoidal result is similar to the measured inelastic values, in contrast to the results obtained with the spherical model.

In this instance it is not possible to distinguish between spherical and deformed models on the basis of average total and elastic scattering cross sections. However,

---- the analysis of the fluctuations clearly indicates a preference for the ellipsoidal coupled-channel model. In addition, the ellipsoidal calculations lead to an intermediate resonance structure similar to that observed without recourse to other reaction mechanisms.

The above methods were applied to the evaluation of the total cross sections of cobalt. High resolution experimental data is available at energies  $\gtrsim 0.45$  MeV with apparently no equivalent information between. The fluctuating cross sections were calculated from the optical model, statistically verified against the experimental results available both below and above the region of ignorance and then used to interpolate across the experimental gap. The resulting evaluated cross section is shown in Fig. 18. It is difficult to distinguish the model-interpolated region from the adjoining experimentally-based values. Ultimately the above procedures have a potential for the direct provision of fluctuating cross sections by

analytical means thereby avoiding the increasing enormity of evaluated numerical files and providing a physical insight well beyond the experimental capability.

#### IV. Summary Comment

The above integrated program of models, measurements and evaluations highlights some general conclusions.

- There is no substitute for as good an experimental data base as possible. It is essential to reliable models and evaluations.
- Models have their primary strengths in the extrapolation, interpolation and physical interpretation of measured values.
- Models extending too far from the experimental foundation should be applied with considerable caution and only when no other alternative is available.
- The provision of evaluated data is an integrated physical endeavor consisting of measurements, interpretation and evaluation. They are not separate disciplines and, in particular, evaluation in itself cannot create information or knowledge.

## References

Only basic references are given, detailed references are found therein.

1. P. Hodgson, The Optical Model of Elastic Scattering, Clarendon Press, Oxford (1953), and refs. contained therein.
2. T. Tamura, Rev. Mod. Phys., 37, 679 (1965).
3. A. Smith et al., Argonne Natl. Lab. Report, AP/CTR/TM-4 (1973), See also Z. Phys., 264, 379 (1973).
4. P. Guenther et al., Argonne Natl. Lab. Report, ANL/NDM-6 (1974).
5. P. Guenther et al., Argonne National Lab. Report, ANL/NDM-1 (1973). See Also A. Smith et al., CHIX See also A. Smith et al., Chicago Meeting of the AM. Phys. Soc., Feb. (1974).
6. A. Smith et al., BAPS. 18, 648 (1973).
7. A. Smith et al., Argonne Natl. Lab. Memorandum, Comments on Inelastic Neutron Scattering from U-238 (1973).
8. P. Guenther et al., Argonne Natl. Lab. Report, ANL/NDM-5 (1974).
9. E. Barnard et al., Argonne Natl. Lab. Report, ANL/NDM-3 (1973). See also P. Moldauer et al., BAPS. 18, 648 (1973).
10. F. Perey, Priv. Communication (1974).
11. S. Cierjacks et al., Kernforschung Report, KFK-1000 (1968).
12. C. Engelbrecht and H. Fiedeldey, Ann. Phys., 42, 262 (1967).
13. F. Perey et al., Series of Oak Ridge Natl. Lab. Reports, See for example W. Kinney and F. Perey, ORNL-4549 (1970).
14. B. Holmqvist and T. Wiedling, Aktiebolaget Report, AE-430 (1971).
15. Nuclear Data sheets, see respective a chains.
16. P. Stelson and L. Grodzins, Nucl. Data, 1A, 21 (1965).
17. Evaluated Nuclear Data file/B-III, National Neutron Cross Section Center, Brookhaven Natl. Lab. (ENDF/B).
18. K. Brueckner, Phys. Rev., 96, 508 (1954).
19. F. Perey and B. Buck, Nucl. Phys., 32, 353 (1962).
20. A. Lane, Nucl. Phys., 35, 676 (1962).
21. A. Lane et al., Phys. Rev. Lett., 2, 424 (1959). See also W. Vonach et al., Phys. Lett., 11, 331 (1964).

22. F. Becchetti and G. Greenlees, Phys. Rev., 182, 1190 (1969).
23. W. Hauser and H. Feshbach, Phys. Rev., 87, 366 (1952), See also L. Wolfenstein, Phys. Rev., 82, 690 (1951).
24. P. Moldauer, Rev. Mod. Phys., 36, 1079 (1964).
25. J. Kammerdiener, Lawrence Livermore Lab. Report, UCRL-51232 (1972).
26. P. Moldauer, Priv. Communication (1974).
27. B. Mottelson and S. Nilsson, K. Danske Vidensk. SELSK., MAT-FYS. SKR. 1, No.-8(1959).

## FIGURE CAPTIONS

1. Schematic outline of the interrelation of nuclear forces, optical and coupled-channel models and calculable observables.
2. Total neutron cross section of nickel (8). Present measured values are indicated by  $\odot$  ( $E > 1.5$  MeV) and the solid curve ( $E < 1.5$  MeV) and the evaluation is shown by the dotted line. Measured elastic scattering values are indicated by  $\blacksquare$ .
3. Measured and calculated total cross sections of nickel (8). The "experimental" values were constructed from a number of sources (e.g. Refs. 10 and 11). The calculation was obtained using a coupled-channel model.
4. Elastic neutrons scattering cross sections of iron and niobium (3, 4) present measured values are indicated by data points. The curves indicate the results of legendre-fits to the data. Intermediate structure is evident in iron at lower energies.
5. Differential elastic scattering cross sections of nickel and cobalt (5,8). Measured values are indicated by symbols with the present results denoted by "o". The curves indicate the results of model calculations using spherical (cobalt) and ellipsoidal (nickel) potentials.
6. Measured and calculated differential neutron scattering cross sections of W-186 (6). The experimental values are indicated by symbols and the results of calculations using varying deformations from  $\beta_2 = 0$  to 0.3 are shown by curves. The upper distributions pertain to elastic scattering and the lower to the inelastic excitation of the  $2^+$ , 125 keV state.
7. Differential elastic scattering cross sections of U-238. Measured values are indicated by symbols with the present work given by "o" (7). All the measured values contain some contribution from inelastic neutron scattering. The results of ellipsoidal calculations are indicated by curves with the notations; SE=shape-elastic, CE=compound-elastic, DI=direct-inelastic and

CI=compound-inelastic.

8. Total and elastic scattering cross sections of U-238 (7). The present evaluations are indicated by the heavy curve. That of ENDF/B (17) by the light curve. Data points indicate the elastic scattering cross sections deduced from spherical and ellipsoidal models based upon experiments. Dashed curves indicate a subjective estimate of the limiting uncertainties in the calculated results.
9. Total inelastic scattering cross sections of U-238 (7). Dotted curves indicate the values implied by total and elastic scattering cross sections with respective maximum and minimum limits. The heavy curve indicates the present evaluated total inelastic scattering cross section and the light curve that of ENDF/B (17).
10. Differential elastic scattering cross sections of Mo-92, -96, -98 and -100. Measured values are indicated by data points. The results of a general optical model fit to the data are indicated by curves.
11. Inelastic neutron scattering cross sections of cobalt (5). The measured data is indicated by symbols with the present values given by  $\square$ . The solid curve shows the present evaluation. The dashed and dotted curves refer to model calculations based upon alternate spectroscopic schemes.
12. Evaluated inelastic scattering cross sections of cobalt (5). Curve A is from the present work, curve B from ENDF/B (17).
13. Inelastic neutron scattering cross sections of nickel (8). Measured values are indicated by symbols with the present work given by  $\bullet$ . The evaluation is indicated by the solid curve. Hauser-Feshbach calculations based upon spherical and ellipsoidal models are indicated by dashed and dotted curves, respectively. In addition, the effect of the width fluctuation correction to the calculated excitation of the 1.45 MeV state of Ni-58 is shown.

14. Inelastic excitation of the 45 keV, 2+, state in U-238. Measured values are indicated by symbols (7). The present evaluation is indicated by the heavy curve. Its behavior toward threshold follows the predictions of a coupled-channel model. The same model gives the direct inelastic component indicated by the dotted line. The ENDF/B (17) result is indicated by the light curve.
15. Comparison of measured and calculated total cross sections of titanium (9). The upper curve indicates the experimental values and the lower two those calculated from the statistical model based upon ellipsoidal and spherical potentials.
16. Comparison of measured and calculated cross sections for the excitation of the 948 keV state in Ti-48 (9). The format is identical to that of Fig. 15.
17. Evaluated total cross sections of cobalt (5). The region 0.2 to 0.45 MeV is derived from the statistical calculations described in Section III of the text.

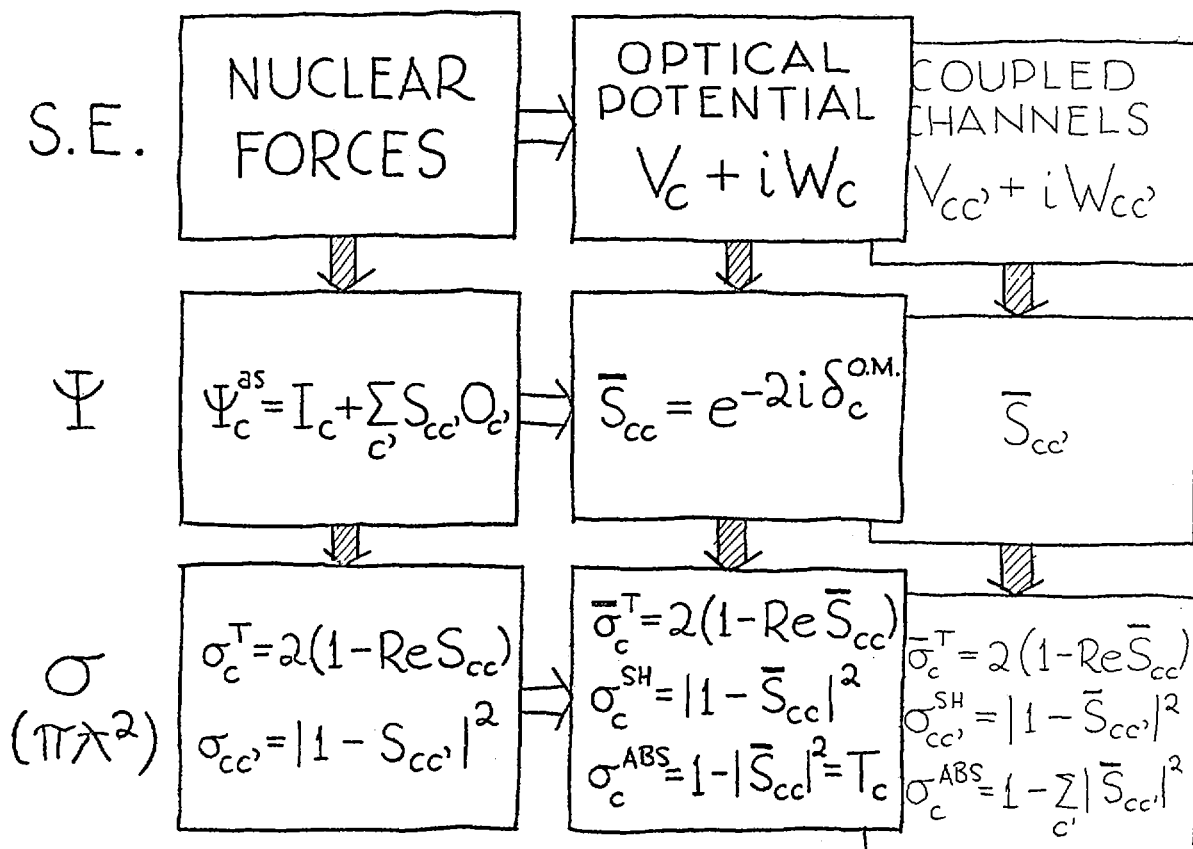


FIG. 1

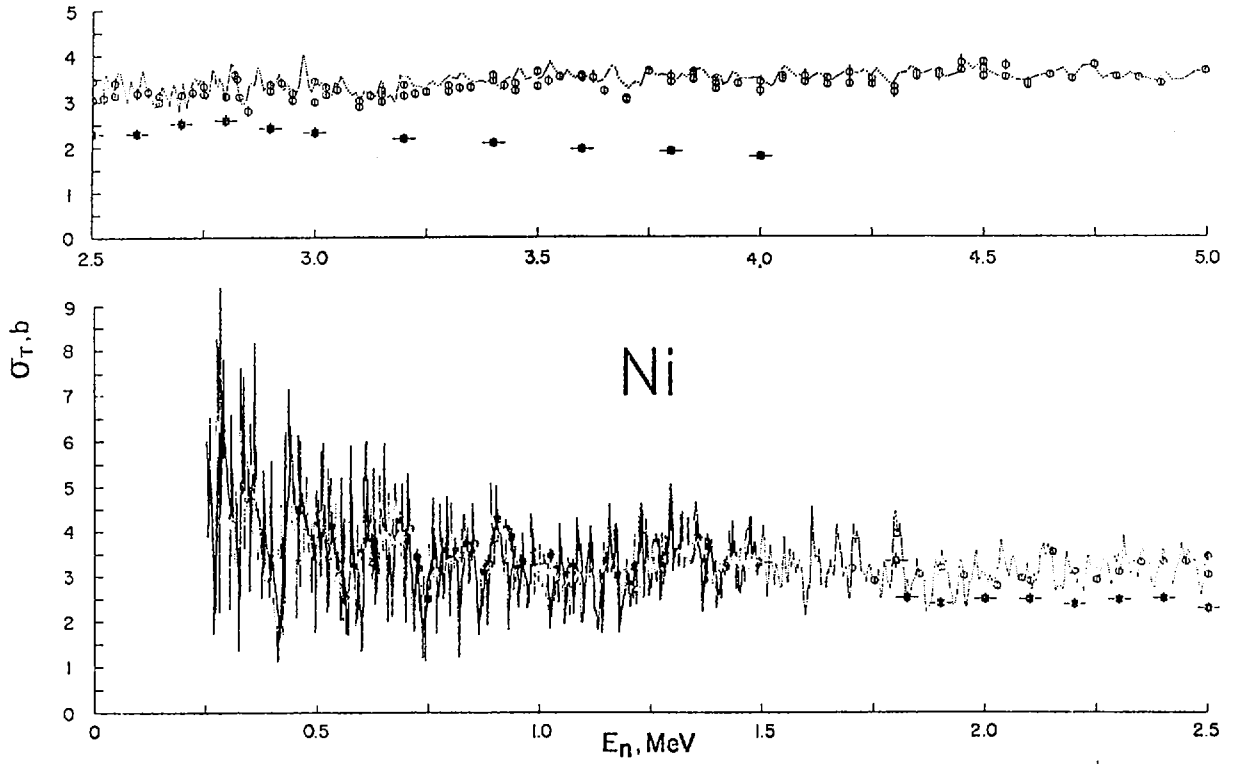


FIG.2

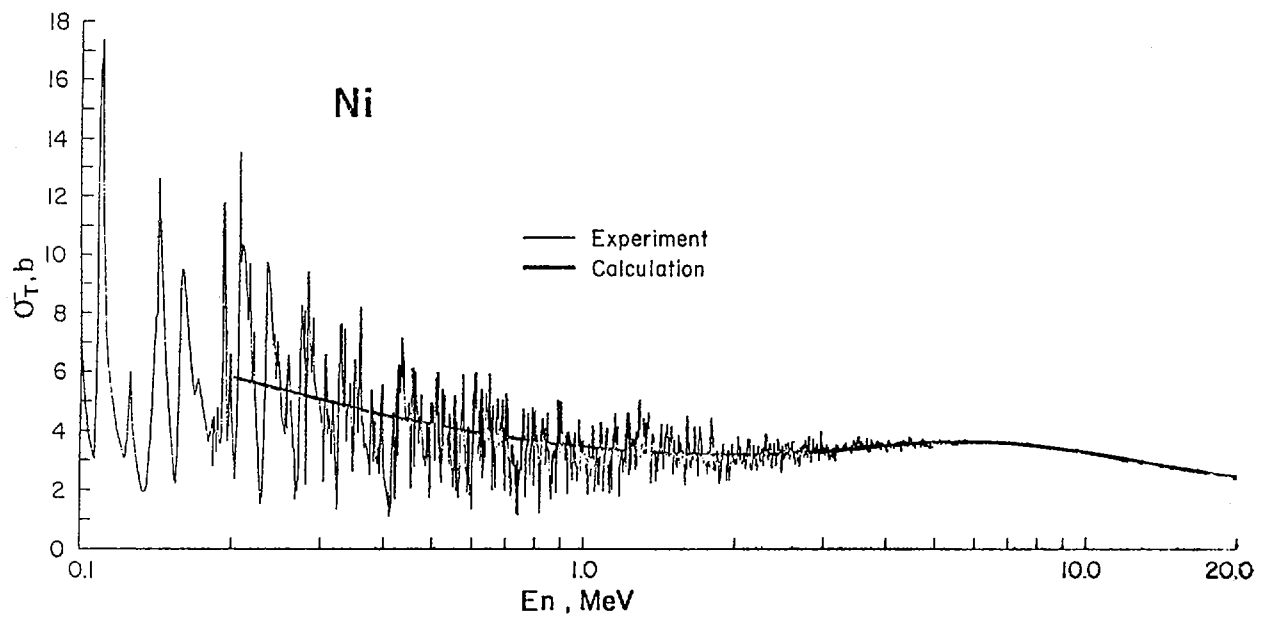


FIG.3

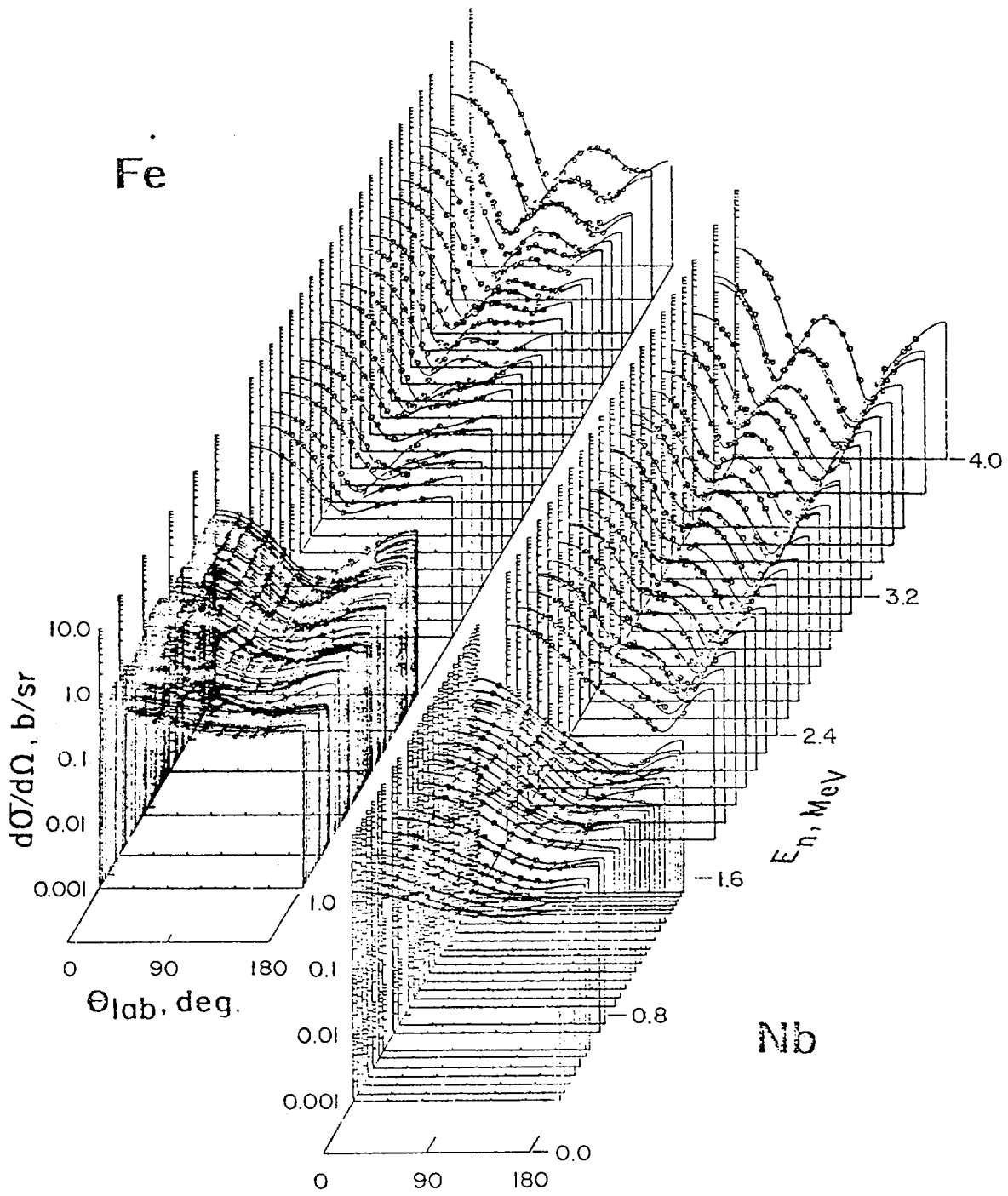


FIG. 4

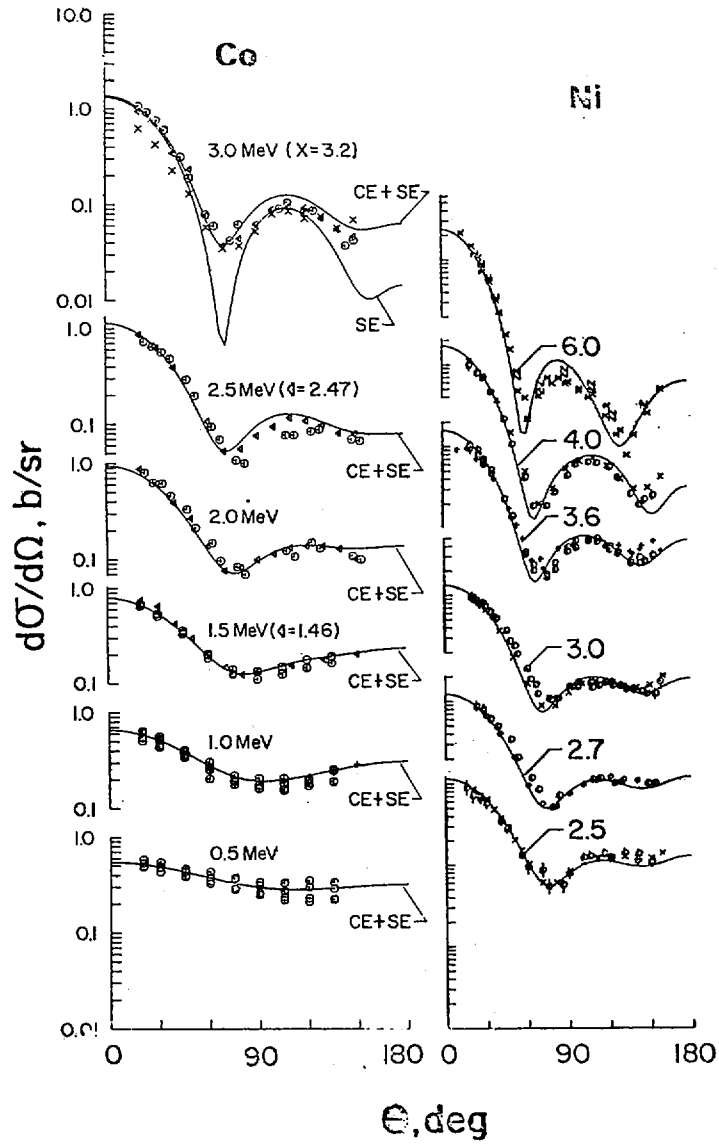


Fig 5

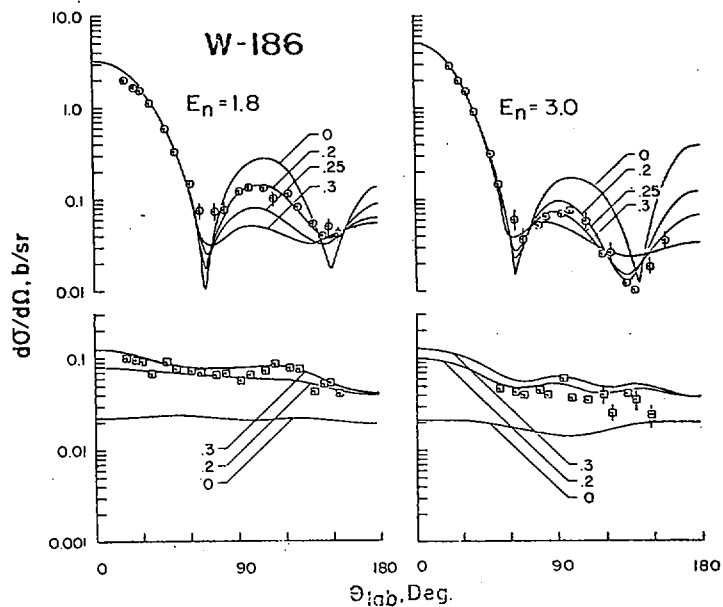


Fig 6

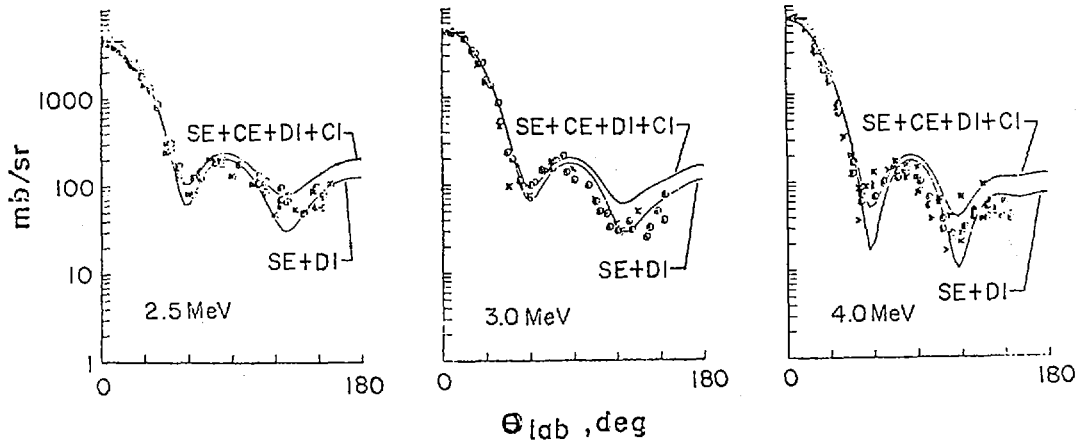


Fig. 7

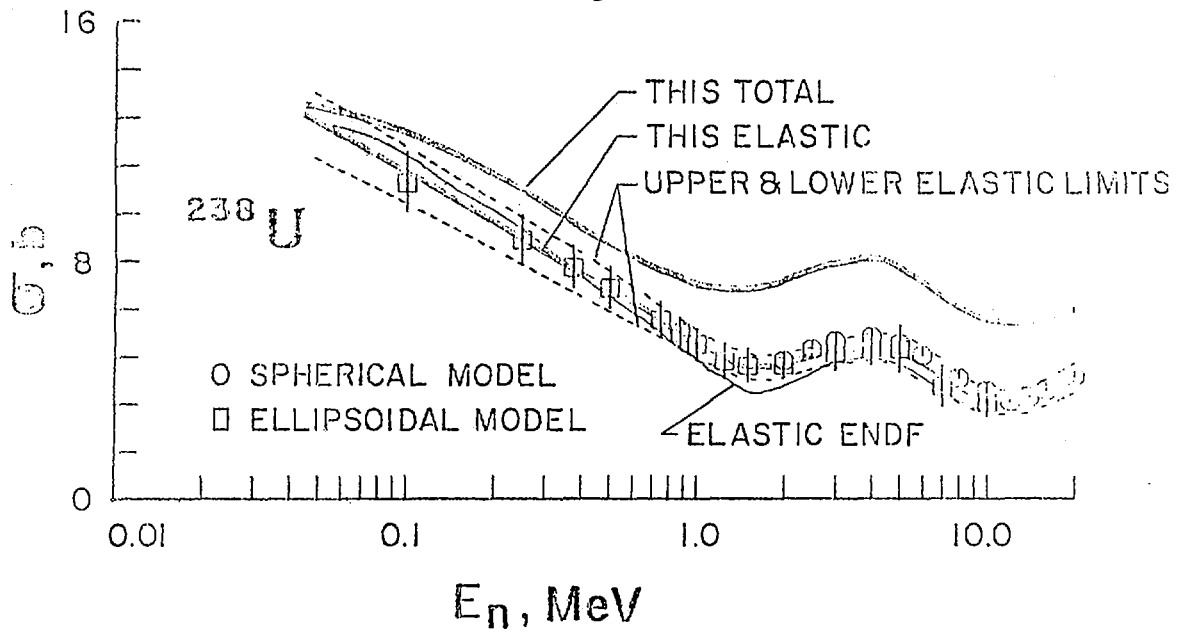


Fig. 8

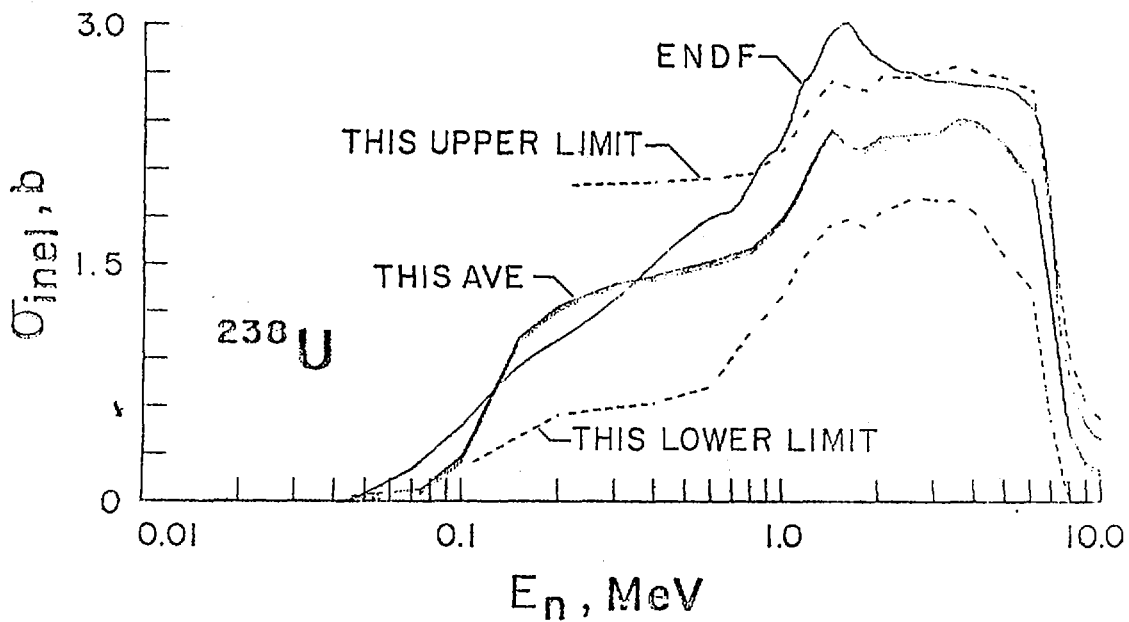


Fig. 9

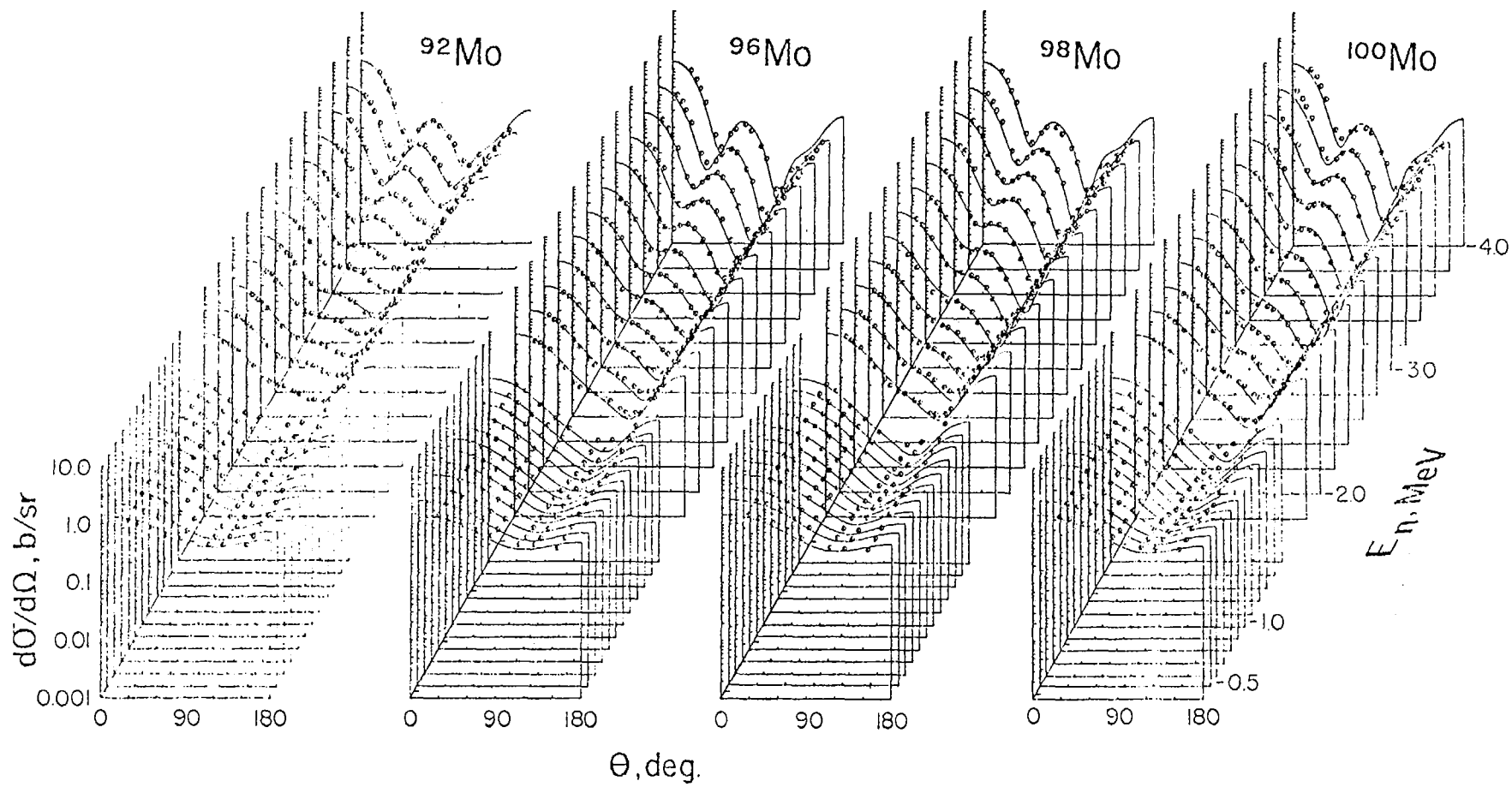


Fig. 10

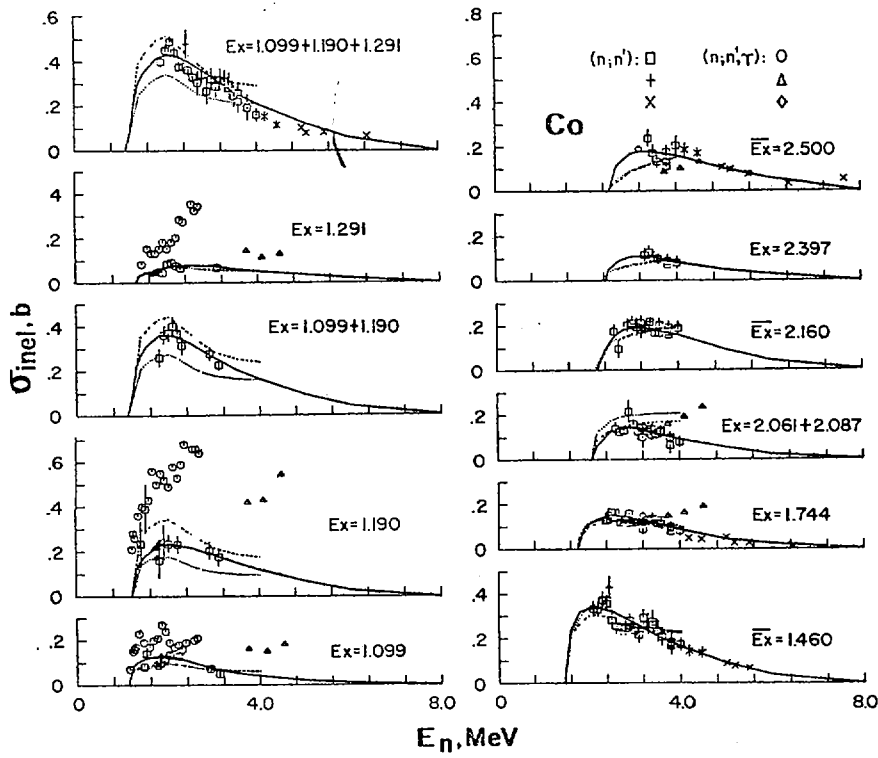


FIG. 11

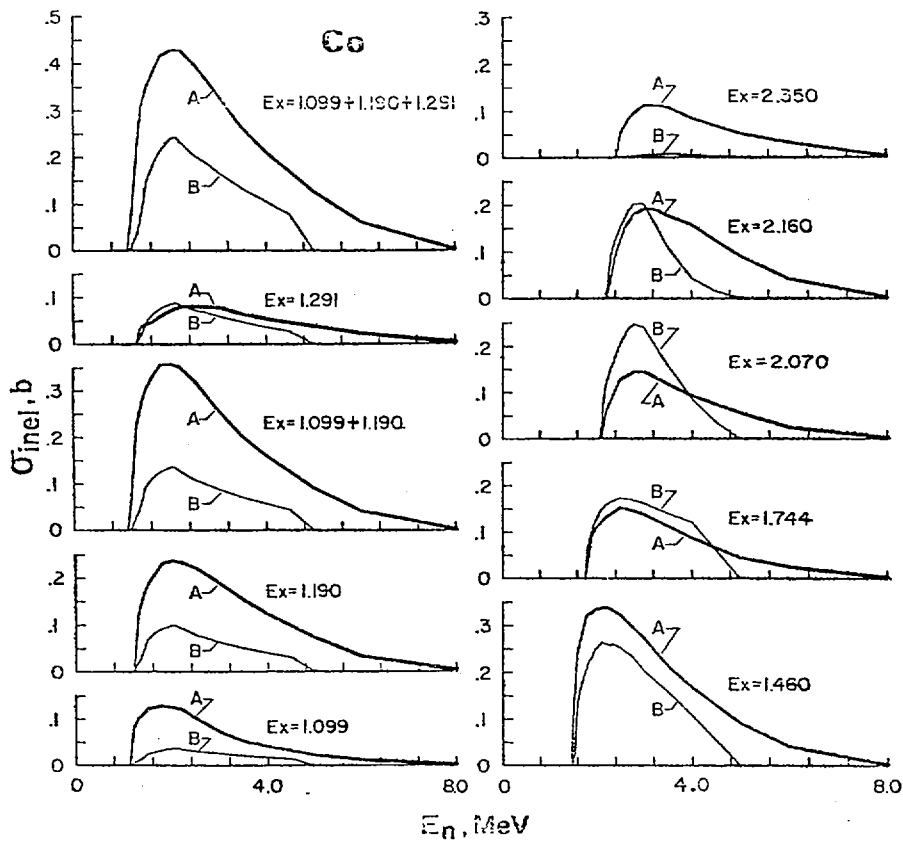


FIG. 12

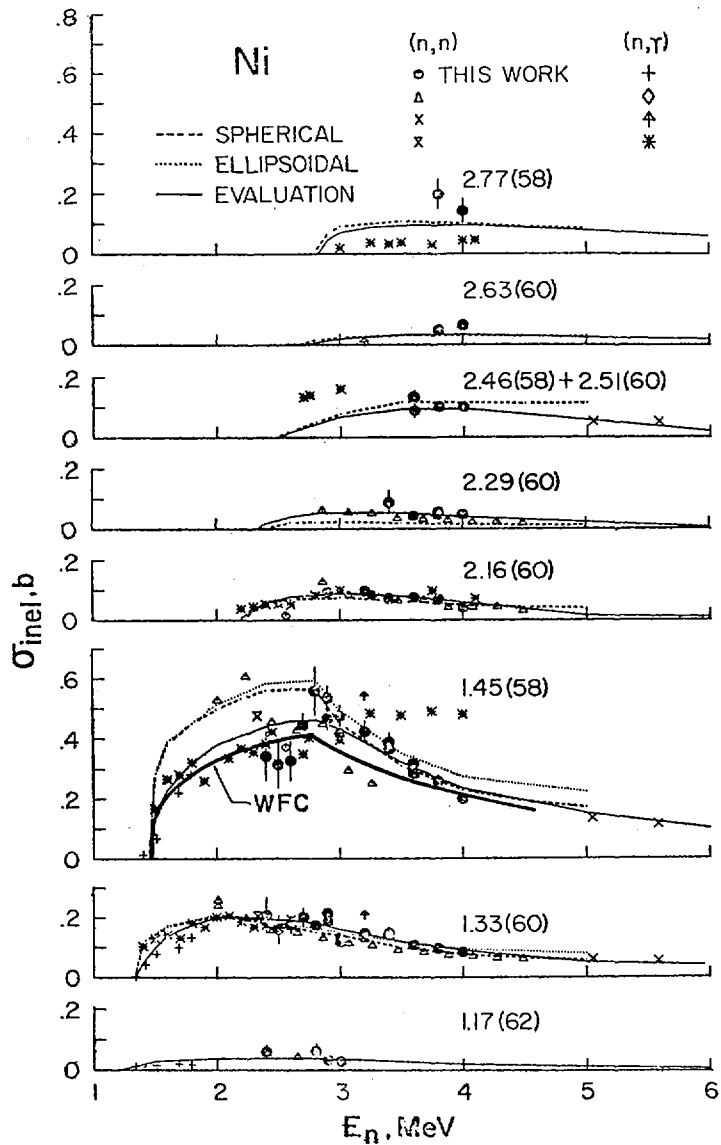


FIG. 13

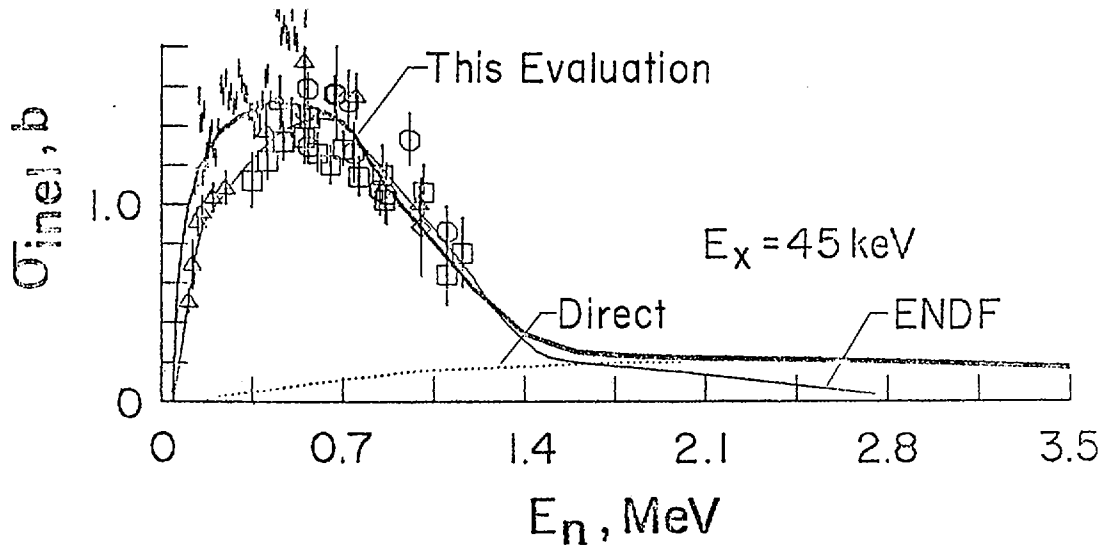


FIG. 14

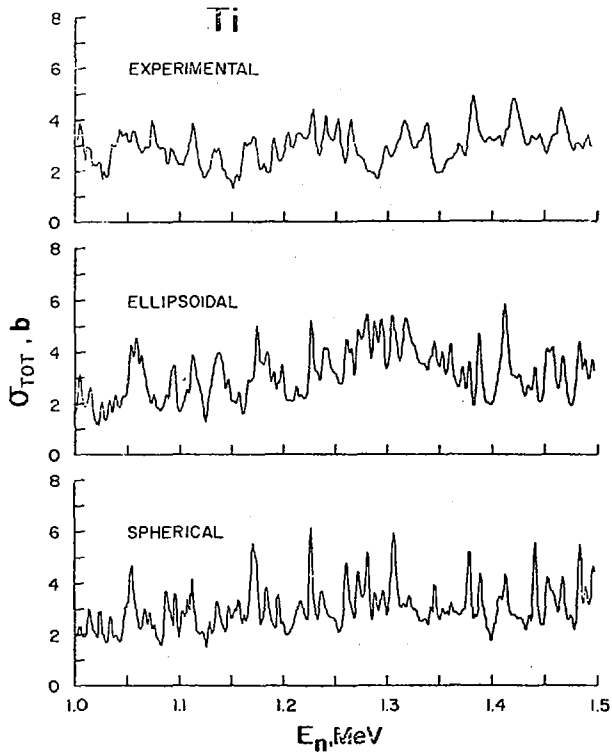


FIG. 15

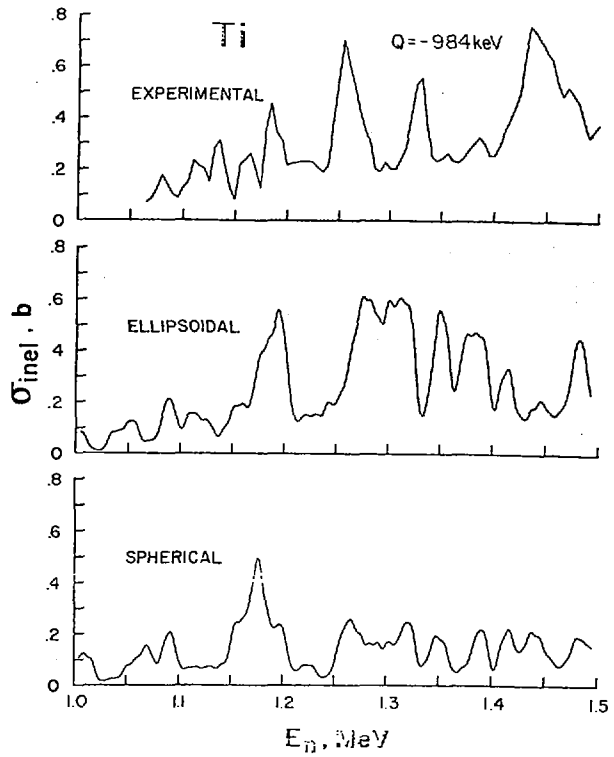


FIG. 16

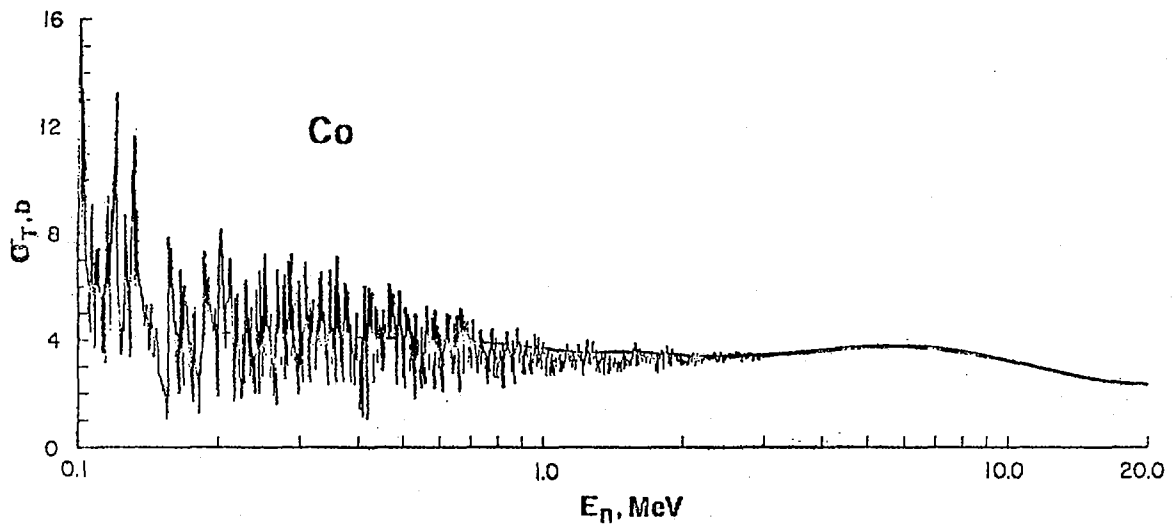


FIG. 17

## DISCUSSION

S. W. CIERJACKS: There has been some time ago some work at Argonne on the investigation of intermediate structure in neutron cross sections. In particular I remember the interpretation of intermediate structure in terms of the intermediate optical potential of Moldauer. Could you comment on the necessity for such a treatment and on the continuation of this kind of work?

H. E. JACKSON, Jr.: This work is certainly continuing. The calculation of fluctuating cross sections from the optical model described in this paper is a continuation of that work.

R. C. BLOCK: You presented some work on  $^{238}\text{U}$  where the elastic scattering was subtracted from the ENDF total cross section, and that in the region  $1 \sim 3$  MeV there was a large difference between the calculated and difference values. At RPI we measured the total cross section of  $^{238}\text{U}$  and found that in the  $1 \sim 3$  MeV region there was a  $3 \sim 5\%$  discrepancy with regard to the ENDF-III value. This is substantiated by the NBS recent measurements. Thus the new difference between total and elastic cross sections will be quite different from the value obtained in your (presented) paper.

## V-1. FREE DISCUSSION

T. FUKETA: The title of this meeting was originally suggested by Prof. W. W. Havens, Jr. at the previous EANDC Meeting. Not to speak of his great contribution to the EANDC, I personally appreciate very much for his advices to this Topical Discussion. We had known that the choice of the title should rather be made by the discretion of the host of the meeting. Aside from that, however, in the program and advisory committee of this Topical Discussion, there has been a criticism on the title of this Discussion Meeting which said that the work "critique" in the title sounds too critical. I myself is not sure about this kind of nuance in English, and I would like to hear about this from the EANDC members at this occasion. But I'm not asking you about the linguistic nuance only.

P. RIBON: Evaluators have a tendency to use the nuclear computer codes as black boxes which provide good answers if good input parameters are entered --- forgetting that there are approximations both in the codes and in the theories.

I have the feeling that Prof. W. W. Havens proposal was to use the opportunity of this topical discussion to remind the approximations used in the theories and in order that physicists tried to define clearly the field of application of these theories and the consequences of various approximations.

J. S. STORY: Dr. Motz showed an R-matrix analysis of the  $n\text{-He}^4$  reactions. In comparison he showed the data from the ENDF/B3 file (MAT-1088); the  $\sim 2$  MeV resonance being slightly shifted in energy. So far as I recall the ENDF/B file was based on a coupled-channel optical model analysis: it might seem surprising at first that the optical model has applications in resonance analysis but so it is. (Another excellent example may be found in the work of Reynolds et al. Phys. Rev. 176, 1213 (1968) in relation to neutron scattering by C-12.) In comparison the ordinary R-matrix theory suffers from being based on the rather artificial concept of the infinite square well and may run into difficulties when applied over an energy range of several MeV; this theory can only be justified by its ability to interpret experimental data.

I should like to utter a further caution against too much reliance on predictions derived from R-matrix theory. The analysis can only be used reliably if one knows all the levels, and even for the light compound nucleus involved in the  $n\text{-Li}^6$  reaction, one does not know the details of all the levels.

A. MICHAUDON: It is a well-known fact that fission theory cannot predict relevant cross sections within 1% accuracy, but there are cases where experimental data are very scarce and for which a crude estimate of the cross sections would be useful. Could a real data user care to comment on this?

It would seem that the development of fission reactors should be sensitive to progress which can be made in the understanding of the fission process. In fact, a break-through has been made in the understanding of the fission process this last decade; for example, fission isomerism, intermediate structure in fission cross sections etc. This makes now the study of the fission process to be quite active now. On the other hand, this activity seems to have little impact on model calculations of fission cross sections. I would like to know, from a user of nuclear data, if more elaborated model calculations of fission data present some interest.

P. RIBON: In most cases the request is for a more accurate knowledge of the absolute value of the average cross section, and for the knowledge of its smooth variation with energy. The nuclear fission theories do not allow, presently, to predict these properties with a good enough accuracy.

J. S. STORY: I thought that Dr. Michaudon's presentation on the calculation of fission cross-sections was valuable. In the future the cross-sections of the transplutonium materials will be required and some of these must be obtained by calculation. At present some are not known to a factor of 2.

List of Participants of the 17th EANDC Meeting

CANADA	Dr. W. G. Cross Biology and Health Division Atomic Energy of Canada Ltd. Chalk River Ontario
EURATOM	Dr. K. H. Böckhoff Bureau Central de Mesures Nucleaires Steenweg naar Retie B-2440 GEEL BELGIUM
FRANCE	Dr. Pierre Ribon Service de la Métrologie et de la Physique Neutroniques Fondamentales Commissariat à l'Energie Atomique Centre d'Etudes Nucléaires de Saclay B.P. No. 2 F-91190-Gif-sur-Yvette
GERMANY	Dr. Siegfried Cierjacks Institut für Angewandte Kernphysik Kernforschungszentrum Karlsruhe D-75 Karlsruhe Postfach 3640
ITALY (Absent from the 17th Meeting)	Prof. V. Benzi Comitato Nazionale per l'Energia Nucleare Centro di Calcolo Via Mazzini 2 40138 Bologna
JAPAN	Dr. Kineo Tsukada Division of Physics Japan Atomic Energy Research Institute Tokai-mura, Naka-gun, Ibaraki-ken
SWEDEN <u>Scientific Secretary</u>	Dr. Henri Condé Research Institute of National Defence FOA 4 S-104 50-Stockholm-80
SWITZERLAND	Dr. Theodor Hürlimann Eidgenössisches Institut für Reaktorforchung CH-5303 Würenlingen
NEA	Mr. J. A. G. Rosen Nuclear Information Division OECD Nuclear Energy Agency 38 Boulevard Suchet F-75016 Paris FRANCE

NEA  
Secretary

Dr. Jacques Royen  
NEANDC Secretariat  
Nuclear Information Division  
OECD Nuclear Energy Agency  
38 Boulevard Suchet  
F-75016 Paris  
FRANCE

UNITED KINGDOM  
Chairman

Mr. John S. Story  
Fast Reactor Physics Division  
Building A.32  
United Kingdom Atomic Energy Authority  
Atomic Energy Establishment  
Dorchester  
Dorset DT2 8DH

Dr. Michael G. Sowerby  
Nuclear Physics Division  
Building 418  
United Kingdom Atomic Energy Authority  
Atomic Energy Research Establishment  
Harwell  
Didcot  
Oxfordshire OX11 0RA

UNITED STATES

Dr. Robert E. Chrien  
Department of Physics  
Brookhaven National Laboratory  
Upton, New York 11973

Dr. Harold E. Jackson  
Argonne National Laboratory  
9700 South Cass Avenue  
Argonne, Illinois 60439

Dr. Henry T. Motz  
Physics Division  
Los Alamos Scientific Laboratory  
P.O. Box 1663  
Los Alamos, New Mexico 87544

Dr. George L. Rogosa  
Division of Physical Research  
U.S. Atomic Energy Commission\*  
Washington, D.C. 20545  
(\*now: U.S. Energy Research and  
Development Administration)

Local Secretary

Dr. Toyojiro Fuketa  
Division of Physics, JAERI  
Tokai-mura, Naka-gun, Ibaraki-ken

EACRP Member

Dr. Jitsuya Hirota  
Division of Reactor Engineering, JAERI  
Tokai-mura, Naka-gun, Ibaraki-ken

Observer

Prof. Kazuo Hisatake  
Department of Applied Physics  
Tokyo Institute of Technology  
2-12-1 Ookayama, Meguro-ku  
Tokyo

Dr. Sin-iti Igarasi  
Division of Physics, JAERI  
Tokai-mura, Naka-gun, Ibaraki-ken

Dr. André Michaudon  
Service de Physique Nucléaire  
Centre d'Etudes de Bruyères-le-Châtel  
B.P. No. 61  
F-92120 Montrouge  
FRANCE

Dr. Shigeya Tanaka  
Division of Physics, JAERI  
Tokai-mura, Naka-gun, Ibaraki-ken

Prof. R. C. Block  
Research Reactor Institute  
Kyoto University  
Kumatori, Sennan-gun, Osaka  
(present address:  
Nuclear Engineering and Science  
Department  
Rensselaer Polytechnic Institute  
Troy, New York 12181  
U. S. A.)

AUTHOR INDEX

Arabic numerals underlined refer to the first page of a paper.  
Other Arabic numerals refer to a contribution to the discussions.

- Benzi, V.: 83
- Bhat, M.R.: 245
- Block, R.C.: 31, 32, 82, 211,  
229, 244, 298
- Chrien, R.E.: 136, 158, 256,  
268
- Cierjacks, S.W.: 31, 229, 230,  
244, 298
- Dodder, D.C.: 1
- Duchemin, B.: 68
- Fabbri, F.: 83
- Fuketa, T.: 299
- Guenther, P.: 269
- Hale, G.M.: 1
- Harada, K.: 103
- Igarasi, S.: 103, 118
- Jackson, H.E.: 118, 119, 268,  
298
- Jary, J.: 76
- Kitazawa, H.: 137, 158
- Kitazoe, Y.: 34, 49
- Lagrange, Ch.: 51, 58
- Michaudon, A.: 49, 82, 300
- Moldauer, P.: 269
- Mori, A.: 103
- Motz, H.T.: 31, 32
- Newstead, C.M.: 230
- Nishimura, K.: 229
- Nisley, R.A.: 1
- Prince, A.: 245
- Reffo, G.: 83
- Ribon, P.: 191, 211, 299, 300
- Sekiya, T.: 34
- Sierra, J.M.: 193
- Smith, A.: 269
- Story, J.S.: 299, 300
- Takahashi, H.: 257
- Tanaka, S.: 82, 212, 229, 256
- Thomet, P.: 71
- Turinsky, P.J.: 193
- Witte, K.: 1
- Yamakoshi, H.: 159, 191
- Yamamuro, N.: 137
- Young, P.G.: 1